

**Importance of CVD-process parameters for the synthesis of
novel Al/Al₂O₃ and Ga/Ga₂O₃ composite nanostructures**

Dissertation

zur Erlangung des Grades
des Doktors der Ingenieurwissenschaften
der Naturwissenschaftlich-Technischen Fakultät III
Chemie, Pharmazie, Bio- und Werkstoffwissenschaften
der Universität des Saarlandes

Von

Eve Awa SOW

Saarbrücken

2008

Tag des Kolloquiums:	29.08.2008
Dekan:	Prof. Dr. U. Müller
Vorsitzender:	Prof. Dr. rer. nat. W. Possart
Berichterstatter:	Prof. Dr. M. Veith Prof. Dr. W. F. Maier
Akad. Mitarbeiter:	Dr. Ing. F. Soldera

Danksagung

Ich bedanke mich recht herzlich bei allen Mitarbeitern des Arbeitskreises von M. Veith sowie des Leibniz-Instituts für neue Materialien, die auf verschiedenste Weise zum Gelingen dieser Arbeit beigetragen haben.

Meinem Doktorvater, Prof. Dr. Michael Veith, danke ich für die spannende Themenstellung, wertvolle Hinweise und herzliche Unterstützung.

Dr. Ulf Werner bin ich besonders dankbar für die hervorragende Arbeit bei den TEM-Messungen und für seine Diskussionsbereitschaft.

Weiterhin danke ich Dr. Christian Holzapfel für die Einführung in die Rasterelektronenmikroskopie und die Zusammenarbeit.

Dr. Volker Huch danke ich für die Durchführung der Röntgenbeugungsanalysen.

Dr. Frank Müller gilt mein Dank für die Durchführung der ESCA-Analysen.

Ich bedanke mich bei allen Kollegen, insbesondere Hakima Smail, Amadou L. Ndiaye und Dr. M. Ehses für die zahlreichen Ratschläge und die freundliche Atmosphäre.

Ein ganz besonderer Dank gilt meiner Familie, insbesondere meiner Mutter, die mich mit ihrer unendlichen Unterstützung bis hierher begleitet hat.

Ich bedanke mich bei meinem Lebensgefährten Dr. Antoine Laurent, der mich mit seinem festen Glauben an meine Person immer wieder bestärkt hat und so einen entscheidenden Beitrag zum Entstehen dieser Arbeit geleistet hat. Vielen Dank.

Unserem ungeborenen Kind danke ich auch, weil es bei dem Zusammenschreiben immer dabei war und mir währenddessen Mut gemacht hat.

Table of contents

Table of abbreviations	iv
Zusammenfassung auf Deutsch	vi
Abstract	vii
1 Introduction and aim of the work	1
1.1 Introduction	1
1.2 Goals of the study	3
2 State of the art	5
2.1 Formation of composite nanostructures by CVD	5
2.2 CVD synthesis of aluminium and aluminium oxide layers	9
2.3 Al/Al ₂ O ₃ composite layers by AK. Veith	11
2.4 Ga/Ga ₂ O ₃ composite layers by AK Veith	17
3 Influence of the CVD parameters on the properties and structure of Al/Al₂O₃ composite layers obtained from the precursor [H₂Al(O^tBu)]₂	21
3.1 Influence of process parameters	22
3.2 Generalities	26
3.3 Evolution of crystallinity	29
3.3.1 Evolution of crystallinity with the time at low precursor flow	30
3.3.2 Evolution of crystallinity with the time at high precursor flow	35
3.3.3 Evolution of crystallinity with the substrate temperature by low precursor flow	38
3.3.4 Evolution of crystallinity with the substrate temperature at high precursor flow	40
3.3.5 Formation of a crystalline phase with unknown composition	41
3.4 Morphological variations	49
3.4.1 At low temperature (490 °C)	49

3.4.2	Deposition at 530 °C	60
3.4.3	Deposition at 560 °C	64
3.4.4	Deposition at high temperature (above 560 °C)	67
3.5	Conclusion	71
4	Structural study of the Al/Al₂O₃ nanowires	75
4.1	Core shell one dimensional nanostructures	75
4.1.1	Synthesis and properties.....	75
4.1.2	One-dimensional Al ₂ O ₃ nanostructures.....	80
4.2	Morphology of Al/Al ₂ O ₃ nanowires	83
4.3	Composition and crystallinity of Al/Al ₂ O ₃ core shell nanowires.....	103
4.4	Effects of intensive electron irradiation.....	121
4.5	Effects of temperature on the sample.....	131
4.6	Conclusion	138
5	CVD with [H₂Ga(O^tBu)]₂ as precursor	141
5.1	Gallium oxide layers	141
5.2	Morphology and composition of the layers obtained by CVD of [H ₂ Ga(O ^t Bu)] ₂	142
5.2.1	On stainless steel.....	142
5.2.2	On copper	150
5.2.3	On Si (100).....	158
5.3	Layers grown with [H ₂ Ga(O ^t Bu)] ₂ and [H ₂ Al (O ^t Bu)] ₂	167
6	Conclusion and outlook	169
7	Experimental part.....	177
7.1	Methodology.....	177
7.1.1	NMR Spectroscopy in solution	177
7.1.2	IR-Spectroscopy.....	177
7.1.3	Powder X-ray Diffraction	177
7.1.4	ESCA	178

7.1.5	Digital camera	178
7.1.6	Scanning electron microscopy (SEM), focused ion beam (FIB), energy dispersive spectroscopy (EDX),	178
7.1.7	Transmission electron microscopy (TEM), SAED and EDX	179
7.2	Synthesis of the precursor molecules.....	179
7.2.1	Synthesis of $[H_2Al(O^tBu)]_2$	179
7.2.2	Synthesis of $[H_2Ga(O^tBu)]_2$	180
7.3	MOCVD Technique	181
7.3.1	Substrate preparation.....	182
7.3.2	High frequency generator.....	182
7.3.3	Vacuum system.....	182
7.3.4	CVD process	182
7.3.5	CVD with $[H_2Al(O^tBu)]_2$	183
7.3.6	CVD with $[H_2Ga(O^tBu)]_2$	184
7.3.7	CVD with $[H_2Al(O^tBu)]_2$ and $[H_2Ga(O^tBu)]_2$	185
References		187
Figures.....		194
Tables		201

Table of Abbreviations and compounds

AFM	Atomic Force Microscopy
AK Veith	Research group of M. Veith
CVD	Chemical Vapor Deposition
1D	One dimensional
3D	Three dimensional
d	Lattice spacing
Dc	Lattice spacing recorded in the crystallite
Dh	Lattice spacing recorded in the head
Ds	Fractal dimension
EDX	Energy Dispersive X-ray Analysis
ERAS	External Reflection Absorption Spectroscopy
FIB	Focussed Ion Beam
FTIR	Fourier Transformed Infrared
HF	High frequency
HRTEM	High Resolution Transmission Electron Microscopy
ICDD	International Centre for Diffraction Data
IR	Infra red
JCPDS	Joint Committee on Powder Diffraction Standards
MOCVD	Metal-organic chemical vapor deposition
NMR	Nuclear magnetic resonance
PDF	Powder diffraction files
PVD	Physical Vapor Deposition
SAED	Selected Area Electron Diffraction
SEM	Scanning Electron Microscopy

TEM	Transmission Electron Microscopy
UV	Ultra violet
VLS	Vapor Liquid Solid
VS	Vapor Solid process
XRD	X-Ray Diffractometry
θ	Angle
λ	Wavelength
B	Integral peak breadth
K	Size factor= 1
R	Volume average particle size
R _a	Mean roughness
T	Temperature
Al/Al ₂ O ₃	Aluminium-aluminium oxide composite
AlCl ₃	Aluminium chloride
AlH ₃	Aluminium hydride
^t BuOH	Tertbutanol
HAIO	Oxoaluminiumhydride
LiAlH ₄	Lithium aluminium hydride
[H ₂ AlO ^t Bu] ₂	Bis[(tert-butoxy)-aluminium dihydride]
[HAl(O ^t Bu) ₂] ₂	Bis[(di-tert-butoxy)-aluminium hydride]
LiGaH ₄	Lithium gallium hydride
Ga/Ga ₂ O ₃	Gallium-gallium oxide composite
GaCl ₃	Gallium chloride
GaH ₃	Gallium hydride
[H ₂ GaO ^t Bu] ₂	Bis[(tert-butoxy)-aluminium dihydride]
[HGa(O ^t Bu) ₂] ₂	Bis[(di-tert-butoxy)-aluminium hydride]

Kurzzusammenfassung

Es wurden mittels chemischer Gasphasenabscheidung aus dem *Single-Source-Precursor* $[\text{H}_2\text{Al}(\text{O}^t\text{Bu})]_2$ Komposit-Al/ Al_2O_3 Schichten hergestellt. Zur Herstellung unterschiedlicher Schichten wurden Prozessparameter wie z. B. Abscheidungsdauer, Targettemperatur und Precursorfluss variiert. Anschließend wurde eine systematische Untersuchung der Kristallinität (XRD), Zusammensetzung (EDX), Struktur und Morphologie (REM und TEM) der Schichten durchgeführt und es hat sich gezeigt, dass sich bei einer Targettemperatur unterhalb von $510\text{ °C} \pm 15\text{ °C}$ sphärische Partikel und oberhalb eindimensionale Nanodrähte bilden. Sowohl die Partikel als auch die Nanodrähte bestanden aus in Aluminiumoxid eingebetteten Aluminiumkristalliten (Core-Shell Struktur). Die kristallinen Struktureigenschaften der Schichten spielen dabei eine wichtige Rolle für das eindimensionale Wachstum. Da kein Katalysator benötigt wurde, ist zu vermuten, dass es sich um ein selbst katalytisches eindimensionales Wachstum handelt.

Ferner wurden auch mit dem Precursor $[\text{H}_2\text{Ga}(\text{O}^t\text{Bu})]_2$ Schichten hergestellt. Untersuchungen mittels REM und EDX haben gezeigt, dass mit $[\text{H}_2\text{Ga}(\text{O}^t\text{Bu})]_2$ im Vergleich zu $[\text{H}_2\text{Al}(\text{O}^t\text{Bu})]_2$ Schichten mit einer wesentlich größeren Vielfalt an unterschiedlichen Strukturen erhalten werden. Es wurden Galliumnanodroplets, sowie 1D- und 3D-Nanostrukturen mit unterschiedlicher Menge an Gallium, Galliumoxid und Kohlenstoff gewonnen. Dabei waren auch die Eigenschaften des Substrats von großer Bedeutung.

Abstract

Composite Al/Al₂O₃ films are deposited by chemical vapor deposition (CVD) of the precursor [H₂Al(O^tBu)]₂. Deposition parameters like precursor flow, substrate temperature and deposition time are varied to obtain different layers. They are systematically characterised to investigate their crystallinity (XRD), composition (EDX), structure and morphology (SEM and TEM). Either ball-like core shell structures of aluminium and alumina or with raising temperature (510°C to 600°C) nanowires of aluminium embedded in Al₂O₃ are produced. Interesting parallelism between the crystalline structure and morphology is drawn to confirm the role of aluminium in the one dimensional growth. No catalysis is needed to produce the different morphologies, as the growth mechanism proceeds in a self catalytic way. Preliminary investigations on layers grown with similar conditions are carried out with the homologue precursor [H₂Ga(O^tBu)]₂. SEM and EDX analysis evidenced high diversity of the layers obtained. Gallium nanodroplets, 1D and 3D nanostructures with varying amount of gallium, Ga₂O₃ and carbon are synthesised. Particularly, the substrate nature played an important role in this case.

1 Introduction and aim of the work

1.1 Introduction

Nanotechnology is design, fabrication, and application of nanostructures or nanomaterials, and the fundamental understanding of the relationships between physical properties and material dimensions. It is a highly multidisciplinary field, such as applied physics, materials science, colloidal science, device physics, supramolecular chemistry, and even mechanical and electrical engineering. Nanotechnology can be seen as an extension of existing sciences into the nanoscale. It is a challenging area in expansion.

Nanostructures - structures that have at least one dimension between 1 and 100 nm have received growing interest due to their peculiar and fascinating properties and applications superior to their bulk counterparts. The ability to generate such miniscule structures is essential to much of modern technology for example in microelectronics, where smaller means greater performance, faster operation, lower cost and less power consumption.

Two main approaches are used to synthesise nanostructures. In the "top-down" approach, nano-objects are constructed from larger entities by miniaturisation. In the "bottom-up" approach, materials and devices are built from molecular components which assemble themselves chemically.

Among the "bottom-up" approaches, chemical vapor deposition (CVD) is widely used as it is able to produce thin layers of almost every material categories and even composite materials. Therefore, the materials synthesised by CVD present a high diversity and can be used in different areas including microelectronics,

optoelectronics, protective coatings against corrosion or oxidation, energy conversion devices and refractory ceramic materials.

The key element that has increased the use of the CVD processes has been the ability to deposit films with a reproducible nanostructure, like for example one dimensional nanostructures.

Since the discovery of carbon nanotubes, one-dimensional nanostructures such as wires, rods, belts and tubes have been the focus of intensive research owing to their versatile properties and applications. One dimensional nanostructures provide a good system to investigate the relationship between electrical transport, optical and other properties with size confinement. Moreover, by introducing material diversity within nanoarchitecture, composite nanowires are created: they have become very attractive in the last years as they act as active components for electrical and optoelectrical devices. Thus, coaxial core shell structure can be realized, therefore the properties and application are multiplied; for instance nanocables can be realised with a conductive core surrounded by an insulator shell.

One of the crucial factors in the synthesis of nanowires is the control of composition, morphology, size and crystallinity. CVD has been widely employed to fabricate nanowires because of the versatility of materials that can be deposited, but also because of the possibility to manage precisely the characteristic of the film by controlling the significant deposition parameters: substrate temperature, precursor flow and deposition time. By varying the deposition temperature, the research group of M. Veith (AK Veith) succeeded to grow layers with totally different composition, morphology, roughness and crystallinity with the single source molecular precursor $[\text{H}_2\text{Al}(\text{O}^t\text{Bu})]_2$.

Among the variety of technically relevant inorganic thin films made by CVD, a lot of materials contain elements of the group XIII and their oxides (Al, Ga, In), which exhibit electrical, optical and chemical sensing characteristics; they are mainly used in the advanced technology for example for semiconducting devices or biosensors. Introducing a small amount of metallic aluminium (or gallium) in an aluminium oxide (or gallium oxide) nanostructure permits to diversify the properties of the ceramic by adding metallic properties, like for example good conduction.

1.2 Goals of the study

Following the works carried out by AK. Veith, the objective of the present dissertation are the following:

Characterisation of the composite layers made by different CVD parameters:

To control the material synthesis it is essential to know which parameters interfere in the nanostructure, crystallinity, composition and morphology of the layer. It has for instance already been noted that the final colour of the composite layer made by AK Veith, depends on the deposition substrate temperature. In this work the CVD parameters, which influence mostly the obtained layers, will be varied and a systematic study of the morphology and microstructure will be carried out with scanning electron microscopy (SEM). The identification of the crystal phases as well as the evolution of the crystallinity will be studied by XRD.

The Al/Al₂O₃ layers at high temperature-a core-shell nanowires system:

In the present study it will appear that above 530°C the layers display a one dimensional nanostructure, which differs totally from the fractal structure published in reference 19 by M. Veith. The transmission electron microscope (TEM) will be used as the unique adequate method to analyse the nanowires composition, morphology and nanostructure. Electron scattering will analyse the amorphous and crystalline fractions at the nanoscaled. An attempt to describe this exceptional growth process will be presented.

Layers obtained by deposition of the equivalent gallium precursor:

Gallium is in the same group as aluminium in the periodical classification; [H₂Ga(^tBuO)]₂ has a low melting point and is quasi liquid at room temperature thus it is a good candidate for CVD. Stefan Faber, a precedent member of AK Veith succeeded to grow layers with this precursor. A further goal of this work is the characterisation of layers grown with [H₂Ga(^tBuO)]₂ by varying CVD parameters on many substrates. An preliminary investigation will be performed to deposit a film with both [H₂Al(^tBuO)]₂ and [H₂Ga(^tBuO)]₂ precursors.

2 State of the art

2.1 Formation of composite nanostructures by CVD

Chemical vapour deposition (CVD) is the most practical method for preparing thin films for large-scale applications¹.

Chemical Vapour Deposition involves the dissociation and/or chemical reactions of gaseous reactants in an activated (heat, light, plasma) environment, followed by the formation of a stable solid product. The deposition implicates homogeneous gas phase reactions, which occur in the gas phase, and/or heterogeneous chemical reactions which occur on/near the heated surface leading to the formation of powders or films, respectively. The CVD process has been very extensively studied and very well documented^{1, 2, 3}. Chemical vapor deposition represents the method-of-choice for thin film growth, as well as nanomaterials such as carbon nanotubes. The advantages of this technique include low cost and strict control over the resultant film stoichiometry, morphology, and thickness. There has been a continuing interest in the development of new CVD precursors, that would be useful for many applications. This chapter will give an overview about the advantages and principles of the CVD process followed by some examples of applications, whereas the process parameters which influence most of the deposition, will be discussed in chapter 3.

Among the possible deposition technologies CVD has a number of key benefits that make it an attractive technology in research, development and production. For example it is able to produce conformable coatings and large area deposition to handle materials with high vapour pressure (e.g. Pb⁴) and to produce multi-layers as well as composite layers.

CVD has the following distinctive advantages in comparison with other deposition methods:

- Production of highly dense and pure materials.
- Production of uniform films with good reproducibility and adhesion at reasonably high deposition rates.
- CVD is a non-line-of-sight process with good throwing power. Thus, coating of complex shaped components.
- Control of crystal structure, surface morphology and orientation of the CVD products by controlling the CVD process parameters.
- Reasonable processing cost
- The flexibility of using a wide range of chemical precursors such as halides, hydrides and organometallics, which enable the deposition of a large spectrum of materials including metals, carbides, nitrides, oxides, sulphides, III–V and II– VI materials.
- Relatively low deposition temperatures and the desired phases can be deposited in-situ at low energies through vapour phase reactions and nucleation and growth on the substrate surface.

However CVD presents some disadvantages like:

- Chemical and safety hazards caused by the use of toxic, corrosive, flammable and/or explosive precursor gases.
- Difficult to deposit multicomponent materials with well controlled stoichiometry using multi-source precursors because different precursors have different vaporisation rates. However, this limitation can be overcome using single source chemical precursors.
- The use of a more sophisticated reactor and/or vacuum system by CVD variants tends to increase the cost of fabrication.

Recently, the use of CVD in different areas like aerospace, military, science and engineering has been increasing. Advanced products can be realised including bulk materials as well as composites, coatings and films. The application categories are the following:

- Extraction and pyrometallurgy,
- Electronic and optoelectronic materials,

- Surface modification coatings,
- Ceramic fibres and Ceramic matrix composites
- Rapid prototyping including free standing shapes
- Nanostructured materials, in particular one-dimensional structures

The versatility of CVD permits a considerable increase and it has become a leading method for the deposition of thin films and coatings for a wide range of applications, including semiconductors (e.g. Si, Ge, Si_{1-x}Gex, III–V, II–VI) for microelectronics, optoelectronics, energy conversion devices (e.g. solar cells); dielectrics (e.g. SiO₂, AlN, Si₃N₄) for microelectronics; refractory ceramic materials (e.g. SiC, TiN, TiB₂, Al₂O₃, BN, MoSi₂, ZrO₂) used for hard coatings, protection against corrosion, oxidation or as diffusion barriers; metallic films (e.g. W, Mo, Al, Au, Cu, Pt) for microelectronics and for protective coatings; fibre production (e.g. B and SiC monofilament fibres) and fibre coating. It has become one of the main processing methods for the deposition of amorphous, single-crystalline and polycrystalline thin films and coatings.

In general, the CVD process involves the following key steps, that are illustrated on the figure 2.1:

- (1) Generation of active gaseous reactant species.
- (2) Transport of the gaseous species into the reaction chamber.
- (3) Gaseous reactants undergo gas phase reactions forming intermediate species:

At a high temperature above the decomposition temperatures of intermediate species inside the reactor, a homogeneous gas phase reaction can occur where the intermediate species undergo subsequent decomposition and/or chemical reaction, forming powders and volatile by-products in the gas phase. The powder will be collected on the substrate surface and may act as crystallisation centres, and the by-products are transported away from the deposition chamber. The deposited film may have poor adhesion.

At temperatures below the dissociation of the intermediate phase, diffusion/convection of the intermediate species across the boundary layer occur. These intermediate species subsequently undergo steps (4)–(7).

(4) Absorption of gaseous reactants onto the heated substrate and the heterogeneous reaction occurs at the gas–solid interface (i.e. heated substrate) which produces the deposit and by-product species.

(5) The deposits will diffuse along the heated substrate surface forming the crystallisation centre and growth of the film.

(6) Gaseous by-products are removed from the boundary layer through diffusion or convection.

(7) The unreacted gaseous precursors and by-products will be transported away from the deposition chamber.

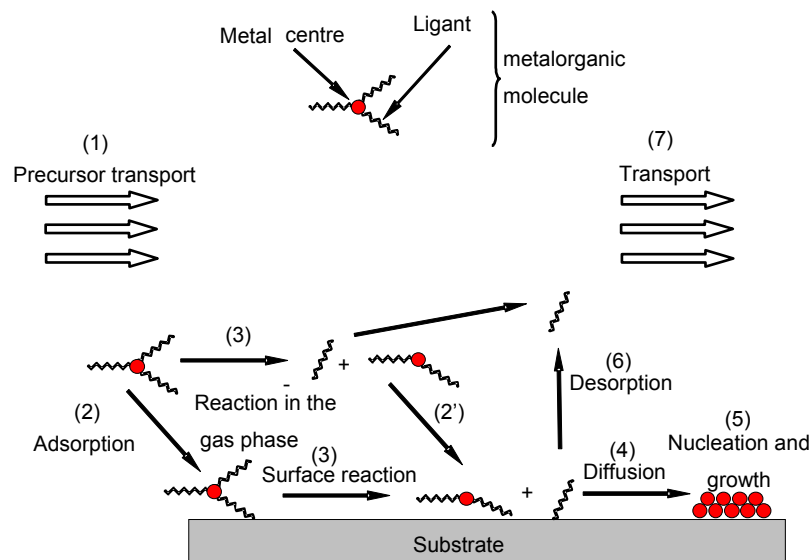


Figure 2-1: Schematic representation of the key steps of the CVD process.

The most critical component of the MOCVD process is the precursor that is employed. Hence, there has been a continuing interest in the development of new MOCVD precursors that would be useful for a range of thin film applications. The metal alkoxides offer essentially the simplest precursors as they show a reasonable vapour pressure. They have been used very successfully for a number of materials, such as the widely used tetraethoxilane for SiO_2 deposition with excellent conformality⁵.

2.2 CVD synthesis of aluminium and aluminium oxide layers

Many reports describe the formation of layers containing the elements aluminium, oxygen and hydrogen by chemical vapour deposition; some of them are discussed in following chapter. For more information, an extensive overview is given in reference 6.

The most common molecule to form thin aluminium films is trimethylaluminium ($\text{Al}_2(\text{CH}_3)_6$)⁷, which decomposes under H_2 atmosphere at temperatures between 350 °C and 550 °C into aluminium and methane. At lower temperatures (between 200 °C and 350 °C) triisobutylaluminium ($\text{Al}(\text{CH}_2\text{-CH}(\text{CH}_3)_2)_3$) decomposes into aluminium isobutene and hydrogen⁸. Metalorganic molecules like dimethylaluminium-hydride ($(\text{CH}_3)_2\text{AlH}$) are rarely used⁹ but, as reviewed in reference 10, the so called alane-precursors are popular for the formation of aluminium films. Apart from the precursor used in this work, trimethylamine alane ($\text{H}_3\text{Al}\cdot\text{N}(\text{CH}_3)_3$)¹¹ and dimethylethylamine alane ($\text{H}_3\text{Al}\cdot\text{N}(\text{CH}_3)_2\text{C}_2\text{H}_5$)¹² are the most useful alane-precursors. During deposition of alane precursors, β -elimination is established; the resulting film shows high purity. These precursors are attractive since they are often liquid at room temperature which allows the facile control of transport properties relative to solid precursors, and the lack of Al-C bonds result in low carbon content of the resulting layers.

The most common reaction for direct deposition of Al_2O_3 by CVD is based on the gas mixture $\text{AlCl}_3/\text{H}_2/\text{CO}_2$ ¹³, where a high temperature process (>1000 °C) is applied for the growth of α - Al_2O_3 . Alumina coatings can be also produced directly at lower temperature by pyrolytic Al_2O_3 decomposition of metalorganic precursors in the presence of oxygen sources. By using aluminium triisopropoxide^{14, 15}; aluminium-tris-*sec*-butoxide¹⁶, aluminium acetylacetonate^{17,18} and aluminium hexafluoroacetylacetonate¹⁹ the deposition temperature may be reduced to 200 °C till 600 °C, but the resulting layer will be amorphous Al_2O_3 or γ - Al_2O_3 but not the most stable α - Al_2O_3 phase.

M. Veith and co-workers demonstrated the possibility of using alkoxi- and siloxi-alanes, beside the alkyl- and alkylamine-alanes, as precursors to form aluminium oxide or aluminium/ aluminium oxide composite layers^{20, 21}. The work done by AK

Veith will be discussed in the next chapter, but there are many other alkoxialane precursors with general formula $(RO)AlH_2$ or $(RO)_2AlH$ ^{22, 23, 24}. They nevertheless do not produce composite materials. They include $[Ph_3(CO)_2AlH(THF)]$, $[(2,6\text{ tBu}_2\text{ 4-Me-H}_2\text{C}_6\text{O})_2AlH(OEt_2)]$, $[(tBu)_2MeCOAlH_2]_2$, $[(iPrO)_2AlH(iPrO)AlH_2]_2$, $[tBuMeHCOAlH_2]_4$, $[iC_3H_7OAlH_2]_2$ and $[(iC_3HH_7O)_2AlH]_2$. According to their sterical constrains, these molecules are mono-, di- oligo- or polymers. $[tBuMe_2SiOAlH_2]$ developed by M. Veith and co-workers is an example of siloxyalanes used as precursor for the CVD²¹.

Alkoxyalanes are synthesised by an in situ reaction of AlH_3 with the corresponding alcohol. The substitution of the hydride by alkoxi-groups occurs gradually depending on the stoichiometry of the reactants. AlH_3 is synthesised in situ from $LiAlH_4$ and $AlCl_3$. First an etherate is obtained, which polymerises, if it is not used immediately.

Usually, the formation of metal/ metal oxide composite layers is due to the disproportionation of a metal, which was in a middle oxidation state. No aluminium molecular precursors are yet available in the oxidation number (+1); therefore no aluminium/aluminium oxide layers have been produced by this way. An alternative approach is to use an aluminium precursor with oxidation number (+3) and to introduce a reduction agent in the precursor molecule, which will generate the creation of an intermediate with formal oxidation number (+1), that can later disproportionate. The precursor used in this work, $[H_2Al(O^tBu)]_2$, presents this characteristic.

The compound tert-butoxyalane $[H_2Al(O^tBu)]_2$ was synthesised in 1968²⁵, but the crystal structure was discovered in 1996 within the PhD work of S. Faber supervised by M. Veith²⁶. The molecular structure is illustrated in figure 2-2. A simple synthesis, which is illustrated by equations 2.1 and 2.2 was proposed²⁷ and a patent was applied²⁸.



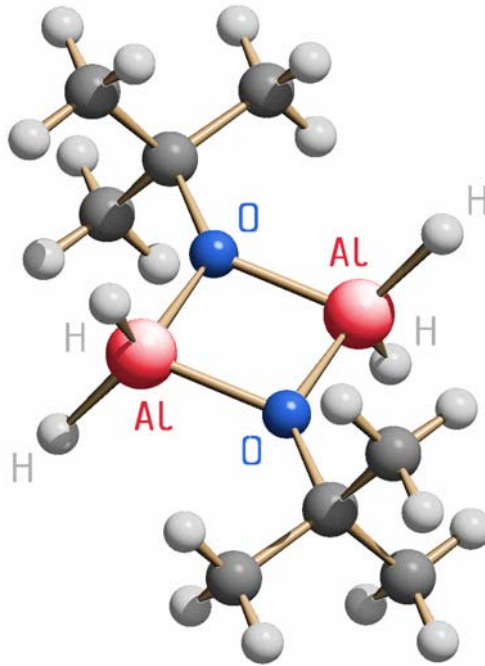


Figure 2-2: Molecular structure of the precursor $[\text{H}_2\text{Al}(\text{OtBu})]_2$ as described in reference 27.

The molecule crystallises in a monoclinic crystal system in the space group $P2_1/n$. The molecule is constituted of 2 identical units, it possesses an inversion centre and quasi the point symmetry $2/m$ (C_{2h}). The molecule is composed of a centrosymmetric, planar 4-ring of Al-O-Al-O. Tert-butoxy rests are attached to both trigonal planar coordinated oxygen atoms. Both tetrahedra coordinated aluminium atoms are bounded to two hydrogen atoms. The described molecule constitutes an efficient single source precursor for the fabrication of hydrogen-aluminium-oxygen compounds or aluminium/ aluminium oxide materials. The main studies to this are reported in many articles cited in next chapter and in PhD works done in AK. Veith by S. Faber²⁷, E.W. Fritscher²⁹, J. Blin³⁰, K. Andres³¹, Y. Wolf³² and C. Petersen³³. In the following the results obtained about the fabrication and characteristics of the aluminium/aluminium oxide layers will be summarised.

2.3 Al/Al₂O₃ composite layers by AK. Veith

Since 1986, our group, AK Veith at the University of Saarland has concentrated a lot of efforts on the synthesis and characterisation of thin inorganic films made by CVD-process through the deposition of alkoxide single source precursors. With tert-

butoxyalane, a lot of results have been gathered, which differ according to the substrate type (silicon, quartz, glass or metals) or to the temperature range used. Faber used for example a hot wall CVD reactor with temperatures between 300 °C and 400 °C on quartz and glass substrates. Mass spectroscopic measurements showed that the pyrolysed gas contains water as mass / charge ratio equals 18 ($m/z=18$). In the results presented in Faber's dissertation²⁷, adsorbed water played a certain role. On quartz the layers obtained are constituted by spherical particles (app. several μm), which display a fractal distribution of aluminium cores embedded in aluminium oxide shells³⁴. The fractal nature of the spheres was investigated via atomic force microscopy and small angle neutron scattering; a fractal dimension of $D_S=2.26\pm 0.05$ is calculated. Energy dispersive X-Rays (EDX) demonstrated that the stoichiometric ratio in the layers meets the ratio of the elemental components from the precursor, i.e. aluminium / oxygen = 1/1. Moreover, due to the ligand's nature, a cascade of reactions occurs, thus only few products form and therefore almost no contamination of the solid material^{35, 36} is observed. According to infra red (IR) and nuclear magnetic resonance (NMR), the hydrogen atoms are mainly hydride, i.e. bridging hydrogen atoms bonded to aluminium. X-Ray diffraction (XRD) and transmission electron microscopy (TEM) detected as single crystalline phase metallic aluminium particles with diameters between 5 nm and 140 nm, no crystalline aluminium oxide was detected.

Faber has also deposited $[\text{H}_2\text{AlOtBu}]_2$ on metallic substrates (copper, nickel and aluminium) in a cold wall reactor, the same type as used in the present work. No difference was noticed between the three metals, which were heated at temperatures between 250 °C and 520 °C. Two types of layers were obtained depending on substrate temperature. The precursor decomposes on metal surfaces heated to 300 °C and under reduced pressures of 0.01-0.1 atm with elimination of dihydrogen and isobutene to form a glasslike, amorphous film, which is composed of equimolar parts of hydrogen, aluminium and oxygen (HAIO)³⁷. At higher temperature and under further evolution of hydrogen, the formation of black Al/Al₂O₃ composite layers displaying a globular fractal microstructure was reported³⁴. In the following, the properties and applications of the layers grown at low substrate temperature will be summarised shortly. Then an exhaustive summary of the characteristics of the layers grown at higher temperature will be done, as it is a starting point for present work.

Below 450 °C the layers obtained are particularly smooth ($R_a = 5 \text{ nm}$)³¹. By increasing the precursor flow rate (0.23 mbar), the roughness grows ($R_a = 47 \text{ nm}$). It is probably the formation of the spherical structure characterised by Faber. According to Wolf³², a substrate change induces variations in the hydrogen atom fraction. The evaluation occurs on platinum substrates in a temperature range between 250 °C and 310 °C, where the hydrogen fraction reaches app. 80%. By extrapolation it has been calculated that at 238 °C the layer obtained should have the composition H:Al:O = 1:1:1. But the precursor cannot decompose by such a low temperature. An important characteristic of the layers made at low temperature is that no crystalline phase is detected either by XRD or by TEM. More details about the composition of HAIO layer are given in reference 32. In particular HAIO have intensively been analysed by IR,^{38, 34} the interesting results obtain do not play any role in following analysis of the composite layer, therefore they won't be related here. Mass spectroscopy allows the analysis of the pyrolysed gas; the decomposition mechanism will therefore be deduced. The resulting $(\text{HAIO})_n$ in the schematic representation of the reaction (Figure 2-3), stands for the ideal product H:Al:O=1:1:1 available at 238 °C according to Wolf's calculations.

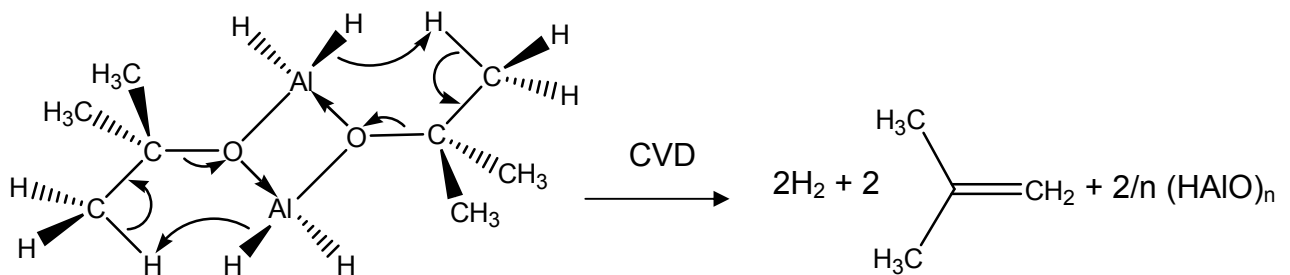


Figure 2-3: Reaction of $[\text{H}_2\text{Al}(\text{O}^t\text{Bu})]_2$ in the CVD apparatus at low temperature ($< 500 \text{ °C}$)

At the moment no persuasive proof is available about the exact structure of the HAIO layer, but some suggestions are given. For example K. Andres³¹ and later M. Burckhart³⁸ compared the structure of HAIO to the one of CIAIO; a layer model based on bridging hydrogen atoms was also proposed.

The HAIO layers have been manipulated and divers experiments, like annealing³¹ or laser structuring³³, have been performed. Faber has shown that HAIO displays a high stability over aging in water but not over temperature²⁶. The main effects of annealing

on the HAIO layer are stepwise elimination of hydrogen and black colouring. Figure 2-4 schematises the reaction during annealing.



Figure 2-4: Reaction of (HAIO)_n during annealing.

A composite material, where EDX detected Al:O=1:1 and XRD proved the presence of metallic aluminium beside $\gamma\text{-Al}_2\text{O}_3$, is formed when hydrogen is eliminated.

Stefan Faber²⁶, Joël Blin³⁰, Katrin Andres³¹, Yann Wolf³² and Christian Petersen³³ performed some transformation experience of the metastable HAIO layer into Al/Al₂O₃ by CO₂ and Nd:YAG laser irradiation. When the transformation occurs with laser process, it leads to films which are structured at the microscopic scale³⁹. Hence systems with phases with different chemical properties are coexisting on the layers; this diversity on the films is of big interest in the nanotechnology because it engenders many applications like for example nanochips fabrication or selective immobilization of molecules. One of the goals of laser patterning is to permit cell differentiation on the surface. Preliminary results on the cell growth onto the HAIO surface are available in Christian Petersen's dissertation³³.

The second type of layer (produced by CVD of [H₂Al(O^tBu)]₂ by high substrate temperature) is the object of the present work. Contrarily to HAIO layers, these layers display a high roughness (Ra≈360 nm) and are black. Scanning electron microscope (SEM) analysis made by K. Andres on layers grown by high precursor (4.10⁻¹ mbar) flow by 500 °C, show that the layers are constituted of spherical particles with few μm diameter, on which some smaller particles grow^{20, 34}. At lower precursor flow (4.5.10⁻² mbar) bigger agglomerates with diameters over 15 μm are detected. EDX shows, like in S. Faber's work, equimolar fraction of aluminium and oxygen and a small amount of hydrogen and carbon. Mass spectroscopy attests the decomposition reaction illustrated by Figure 2-5.

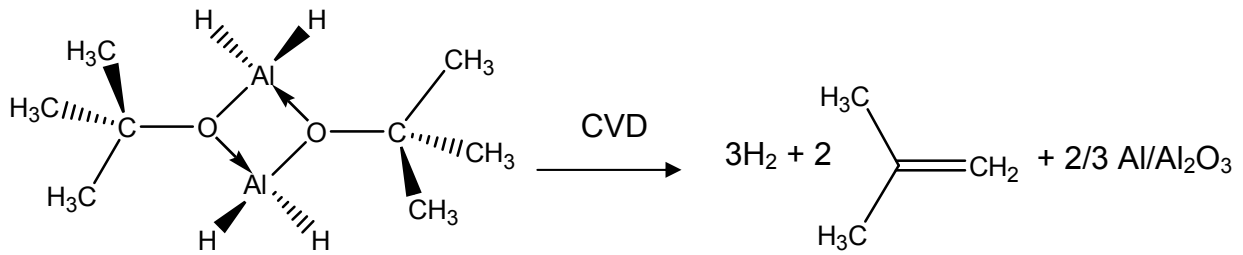


Figure 2-5: Reaction of $[\text{H}_2\text{Al}(\text{O}^t\text{Bu})]_2$ in the CVD apparatus above 450 °C.

A significant difference to the layers grown at low temperature is the presence of metallic aluminium evidenced by XRD and ^{27}Al MAS NMR. The size of the aluminium crystals averages 40 nm for layers grown at high precursor flow by 500 °C according to K. Andres' XRD results. The presence of aluminium crystallites was also testified by Wolf³² via electron diffraction. Above 500 °C, XRD measurements show new peaks, which are assigned by S. Faber as $\kappa\text{-Al}_2\text{O}_3$. K. Andres³¹ succeeded to form aluminium oxide between 450 °C and 500 °C by a low precursor flow ($5.2 \cdot 10^{-2}$ mbar); $\gamma\text{-Al}_2\text{O}_3$ has been detected by XRD³¹. By increasing precursor flow aluminium oxide is detectable via XRD only if annealing 10 minutes at 600 °C under vacuum is performed. Some contamination coming from the organic rests of the precursor molecule (mainly carbon) is detected. The contamination is higher by growing precursor flow. K. Andres even observed the growth of aluminium carbide crystals (Al_3C_4) by XRD after annealing the samples by 600 °C. According to Electron Spectroscopy for Chemical Analysis (ESCA) measurements performed by K. Andres and Y. Wolf, in most of the cases, only one sort of aluminium is present at the surface (at 74.2 eV), even after longer sputtering on the surface, and it is assigned to aluminium oxide. The aluminium clearly detected by XRD and NMR is not detected by a surface sensitive method which seems to be contradictory at first sight, but the logical explanation is that aluminium is not present on the surface. At the moment, it was supposed that the layers present a core shell structure, where the aluminium crystals are recovered by aluminium oxide, but no microscopic evidence was delivered to localise exactly the aluminium particles. Surprisingly, Wolf succeeded occasionally to detect the metallic aluminium with ESCA³¹. At this stage, examination of the layer morphology at the nanometric scale to localise the aluminium crystals is indispensable to clarify the ESCA results. The following illustration (Figure2-6) is a schematic illustration with only the most important results obtained about the direct deposition of $[\text{H}_2\text{Al}(\text{O}^t\text{Bu})]_2$. The summary is not exhaustive as some deposition

conditions like substrate nature, pressure or substrate nature are not taken into account.

Deposition Temperature	Composition	Comments about resulting layer
238 °C	HAIO 1:1:1	Equimolar composition. Temperature calculated by extrapolation ³³
310 °C	H _{0,8} AlO	80% Hydrogen measured by FTIR ³²
400 °C	Al/Al ₂ O ₃	Al:O=1:1, smooth layer, size of Al particles between 5 nm and 140 nm, Al ₂ O ₃ is amorphous ³⁵
450 °C	Al/Al ₂ O ₃	Structure is globular and fractal. ^{27, 20} Spheres with diameters app. 15 µm
500 °C	Al/Al ₂ O ₃	Spheres and smaller particles. Crystalline κ-Al ₂ O ₃ ²⁷

Figure 2-6: Summary about the layers obtained after direct CVD of [H₂Al(O^tBu)].

A lot of results have been gathered concerning Al/Al₂O₃ layers, nevertheless a lack of generality remains because each investigation has been performed by a defined window of conditions. An analysis of the composite layer by varying systematically the CVD parameters in a wide range has not been performed.

2.4 Ga/Ga₂O₃ composite layers by AK Veith

Equivalently to [H₂Al(O^tBu)]₂, the molecules [H₂Ga(O^tBu)]₂ and [HGa(O^tBu)]₂ are synthesised²⁷ and their crystal structure is illustrated in figure 2-7. The structure of both molecules is similar to the aluminium precursors.

They can be used as precursor for the formation of layers by CVD. This attempt was done by S. Faber²⁷ in his dissertation.

The substrate used to grow layers with [HGa(O^tBu)]₂ is silicon. The substrate temperature was 400 °C in a hot wall reactor, a dynamic vacuum (1.5·10⁻¹ to 2.0·10⁻¹ mbar) was produced and the precursor was heated at app. 50 °C to get sufficient precursor flow.

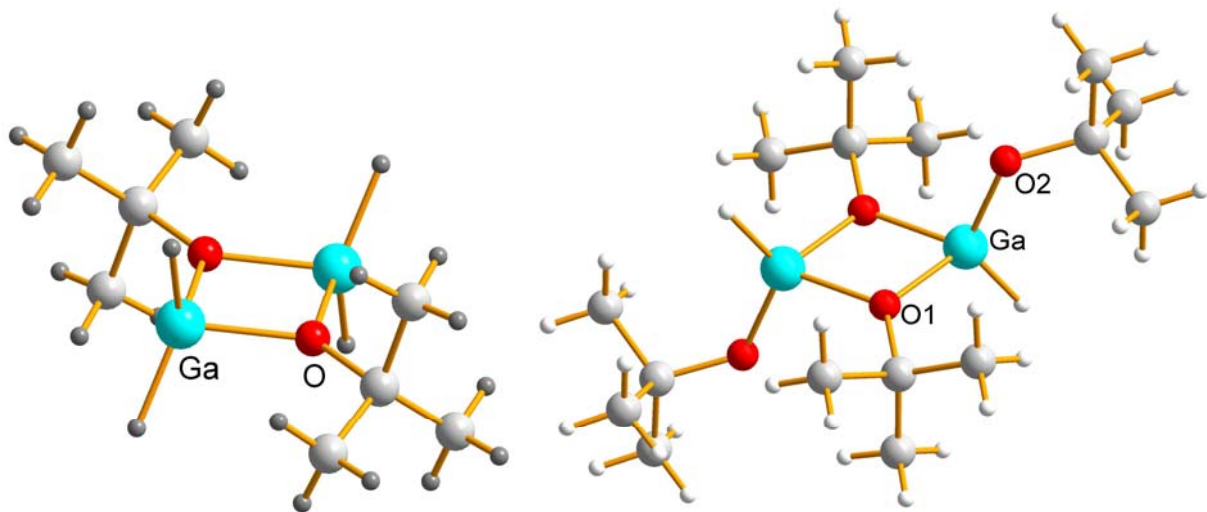


Figure 2-7: Molecular crystal structures of the precursors [H₂Ga(O^tBu)]₂ and [HGa(O^tBu)]₂ as described in reference 28.

Mass spectroscopic analysis revealed, that the fraction tert-butanol / isobutene in [HGa(O^tBu)]₂ is considerably higher than in the pyrolysed gas for the aluminium compound. Moreover, hydrogen partial pressure is lower. It means that the gallium / oxygen ratio, which was 4:2 in the precursor molecule, tends to displace in gallium direction after decomposition. Thus the thermal decomposition can be formulated as illustrated in Figure 2-8.

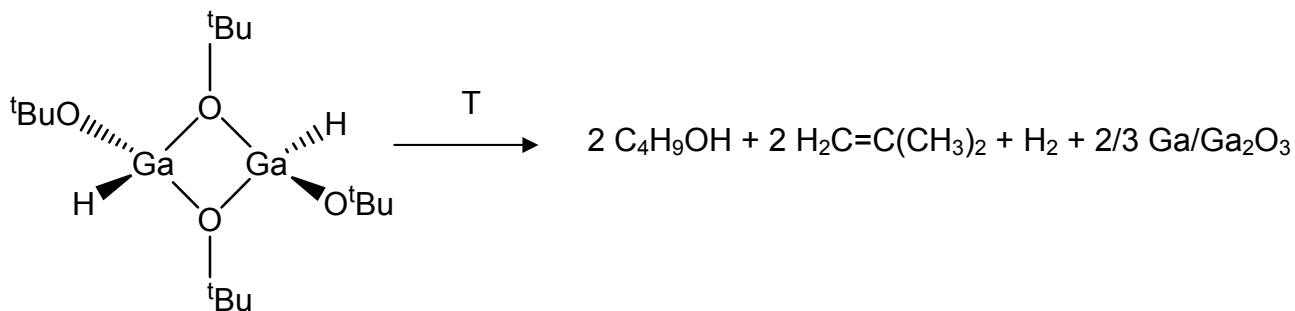


Figure 2-8: Decomposition of $[\text{HGa}(\text{O}^t\text{Bu})_2]_2$ during the CVD process.

The layers obtained present the same colour interferences as their aluminium equivalents at the beginning of deposition and become black-grey at the end. SEM analysis reveals that the layers have the same morphology like the Al/Al₂O₃ layers grown on quartz or glass. It means that homogeneous layers of half spheres with diameters about 350 nm, which are again composed of smaller particles, are obtained. Quantitative EDX analysis could have been performed by using gallium oxide as standard; they reveal that the layer is approximately composed of 50% gallium and 50% oxygen. These results do not correspond to the ratio in the precursor molecule but are in accord with the mass spectroscopic measurements. Thus a composite of gallium and gallium oxide has been obtained. XRD cannot demonstrate the presence of metallic gallium, but some peaks could correspond to γ -Ga₂O₃.

Deposition on silicon substrates heated at 250 °C - 260 °C were performed in a hot wall reactor with $[\text{H}_2\text{Ga}(\text{O}^t\text{Bu})]_2$ as precursor at app. 2 mbar and white-grey layers were obtained. On nickel heated at 260 °C no reproducible results were obtained, the main part of the gas decomposed on the sample holder or on reactor walls.

Mass spectroscopic analysis of the pyrolysed gas showed exclusively the formation of hydrogen and tert-butanol. Hence the proposed reaction is illustrated on figure 2-9.

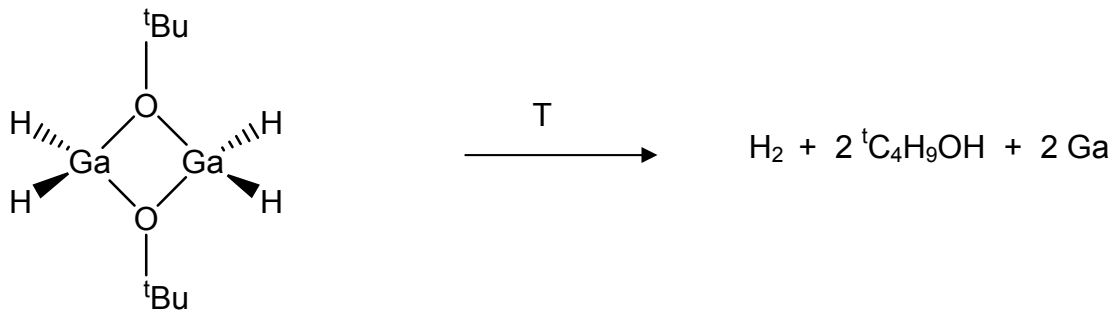


Figure 2-9: Decomposition of $[\text{H}_2\text{Ga}(\text{O}^t\text{Bu})]_2$ during CVD at 250 °C.

Microscopic observation shows a regular assembly of liquid gallium droplets. The evaluation of the droplet size distribution shows that the droplets average 670 nm, their diameters are between 50 nm and 2.21 μm .

Although the results on nickel were not reproducible, an interesting example is the formation of a layer with regular spheres reaching more than 10 μm diameters. EDX shows that these particles contain beside gallium, nickel and oxygen.

S. Faber did not process to more investigations although $\text{Ga}/\text{Ga}_2\text{O}_3$ or metallic gallium layers were not fully characterised. These preliminary results show the possibility of growing different types of layers with various morphologies and compositions by varying the substrate. It is also promising to try the deposition by higher temperatures, indeed the temperature range analysed by Stefan Faber was very narrow.

3 Influence of the CVD parameters on the properties and structure of Al/Al₂O₃ composite layers obtained from the precursor [H₂Al(O^tBu)]₂

Control of the CVD process parameters is indispensable for a selective layer preparation. For industrial applications (or basically to write a patent), a perfect knowledge of the properties of the grown layers is needed. For a given precursor, the so called parameters are mainly temperature of the substrate, precursor flow and deposition duration.

S. Faber²⁷ and K. Andres³¹ have concentrated on the study of some particular layers obtained by MOCVD of [H₂Al(O^tBu)]₂. Their principal conclusions were that amorphous HAIO layers could be obtained at low temperature (300°C) whereas Al/Al₂O₃ crystalline composite layers could be obtained above 500°C. For industrial applications, the main drawback of these studies is the lack of generality in the obtained results. The lack of generality is due to two reasons: first, the layers fabricated by S. Faber are grown at different conditions compared to the layers grown by K. Andres; second, the analyses have been performed by different instruments in both cases. The differences between the layers obtained at low temperature (HAIO) and the composite material Al/Al₂O₃ have been explained but remain vague as no precise value is given to indicate exactly under which conditions a composite material is obtained. The diversity of measuring instruments that have been used in both cases leads to a variety of different information about the layers. For example XRD and ESCA use totally different particle/matter interactions; as a result, these two instruments give information about different sample properties. XRD allows a qualitative and a quantitative crystal phase analysis in the whole sample. ESCA is surface sensitive and can detect all elements except H and He.

One of the surprising results observed by K. Andres³² and Y. Wolf³³ in the Al/Al₂O₃ system is the mismatch between the presence of metallic aluminium detected by

XRD and ESCA results, which most of the time only detect aluminium oxide and sometimes detect both aluminium and aluminium oxide. Combining these different results permit to deduce that aluminium crystals are present but not at the sample surface, i.e. we sometimes have to deal with a core-shell system.

In this chapter, a systematic analysis of the fabricated layers is performed with different instruments (mainly XRD, SEM and EDX) and with different process parameters; therefore different layer properties will be obtained. A combination of the results delivered by the different instruments will permit to deduce in which conditions a composite layer is obtained. The systematic analysis will permit to prevent a lack of unity in the results.

A range of layers obtained at 490°C, 530°C, 560°C and 600°C at low or high precursor flow (chamber pressure is $3 \cdot 10^{-1}$ mbar) with deposition time from 1 Minute, 30 Minutes, 1 hour and 2 hours is analysed and constitutes a wide sample basis, which is indispensable to get reliable results. Nevertheless to avoid repetitions in the following text, representative samples have been selected among the grown layers.

This study will permit to delimitate the temperature, time and flow range in which an Al/Al₂O₃ composite material can be grown. Then, layer morphology and structure will be examined more closely by scanning electron microscopy. Thus a sort of database is obtained where all possible compositions and structures are reported according to the fabrication conditions. In the future it will be possible to relate the layer properties with the structure, the composition and the fabrication methods.

3.1 Influence of process parameters

The most important element that has facilitated the increase of layers formed by MOCVD is the ability to deposit them in a reproducible manner with the correct crystal structure. Many chemical reactions that include pyrolysis, oxidation, reduction, hydrolysis or a combination of these are involved in the CVD processes. The chemical reaction determines the operating temperature range required. The reproducibility is complicated as CVD is a complex chemical system, which is influenced by the thermodynamics, chemical kinetics and mass transport. The use of single source precursors has minimised the CVD process parameters that need to be controlled.

Choy has related the effects of the process parameter on the composition and microstructure of the coatings and Fahlman the recent advances of CVD^{1, 2}.

Usually, the growth temperature is known to influence film properties more significantly than any other growth parameters as it controls both the thermodynamics and the kinetics of the coating. The deposition temperature must be adjusted to get an appropriate microstructure (e.g. grain size and shape). Small temperature variations (e.g. 25 °C) may change the reaction, and/or its kinetics, resulting in an undesired coating. Uniformity of the coating is determined by the ability of the reactant gases to reach the substrate surface and the temperature at which the reaction runs. Transport of reactant gases to the substrate surface is controlled by the reactant-gas partial pressure, the total reactor pressure, the reactor geometry and the substrate architecture.

At atmospheric pressure, the growth processes are often considered to be “transport controlled”. In order to reduce the dependence of growth rate and film composition on the hydrodynamics in the CVD reactor, many CVD processes are carried out at low total gas pressures where chemical reactions become more important in determining the characteristics of the deposited films. The actual quantity of the reactant gaseous products influences their movement path in the reactor and around the substrate. Thus, optimising the gas flow for reactant supply to the substrate is crucial for achieving satisfactory deposition.

Depletion of reactants can result in a non-uniform coating thickness or composition variations. The adhesion of coating onto substrate can be enhanced by avoiding substrate contamination, the attack of corrosive unreacted precursors and/or by-products on the substrate.

Accurate measurement and careful monitoring of the process parameters during the CVD process is needed. There are two categories of measuring methods: physical probes and optical devices. Physical probes present lower cost and are simple to use. However, they are limited to analysis of localised regions, and tend to be intrusive methods, which disturb the transport phenomena and reaction near the substrate surface. Optical methods do not use any intrusive probes, and they have high spatial resolution in the presence of a rapidly changing environment (e.g. temperature and active chemical species, etc). However, the use of optical analysis methods requires some modification of the CVD reactors to allow for the necessary access for the optical devices. Moreover, they are more expensive and sophisticated

analysis methods. Most of the process monitoring of the CVD processes have been intensively investigated for example for the microelectronics industry since they require very precise control of the deposition to guarantee purity, uniformity, reproducibility and quality of the thin films.

The deposition process and processing parameters affect the nucleation and growth which in turn influence the microstructure and hence the properties of the coatings.

Heterogeneous reaction is needed to get dense films and coatings. Whereas, a combination of heterogeneous and homogenous gas phase reaction is used for the deposition of porous coatings.

The nucleation and growth kinetics are influenced by the deposition temperature and super saturation (concentration of reactive species). The super saturation is dependant of the total pressure and partial pressure of the active gaseous species in the reactor. Higher temperature increases the surface mobility of the absorbed species on the substrate surface. Deposition rate can be adjusted readily. Low deposition rate is favoured for the growth of epitaxial thin films for microelectronic applications. However, for the deposition of thick protective coatings, a high deposition rate (> tens of μm per hour) is preferred.

The reactions in the gas phase, usually at high deposition temperature and super saturation, lead to the homogenous nucleation of solids from the gas phase. This results in the formation of stable solid reaction product in the form of fine powder. Such formation is useful for the production of ultra fine powder but not for the formation of a coating since the presence of the homogeneous nucleation together with the heterogeneous reaction will influence the deposited coating structure. Heterogeneous reactions in the neighbourhood of the substrate surface result in the adsorption of mobile atoms/monomers on the substrate surface, which diffuse to the preferred sites on the substrate surface to form stable nuclei. The monomers will accumulate on sites with lowest free energy to form crystallites. A thin crystal is formed upon coalescence.

Heterogeneous reactions can lead to various structures depending on two-dimensional growth including:

- Epitaxial growth

This type of growth is characterised by crystals having the same orientation as the perfect crystalline substrate. Such deposition often occurs at low super saturation

and high substrate temperature to provide rapid surface diffusion, leading to the nucleation and growth of solid in a particular preferred orientation which has the lowest interfacial free energy than any other orientation. Deposition at low pressure or under vacuum is often used to avoid contamination by facilitating desorption of impurities, and thus helps to lower the deposition temperature. This type of microstructure is useful for semiconductor and superconductor applications.

- Polycrystalline growth

Polycrystalline growth is nucleation that occurs at different substrate surface sites leading to the growth of islands which coalesce to form a polycrystalline layer. Nucleation depends strongly on substrate nature and absorbed species. The control of polycrystalline growth and, in particular, the size and nature of the crystallites is important in determining the properties of the CVD films. Polycrystalline growth can lead to different microstructures: Columnar microstructure is a result of high supersaturation and low substrate temperature and hence more limited diffusion. Even higher supersaturation leads to equiaxed structure which consists of fine and randomly oriented grains.

- Whiskers

This type of microstructure results from preferential growth. It involves nucleation at preferred locations such as defects on the substrate surface. A whisker, also called nanowire, can form when a substrate meets a screw dislocation having its Burgers vector normal to the substrate surface. Whisker growth occurs by the adsorption of atoms on the sites of the whiskers followed by diffusion to the tip. Growth rate depends on the geometry of whiskers, reactant concentration and the resident time of the adsorbed atom in the whiskers. More details about nanowires growth will be given in chapter 4.1.

- Amorphous

This structure tends to form at low substrate temperatures where the mobility of the absorbed species is relatively low, thus preventing these species from migrating to more energetic sites where nucleation can occur.

Other less common coating microstructures include platelets and dendrites. One of the advantages of CVD is the ability to control and vary the coating microstructure by varying the process parameters.

3.2 Generalities

Before analysing the disparities of the layers in details, summing up the main common properties is helpful for a clearer understanding.

Materials are classified into three main categories, called polymers, metals and ceramics. A material composed of phases which belongs at least two different categories is called a composite material. Al₂O₃ is a ceramic whereas aluminium is a metal. In the following a layer in which XRD has detected metallic aluminium, will be called a composite layer, in opposition to aluminium oxide layers or HAIO metastable layers. In the following the temperatures shown are measured with a thermocouple, due to deposition on the thermocouple itself, the measured temperatures are not realistic but are previously calibrated with values of a pyrometer. The pyrometer could not have been used to measure the substrate temperature as it is an optical method and the reaction walls do not remain transparent during deposition. Table 3-1 shows the correspondences between the temperature measured by the thermocouple and the ones cited in present work.

Temperatures measured (thermocouple)	Real temperature (pyrometer)
350 °C	450 °C ± 20 °C
370 °C	490 °C ± 20 °C
400 °C	530 °C ± 20 °C
425 °C	560 °C ± 20 °C
445 °C	600 °C ± 20 °C

Table 3-1: Temperature correspondences between thermocouple and pyrometer

Thermocouple and optical pyrometer have both severe practical drawbacks. Thermocouples are often inaccurate because they make poor thermal contact with the sample, while pyrometers require frequent calibration, a task complicated by radiative emission from sources other than the substrate and by changes in spectral absorption in the viewing window caused by the deposition of growth material. Despite of these drawbacks, a thermocouple previously calibrated with a pyrometer

is suitable for present work. The resulting fault in the measurement (± 20 °C) was evaluated by repeating the measurements at least three times.

Figure 3.1 shows digital pictures of layers prepared by CVD with [H₂Al(O^tBu)]₂ on 22 mm diameter steel targets. The main visible difference in the layers obtained is their colour and brightness (Table 7-1).



Figure 3-1: Pictures of films from [H₂Al(O^tBu)]₂ deposited by MOCVD on steel targets at 490 °C, 450 °C and 600 °C.

Layers with high surface coverage and macroscopic homogeneity are obtained. Depending on the preparation the layers obtained are grey, gold or black; moreover, their aspect can be bright or not (see chapter 7.3.5).

It has already been demonstrated that the layers contain aluminium metal particles (XRD) and amorphous aluminium oxide (ESCA)³¹. According to EDX measurements, the molecular fraction between aluminium and oxygen is 1:1 in most of the cases.

The layers' visual disparities reveal probably differences in the structure, composition or crystallinity; nevertheless no differences can be noticed in the composition by surface analysis (ESCA) or by energy dispersive spectroscopy (EDX). Hence further appropriated methods must be used to determine which characteristics fluctuate with changing deposition parameters.

The first detectable crystalline phase near to the steel substrate (PDF: 85-1410) is aluminium (PDF:85-1327), whereas alumina is amorphous at lower temperatures. Figure 3.2 is an overview on a typical XRD pattern obtained at 550 °C. Most of the XRD patterns show 4 main diffraction peaks at $2\theta = 45^\circ$, 52° , 77° and 94° and a wavy background.

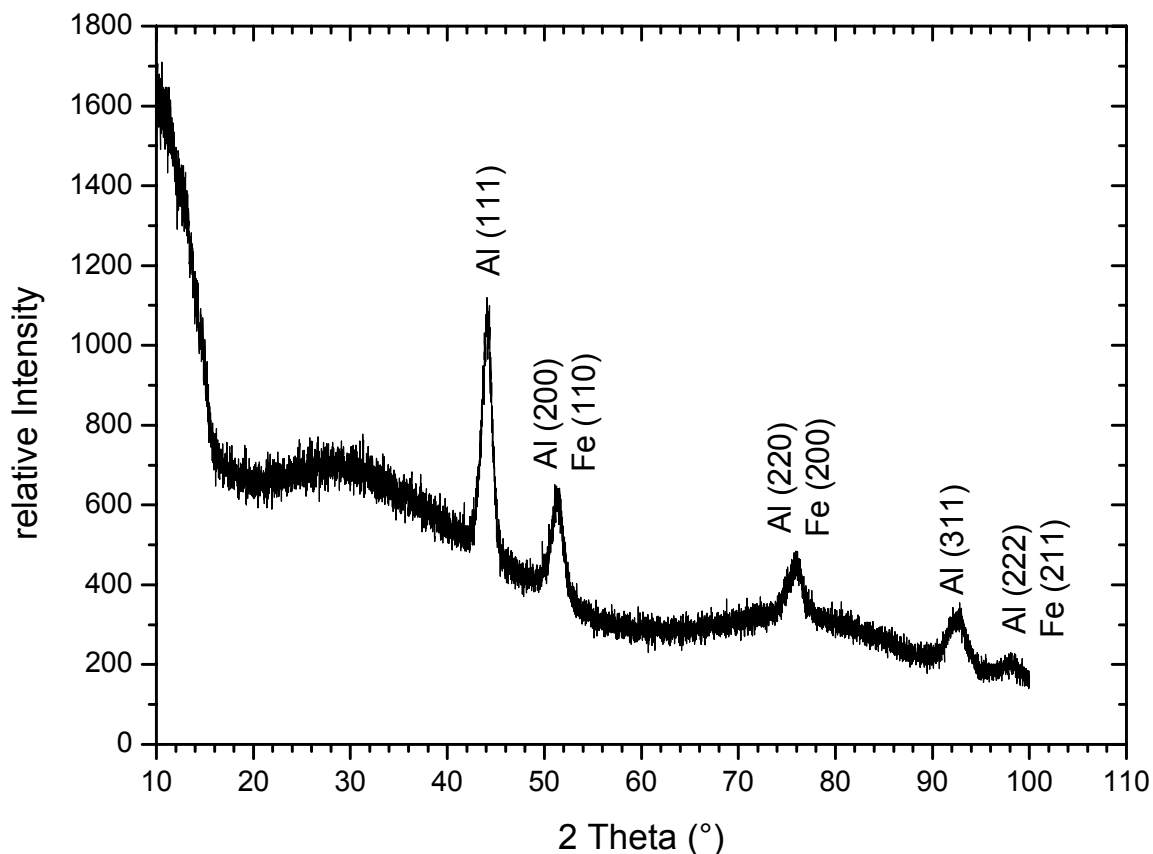


Figure 3-2: Typical representative XRD pattern of a composite layer

The peaks at 45° and 94° are suitable for further calculations as they are specific to aluminium contrarily to the peaks at 52° and 77° which give also information about the substrate. The wavy background must correspond to coexisting amorphous aluminium oxide which has already been detected by ESCA or to very fine crystals which are beneath the resolution limit of the diffractometer.

Figure 3.3 shows an ESCA spectrum of a layer made at 600 °C during 1 hour at low pressure. By zooming aluminium, oxygen and carbon can be detected; the aluminium peak at 74.3 eV corresponds to Al₂O₃ band (74.2 eV). Although it has already been possible to detect 2 aluminium peaks for elemental aluminium and aluminium oxide³⁷, in the present work all layers measured show one unique Al band. Hence the spectrum shown can be considered as specific and representative of the composite layers obtained during the present study.

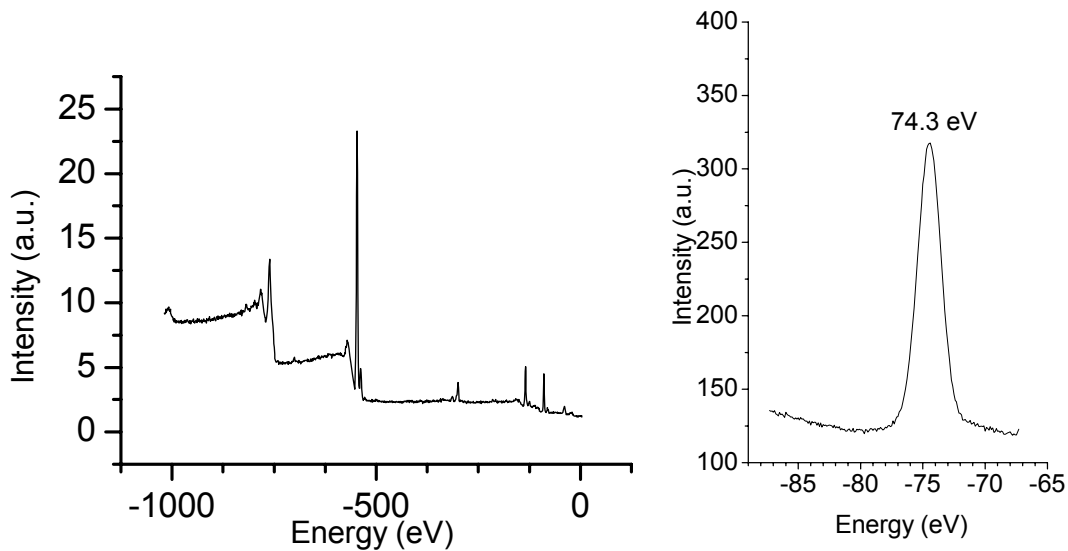


Figure 3-3: ESCA spectrum of a typical Al/Al₂O₃ layer and enlargement on the aluminium band.

EDX shows an equimolar concentration of aluminium and oxygen. The results of EDX are reliable qualitatively but quantitative analysis must be taken into account very carefully due to the weak detection of oxygen by X-rays. Nevertheless the reproducibility of the equimolar detection and previous work with calibrated EDX confirm this result. According to XRD, ESCA and EDX analysis, the composition of the layers is hence Al/Al₂O₃. Despite of this result, the aluminium is not visible on ESCA spectra in most of the cases; it means that aluminium is not present on the surface. Metallic aluminium must be covered by aluminium oxide. A metastable (AlO)_x phase, with unknown composition can also be envisaged.

3.3 Evolution of crystallinity

X-Ray powder diffractometry is an appropriated tool to detect crystallites on a solid surface and to proceed to a qualitative analysis of the crystal phases in the sample. XRD pattern of metallic aluminium has already been observed in composite layers in precedent studies but no quantitative analysis has been performed. According to Scherrer's equation the form of a peak in a XRD pattern is correlated to the crystallite size of the sample.

β = integral peak breadth

θ = measured angle

λ = wavelength

R= volume average particle size

K= size factor= 1

$$\beta = \frac{K \cdot \lambda}{R \cdot \cos \theta}$$

By fitting the obtained XRD pattern, it is possible to calculate the integral peak breadth β and deduce the volume average particle size R. The effect of diffraction peak broadening is commonly used as a convenient tool for the grain size determination of fine crystalline powders. Among other things, the accuracy of the crystallite size measurements depends on the level of noise present in the experimental diffraction patterns⁴⁰. Scherrer's equation is one of the possibilities to calculate the crystallite size but the reliability of the results is not high because of many approximations that are contained in the Scherrer's equation. The approximations about the size distribution and the shape of the crystals engender many errors; therefore Scherrer's equation is often not suitable. Because it is available with our XRD software, Scherrer's equation will be used here, but only to compare the calculated crystal size for different layers (the absolute value will not be taken into account). If no aluminium crystals are detected it means that the layer is not a composite or that the aluminium particles are too small for XRD detection. For each case it will be individually discussed to determine if the material is a composite or not. In the following the evolution of the peak form has been followed and reported against the deposition time, substrate temperature and precursor flow to deduce the aluminium crystal growth.

3.3.1 Evolution of crystallinity with the time at low precursor flow

The precursor can be maintained at 0 °C in an ice bath to diminish the vapour pressure, thus, the precursor flow will stay low; in this case the chamber pressure was 3.10⁻² mbar. The evolution of crystallinity with the time at low precursor flow is similar for the layers grown at 530 °C, 560 °C and 600 °C. Therefore, it is not necessary to show the results for each temperature. Five layers grown at 600 °C

have been selected to represent the evolution of the crystallinity with the deposition time.

Figure 3-4 shows an overview of their XRD patterns and a magnification for deposition time reaching 1 minute, 30 minutes, 1 hour, 1 hour 30 minutes and 2 hours.

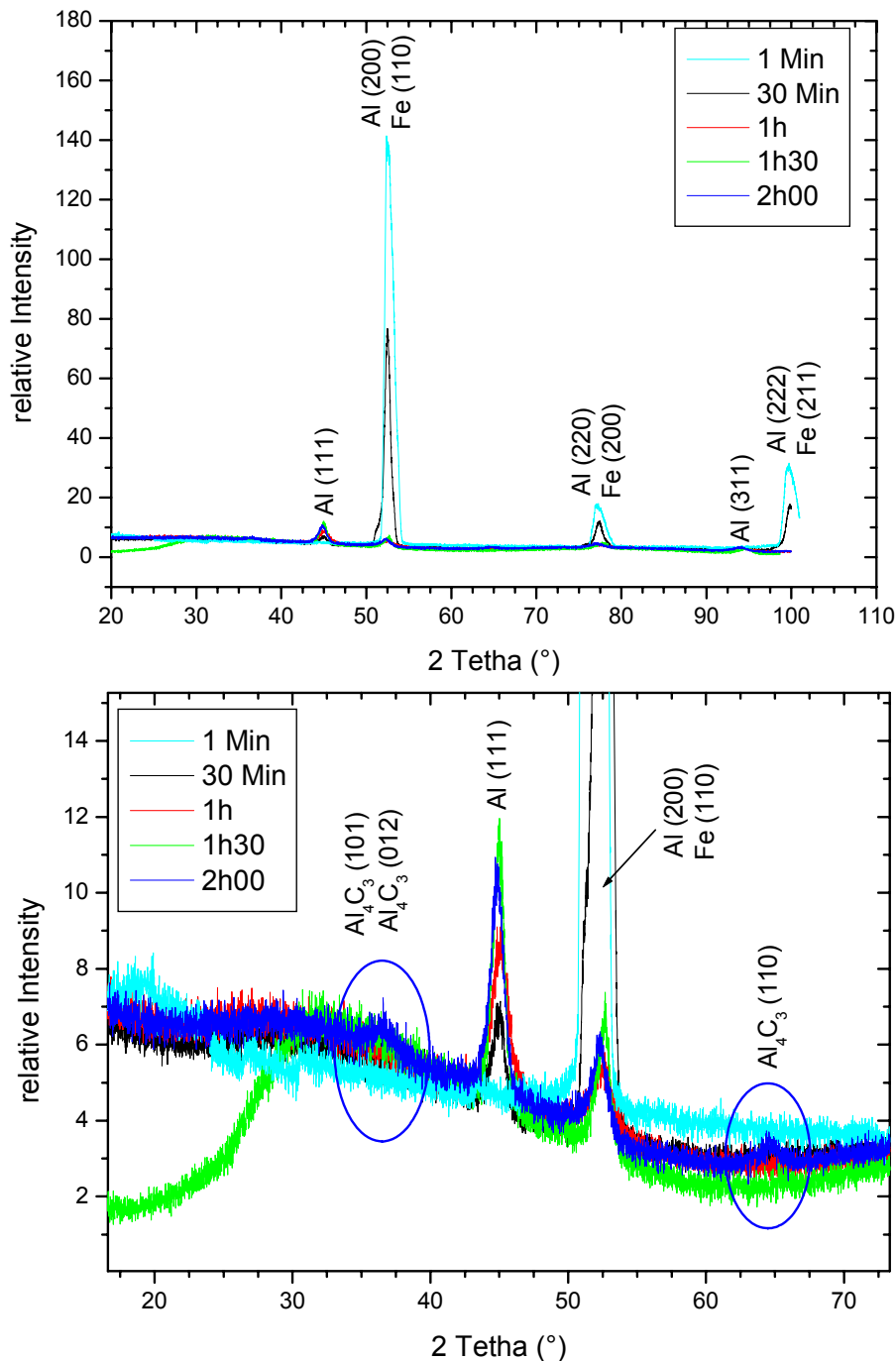


Figure 3-4: XRD of Al/Al₂O₃ layers grown at 600 °C at low deposition rate overview (above) and magnification (below), where aluminium carbide [PDF 79-1736] crystals are detected.

Like for the typical XRD pattern shown before, aluminium and iron can be seen. At lower incident angles, the irregular baseline corresponds to the amorphous fraction. The layer grown during 2 hours shows two small peaks at $2\theta = 37^\circ$ and 65° additionally to the four peaks of aluminium and iron. These peaks are assigned to aluminium carbide [PDF 79-1736].

Figure 3-5 focuses on the peak at $2\theta = 45^\circ$ of the diffraction patterns of the 5 layers. This peak allows following the evolution of aluminium crystals during deposition as it is characteristic for the most intensively diffracting plane of metallic aluminium i.e. plane (111).

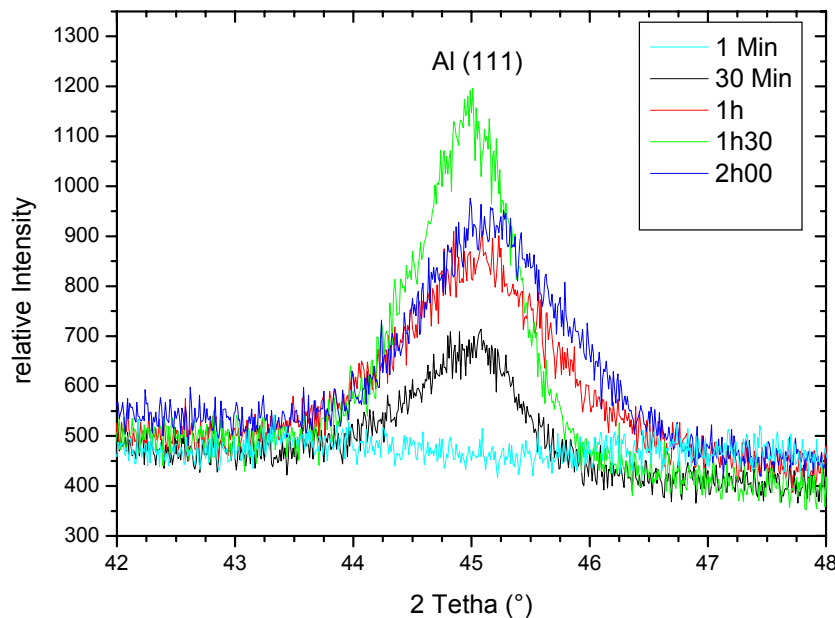


Figure 3-5: Evolution of the aluminium crystallites by increasing deposition time: focus on (111) aluminium peak of XRD pattern of precedent figure (Fig. 3-4).

After one minute deposition the diffraction peak corresponding to (111) diffraction plane of aluminium is not visible, it means either that the aluminium particles are too small to be detected or that no aluminium at all is formed. After 30 minutes deposition the aluminium peak can clearly be seen, this peak increases with deposition time. The aluminium grain size calculated from the fitting of these graphs with help of Scherrer's equation is shown in figure 3-6.

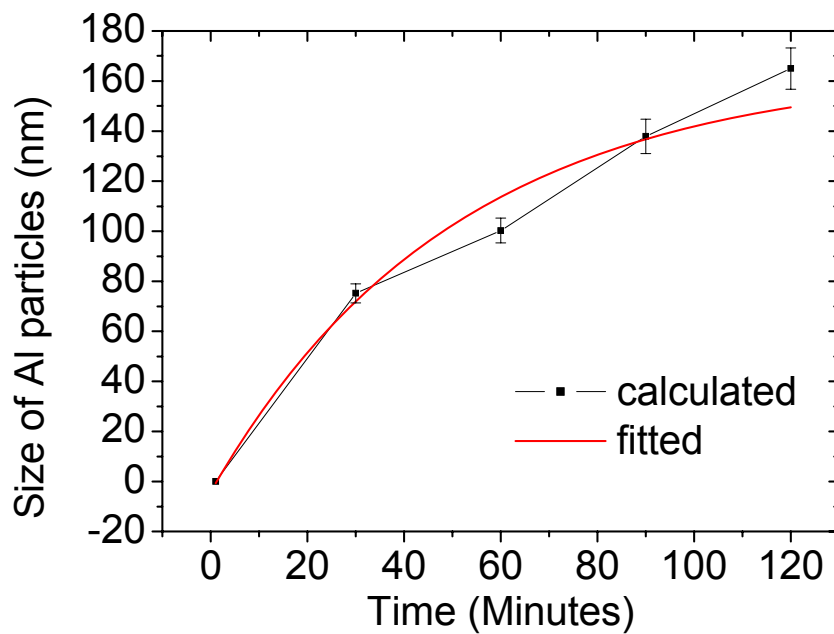


Figure 3-6: Calculated grain size of aluminium particles for layers grown with $[\text{H}_2\text{Al}(\text{O}^t\text{Bu})_2]$ at 600 °C at low precursor flow (chamber pressure $3 \cdot 10^{-2}$ mbar) by different temperatures.

According to Scherrer's equation the aluminium particles are 60 nm big after 30 minutes deposition and grow till 160 nm after 2h00 deposition. After one minute the fitted curve shows an aluminium size less than 10 nm: the eventually existing aluminium is therefore impossible to detect with XRD. The evolution of the particle size given by this graphic is reliable whereas the absolute size value makes sense on one condition: the aluminium particles have to be spherical as the size factor K used equals 1.

According to figure 3-6 the growth rate is slowly diminishing with deposition time, particularly after 2 hours deposition. The diminishing of aluminium crystal growth can be explained by the beginning of aluminium carbide growth.

By comparing the iron peaks at $2\theta=52^\circ$, figure 3-4, the surface coverage of the layers grown at 600 °C can be estimated. Figure 3.7 is a magnification of the XRD pattern of layers grown at low precursor flow (chamber pressure is $3 \cdot 10^{-2}$ mbar.) at 600 °C.

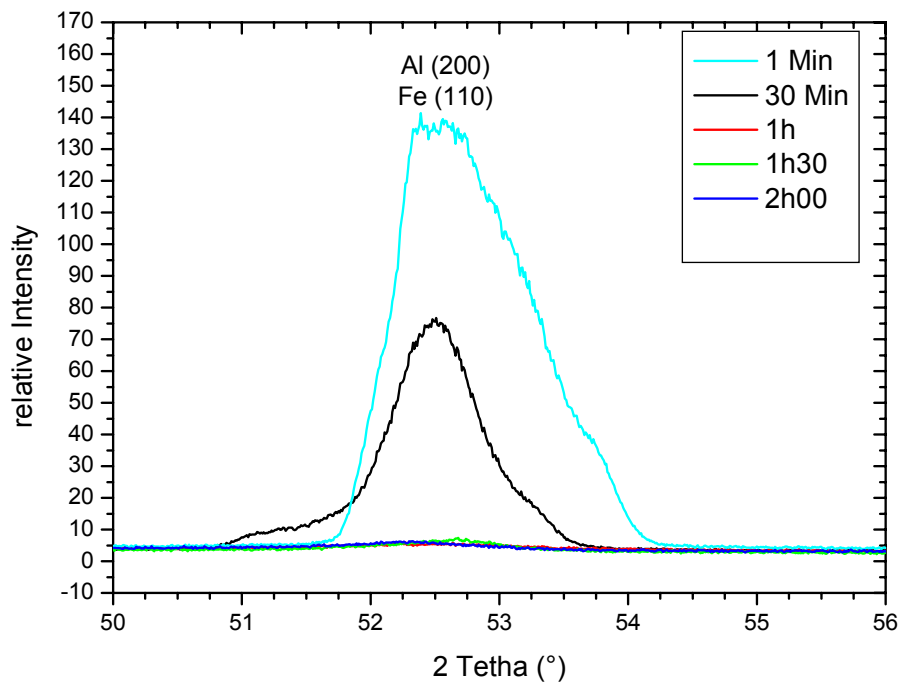


Figure 3-7: Focus on (100) iron peak of XRD pattern of layers grown with $[H_2Al(O^tBu)]_2$ at 600 °C with low precursor flow (chamber pressure $3 \cdot 10^{-2}$ mbar).

The quantity of substrate detected on the layer is inversely proportional to the surface coverage. After one hour deposition the surface is totally covered i.e. no substrate is detected.

To conclude, the aluminium particles grow continuously during deposition with a decreasing growing rate. Crystalline aluminium can be identified clearly by XRD after 30 minutes deposition. After 2 hours deposition the aluminium aggregates slower and forms aluminium carbide crystals. No information about the absolute size of these particles can be drawn as far as we do not have information about the real shape of the aluminium particles. These results are valid for deposition temperatures between 530 °C and 600 °C.

At 490 °C a composite can be obtained with a light grey colour. Aluminium crystallites are detected after one hour deposition, prior to one hour, the aluminium crystals are probably too small for XRD detection. Contrarily to films grown at 600 °C, deposition at 490 °C cannot exceed 1h30 otherwise the film breaks. Below 490 °C, the layers obtained are not grey but golden and transparent, they are HAIO layers and the study of such layers is not the object of the present work.

3.3.2 Evolution of crystallinity with the time at high precursor flow

The precursor is maintained at room temperature, thus, the precursor flow will be high in contrast to chapter 3.3.1, and in this case the chamber pressure is $3 \cdot 10^{-1}$ mbar. The evolution of crystallinity with the time at high precursor flow is similar for the layers grown at 560 °C and 600 °C. Therefore, it is not necessary to show the results for each temperature. Five layers grown at 600 °C have been selected to represent the evolution of the crystallinity with the deposition time.

Figure 3-8 shows their measured XRD patterns for deposition time reaching 1 minute, 30 minutes, 1 hour, 1 hour 30 minutes and 2 hours. The main difference with the XRD patterns at lower deposition flow is that aluminium can already be detected after one minute deposition. By increasing the precursor temperature it is thus possible to enhance the growth of aluminium in the layer i.e. the composite material is formed faster. The formation of aluminium carbide is also enhanced as it is sometimes already detected after 30 minutes deposition (figure 3-8 below) instead of 2 hours for a cooled precursor (Figure 3-4). At high precursor flow the composite obtained resists less to the air, therefore films prepared at lower temperature (530 °C) as well as at longer deposition time (more than 1h30 at 560 °C) break in contact with air (see table 3-2). We probably have to deal with homogeneous nucleation, which diminish the coating properties therefore the stability and mechanical properties are limited.

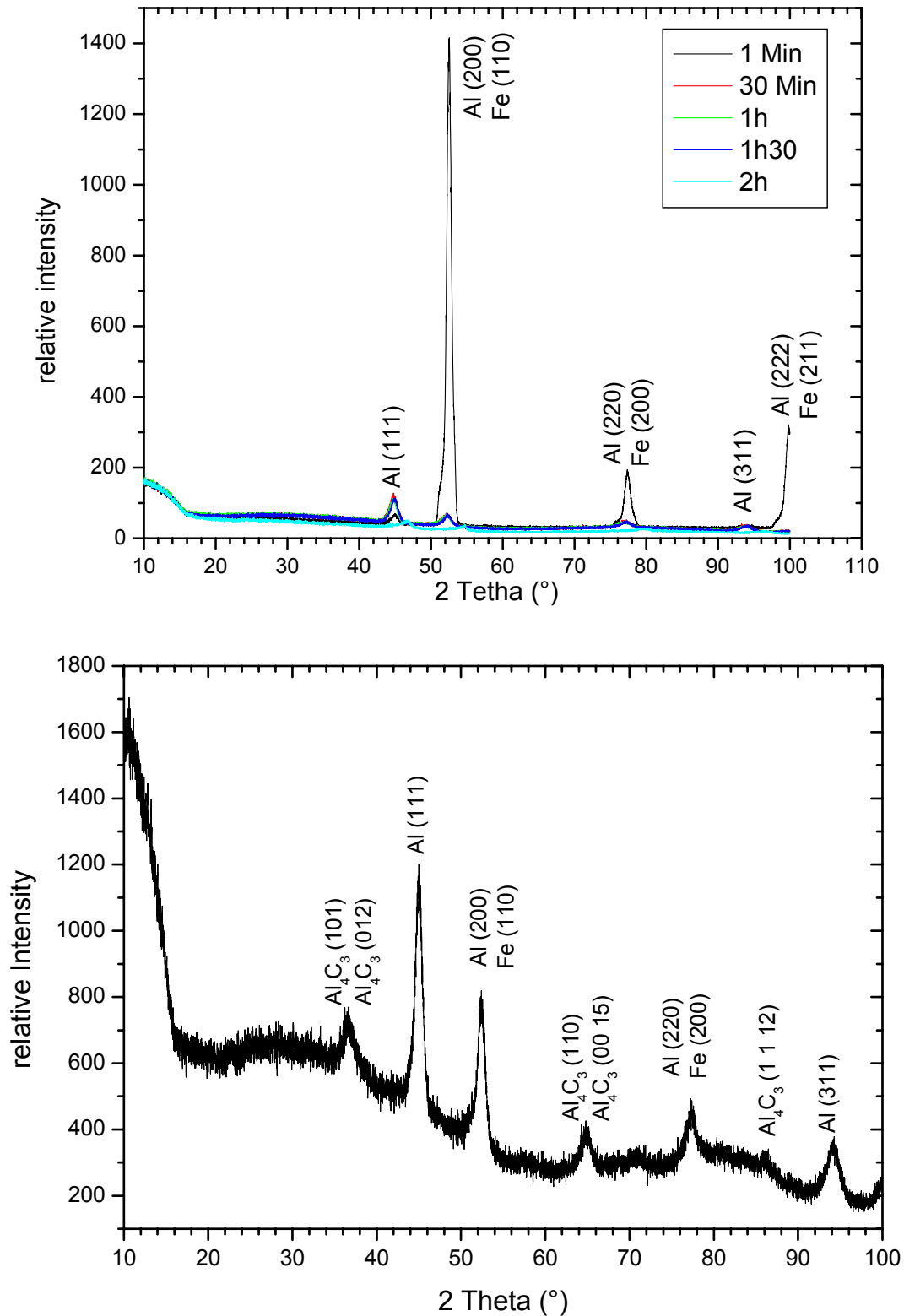


Figure 3-8: XRD patterns of layers grown with [H₂Al(OⁱBu)]₂ at 600 °C at high deposition rate(chamber pressure 3.10⁻¹ mbar) and XRD of a layer where Al₄C₃ can be detected after 30 minutes deposition.

In general, increasing the precursor flow allows to get a thicker layer with bigger aluminium crystals in a shorter time. At low temperature (490 °C and 530 °C) it is nevertheless, not easy to get a stable layer with a precursor at room temperature. The only layers which have been stabilised are grown during 1 to 2 hours and no aluminium crystals are detected, although the layers are probably composite (light grey colour): crystallites are too small. Figure 3-9 shows such a layer, where only the iron substrate [PDF 6-695] and its oxide [PDF 39-1346] are detected.

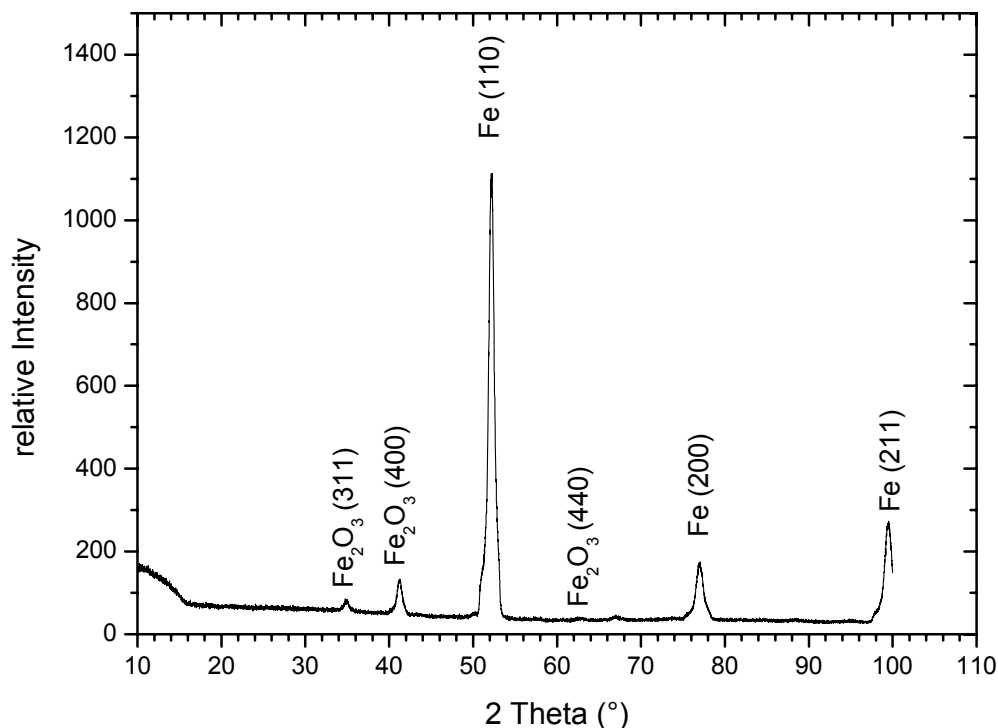


Figure 3-9: XRD of an Al/Al₂O₃ layer grown by 490 °C at high precursor flow (chamber pressure 3.10^{-1} mbar): only the substrate peaks are detected.

At low temperature, it is not recommended to increase the precursor flow because the layers display less mechanical resistance. The increase of precursor flow presents drawbacks at higher temperatures (more than 530 °C) as well, because the formation of the undesired aluminium carbide phase is accelerated.

3.3.3 Evolution of crystallinity with the substrate temperature by low precursor flow

5 Layers grown during 1 hour have been selected to demonstrate the evolution of the crystallinity with growing temperature. They are grown with a low deposition flow (precursor cooled with ice, chamber pressure is $3 \cdot 10^{-2}$ mbar.) at 450 °C, 490 °C, 530 °C, 560 °C and 600 °C. Figure 3-10 shows their measured XRD patterns.

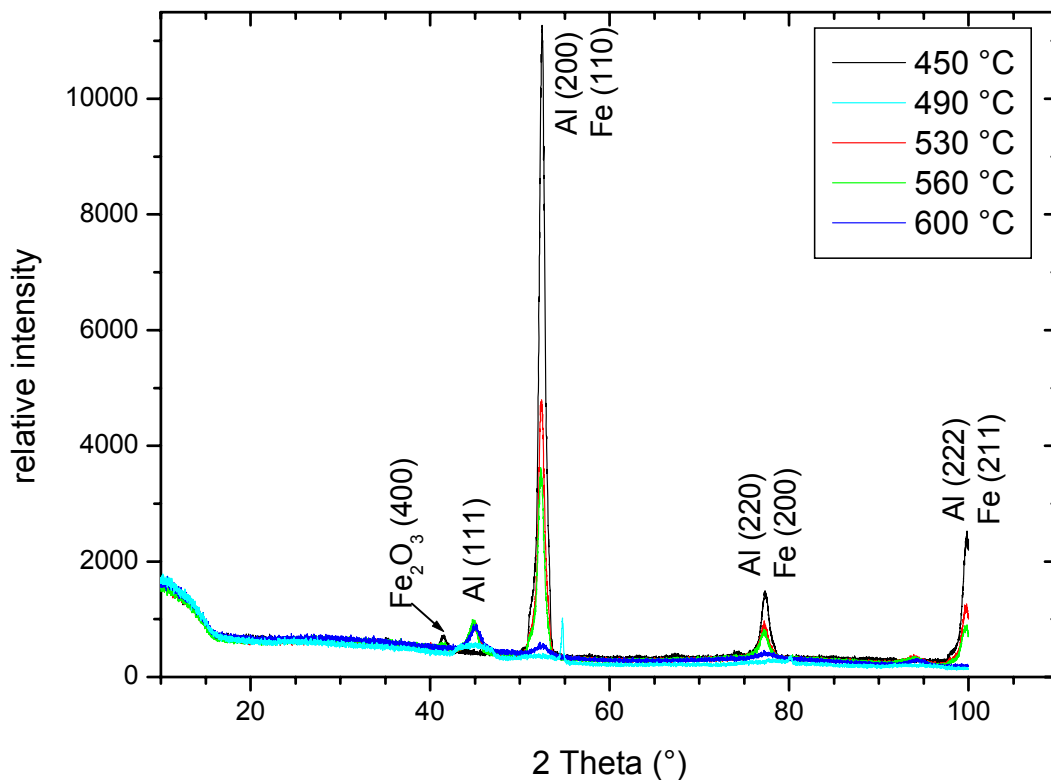


Figure 3-10: XRD pattern of layers grown with $[H_2Al(O^tBu)]_2$ at low precursor rate (chamber pressure $3 \cdot 10^{-2}$ mbar) during one hour.

Most of the XRD patterns show 4 main diffraction peaks at $2\theta = 45^\circ$, 52° , 77° and 94° and a wavy background, like in precedent chapter the peaks are assigned to aluminium and iron. The layer grown at 450 °C is totally amorphous despite of one hour deposition, only the substrate is visible on XRD pattern. Above 450 °C aluminium particles are detected by focussing on the Peak at $2\theta = 45^\circ$ (Figure 3-11). Thus the layer grown at 450 °C will be considered as HAIO whereas the layers grown above 490 °C will be called composite.

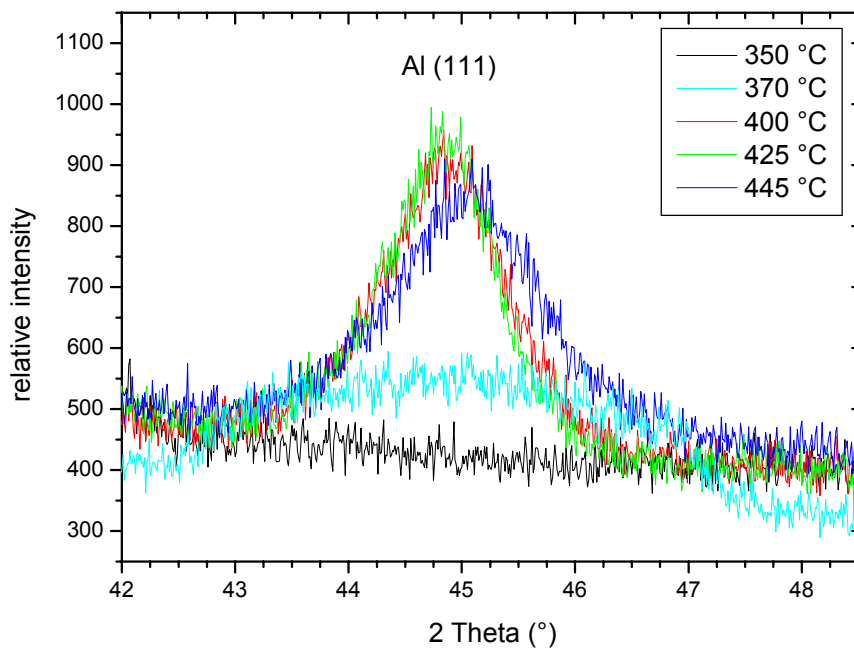


Figure 3-11: Evolution of the aluminium crystals by increasing temperature: focus on (111) aluminium peak of XRD pattern of figure 3-10.

Like in precedent chapter it is possible to calculate the particle size with Scherrer's equation. Figure 3-12 shows the results of this calculation.

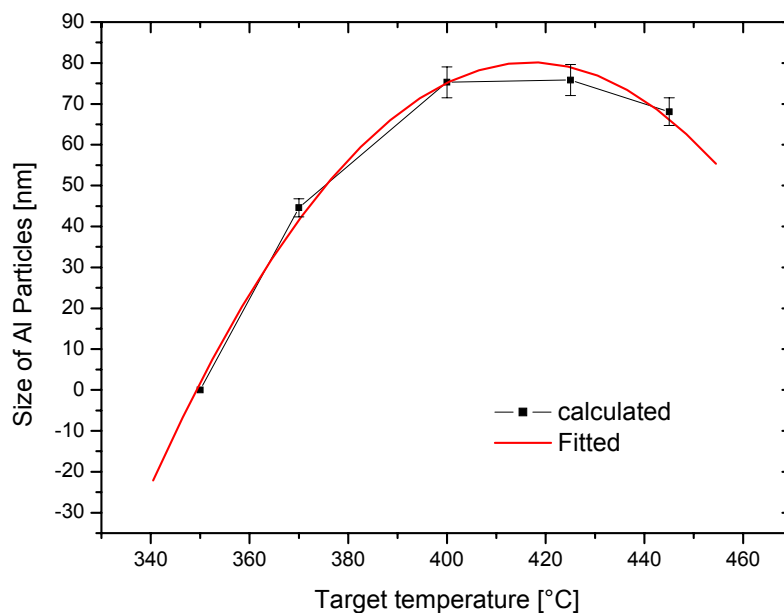


Figure 3-12: Calculated grain size of aluminium particles for layers grown with [H₂Al(O^tBu)]₂ during one hour at low precursor flow (chamber pressure 3.10⁻² mbar).

At 490 °C the aluminium particles are 45 nm big, they grow with increasing temperature until a maximum of 75 nm at 560 C. Above 560 °C increasing temperature leads to smaller particles, it means that another phenomenon is occurring. No aluminium carbide is detected on layers deposited during one hour at low precursor flow; however, new peaks have been detected and will be discussed later (chapter 3.3.5). The occurring phenomenon can also be related to a new arrangement of aluminium crystals; hence the growth must be known to understand why the aluminium crystals stop expanding. The observation of the structure in next chapter will give more information about the growth of the aluminium crystals.

3.3.4 Evolution of crystallinity with the substrate temperature at high precursor flow

3 Layers have been selected to demonstrate the evolution of the crystallinity with growing temperature. They are grown during 1 hour with a high deposition flow at 490 °C, 560 °C and 600 °C. The layer grown at 530 °C could not have been measured as it breaks off after deposition. At 530 °C it is possible to grow layers during a very short time (one minute) or a very long time (2 hours) in the time interval between one minute and 2 hours the layers do not have sufficient mechanical resistance.

Figure 3-13 shows the measured XRD patterns.

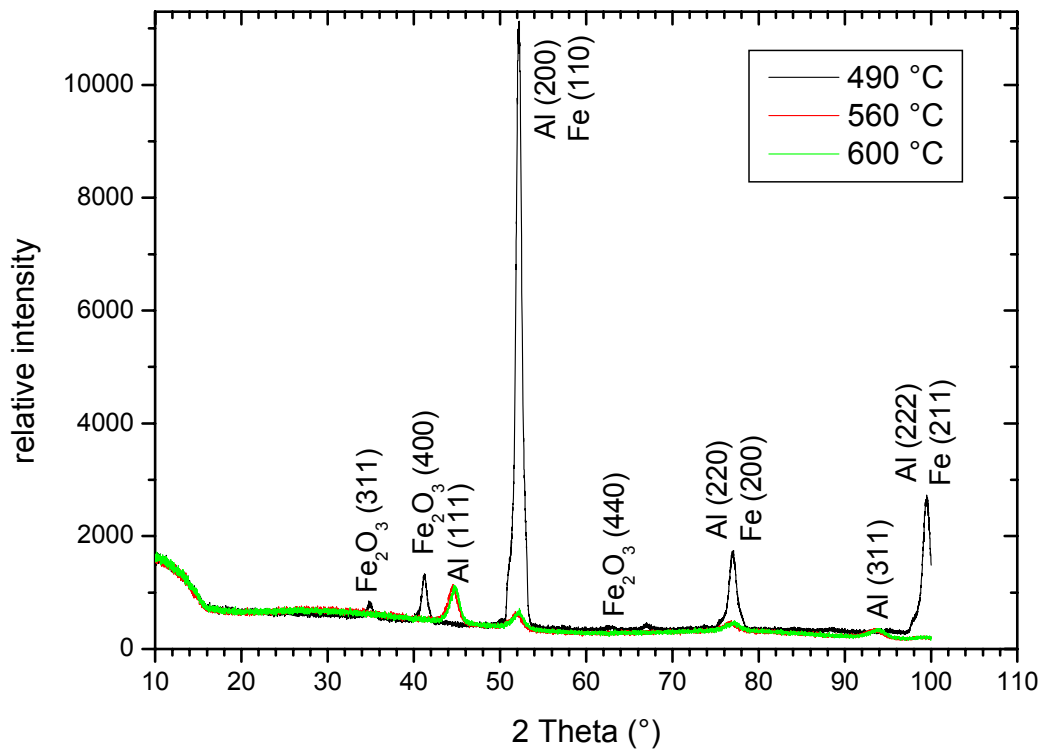


Figure 3-13: XRD pattern of layers grown with $[\text{H}_2\text{Al}(\text{O}^i\text{Bu})_2]$ at high precursor rate (chamber pressure $3 \cdot 10^{-1}$ mbar) during one hour.

Like for a low precursor flow (chamber pressure is $3 \cdot 10^{-2}$ mbar.) no aluminium is detected in layers grown under 490 °C. However layers grown at 490 °C showed aluminium at low flow deposition, here no aluminium is seen even with one hour deposition. At 490 °C the observed peaks correspond to iron and iron oxide [PDF: 39-1346] from the substrate. With precursor at room temperature (chamber pressure is $3 \cdot 10^{-1}$ mbar.) composite material cannot be formed under 560 °C. No new peaks can be noticed in these conditions.

3.3.5 Formation of a crystalline phase with unknown composition

Alumina has a large number of metastable crystalline phases in addition to the thermodynamically stable rhombohedral α -Al₂O₃, or corundum phase. These metastable alumina polymorphs include γ (cubic spinel), δ (either tetragonal or orthorhombic), θ (monoclinic), η (a second cubic spinel), κ (orthorhombic), χ (cubic), and β (hexagonal). Among the most common metastable alumina polymorphs (γ , δ and θ) the only cubic phase is γ –alumina.

Formation of a metastable crystalline phase, called {Al·O} is observed in some layers grown with [H₂Al(O^tBu)]₂. The peaks corresponding to this phase appear at 2θ = 46 °, 54 °, and 79 ° and they are very sharp. This phase has been observed in layers grown at various conditions but could not be reproduced deliberately by repeating the process conditions. Figures 3-14 to 3-16 show the XRD pattern of the samples where this phase has been detected.

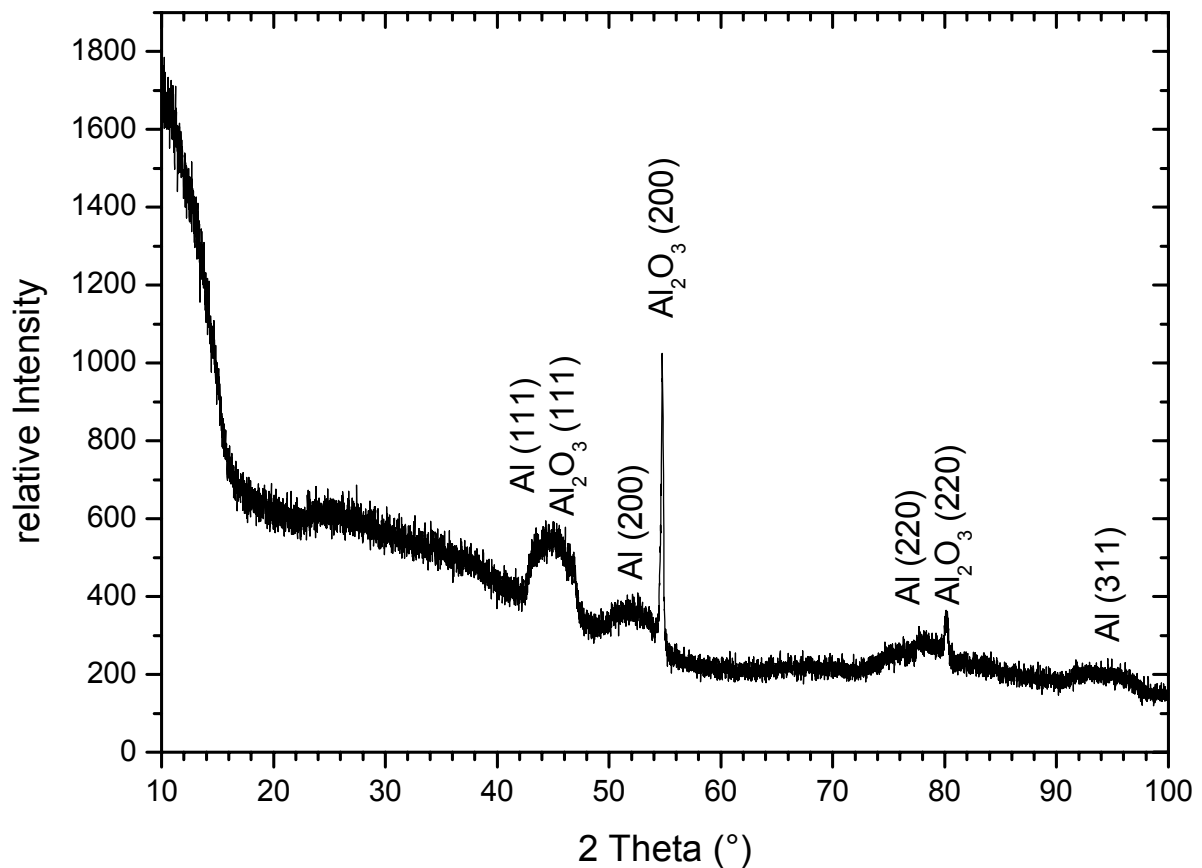


Figure 3-14: XRD pattern of a layer grown with [H₂Al(O^tBu)]₂ at 530 °C during 2 hours at low precursor flow. {Al·O} crystals are detected and assigned to γ'-Al₂O₃ on the graph.

Close to the aluminium pattern 2 main peaks can be clearly seen on figure 3-14 at 2θ = 54 ° and 79 °. The rounded forms of the aluminium peaks, which correspond to very small aluminium particles, contrast to the sharp peaks at 55 ° and 79 °. According to the ICDD Data base the only phase which could match to the 2 peaks is the aluminium oxide [PDF: 75-921], which was obtained by electrolytic oxidation of an aluminium electrode.⁴¹ . Table 3-2 shows the measured 2θ from figure 3-16 and the crystallographic data of this cubic aluminium oxide, where a = 3,950 Å.

Interplanar distances [Å]	2θ [°]	measured 2θ [°]	Intensity [a.u.]	h k l
2.2805	46.186	46.7	49	111
1.9750	53.860	54.6	999	200
1.3965	79.658	80.0	941	220
1.1910	97.363	97.1	1	311
1.1403	103.339	∅	94	222

Table 3-2: Crystallographic data of γ'-Al₂O₃ from PDF 75-921 compared to the measured peaks from figure 3-16.

They found that the structure of this oxide varies according to the method of preparation of the oxide layer. Sometimes it consists of amorphous Al₂O₃, under other conditions the X-Rays diagram showed that a cubic form of Al₂O₃ is obtained. The X-Ray diagram of this cubic oxide proves that it is closely related to γ-Al₂O₃. The diffractograms are, however, not identical. Both the amorphous oxide and the cubic form are transformed into γ-Al₂O₃ when the substances are heated during a few hours at 900 °C. The structure is called γ'-Al₂O₃ and may therefore be described as a simple face-centred lattice of oxygen ions in which the Al³⁺ ions are distributed over all the available interstices in such a way that about 70% of the latter occupy an octahedron hole (coordination number 6) and 30% a tetrahedron hole (coordination number 4).

Aluminium oxide [75-921] has a poor stability at room temperature; hence it is very probable to detect it just after deposition but not after several days aging. After aging the layers analysed do not show these sharp peaks anymore, only aluminium crystals are detected.

Further layers, like in Figure 3-15 or 3-16, show the presence of the unknown {Al-O} phase.

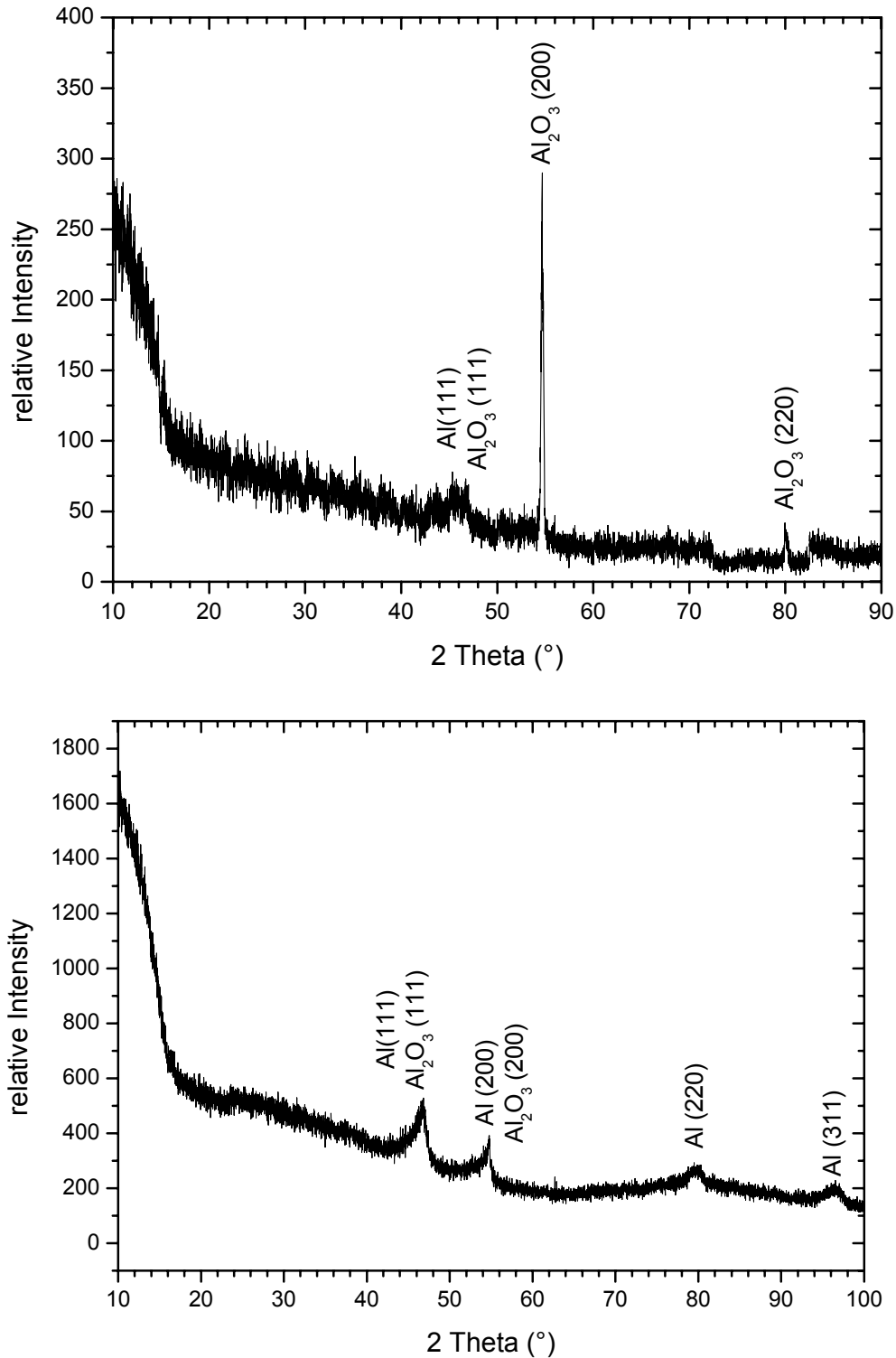


Figure 3-15: XRD pattern of two layers showing {Al-O} crystals. The layers are grown at 560 °C, 2h, low precursor flow (above) and at 600 °C, 2h, high precursor flow (below).

According to figure 3-15 a third peak is present at $2\theta = 46^\circ$: The (111) plan of the aluminium oxide [75-921] diffracts at $2\theta = 46,186^\circ$. Another cubic Al₂O₃ [PDF

10-425] with $a = 7.90 \text{ \AA}$, is also conceivable because it shows peaks at about 46° , 53° and 79° . Table 3-3 sums up the crystallographic data of Al₂O₃ [10-425].

Interplanar distances [Å]	2θ [°]	Intensity [a.u.]	h k l
4.5600	22.625	40	111
2.8000	37.260	20	220
2.3900	43.957	80	311
2.2800	46.197	50	222
1.9770	53.801	100	400
1.5200	72.098	30	511
1.3950	79.764	100	440
1.1400	103.374	20	444
1.0270	121.142	10	731
0.9890	129.494	10	800

Table 3-3: Crystallographic data of γ -Al₂O₃ from PDF 10-425. The marked areas correspond to the peaks detected by XRD on figure 3-15.

The few sharp peaks which have been detected indicate that the unknown phase is probably cubic. After comparison with databases, two phases could have engendered these peaks γ -Al₂O₃ from PDF 10-425 and γ' -Al₂O₃ from PDF 75-921. Among these two phases, γ -Al₂O₃ is less probable because some peaks, which are supposed to show relatively high intensity (for example at $2\theta=43.957^\circ$ and $2\theta=72,098^\circ$) are missing on the XRD pattern (table 3-3). However, γ' -Al₂O₃, which is the most suitable phase encountered, does not perfectly match as well because the intensities of the peaks measured are not the one predicted by the literature. After table 3-2, the peaks at $2\theta=53^\circ$ and 79° should show similar intensities but it is not the case in the XRD pattern where the ratio is app. 1/5 (figure 3-16).

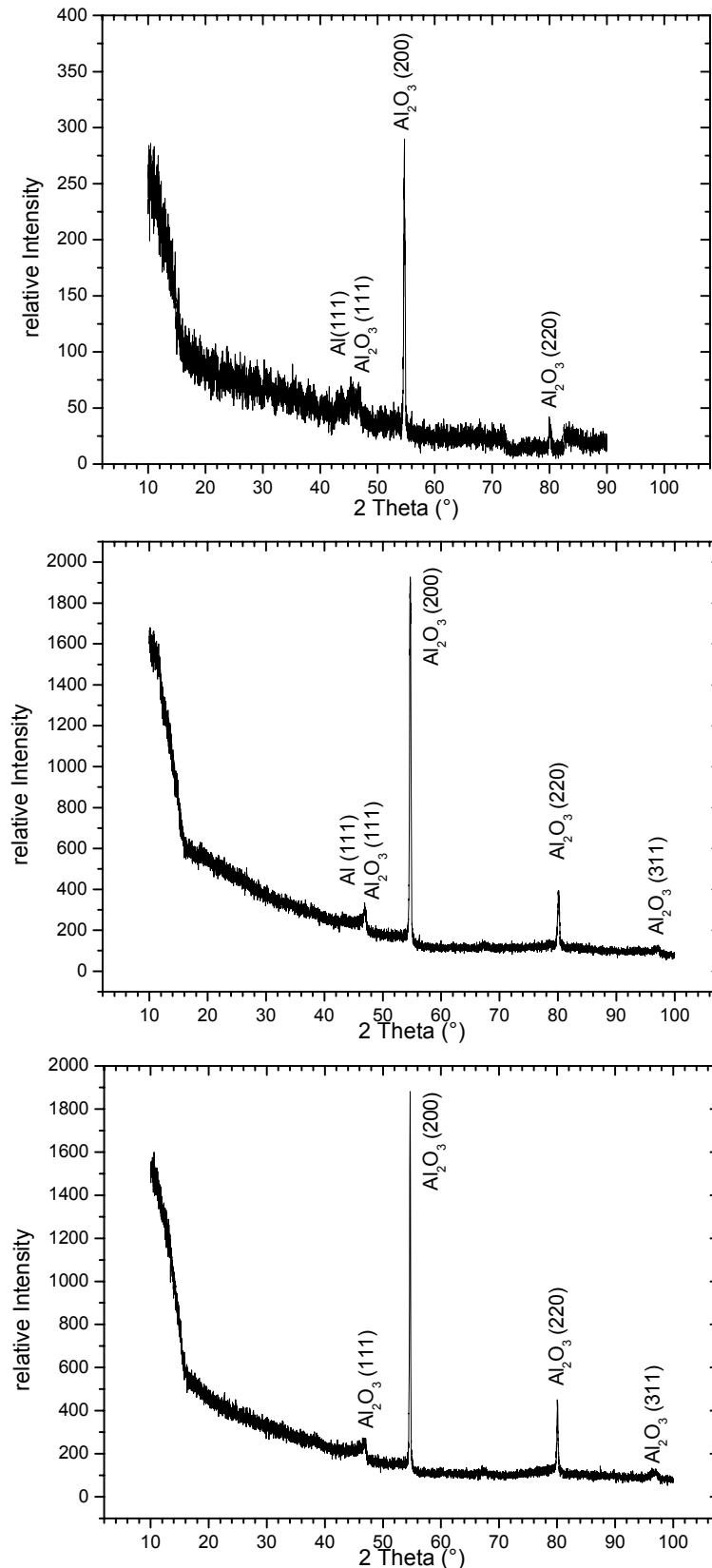


Figure 3-16: XRD pattern of layers with {Al-O} peaks assigned to γ' -Al₂O₃ (or γ -Al₂O₃). The layers are grown at 560 °C, 1h30 with low precursor flow (above), 530 °C, 1h30 with low precursor flow (middle) and 560 °C, 1 minute with high precursor flow (below).

Finally, the phase, which has engendered the three sharp peaks at about $2\theta = 46^\circ$, 53° and 79° does not perfectly match to any of the recorded aluminium oxide phases from the literature. Figure 3-15 shows very small aluminium crystals next to the sharp peaks. The sharp peaks can therefore be attributed to a distorted aluminium lattice, in which oxygen insertion enlarges the lattice constant. Thus the layer is probably composed of small aluminium crystals, bigger distorted aluminium crystallites with oxygen in the lattice and amorphous aluminium oxide.

In conclusion the sharp peak is produced by a cubic phase with undetermined {Al·O} stoichiometry. As no direct relation can be found between the layers growth parameter and the {Al·O}, the phase is probably engendered by another factor, which is not monitored in this study like for example the oxygen amount in the CVD apparatus. The pressure in the reaction chamber as well as the room temperature, are controlled and an effort is put to deposit all layers by same reproducible conditions. Despite of all precautions, it is quasi impossible to guarantee an exact equal oxygen amount for each preparation. The analysis conditions can also be decisive for the phase detection. The unknown {Al·O} phase is detected exclusively in freshly deposited layers. There is probably oxygen diffusion in the phase. In conclusion we have to deal with a composite of aluminium with amorphous aluminium oxide and {Al·O}. After longer contact with air, the {Al·O} disappear, it is probably transformed into aluminium and aluminium oxide (figure 3-17).



Figure 3-17: Instant formation of Al and Al₂O₃ from the unknown {Al·O} phase.

Table 3-4 is a summary of the previous chapter (3.3); the results of the crystallinity analysis in function of preparation conditions are reported.

Substrate Temperature	490 °C		530 °C		560 °C		600 °C	
	Precursor 0°C	Precursor RT	0°C	RT	0°C	RT	0°C	RT
1 Min	No crystal	Film breaks	No crystals	No crystal	No crystal	γ'-Al ₂ O ₃	No crystal	Al
30 Min	No crystal	No Crystal	Al	Film breaks	No crystal	Al	Al	Al
1h	Al		Al	No crystal	Al	Al	Al	Al Al ₄ C ₃
1h30	Al		Al γ'-Al ₂ O ₃	Film breaks	Al γ'-Al ₂ O ₃	Al	Al	Al Al ₄ C ₃
2h	Film breaks		Film breaks	Al γ'-Al ₂ O ₃	No crystal	Al γ'-Al ₂ O ₃	Film breaks	Al Al ₄ C ₃

Table 3-4: Overview on the crystallinity of the layers obtained by CVD of [H₂Al(O^tBu)]₂

3.4 Morphological variations

The formation conditions of the composite material defined in the previous chapter are broad and the aluminium crystal fraction varies from one sample to the other. For these reasons further analyses are needed to verify whether the layers obtained are similar or if they show any structural, morphological or chemical differences. Scanning electron microscope (SEM) and energy dispersive spectroscopy (EDX) are used to identify and analyse the composite layers.

3.4.1 At low temperature (490 °C)

After ten minute deposition at 490 °C with a low precursor flow (chamber pressure is $3 \cdot 10^{-2}$ mbar) a light grey film is obtained. It is composed of small spheres (about 70 nm) which either follow each other to build short chains of about 5 spheres or aggregate to build particles (about 300 nm). Lower magnification allows observing that the spheres can even assemble to take shape of 2 µm big particles (Figure3-18).

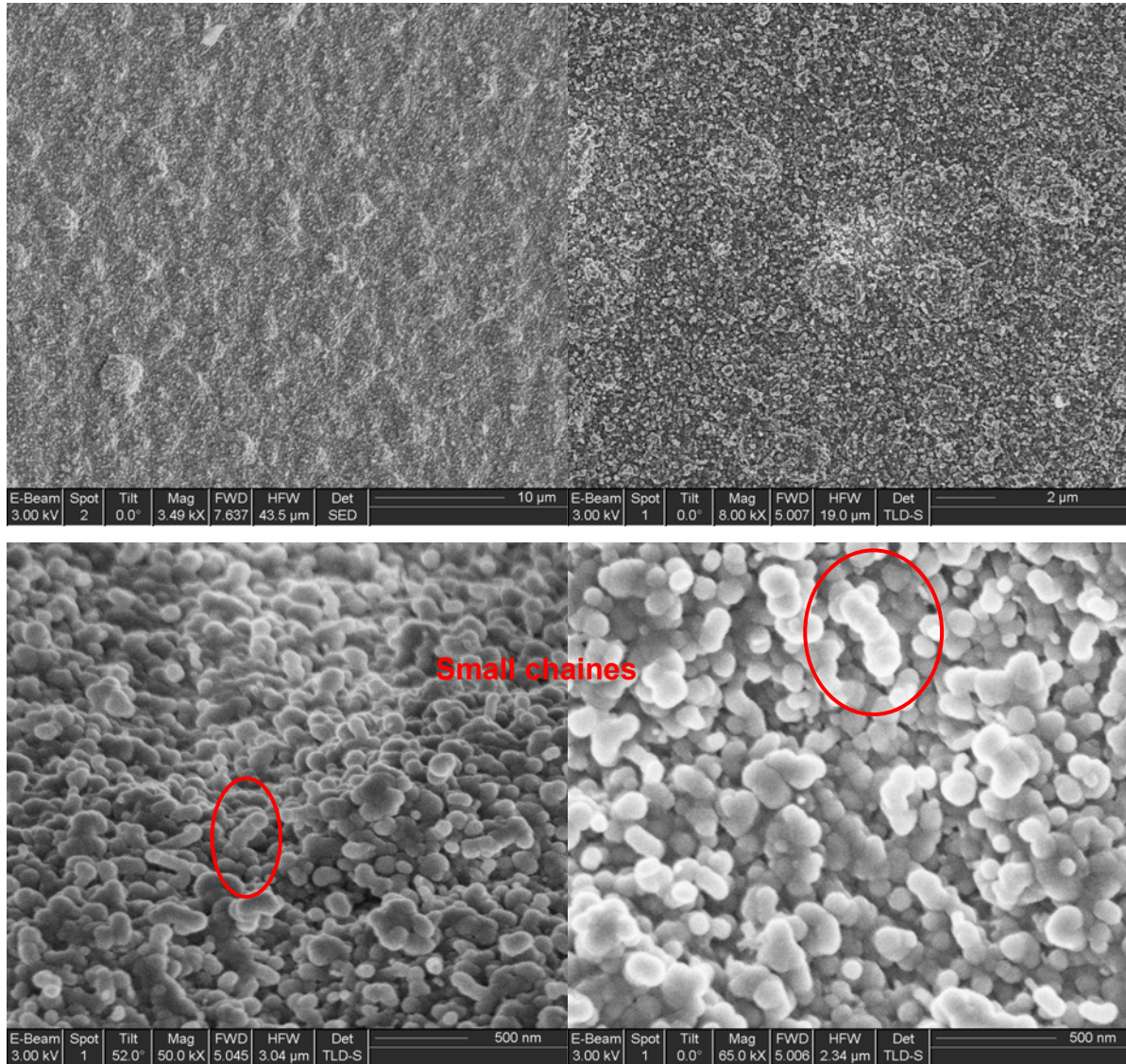


Figure 3-18: SEM images of an Al/Al₂O₃ layer grown at 490 °C with a low precursor flow during 10 minutes. Particles (app. 70 nm) aggregate to form chains or bigger particles.

The aggregation into bigger particles permits to minimize the surface energy of the nanoparticles. Self assembly into chains has been observed for polymers, janus nanoparticles, core shell nanoparticles and metallic nanoparticles, to obtain one dimensional arrangements^{42, 43, 44}. It is nevertheless not usual and by increasing the deposition time to one hour a most stable morphology is observed (Figure 3-19).

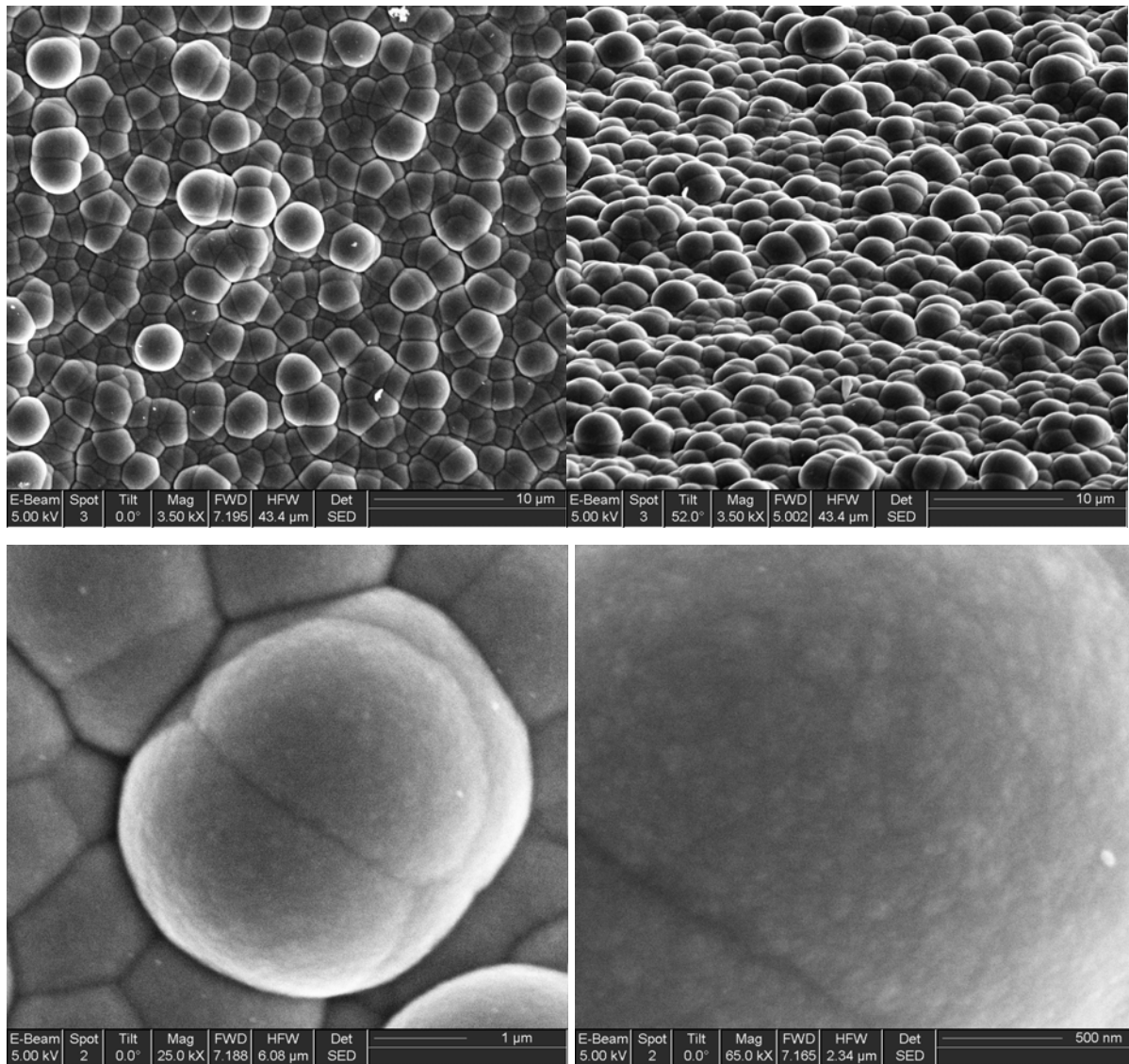


Figure 3-19: SEM images of an Al/Al₂O₃ layer grown at 490 °C with a low precursor flow during 1 hour. Big particles (app. 3 µm) grow densely on the surface.

After one hour at 490 °C a light grey composite layer could have been obtained with a low precursor flow. The grey colour is an indication for the presence of aluminium as Al₂O₃ is white or transparent. With a high precursor flow (chamber pressure is 3.10⁻¹ mbar) the layer obtained is as well light grey but no metallic aluminium was detected (see table 3.2) by XRD. Both layers present a similar surface structure (Figure 3-19 and 3-20).

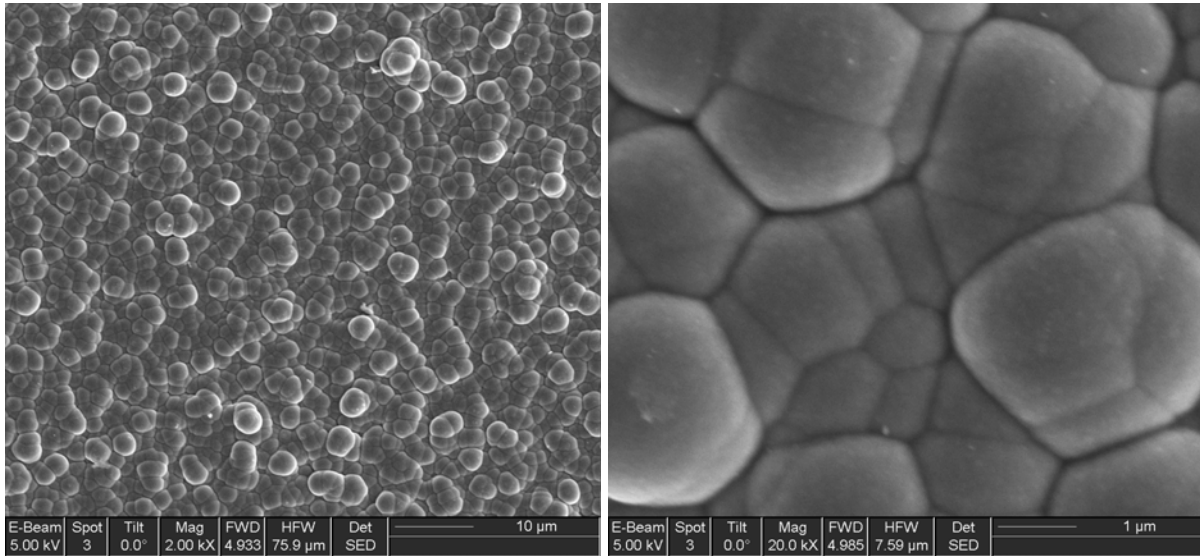


Figure 3-20: SEM images of a layer grown at 490 °C with a high precursor flow during one hour. Big particles (app. 3 µm) grow densely on the surface.

The surfaces of the layers deposited during one hour at 490 °C present a very dense package of spherical particles with an average diameter of 3 µm. The obtained structure is comparable to the one described previously on quartz³⁵, but the particles are much bigger in the latter. This microstructure is typical for the growth of amorphous aluminium oxide^{45,18}. Indeed it can be seen in the corresponding XRD pattern (Fig 3-8) that the crystalline aluminium fraction is very small and indistinguishable at 490 °C: aluminium clusters must be very small. An attempt to localise the aluminium crystals in both layers has been performed by elemental analysis of the surface by an EDX mapping. (Figure 3-21).

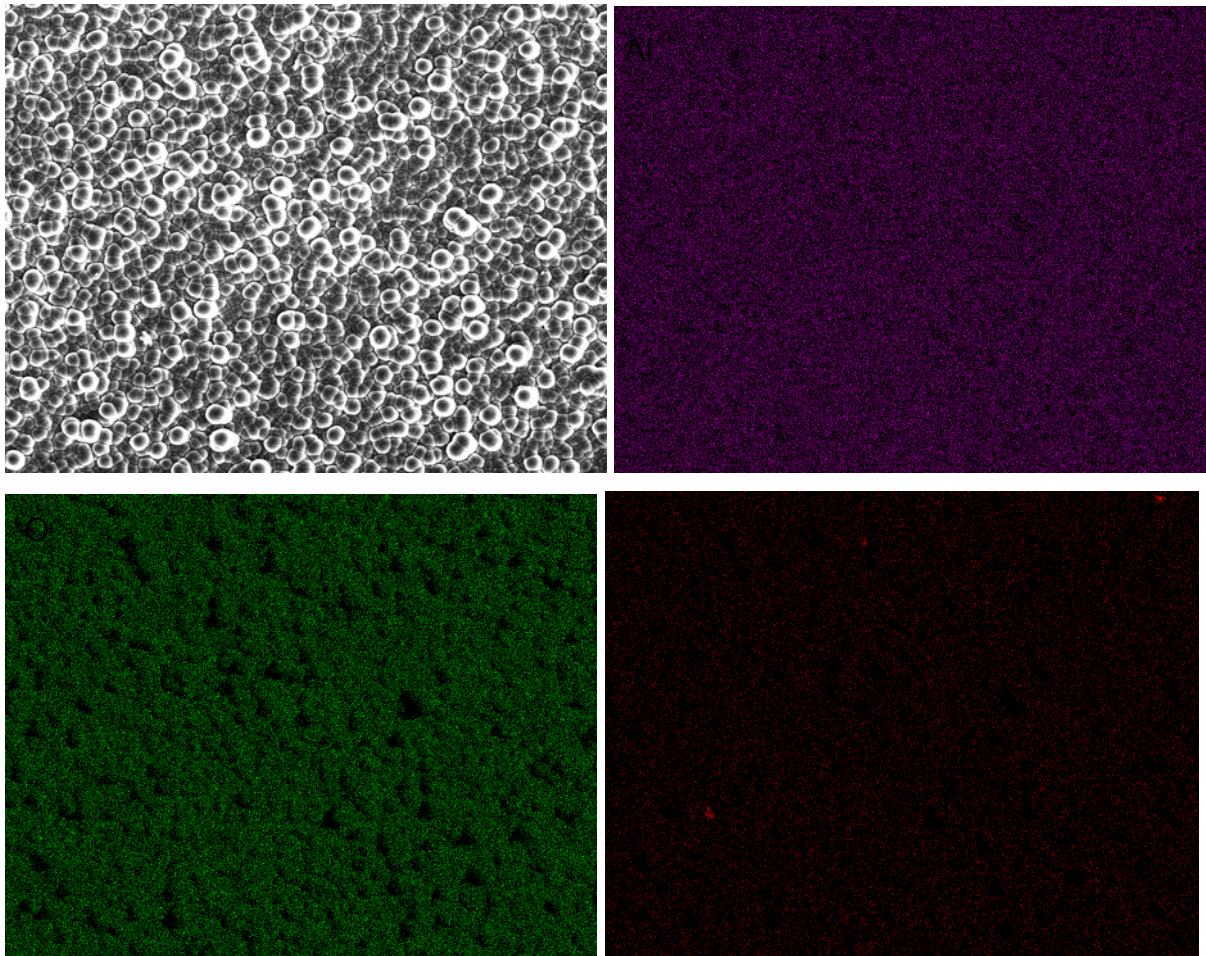


Figure 3-21: EDX mapping of aluminium (above), oxygen (below left) and carbon (below right) in the layer grown at 490 °C at low precursor flow during one hour.

In both case, the elements aluminium and oxygen are homogeneously distributed on the surface. No region with a higher aluminium concentration can be distinguished. Precedent studies on similar layers by neutron scattering have proved that small aluminium particles must show a fractal distribution that's probably the case here that's why the expected aluminium crystals cannot be localised with EDX. The atomic concentration is $50 \pm 3\%$ aluminium and $50 \pm 3\%$ oxygen in both cases, but these values are to be taken with caution as far as oxygen cannot be quantified precisely by EDX.

Focused Ion Beam (FIB) permitted to execute a cross section of the layers (figure 3-22 and 3.23).

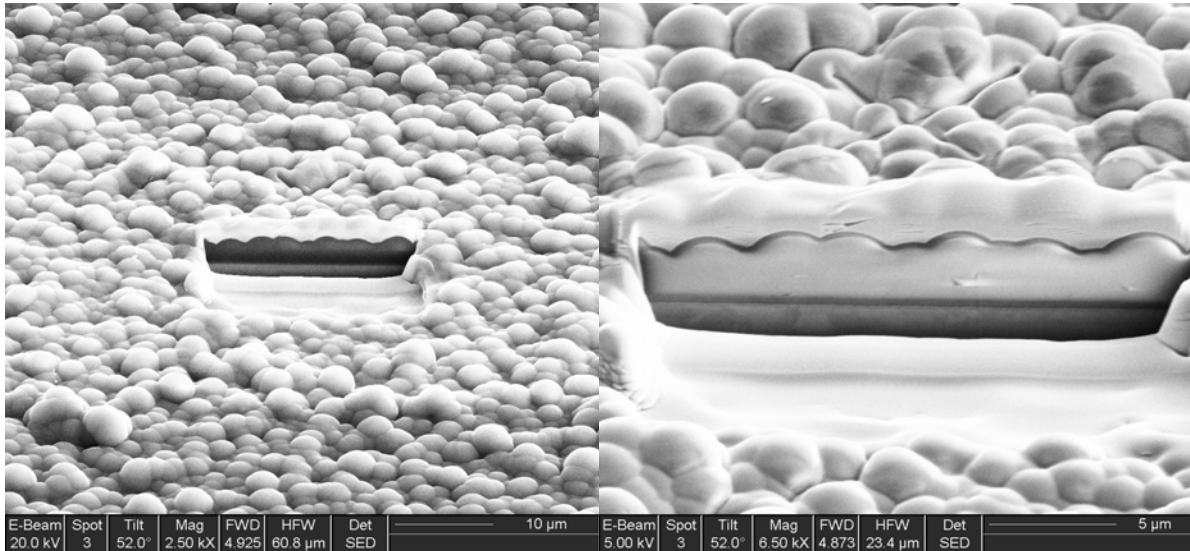


Figure 3-22: Layer profile: SEM images of a cross section performed by FIB on the Al/Al₂O₃ layer grown one hour at 490 °C at low precursor flow.

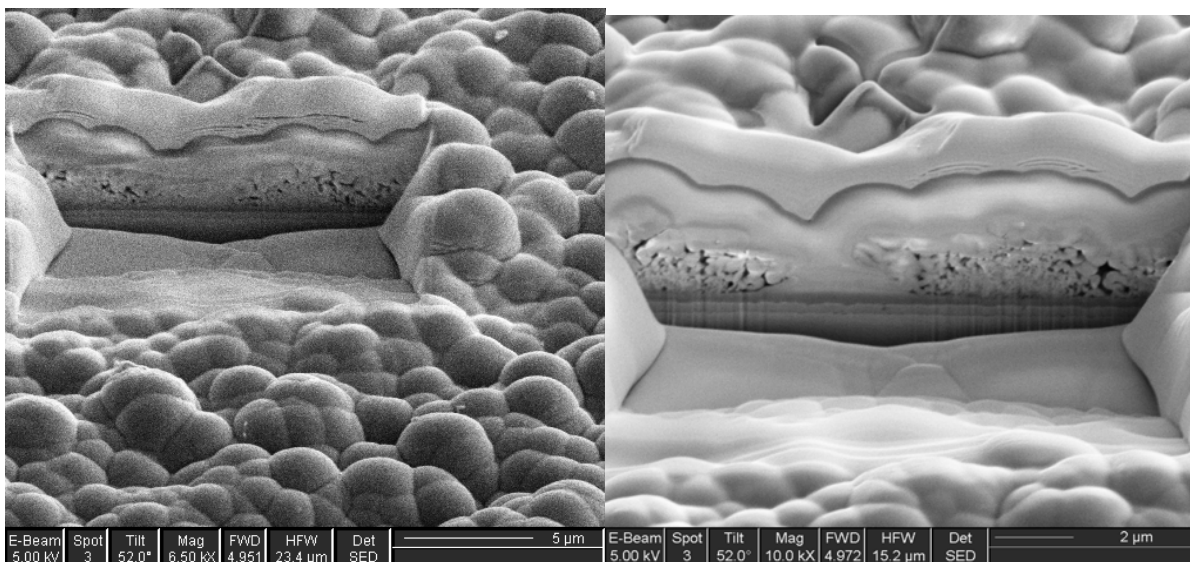


Figure 3-23: Layer profile: SEM images of a cross section performed by FIB on the Al/Al₂O₃ layer grown one hour at 490 °C at high precursor flow.

The layer thickness can be precisely measured; the film at low precursor flow is a little bit thinner than the one at higher precursor flow (3 μm and 5 μm) but the values remain in the same size range. The layer profiles are not identical although their surfaces were very similar. For the layer grown at low precursor flow, the layer is structurally homogenous and dense, whereas the layer grown at higher precursor flow presents some porous areas on its surface. The next chapter (chapter 4) will show that the porous regions correspond to the structure obtained for layers grown at higher temperature (more than 530 °C), thus their must be a variation in the

temperature along the layer thickness. The temperature gradient can easily be explained because the heating is produced by a high frequency generator, the metal target will reach the desired temperature but during film growth if the grown material is an insulator the surface will have a lower temperature than the target. Thus, the real deposition temperature on the insulating aluminium oxide surface is unknown but must decrease along the profile.

The cross sections will be analysed with EDX mapping and scanned with ion beam, in order to localise a phase or element segregation (figure 3-24 and 3-25).

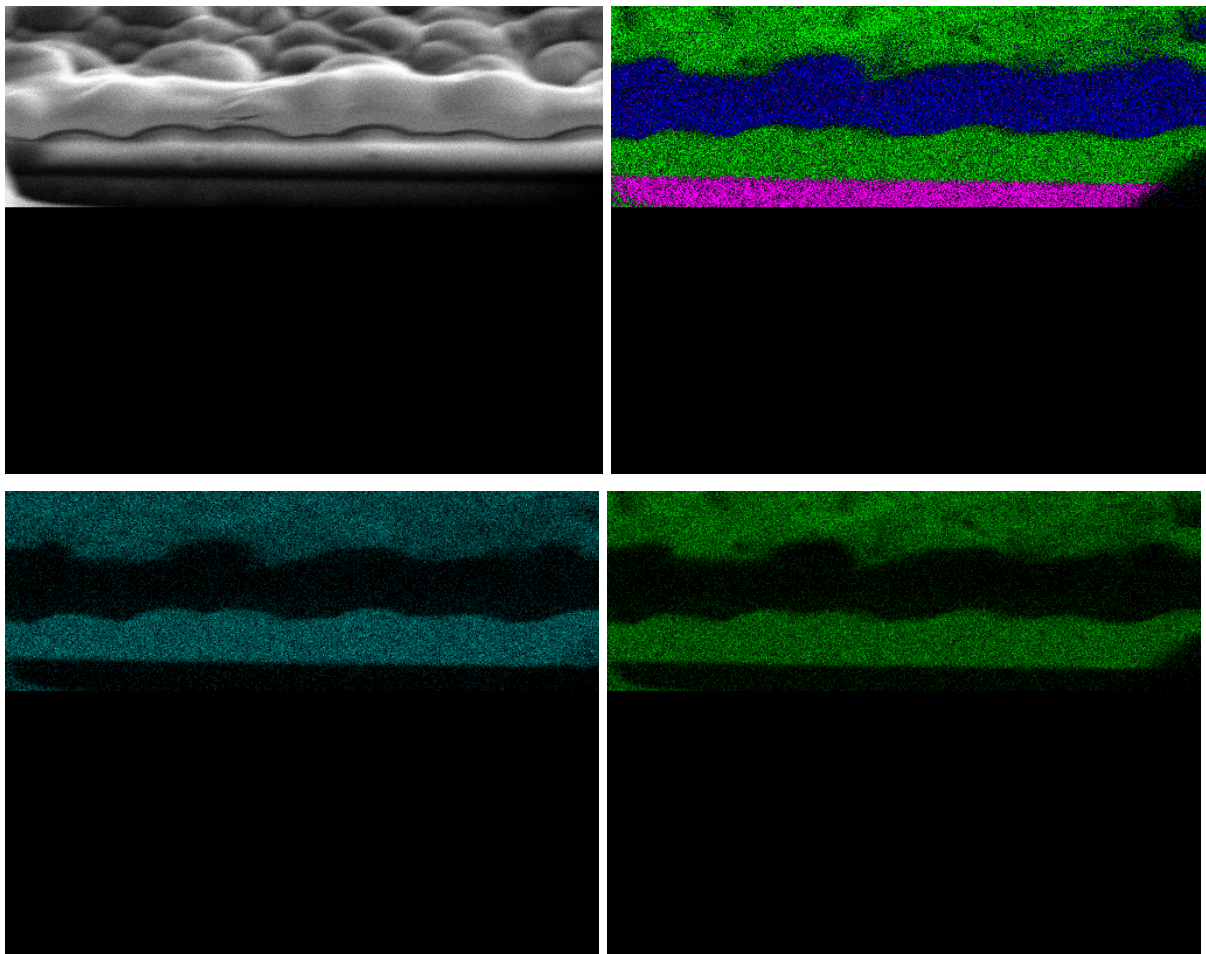


Figure 3-24: EDX mapping in the cross section of the layer grown at 490 °C, one hour with low precursor flow. Iron from the substrate (pink) and the protective platinum layer (blue) are detected. Aluminium (turquoise) and oxygen (green) are homogeneously distributed.

At the top of the EDX map the surface of the layer can be seen, the cross section is situated between the protective platinum layer (blue) and the iron substrate (pink). The elements aluminium (turquoise) and oxygen (green) are homogeneously

distributed in the cross section, moreover their concentration (52/48 atomic %) is similar to the ones on the surface (51/49 atomic %).

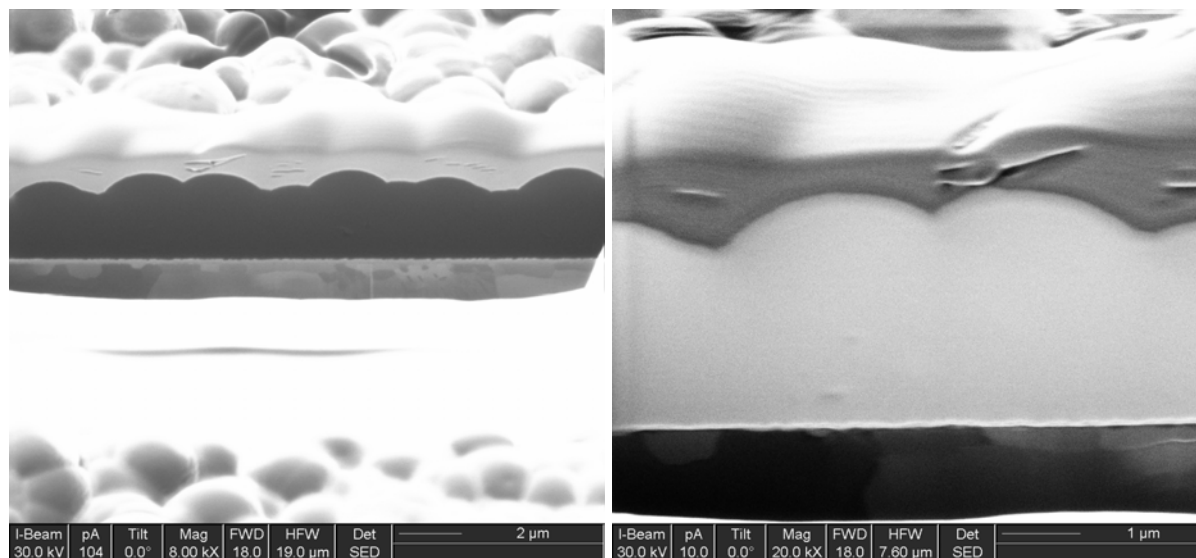


Figure 3-25: Ion beam images of the cross section of the Al/Al₂O₃ layer grown at 490 °C, one hour with low precursor flow.

Ion beam measurements show a homogeneous phase in the profile for the layer grown at low precursor flow. EDX mapping has been performed for layers grown with higher precursor flow (Figure 3-26).

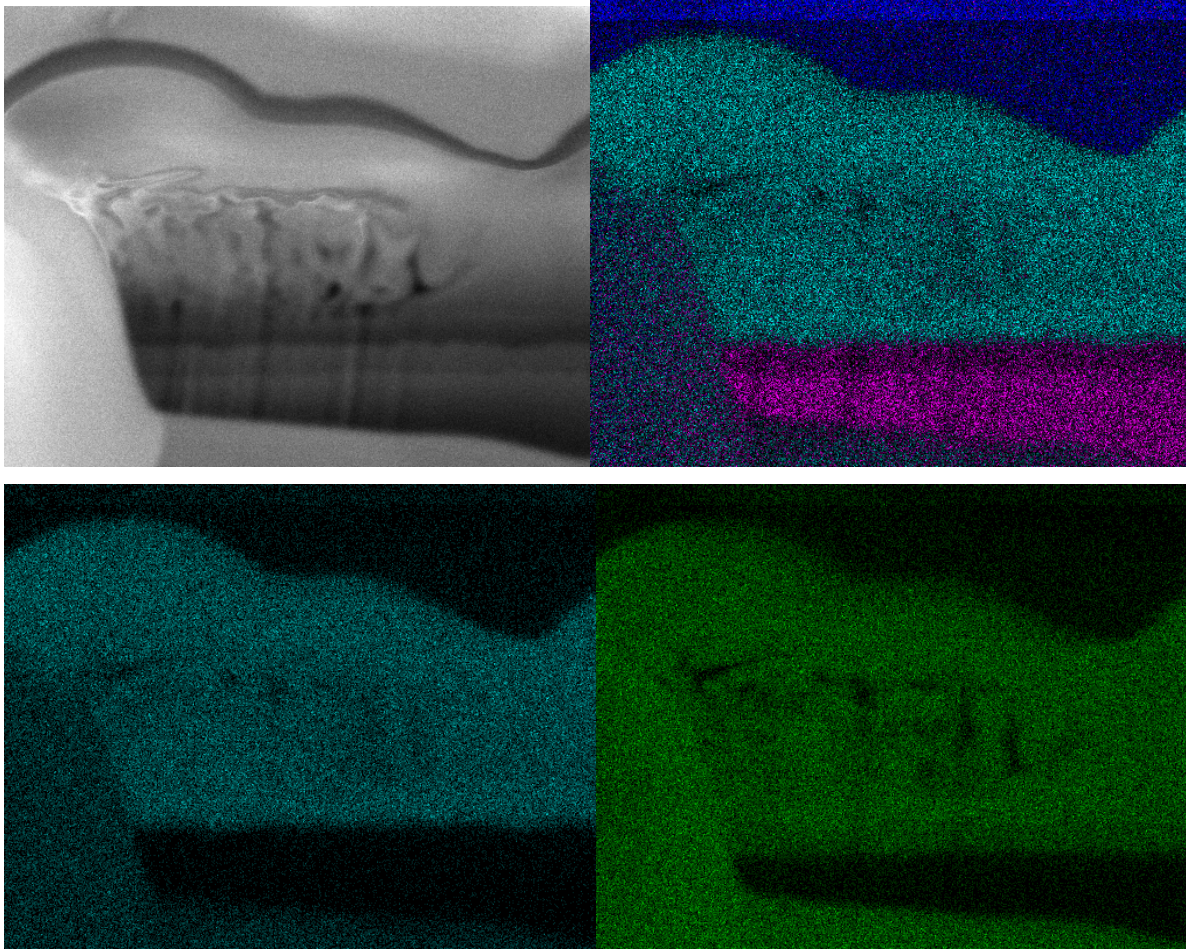


Figure 3-26: EDX mapping in the cross section of the layer grown at 490 °C, one hour with high precursor flow. Iron from the substrate (pink), the protective platinum layer (blue), aluminium (turquoise) and oxygen (green) are detected.

The black regions observed do not correspond to a variation of the composition but to the porous area where less material is detected in the pores.

A linear analysis along the growth direction has been performed on both layers (Figure 3-27 and 3-28) to detect any variations during deposition.

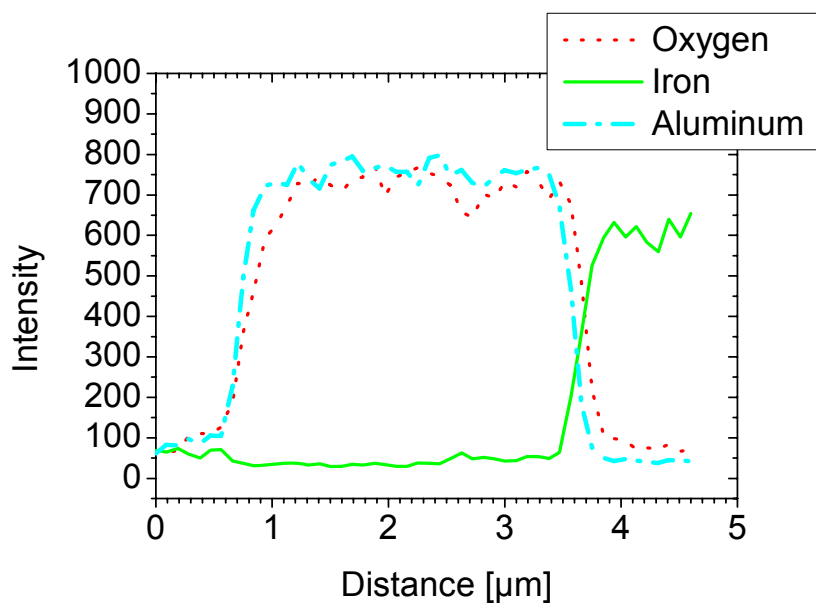
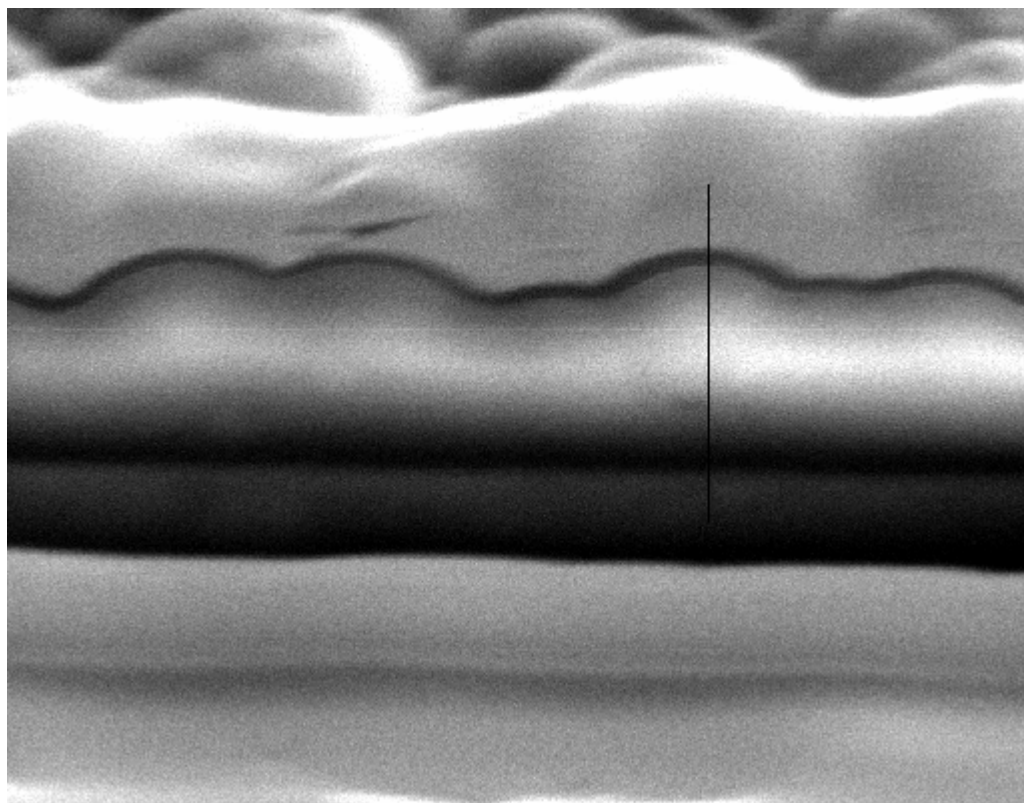


Figure 3-27: Region of interest and EDX analysis along a line in the cross section of the Al/Al₂O₃ layer grown at 490 °C, one hour with low precursor flow.

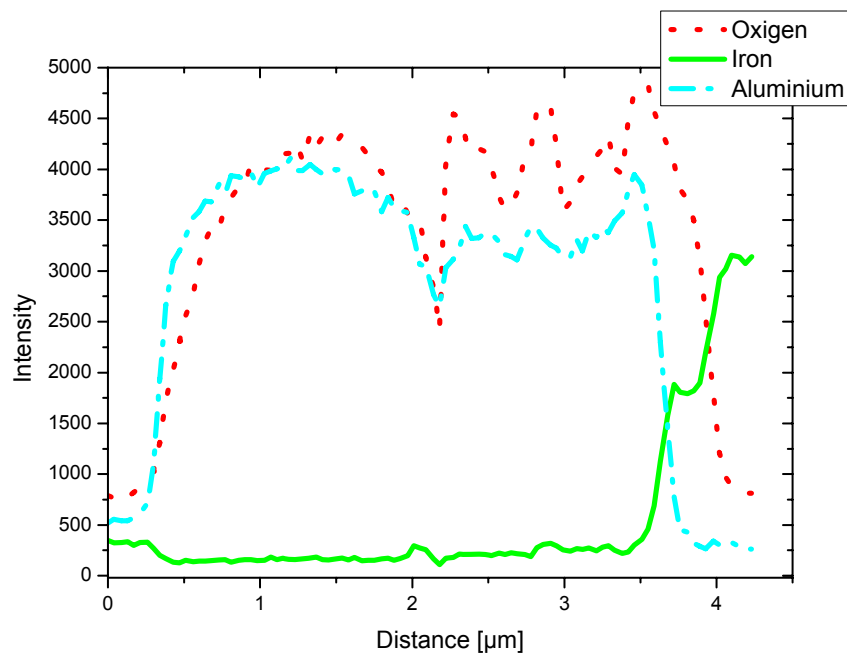
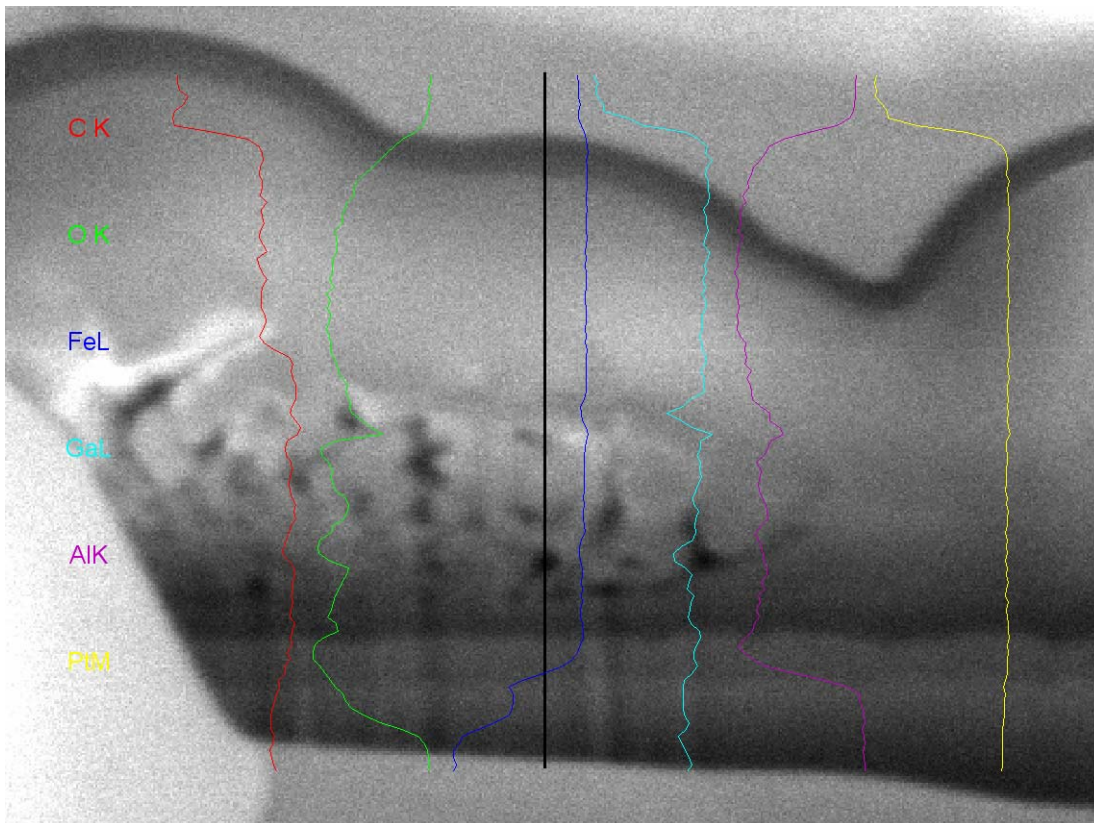


Figure 3-28: Region of interest and EDX analysis along a line in the cross section of a Al/Al₂O₃ layer grown at 490 °C, one hour with high precursor flow.

The linear analysis along the growth direction confirms a homogeneous growth of the layer fabricated at low precursor flow. However, the layer grown at high precursor

flow shows two regions: at the surface the amount of aluminium and oxygen are constant but they vary near the substrate. These variations can be attributed to the lack of material due to the high porosity of the layer near the surface.

At low precursor flow, the layers can be deposited for up to one hour and 30 minutes because longer deposition leads to the destruction of the film. At higher precursor flow, growing a layer is complicated because the film flakes off if the deposition last more than one hour 30 minutes, but as well if the deposition time is too short (less than 30 minutes). The porous structure on the substrate is probably unstable and then it needs to be recovered by the spheres otherwise the layer flakes off.

At the beginning of the deposition (after 10 minutes) small particles (70 nm) with high surface energy are formed. These particles aggregate into chains or bigger particles. After longer deposition (1 hour), bigger particles (app. 3 µm big half spheres) are formed. For both layer types aluminium clusters are embedded in Al₂O₃ (grey colour of the layers) but no aluminium peaks are detected by XRD after 10 minutes deposition because the clusters are too small (see table 3-4). After 1 hour, aluminium has been detected by XRD. At this stage, aluminium crystals are too small to play a role in the morphology of the layer: the half spheres obtained are typical of Al₂O₃ layers without aluminium. According to previous studies, the small aluminium crystallites are distributed fractally in the Al₂O₃ half-spheres³⁵. No TEM analysis has been done to localise precisely the aluminium clusters because the Al₂O₃ spheres, in which aluminium is embedded are too big for TEM measurements.

By increasing the precursor flow a temperature gradient can be created, thus inhomogeneous layers with a porous fraction are obtained.

3.4.2 Deposition at 530 °C

Layers grown at 530 °C with a high precursor flow (chamber pressure is 3.10⁻¹ mbar) are dark gold and transparent whereas at lower precursor flow they are grey and beamless. At 530 °C layers are obtained after one minute deposition and do not breck off even after 2h30 at low precursor flow (chamber pressure is 3.10⁻² mbar). Pictures of layers grown after one hour are shown below (Figure 3-29).



Figure 3-29: Pictures of layers grown one hour at 530 °C at low (left) and high precursor flow (right).

The layer grown with high precursor flow has the same aspect as a HAIO layer (HAIO layers are grown below 490 °C) but is somewhat darker, whereas the layer with low precursor flow seems like a pale composite layer. These visual disparities suits to the results of XRD measurements (Table 3-2) as the layer with low precursor flow is a composite material and the one with high precursor flow does not contain any metal. SEM images of the HAIO like film are shown on figure 3-30.

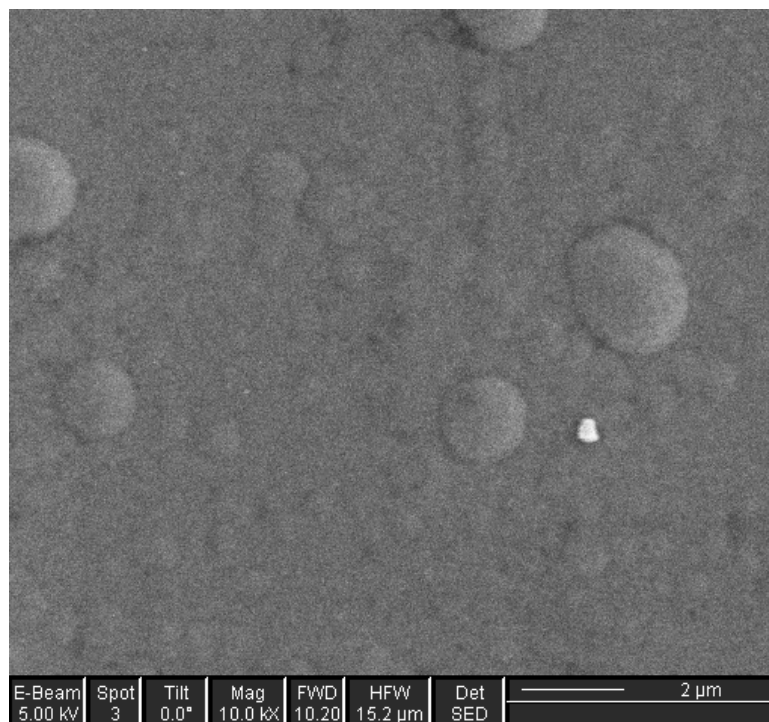


Figure 3-30: SEM image of a HAIO-like layer grown one hour at 530 °C at high precursor flow.

Like HAIO films the layer is relatively smooth as it shows very low secondary electron contrast. FTIR analysis has been performed to compare this layer with a HAIO film (Figure 3-31) with comparable thickness.

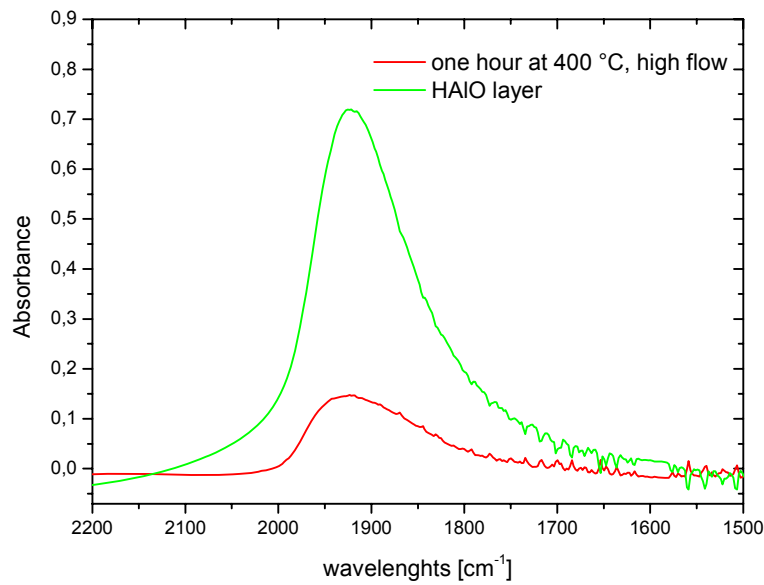


Figure 3-31: FTIR spectra (Al-H band) of a layer grown one hour at 530 °C at high precursor flow compared to a HAIO layer.

In both cases an Al-H absorption band is visible at 1920 cm⁻¹. The relative small size of the absorption band in comparison with a pure HAIO layer shows that less hydrogen is present on this layer. K. Andres already demonstrated this evolution in reference 20. The layer obtained must be a H_nAlO (n<1). For a composite layer, n must near 0 and no Al-H band should be detectable. The colour of the layer associated with XRD, FTIR and SEM analysis shows that the layers grown at high precursor flow are not composite. At high precursor flow, there is obviously no time to disproportionate.

SEM Images of the film grown at 530 °C at low precursor flow during one hour are presented on figure 3-32.

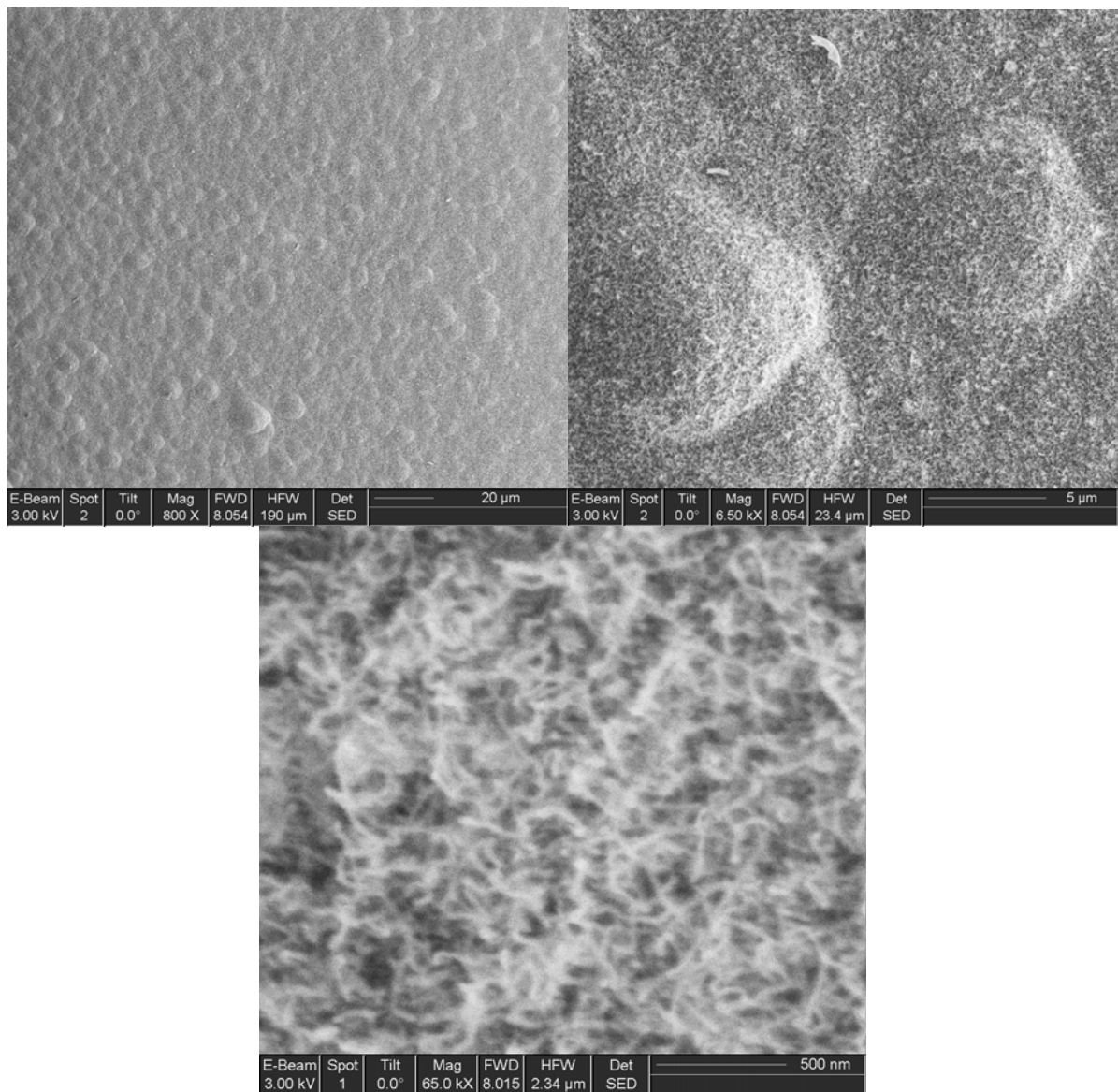


Figure 3-32: SEM images of the surface of a layer grown at 530 °C during one hour at low precursor flow. Short Al/Al₂O₃ nanowires are seen.

With a small magnification, the surface presents morphological similarity with the film deposited at 490 °C (figure 3-19). Indeed, the surface is composed of 5 μm big spheres densely close to one another (Figure 3-32). However, the detailed observation of the 5 μm big particles reveals that they are constituted of entangled nanowires.

There are two possibilities to explain this phenomenon: either the particles have been covered by nanowires or nanowires grow preferentially in spherical shapes. The second hypothesis is more convincing because the deposition temperature cannot increase during deposition and it will be shown that the nanowires are specific for a

high temperature deposition. Nevertheless a spontaneous growth of one dimensional nanostructure on the surface was not expected; hence a study of the nanowires and their growth will be performed in following chapter (chapter 4).

3.4.3 Deposition at 560 °C

At 560 °C nanowires are always formed regardless of the deposition time and flow. However, various surface structures, densities and nanowires' lengths are obtained depending on the deposition conditions.

An interesting example is the fabrication of nanowires which assemble into spheres on the surface at small precursor flow and relatively low temperature. Figure 3-33 shows a SEM image of a layer grown for one hour at low precursor flow (chamber pressure is $3 \cdot 10^{-2}$ mbar) at 560 °C.

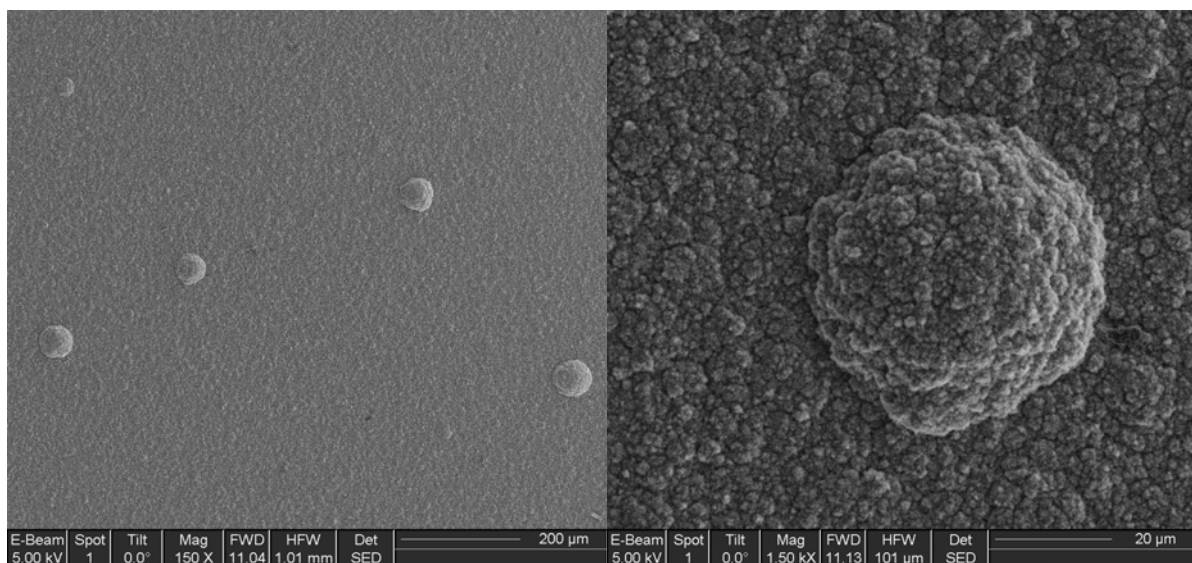


Figure 3-33: SEM images of an Al/Al₂O₃ layer with spherical particles grown for one hour at low precursor flow at 560 °C.

At the microscopic scale the layer is relatively homogeneous and shows little topographical contrast except some spherical particles of about 50 μm diameter. With a 1500 times magnification the surface shows crumple-like topographical contrast and no material or phase contrast between the background of the layer and the grown particle is visible. Figure 3-34 show SEM pictures of the background and of the particle with 80,000 time magnification.

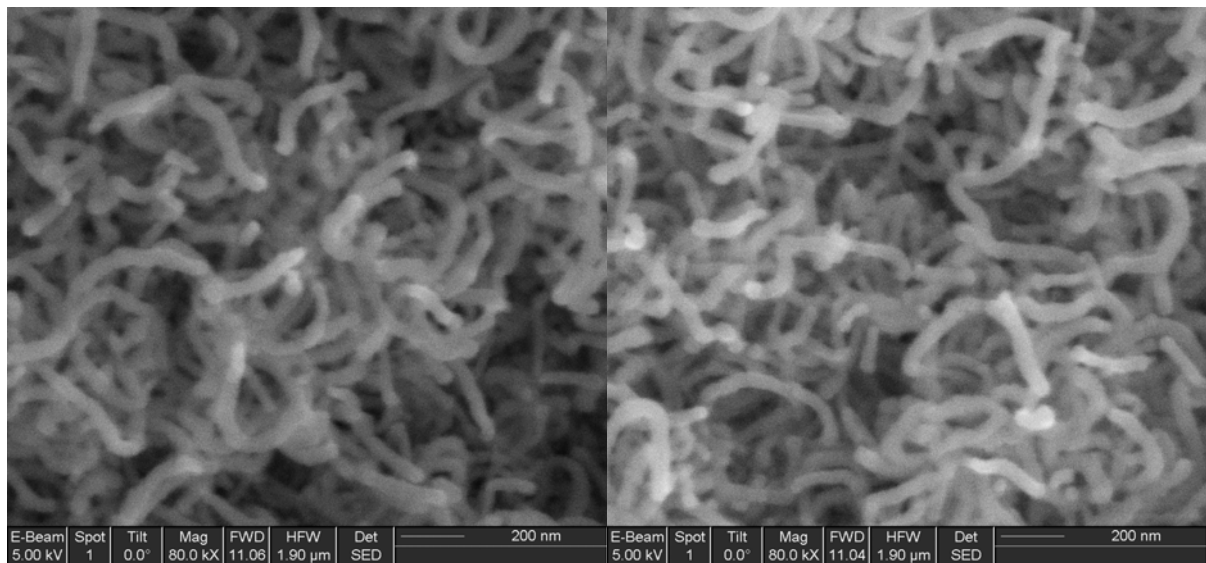


Figure 3-34: SEM pictures of the background and a spherical particle from precedent figure (fig. 3-34) with 80,000 time magnification. Al/Al₂O₃ nanowires are seen in the background as well as in the particle.

Even with a nanometric observation, no difference is observable between the structure of the background and the one of the particle. Indeed the layer is constituted by a one dimensional nanostructure assembly. The nanowires are longer than the one observed at 490 °C; their exact inner structure will be discussed in chapter 4.

Increasing the number of particles grown at the surface of the sample is possible by increasing the deposition duration. Figure 3-35 is a SEM image of a sample grown at 560 °C during 1h30 at low precursor flow.

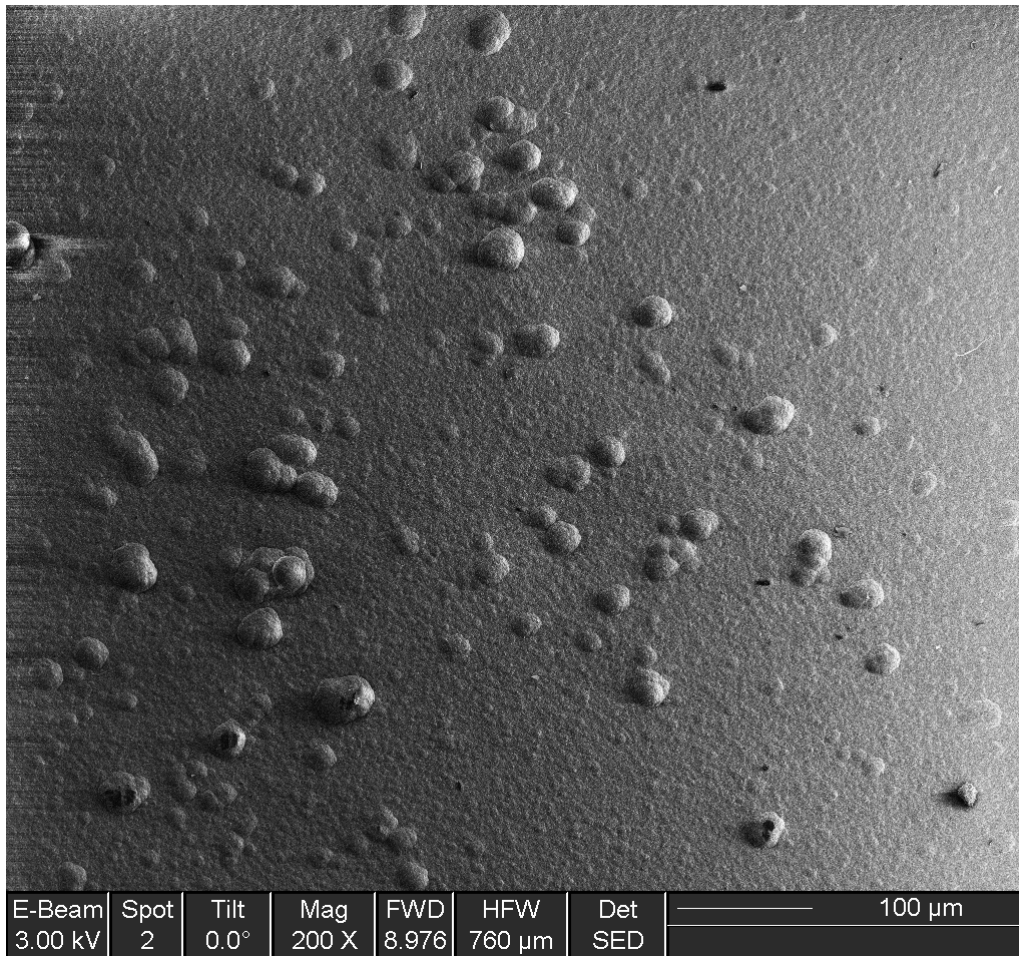


Figure 3-35: SEM image of spherical particles formed on an Al/Al₂O₃ layer grown at 560 °C during 1h30 at low precursor flow

By increasing the deposition time it has been possible to modify the surface structure. The layers grown with a low precursor flow at 560 °C (Fig. 3-35) display a micro- as well as a nanostructure. At the nanometer scale it is relevant to control the surface structure as this can govern many properties. As our approach allows obtaining different surface structures, various surface properties and applications can be expected. Through a combination of micro- and nanostructuring a chemically hydrophobic surface can for example become extremely hydrophobic. C. Petersen has demonstrated in his PhD thesis that layers with a surface like the one shown in Figure 3-35, can show superhydrophobic properties⁴⁶. Now the fabrication conditions of such layers are defined precisely.

Figure 3-36 shows a layer grown at 560°C with high precursor flow (chamber pressure is $3 \cdot 10^{-1}$ mbar) after 1h deposition.

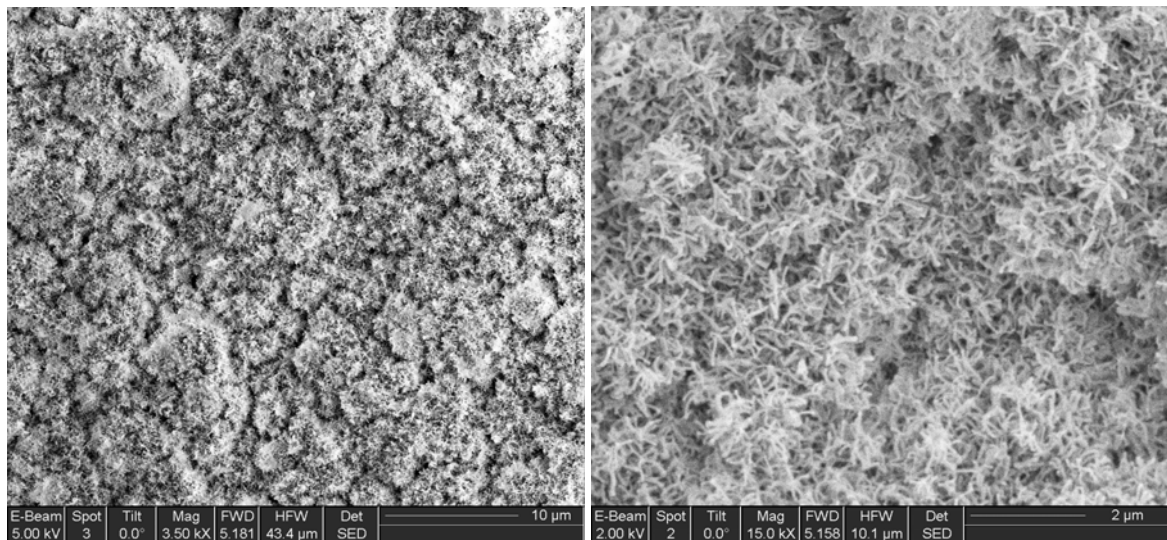


Figure 3-36: SEM images of an Al/Al₂O₃ layer grown at 560 °C with high precursor flow after 1h deposition

By increasing the precursor flow no particles are formed on the surface, a cauliflower like microstructure is obtained whereas at the nanometer scale relatively short wires (or nanorods) are visible. By comparing with the layers obtained at 530 °C with low precursor flow, the nanowires seem longer and denser. The elongation of the nanowires may be due to the deposition at higher temperature whereas the densification is probably related to the precursor flow.

3.4.4 Deposition at high temperature (above 560 °C)

The layers obtained at 600 °C don't present any visual disparities; they are all deep black with blue reflexes and a velvety aspect.

Above 560 °C the nanowires are formed and their assembling density and their length can easily be controlled by varying the precursor flow and target temperature. Figures 3-37 and 3-38 show nanowires formed with a low precursor (chamber pressure is $3 \cdot 10^{-2}$ mbar) flow after one minute and one hour deposition at 600 °C.

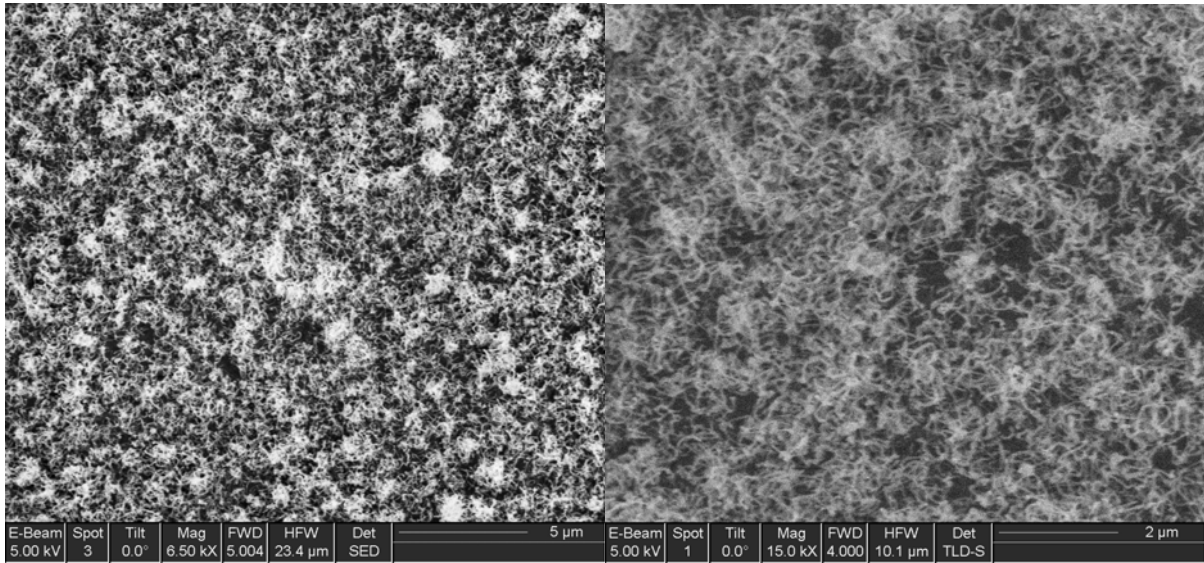


Figure 3-37: SEM images of a Al/Al₂O₃ layer grown at high temperature (600 °C) during one minute.

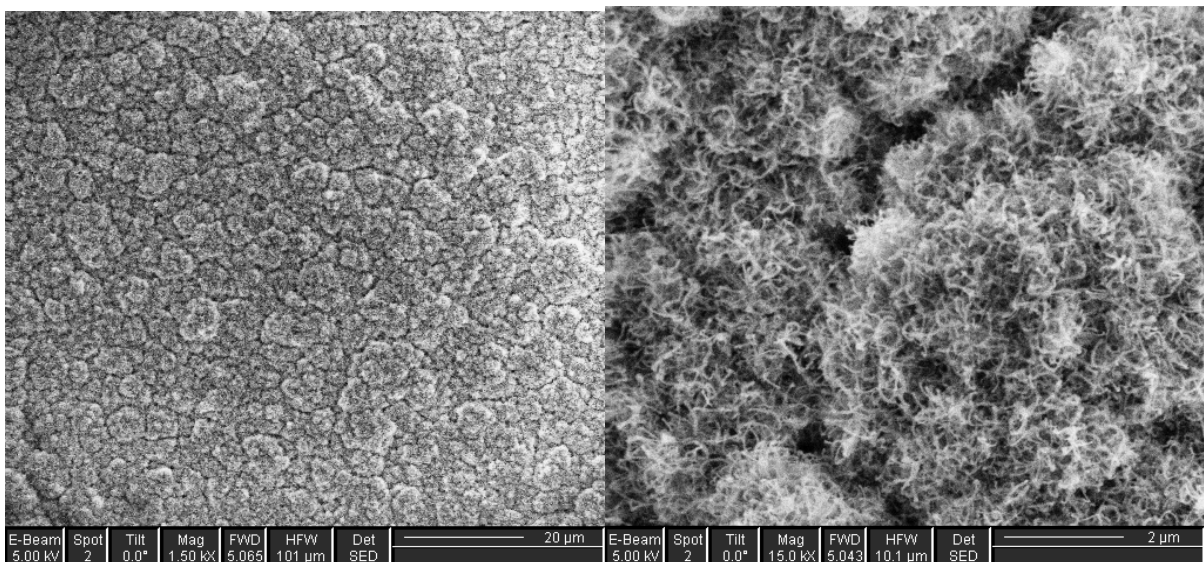


Figure 3-38: SEM images of an Al/Al₂O₃ layer grown at high temperature (600 °C) during one hour.

At 600 °C the surface presents a rough and porous like microstructure, it can be compared to the surface of a cauliflower. The nanowires form denser aggregate when deposited during one hour. A one minute deposition is not sufficient to become a dense coverage of the target. By comparing with layers grown at lower temperature the nanowires are longer at higher substrate temperature. An absolute value for the nanowires lengths is not given as the entangled structure does not permit to separate one single nanowire from the others without damage.

By use of High Resolution SEM mode and increasing the contrast, the one dimensional nanostructure can be seen with more accuracy (Figure 3-39).

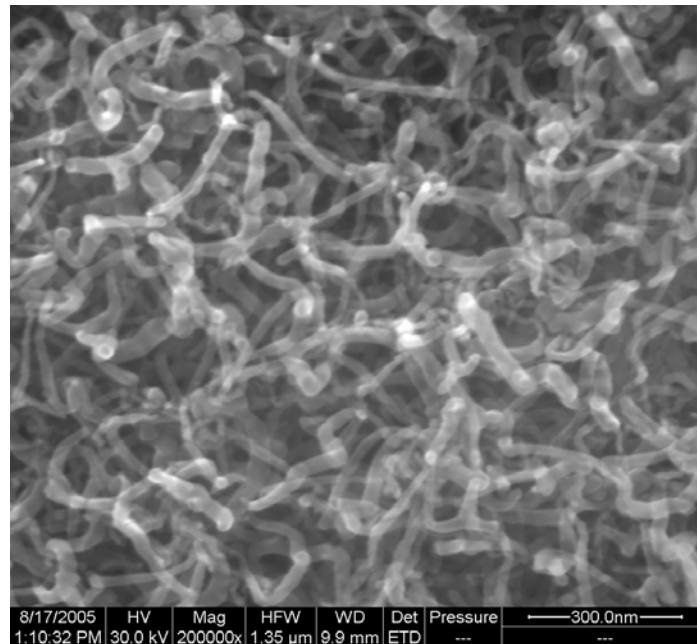


Figure 3-39: Contrast enhanced HR- SEM image of nanowires.

The nanowires are closely interlaced. Each wire is about 30 nm thick for about one micrometer long. No further contrast can be detected although the layer should contain aluminium crystals according to the previous XRD analysis.

Figure 3-40 shows a layer grown at 600 °C during 2 hours. XRD analysis detected aluminium carbide [PDF 79-1736] in this layer.

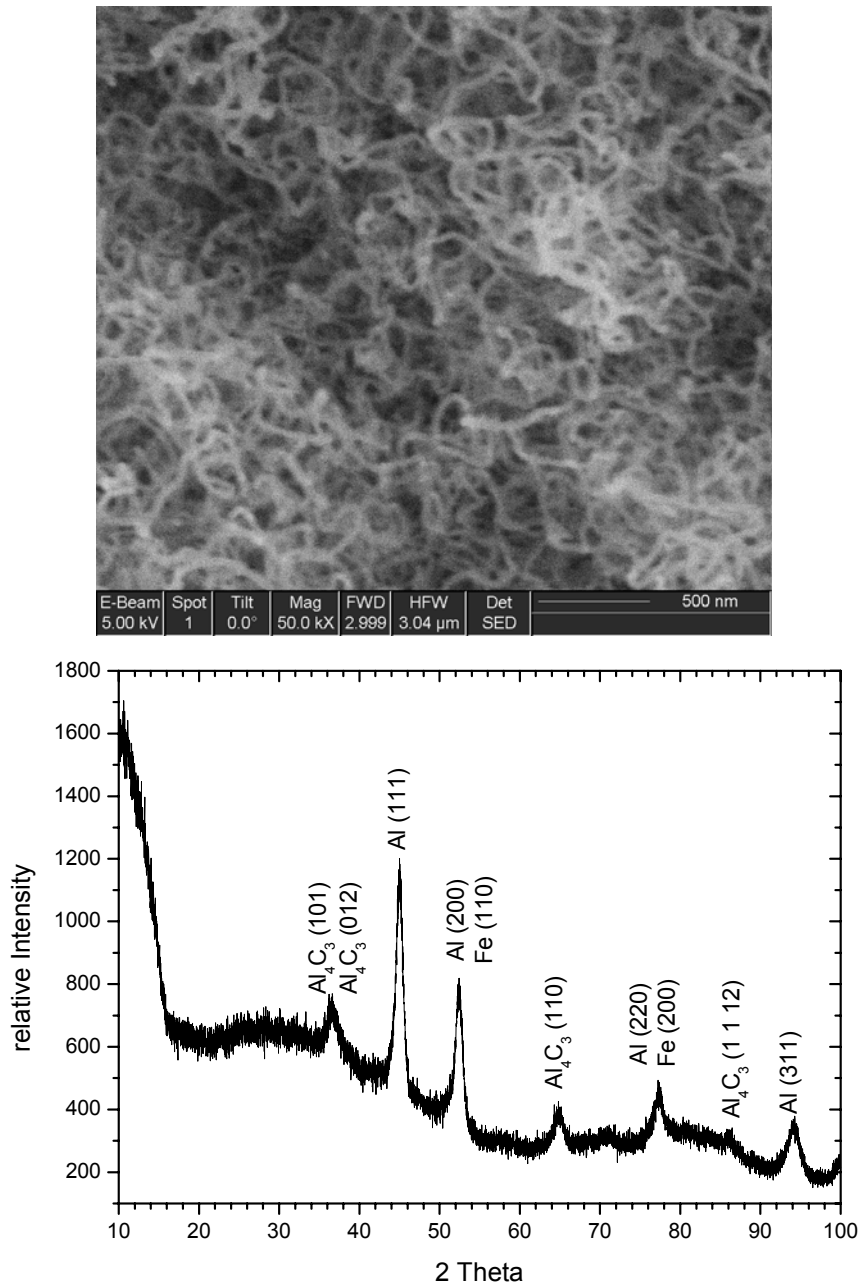


Figure 3-40: SEM image of an Al/Al₂O₃ layer with nanowires containing Al₄C₃ and its XRD pattern.

Nanowires are also obtained: the aluminium carbide formation does not seem to act on the microstructure.

In 2001 a study of alumina coating revealed also the effects of temperature and precursor flow on the morphology of the film surface⁴⁵. For alumina a change of roughness and randomly distributed adatoms have also been observed, nevertheless no nanowires have been created, these results combined with the XRD measurement mean that the one dimensional growth is due to the presence of crystalline aluminium. The image quality is sometimes not good and no EDX analysis

could have been performed on the samples with nanowires structure as they drift a lot during SEM analysis, this indicates that the layer surface must be insulating.

3.5 Conclusion

A composite layer has been defined as a layer where aluminium crystals could have been measured by XRD in an amorphous aluminium oxide matrix. The CVD variables, which enable the formation of Al/Al₂O₃ composite layers could successfully be determined by XRD analysis. Temperature turns out to be the most important variable which influences the layer characteristics. The biggest changes observed when growing conditions are varied are changes in the morphology of the composite layer. Figure 3-41 illustrates the composite layer at various temperatures.

With a precursor at room temperature it was possible to show that aluminium crystals appear after one minute deposition at 530 °C and this phenomenon is followed by the formation of aluminium carbide after 90 minutes deposition. At 600 °C the composite is also formed after one minute and aluminium carbide formation occurs after one hour deposition. By cooling the precursor with ice, the formation of composite occurs at lower temperature (490 °C) but needs more time (30 minutes). The formation of aluminium carbide is also postponed up to 2 hours deposition in this case. An unidentified {Al·O} phase is detected but is not related to the CVD parameters, which are varying in this study. It is probably a cubic oxide called γ' -Al₂O₃, which changes in contact with air. SEM analysis was not able to give any information about the cubic aluminium oxide phase.

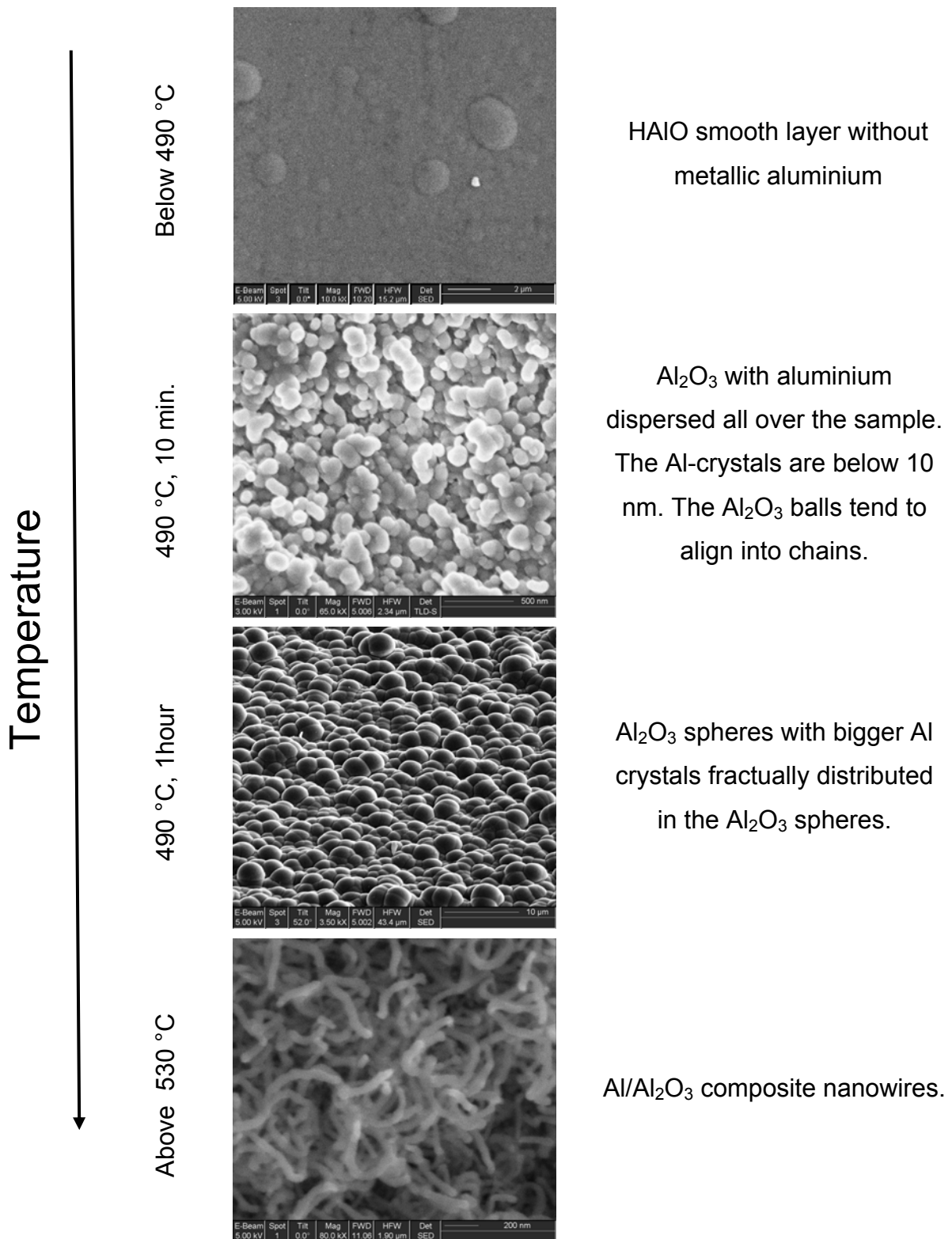


Figure 3-41: Illustration of the different layers grown by varying deposition conditions. SEM images and composition of the HAIO layer grown at 490 °C, the composite layer with ball like structure grown at 490 °C and the Al/Al₂O₃ nanowires grown above 530 °C

At low substrate temperature, the composite Al/Al₂O₃ presents a low fraction of crystalline aluminium which does not influence the microstructure, thus the structure is like the one reported for Al₂O₃, viz. dense assembly of some μm big spheres. EDX imaging did not allow plotting the exact location of the aluminium crystals on the surface or inside the film. By increasing the deposition temperature, the amount of metallic aluminium increases, thus a cauliflower like film structure formed by a dense assemblage of nanowires is obtained. The length and density of the nanowires can be varied by changing the precursor flow. For a given temperature the increase of the deposition time allows to form thicker films with denser nanowires. To get short nanowires a low deposition temperature with a high precursor flow (chamber pressure is $3 \cdot 10^{-1}$ mbar) are necessary. Moreover a structure, where a micro and a nano arrangement are present, can be obtained at low temperature and low precursor flow (chamber pressure is $3 \cdot 10^{-2}$ mbar). To conclude: the most important parameter is the temperature. At 510 ± 15 °C, i.e. between 490 °C and 530 °C, a transition between ball like and nanowire structure is observed.

Since no material contrast is seen and EDX is impossible at a nanometric scale, the SEM analysis did not permit to localise the aluminium particles, the aluminium carbide or the aluminium oxide phase which are present according to XRD analysis. The entangled one dimensional structure is unexpected as during preparation no inhomogeneity was introduced which could lead to anisotropic growth. Therefore further analysis is necessary to clarify this nanostructure, explain the nanowires growth, and localise the crystals detected by XRD.

A complete description of the nanowires' structure, growth and properties is the object of chapter 4.

4 Structural study of the Al/Al₂O₃ nanowires

It has been shown in the precedent chapter, that by varying the deposition temperature, it is possible to grow one dimensional nanostructures. A simple nanowires structure growth as described in the previous chapter i.e. without metallic catalyst or template is at the moment vary rare by CVD. Hence, above the process parameters, it is relevant to understand the real growth mechanism for this spontaneous nanowires production. As no in situ instruments are available in the CVD equipment, our strategy to acquire information about the growth mechanism is to analyse the nanowires' structures and properties.

The nanowires' morphology, composition, crystallinity and growth mechanism could not have been clarified by SEM and XRD analysis. Therefore, it has been necessary to find further analysis methods, which can measure these properties at the nanoscale. Transmission electron microscopy (TEM) and electron scattering are ideal instruments to analyse the inner morphology, the phase contrast and composition at the nanometer scale.

The usual nanowires' growth mechanism and process from the literature will be discussed below. Then, a complete TEM study of the Al/Al₂O₃ nanowires structure will be presented. The TEM investigation was performed at the Leibniz-Institut für neue Materialien in collaboration with U. Werner.

4.1 Core shell one dimensional nanostructures

4.1.1 Synthesis and properties

Nanostructures have attracted growing interest due to their peculiar, fascinating properties as well as their unique applications complementary to their bulk

counterparts. One dimensional (1D) nanostructured materials refer to materials with lateral dimensions in the range of 1 to 100 nm, whereas their lengths can reach several micrometers. Since the discovery of carbon nanotubes⁴⁷ there has been a continuing growing interest in fabricating different one dimensional nanostructures, such as nanowires, nanorods or nanobelts. Nanowires in particular, provide an excellent model system to investigate the effects of size confinement on electrical transport, optical and mechanical properties. These materials are particularly interesting for applications in advanced electronic devices. For example, nanotubes are capable of converting mechanical movements into electrical signals which offer potential applications for creating high-frequency telephone lines to carry voice and data and making on/off switches for nanoscaled computer chips⁴⁸. Nanowires can be useful for the fabrication of electronic as well as photonic devices; nevertheless the advance in the utilisation of nanowires has been relatively slow. The lack of nanowires at the industrial range is probably associated with the complexity to fabricate nanowires with well-controlled size, crystallinity, chemical composition and phase purity. The ability to synthesise such small structures is central to the advance of many areas such as: electronics, magnetism, optics, energy storage, electrochemistry and biomedical sciences.

Among the methods employed, some are based on vapor phase techniques, while others are solution techniques. Compared to physical methods such as nanolithography and other patterning techniques, chemical methods have been more versatile and effective in the synthesis of inorganic nanowires in copious quantity. Thus, techniques involving chemical vapor deposition (CVD), precursor decomposition, as well as solvothermal, hydrothermal and carbothermal methods have been widely employed.

An important aspect of the 1D nanostructures relates to their crystallization [6], wherein the evolution of a solid from a vapor, a liquid, or a solid phase involves nucleation and growth. As the concentration of the building units (atoms, ions, or molecules) of a solid becomes sufficiently high, they aggregate into small nuclei or clusters through homogeneous nucleation. These clusters serve as seeds for further growth to form larger clusters. Different methods have been developed and reviewed for the synthesis of 1D nanowires. Xia, Yang and co-workers in their famous review articles^{49,50} classified the synthesis of 1D nanostructures into four different categories:

- Anisotropic growth dictated by the crystallographic structure of a solid material
- Anisotropic growth controlled and directed by various templates
- Anisotropic growth kinetically controlled by supersaturation or through the use of an appropriate capping agent,
- Miscellaneous methods with potential to yield controlled 1D nanostructures.

Other exhaustive reviews on inorganic nanowires were published by Rao and co-workers⁵¹ in 2003, Lu in 2006⁵² and Kuchibhalta in 2007⁵³.

Most of the metal oxide nanostructures are grown via the well-developed vapor phase technique, which is based on the reaction between metal vapor and oxygen gas. The governing mechanisms are the vapor–liquid–solid process (VLS) and vapor–solid process (VS). On the other hand, solution-phase growth methods provide a more flexible synthesis process and an alternative to achieve lower cost. In the following a short introduction to each of the four approaches will be given.

Materials with high anisotropic crystal structure

Chalcogenes, in particularly trigonal phase selenium and tellurium, present naturally a high anisotropy: they tend to form helical chains through covalent bonding; the helical chains are packed into a hexagonal lattice through weaker van der Waals interactions. Thus crystallisation tends to occur along the c-axis. As a consequence, these two solids form preferentially 1D structures. Uniform Se and Te nanowires can easily be grown with lengths up to several hundred micrometers^{54, 55}.

Template assisted methods

Template assisted methods represent a direct way to form 1D nanostructures. A template is a central structure within which a network forms in such a way that removal of the template creates a filled cavity with morphological features related to those of the template. If the templates that are used have cylindrical pores of uniform diameter, monodisperse nanocylinders of the desired material are obtained within the voids of the template material. Depending on the operating parameters, these nanocylinders may be solid (a nanowire) or hollow (a nanotube). The nanostructures can remain inside the pores of the templates or they can be freed and collected as an ensemble of free nanoparticles. Thus, with the template approach, one is able to

prepare monodisperse nanorods and nanotubes of almost any desired geometry and material.

Nearly any solid matter can be synthesized within nanoporous templates, if a suitable chemical pathway can be developed. There are essentially five representative strategies, these include: electrochemical deposition, electroless deposition, chemical polymerisation, sol gel deposition and chemical vapour deposition. The main drawback of template assisted techniques is that the material obtained is generally not crystalline.

At the moment, most of the studies in template synthesis have entailed the use of two types of nanoporous materials, polymeric membranes⁵⁶ and porous alumina or silica membranes⁵⁷. However, there are a variety of other, both natural and synthetic materials that could be utilized as templates. Formerly synthesized nanostructures, like nanotubes can also be used as templates^{58, 59}.

Vapor phase growth

The vapor phase approach is probably the most explored growth route for 1D nanostructures, nevertheless, the growth mechanism is not clear yet. The VS process occurs in many catalyst-free growth processes. The 1D growth was first thought to come from an axial screw dislocation. Now it is generally admitted that controlling the supersaturation at a low level is a crucial key to get 1D morphologies⁶⁰. Experimental and theoretical works have proposed that the minimization of surface free energy primarily governs the VS process. Under high temperature condition, source materials are vaporized and then directly condensed on the substrate placed in the low temperature region. Once the condensation process happens, the initially condensed molecules form seed crystals serving as the nucleation sites. As a result, they facilitate directional growth to minimize the surface energy. The lateral dimensions of the nanowire can then be varied by changing the supersaturation factor, growth time, nucleation size and other parameters.

Vapor-liquid- solid mechanism

In catalysts assisted VLS mechanism, catalyst nanoparticles serve as a preferential site for the absorption and dissolution of reactants from the vapor phase, control the nanowires' growth direction, and define the diameter of the nanowire⁶¹. The whole growth process of a VLS mechanism can be divided into three stages: the nucleation,

the growth of eutectic alloy droplets and the growth of whiskers (or nanowires) through the liquid droplets due to supersaturating. The VLS process is initiated by the formation of liquid alloy droplet which contains both catalyst and source metal. Precipitation occurs when the liquid droplet becomes supersaturated with the source metal. Under the flow of oxygen, nanowires of metal oxide crystal are formed. Normally the resulting crystal is grown along one particular crystallographic orientation, which corresponds to the minimum atomic stacking energy, leading to 1D structure formation. This type of growth is epitaxial, thus it results in high crystalline quality. Wu et al. have provided direct evidence of VLS growth by means of real time in situ transmission electron microscopy observations⁶².

A morphological characteristic of nanowires grown by VLS is that each nanowire is terminated at one end by a catalyst nanoparticle with a diameter app. 1.5 times bigger than that of the nanowire.

Use of capping agents

One can control the final shape of a crystal by introducing appropriate capping reagents to change the free energy of the various crystallographic surfaces and thus to change their growth rate. To obtain the desired materials, one needs to prudently select the species of precursor and surfactants and also set the other parameters, such as temperature, pH value, and concentration of the reactants. With this method, semiconductors and metal nanowires can easily be grown^{63, 64, 65}.

Some other methods, which exhibited little application, can be cited in the following.

Self-assembly

Nanoparticles can serve as building blocks for wire-like structures. It is possible to form chains of nanoparticles by filling the pores of alumina or polymer membranes (self assembly into a template). Spherical colloids can assemble by templating against relief structures patterned in the surfaces of solid substrates⁶⁶. Self assembly also occurs without templates by modifying the surface properties of nanoparticles. The self assembly approaches have been intensively investigated but they demonstrate little control over the morphology and dimensions of the resulting nanostructures.

Size reduction

Isotropic deformation of a polycrystalline or amorphous material, anisotropic etching of a single crystal and near field optical lithography with a phase-shift mask represent the three most promising top down approach to form 1D nanomaterials^{67, 68}. These methods are a cost effective alternative to produce 1D nanostructures that could not have been produced by the bottom up approach.

Process to synthesis Core Shell Nanowires

There are a large number of opportunities that could be realised by fabricating new types of nanowires with heterostructures, especially in the semiconductor technology. VLS is an appropriate method to synthesise core shell or core multi shell nanowires⁶⁹. Generally two steps are necessary to achieve heterostructures. In the first step a nanowire will usually be grown with a catalyst by VLS. The second reactant/precursor can be incorporated preferentially at the catalyst tip (radial growth) or along the wire (axial growth). In the case of axial growth a core shell nanowire will be obtained. It is therefore necessary to control the interfacial kinetics to favour the desired growth mode. In general the growth kinetic is controlled by varying the pressure, the growth rate, temperature, reactant species and gases that are by-products of deposition. In the few reports, which relate to one step formation of core shell nanowires, a catalyst or a template have been necessary to enhance the formation of the 1D structure. One step formation of CdS-ZnS core shell nanowires has been possible by using VLS approach by MOCVD with co-fed single source precursors^{70,71}.

4.1.2 One-dimensional Al₂O₃ nanostructures

Contrarily to pure aluminium, which oxidises very easily, Al₂O₃ was intensively fabricated as one dimensional nanostructures. To the best of our knowledge, aluminium nanowires were only synthesised in situ from AlF₃ single crystals⁷². The following chapter will sum up the publications about Al₂O₃ nanowires.

An innovative method for producing single-crystalline α -Al₂O₃ fibers, using cheap, readily available raw materials at relatively low temperatures has been developed⁷³.

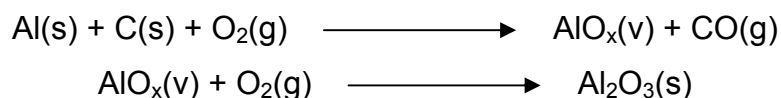
The method, based on the VLS growth mechanism, consists of heating Al and SiO₂ in an alumina crucible under flowing argon at 1300-1500 °C for 2-4 hours. A small amount of Fe₂O₃ was added to the powdered SiO₂. Crystalline alumina nanowires and nanotrees were obtained by heating a mixture of Al, Fe and SiC powders mixed in appropriate ratio at 1700 °C in flowing argon for about an hour⁷⁴. Peng et al. succeeded to grow α -Al₂O₃ nanowires and nanobelts without using iron and at lower temperatures starting from Al pieces and SiO₂ nanoparticles at 1200 °C, respectively, in a flowing Ar atmosphere⁷⁵. The nanowires possess diameters of 20–70 nm and lengths of 15–25 μ m, and the nanobelts are several micrometers long, with a width of 0.1–1 nm and thickness of 10–50 nm. The growth of the nanowires is controlled by a VLS growth process, whereas the growth of the nanobelts may be due to a VS process.

Alumina nanopillar arrays have been grown by simple chemical etching of the ordered porous alumina film on an aluminium surface⁷⁶. The diameter, height and interpillar spacing of the nanopillar arrays can be controlled. High yields of alumina nanowires are obtained by etching porous alumina membranes in an aqueous NaOH solution at room temperature⁷⁷. Using ultrasonic vibrations, alumina nanotubes and nanowires have been fabricated from Al-based porous alumina membranes, which are the products of bulk aluminium in oxalic acid via electrochemical etching. Fine configurations and structures of the alumina nanotubes and nanowires are clearly revealed⁷⁸. Kim et al. reported the first direct observation of the formation process of an alumina nanowire array from a porous anodic alumina membrane employing a simple droplet etching method, not a general immersion etching method in 2006⁷⁹.

A synthetic route (hydrothermal process) to thermally stable alumina nanostructures without the addition of any organic solvent has been reported⁸⁰. By this procedure unidirectional nanostructures, such as nanofibers or nanorods that show unique morphologies depending on the nature of the surfactant, are produced. Boehmite [AlOOH] nanoneedles, nanorods, and nanotubes were successfully synthesized by a facile sol-hydrothermal method without any surfactant. Calcination of the corresponding boehmite nanostructures at 700°C gave the corresponding γ -Al₂O₃ nanoneedles, nanorods, and nanotubes⁸¹.

Alumina nanowires were synthesized on large-area silicon substrate via a simple thermal evaporation method of heating a mixture of aluminum and alumina powders without any catalyst or template. These nanowires usually have a straight morphology and are single-crystalline with the wire axis parallel to the (001) direction. The catalyst-free growth of the alumina nanowires was explained in the framework of vapor-solid growth^{82, 83}. The vapor-solid mechanism is also imputable to the growth of ultra thin α -alumina nanobelts with single-crystalline rhombohedral structure by oxidizing aluminium in moisturized air under reduced pressure⁸⁴.

Nanostructures of Al₂O₃ that include nanowires and other structures have been prepared by the carbothermal process involving the heating of aluminium and graphite powders taken in a zirconia crucible under flowing argon at temperatures of 1300 °C for 6 hours⁸⁵. The single-crystalline nanowire appears to grow in a privileged direction. The growth mechanism of the nanowires can be understood on the basis of a vapor–solid mechanism since extensive microscopic investigations reveal no catalyst/liquid droplets at the ends of the nanowires. The relevant reactions can be written as following:



According to Gundiah et al., the first step should involve formation of the suboxide in vapor form, which gets oxidized to Al₂O₃ in the presence of oxygen, which may be present in the system itself or may be acquired from the zirconia crucibles. A similar procedure leads to the formation of Ga₂O₃ nanowires⁸⁶.

Single crystal α -Al₂O₃ whiskers could have been fabricated by displacement reactions. The methodology is based on studies in which Al-rich powder mixtures, that contain different kinds of metal oxides (MOx) were sintered⁸⁷.

Various methods have been employed to grow one dimensional nanostructures containing Al₂O₃, but Al/Al₂O₃ composite nanowires are not described in the literature. The goal of the following chapter is to describe precisely the composition, phase and structure of the Al/Al₂O₃ nanowires obtained by CVD of [H₂Al(^tBuO)]₂.

4.2 Morphology of Al/Al₂O₃ nanowires

As discussed in chapter 3, the Al/Al₂O₃ nanowires prepared for the present study are formed at different conditions above 530 °C. It has already been shown that their morphologies vary in function of the preparation. It is not possible to systematically analyse the nanowires obtained at all conditions as TEM analysis is particularly time consuming. Two very thin layers have been prepared, as TEM analysis can only occur on thin materials. One layer was prepared at 600 °C and the other one at 615 °C during one minute. The layer obtained at 600 °C has been intensively analysed while the second layer only serves as comparison.

Figure 4-1 shows a bright field image of a layer on a copper grid. The nanowires are tightly entangled with another and no further analysis can be done unless a single wire is successfully separated from the others at the border.

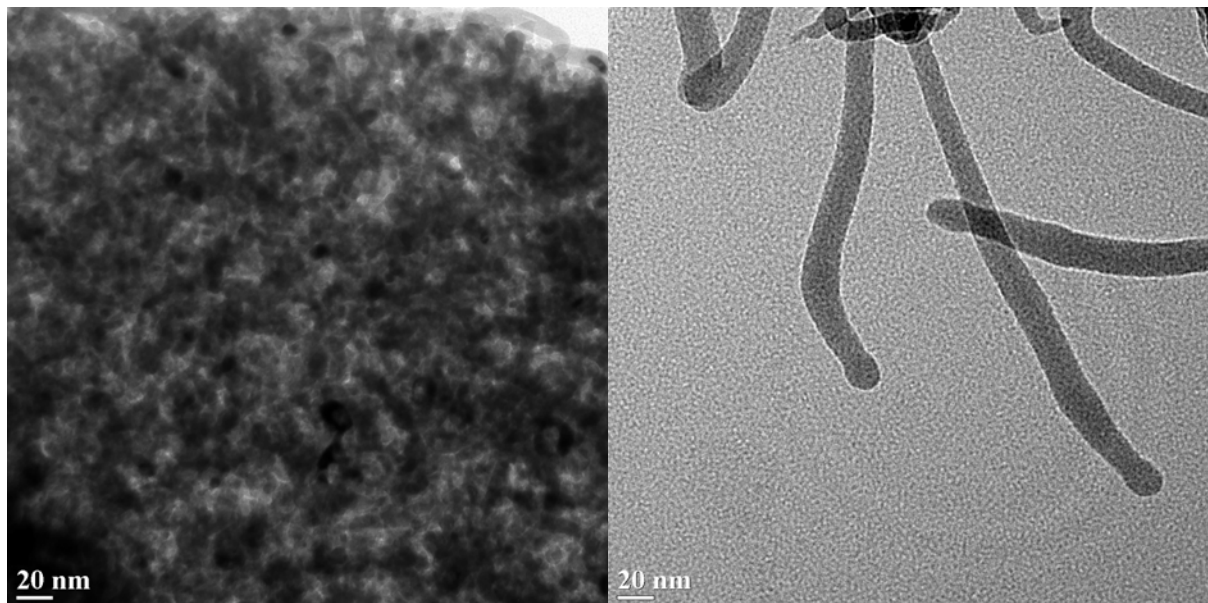


Figure 4-1: TEM bright field image of an area of entangled Al/Al₂O₃ nanowires (left) and single nanowires (right) at the border of the TEM grid

On figure 4-1 (right), single nanowires are distinguished at the border area. It is evident that the single nanowires present a spherical head. This information was not visible on SEM images. By tilting the sample, the scattering angle according to Bragg's law can be reached; it is then possible to detect crystalline phases in the

sample. Figure 4-2 shows a bright and a dark field image of some entangled nanowires, where some crystallites are visible.

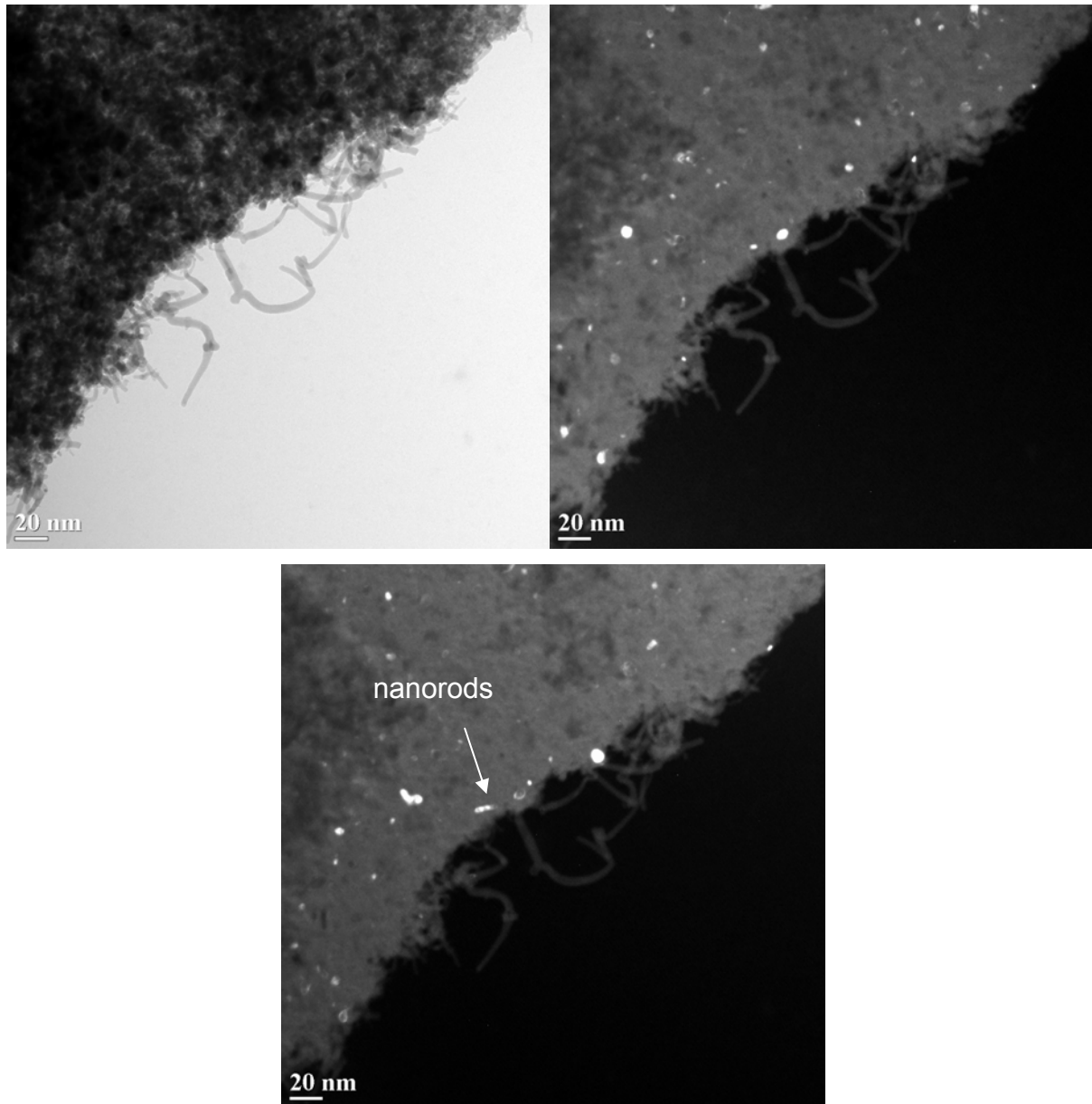


Figure 4-2: bright and dark field images of entangled Al/Al₂O₃ nanowires

The dark field image shows some tiny spherical crystals arbitrarily distributed in the sample, they can reach diameters of 10 nm. The dark field image below shows the same areas with a different tilt, some other crystals, which have the form of nanorods, are detected. To get an optimal image the nanowires must be positioned through the holes of the sample holder and superposition should be avoided to get one single nanowire. This is very complicated to obtain because the nanowires tend to entangle. Moreover aluminium and aluminium oxide display few contrast.

Figure 4-3 shows the inner structure of some single nanowires. The single crystal shown in the nanowires's core and in the head, must be the crystalline aluminium detected previously by XRD. Contrarily to methods used in previous works or to SEM analysis, TEM succeeded to localise the aluminium. Some more advice will be given along this chapter to prove that this crystalline phase is actually aluminium.

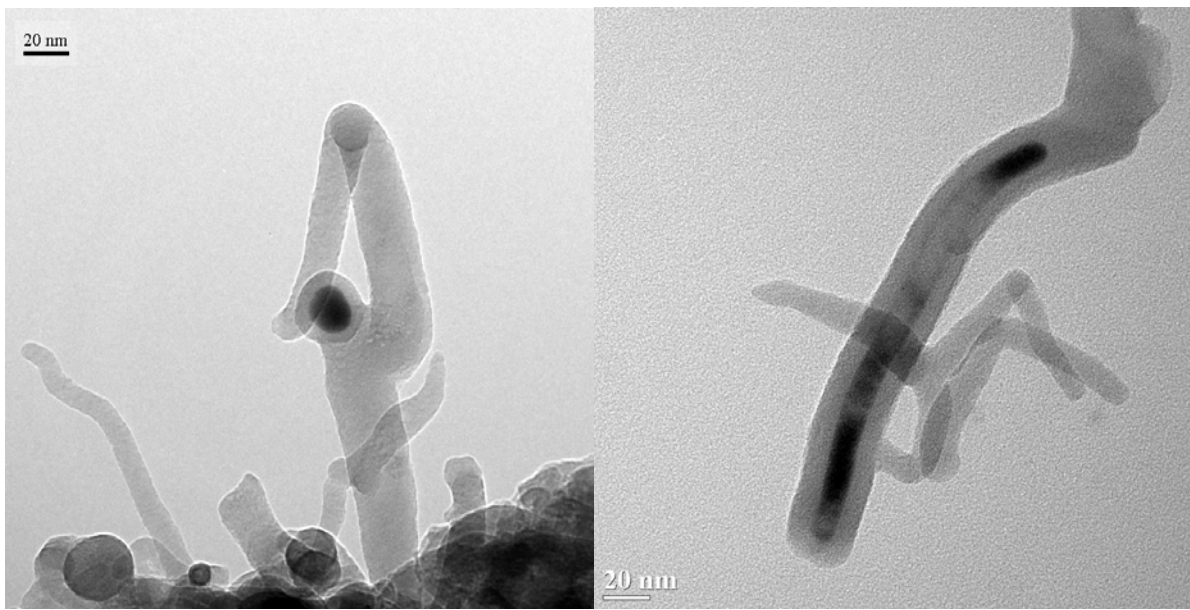


Figure 4-3: Single Al/Al₂O₃ nanowires with head (left) and core filled with single crystalline aluminium (right).

Some nanowires present a spherical head, which is highly crystalline. Others display a crystalline core along the nanowire. The nanowires structure is composed of wires between 100 and 1000 μm long and nearly constant diameters from 10 nm till 80 nm and their spherical heads are a little bit bigger than the nanowires. By adjusting the Bragg's conditions, crystalline core or peaces of crystalline core are often detected in the biggest nanowires (diameters > 30 nm). Most of the nanowire tips have a spherical head (Figure 4-3), which also displays a crystalline core and some nanowires finish with a rounded tip. The diameters of the cores are app. 0.4 time the diameters of the nanowire or the head, respectively. The shells of the nanowire or of the head seem to be amorphous at first sight. The morphological features of the Al/Al₂O₃ nanowires are not expected with a simple one step growth. Therefore it is highly interesting to proceed to further investigations with TEM in order to find out further morphological characteristics. TEM can also elucidate which phases are really involved in the shell and in the core.

Another typical morphological characteristic is that the heads are starting points for further nanowires growth. Branched nanowires are sometimes present. Figure 4-4 shows one head with two and three nanowires growing from it.

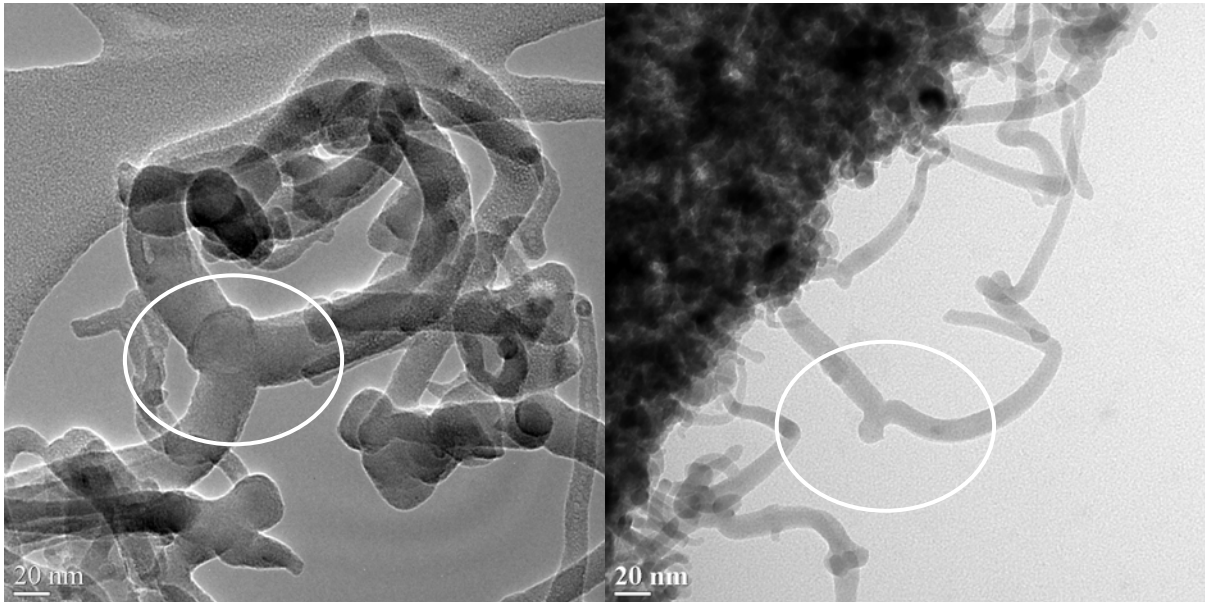


Figure 4-4: Entangled Al/Al₂O₃ nanowires with some heads displaying triple (left) and double (right) nanowires growth

To explain this phenomenon, growth islands can be envisaged at the surface of the nanowires head, the new nanowire can have its source from these growth islands. The branching can come from migration and agglutination of the growth islands. The observed agglomeration of nanoparticles on the nanowire surface (Figure 4-5) can be the source of further nanowires growth. Assuming that many growth islands are formed at the same time (or in a very short time) on the head surface, many nanowires could then grow at the same time (or in a very short time). At least one of the nanowires held the contact to the substrate surface. If the growth islands migrate onto the head surface they can meet and agglomerate so that for example two growing nanowires form one. This agglomeration leads to a minimization of the system energy so that this phenomenon tends to be favoured. This hypothesis can explain the contact of at least one nanowire to the substrate, as well as the branching and the fact that some nanowires display a head and others do not.

Dark field imaging of the triple nanowires region (Figure 4-5) shows some head in or near the Bragg's conditions; they are single crystalline. Some polycrystalline structure can be evidenced on the shell along the nanowires.

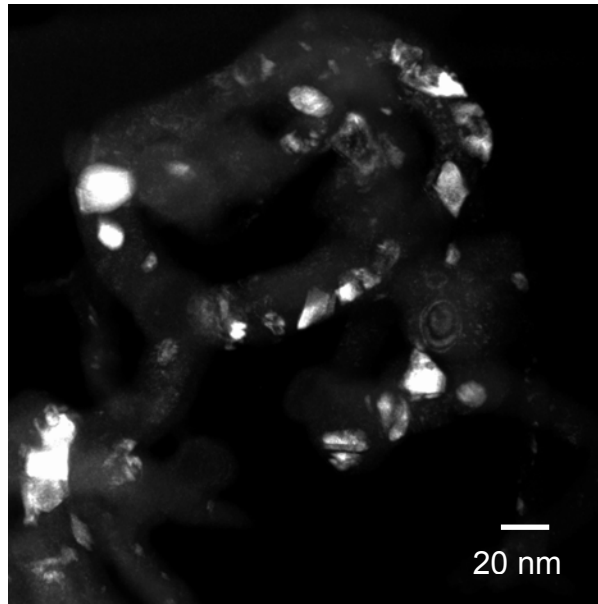


Figure 4-5: Dark field imaging of the area where three Al/Al₂O₃ nanowires are branched.

To get more information about the core shell structure in the head, the nanowire illustrated in figure 4-3 will be investigated with High-Resolution TEM (HRTEM) with a tilt of 24°, where the core of the head meets Bragg's law (Figure 4-6). The crystal structure of the core, whose diameter is app. 0.6 time the diameter of the head, is illustrated with a Fourier filtration to enhance the contrast. In the shell relative few lattice planes are visible. The lattice planes in the head's shell display a lot of defects as they are curved along the head. Therefore a stronger Fourier filtration is necessary. The shell particles are individually analysed and filtered and the resulting filtrated sectors are superposed on the original image. The filtration parameters are modified until optimal concordance with the weak contrasted original image is reached.

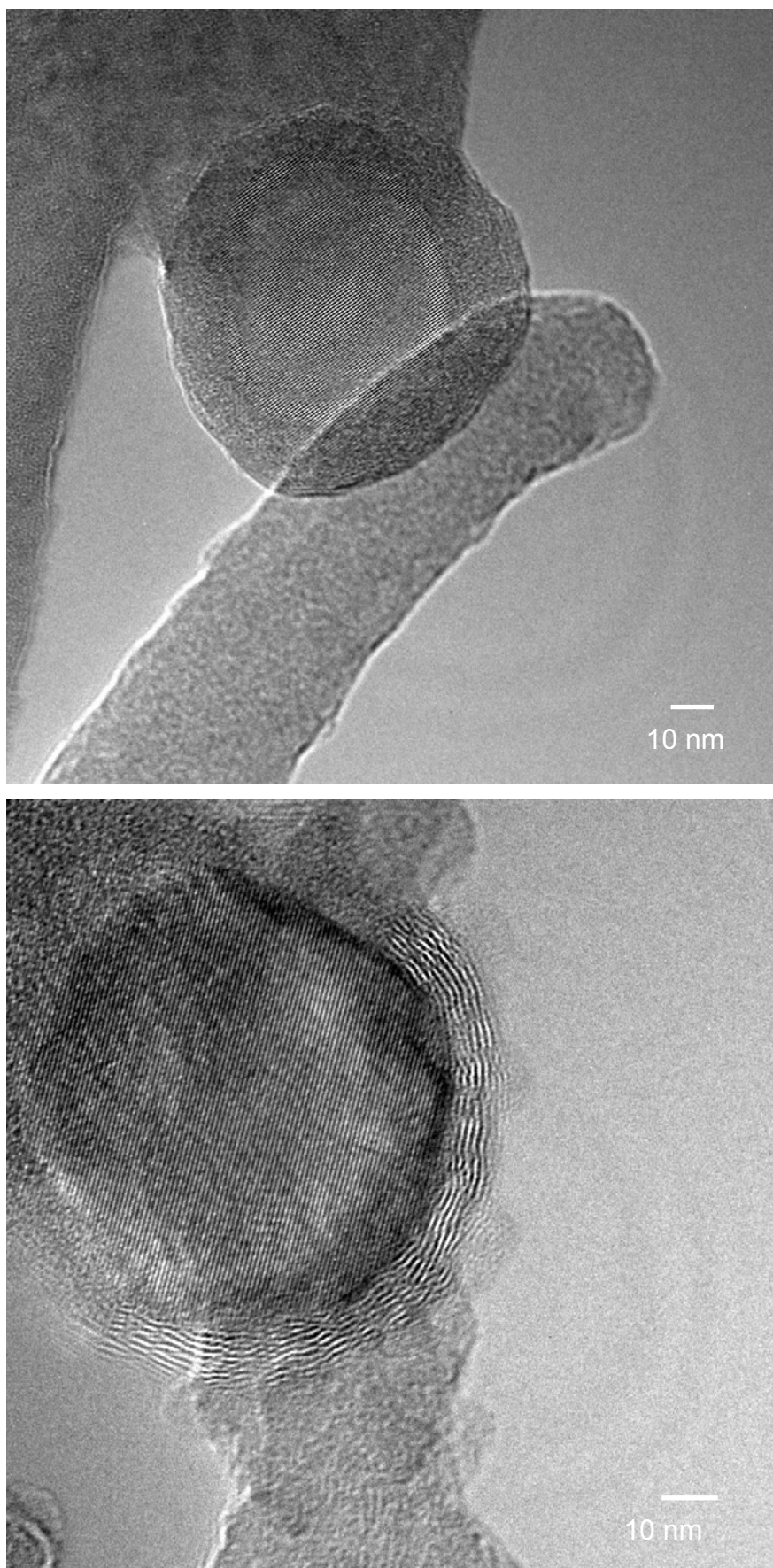


Figure 4-6: HRTEM images of an Al/Al₂O₃ nanowire's head with Fourier filtration of the core (above) and the shell (below).

The core of the head possesses a single crystalline structure. The (111)-crystal plane of aluminium (0.2338 nm), which is supposed to reflect the highest intensity, can be identified with the lattice spacing of about 0.232 nm. The localisation of the metallic aluminium inside the nanowires explains why it was not detected with a surface sensitive method like ESCA. Furthermore; it seems that the shell around the tip is constituted by a continuous, curved lattice fringes band. On closer examination the shell around the tip is composed of nanocrystals with diameters smaller than 3 nm, which are separated by small angle grain boundaries. The recorded lattice spacing is between 0.32 nm and 0.38 nm, corresponding approximately to the lattice spacing of (113) crystal planes of tetragonal δ -Al₂O₃ (JCPDS 46-1215, 0.3210 nm). Due to the crystal small size, very few lattice fringes are recorded thus no more precise value can be obtained. Despite of the use of Fourier transform to enhance the lattice fringes, the image obtained reflects the reality as it can be seen on figure 4-7.

Figure 4-7 A is the original HRTEM image. Figure 4-7 B shows an assembling of two Fourier filtrated images. Figure 4-7 C is a creation of a mask with reflex selective Fourier filtration and superposition with original image. Figure 4-7 D is Figure 4-7 C with Fourier filtration of the core. Many advices show that the fringes obtained cannot be artefacts like Fresnel's fringes. For example, the structure of the lines does not vary with the discontinuity (at the edges). The spacing between lines and their contrast is constant along the shell's thickness. The border is not particularly marked with a line with strong contrast.

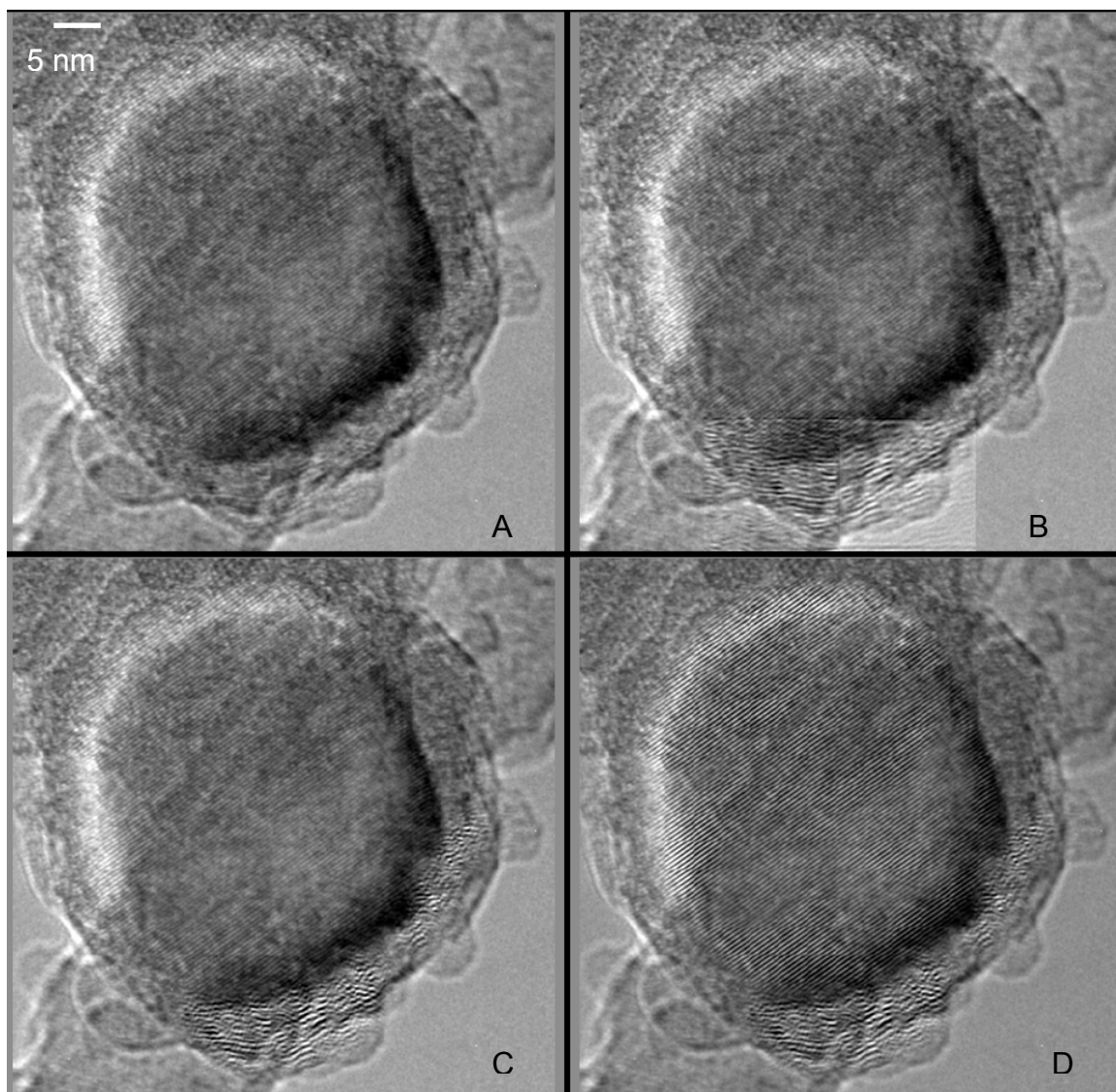


Figure 4-7: HRTEM image of a Al/Al₂O₃ nanowire's head with its core and shell. The images with Fourier transform (B, C, D) correspond to the real image (A).

An interesting area where it has been possible to detect two different lattice planes in the single crystalline core of the head is shown on figure 4-8. The head acts as a source for three nanowires' growth. A HRTEM image with Fourier filtration of the head is shown.

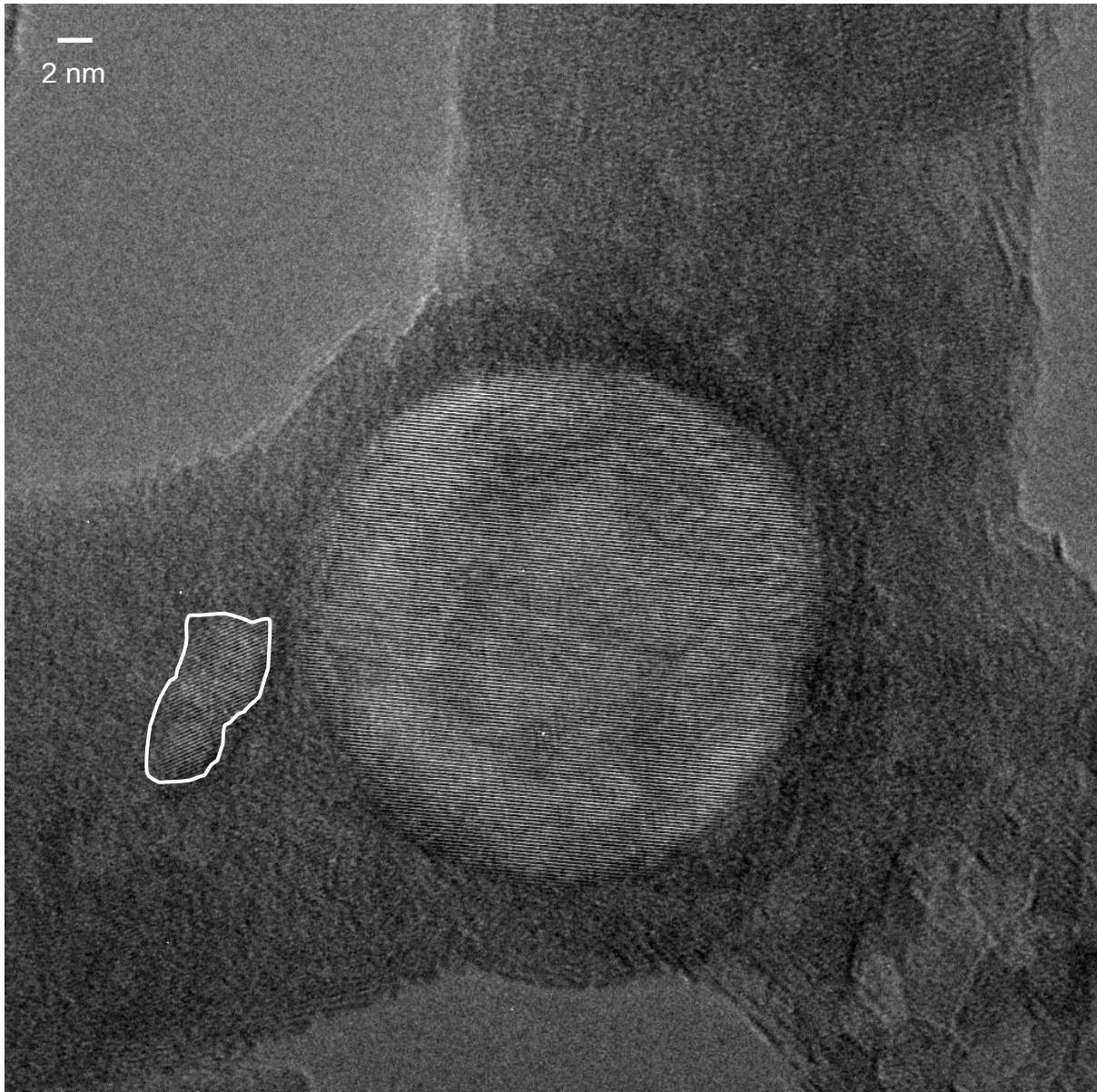


Figure 4-8: HRTEM image of the area where three Al/Al₂O₃ nanowires grow from a head. Lattice fringes are present in the core of the head and in a crystallite from the nanowire's shell

On the HRTEM image it is possible to distinguish lattice fringes in the core and in a crystallite from the nanowire's shell. In the core there are two signals, a strong and a weak one. To visualise both signals on one image, lattice fringes corresponding to both signals, are created by means of inverse Fourier transform. They are added in such a way that the lattice fringes corresponding to the weak signal appear with the same intensity as the one from the strong signal (Figure 4-9).

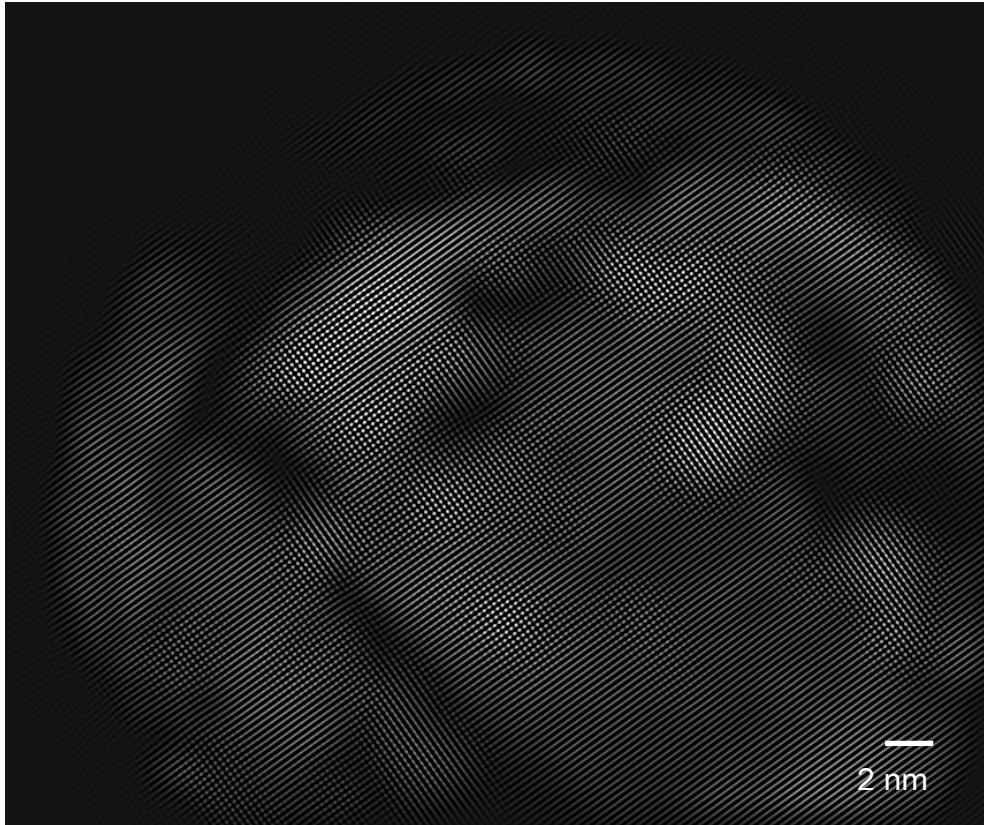


Figure 4-9: Inverse Fourier transform of the signals from the head illustrated on figure 4-8. Two signals for (200) lattice planes are intensified to illustrate the [001] orientation of the head.

The image on figure 4-9 is a superposition of two Fourier transforms to show both crystal planes with same intensity. This manipulation aims to reproduce the image of the atomic column which would have been obtained if the sample would have been tilted in such a way that both reflexes show the same intensity. The lattice structure obtained on figure 4-9 corresponds to the [001] orientation of the face-centred cubic lattice of aluminium. Hence, the crystallite represented on figure 4-8 grows following the (200) lattice plane of aluminium (0.2024 nm). The measured lattice spacing is 0.193 nm; it means that the correction factor is about 1.049.

Figure 4-10 shows a masked Fourier transform and the diffractogram of the area shown on figure 4-8. The crystallite from the shell and the core's head are represented.

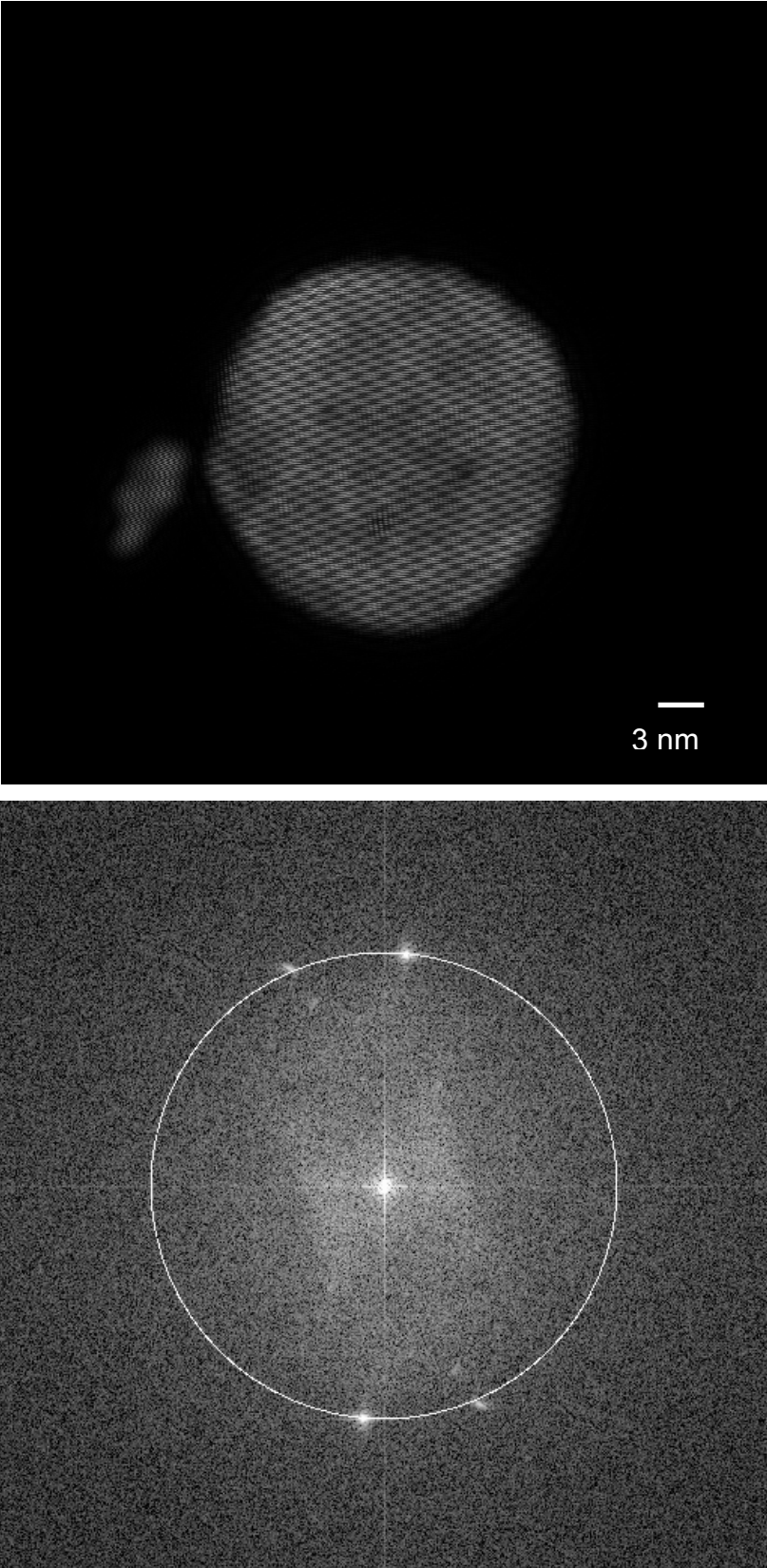


Figure 4-10: Masked Fourier transform of Al core and Al₂O₃ crystallite (above). SAED of the same area shows similar lattice spacing for Al core and Al₂O₃ crystallite.

The lattice spacing collected from the crystallite is similar to the one in the core of the head. Therefore, a coincidence between both crystal structures is highly probable i.e. the crystallite adopted the orientation of the head. A magnification of the crystallite and the head is shown on Figure 4-11

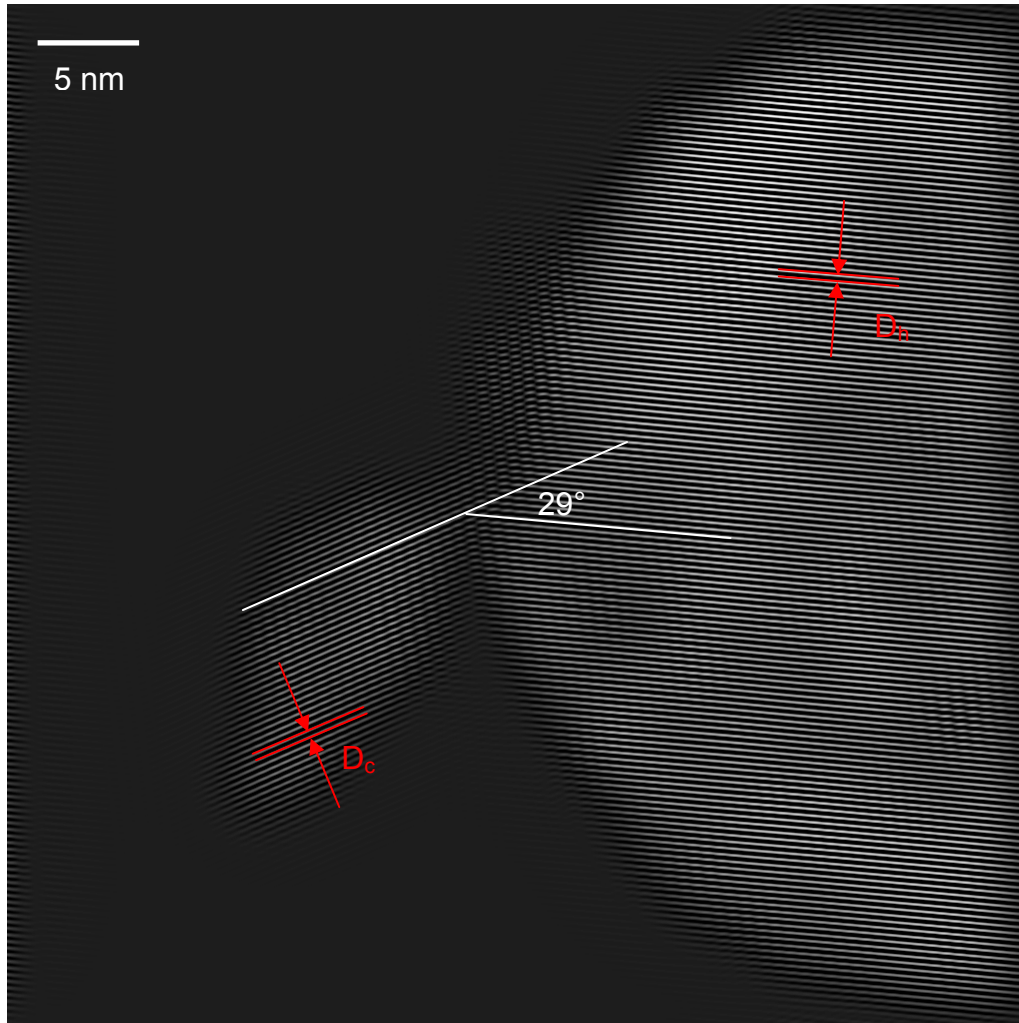


Figure 4-11: Magnification of the masked Fourier transform from figure 4-10. Al core and Al₂O₃ crystallite are oriented with an angle of 28.9 from another.

The magnification confirms that the lattice spacing recorded in the crystallite (D_c) and the one from the head (D_h) are similar ($D_c/D_h = 0.97$). The lattice planes from the crystallite are positioned with an angle of 28.9° relative to lattice planes of the core. A high coincidence between the core and the shell is observed in other areas. Figure 4-12 shows the interface region between the core and a nanowire's shell with a higher magnification.

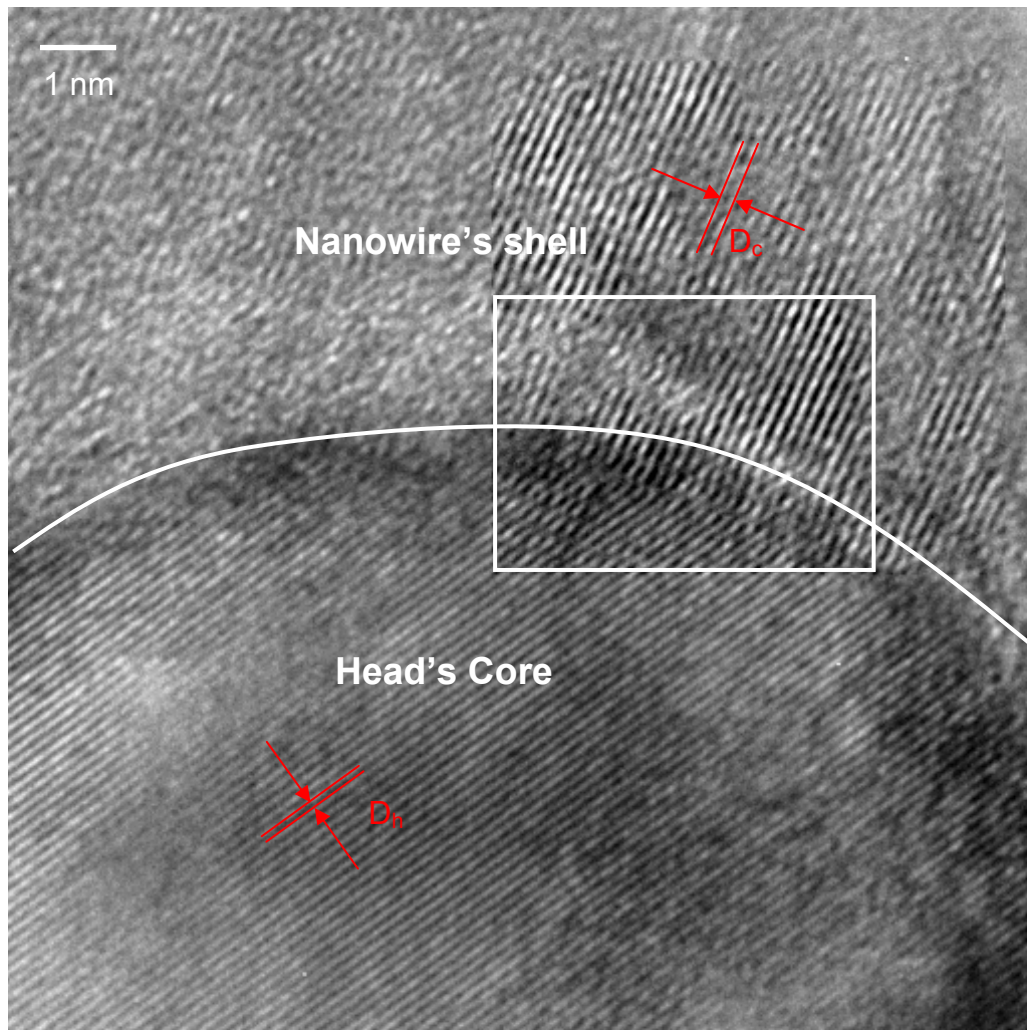


Figure 4-12: Al-core in the nanowire's head displaying lattice fringes (D_h) and nanowire's shell with Al-oxide crystallite displaying lattice fringes (D_c). The area with relatively high coincidence is marked by the square and the boundary between head and nanowire is delimited by the line.

The measured lattice distances in the aluminium core are 1.22 times smaller than the ones in the nanowire's shell ($D_c/D_h = 1.22$). Thereby an angle of approximately 35° between the crystal planes is needed for perfect coincidence. In figure 4-12 an angle of 30.1° is measured, which leads to a rather perfect coincidence: 20 crystal planes of the tip core meet 19 from the wire's shell along 4.97 nm on the image below. In other circumstances, an angle of 27.7° has been measured between head and crystallite. The fact that the lattice planes of the crystallites form an angle of app. 30° with the lattice planes of the Al-core means an intentional formation of grain boundary. Therefore a privileged lattice configurations exist, which controls the growth of a nanowire from the head.

Creating a suitable representation of the coincidence grain boundary between different phases is very complex, in particular if the lattices are not both simple cubic systems. That's why the following model will consider a coincidence between aluminium and a simple cubic γ -Al₂O₃ to mimic the coincidence grain boundaries observed between the aluminium core and the crystallites of the shell. The main conditions are that the aluminium core will be oriented in the [001] direction, like in figure 4-10 and the angle between (002) lattice planes of aluminium and the lattice planes in the aluminium oxide will be app. 30° like in figure 4-10 and 4-12. Figure 4-13 shows a graphical representation of the coincidence grain boundary between two face-centred cubic lattices (Al and γ -Al₂O₃). The black spheres are situated in the unit cell corners and the red ones in the faces.

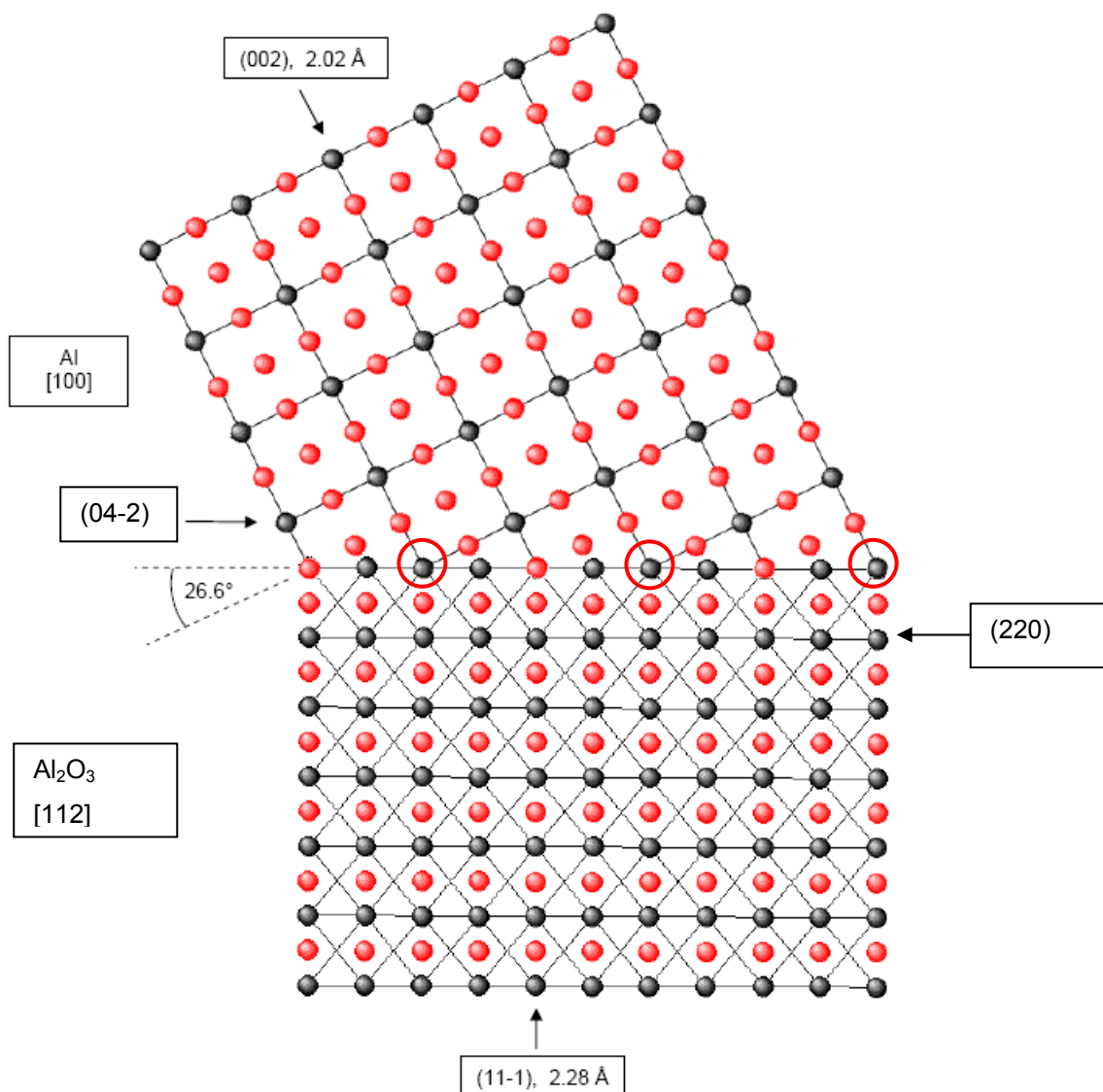


Figure 4-13: Representation of the coincidence grain boundary between Al and γ -Al₂O₃. The atoms circled present perfect coincidence between aluminium and aluminium oxide.

γ -Al₂O₃ (PDF 75-921) oriented in the [112] direction forms a grain boundary, which presents relatively high coincidence with (002) lattice planes of aluminium with an angle close to 30° (26.6°). In this case, the visible bands of lattice planes are (11-1) with lattice spacing of 0.228 nm and $D_c/D_h = 1.13$, which is close to the values recorded for figure 4-12. Among the 11 represented at the interface, three atoms (red circles) match perfectly to both structures.

The γ -Al₂O₃ (PDF 75-921) chosen has a lattice constant of 0.395 nm. With the tilt of 26.6°, the lattice planes, which coincide at the grain boundary are the (04-2) of aluminium and the (220) of γ -Al₂O₃ as illustrated on figure 4-13.

The model exhibits similitude with the crystallites grown from the head shown in figures 4-10 and 4-12, however, some differences with the experimental data cannot be ignored. For example the factor between lattice spacing of the head and the crystallite in the experimental data was 1.22, while it is 1.13 in the model represented in figure 4-11. The coincidence resulting from the model is lower than in figure 4-12, where 20 crystal planes of the aluminium core met 19 from the nanowire's shell. To improve the model, it is necessary to know precisely, which aluminium oxide is involved and its orientation.

Figure 4-14 shows a HRTEM image of a head which allows the growth of two nanowires. In the shell, which envelops the nanowires, crystals of a diameter from up to 20 nm can occasionally be found but due to the presence of deformations in the matrix a relatively big error must be expected in the measurement of the lattice spacing.

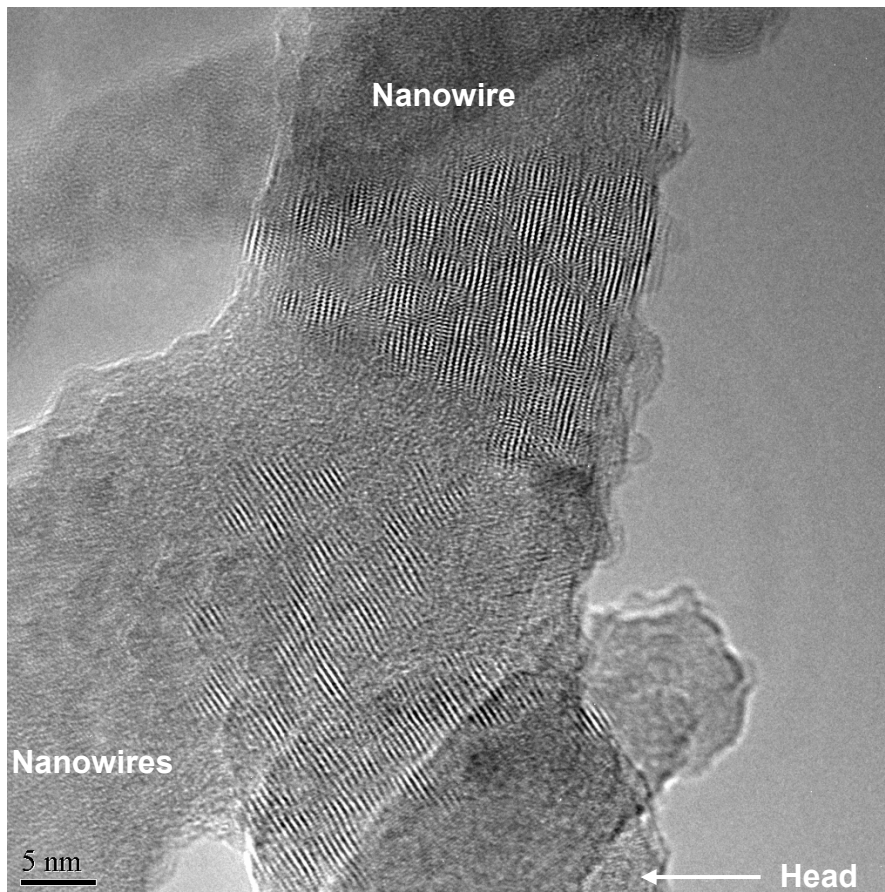


Figure 4-14: HRTEM image with Fourier transform of a double Al/Al₂O₃ nanowire with crystallites on the shell.

By considering simply the measured lattice fringes from 0.437 nm to 0.447 nm, the lattice spacing can eventually correspond to the (111) plane of γ -Al₂O₃ (JCPDS 10-425, 0.456 nm) or the (101) plane of the hexagonal phase (JCPDS 26-31, 0.423 nm) and the (113) plane of tetragonal δ -Al₂O₃ (JCPDS 16-394, 0.457 nm) can also be considered, as the values are not precise due to deformations.

Figure 4-15 shows TEM images of an area of nanowires with crystalline cores and amorphous shell. For this area many TEM images have been made with different tilt to meet Bragg's conditions.

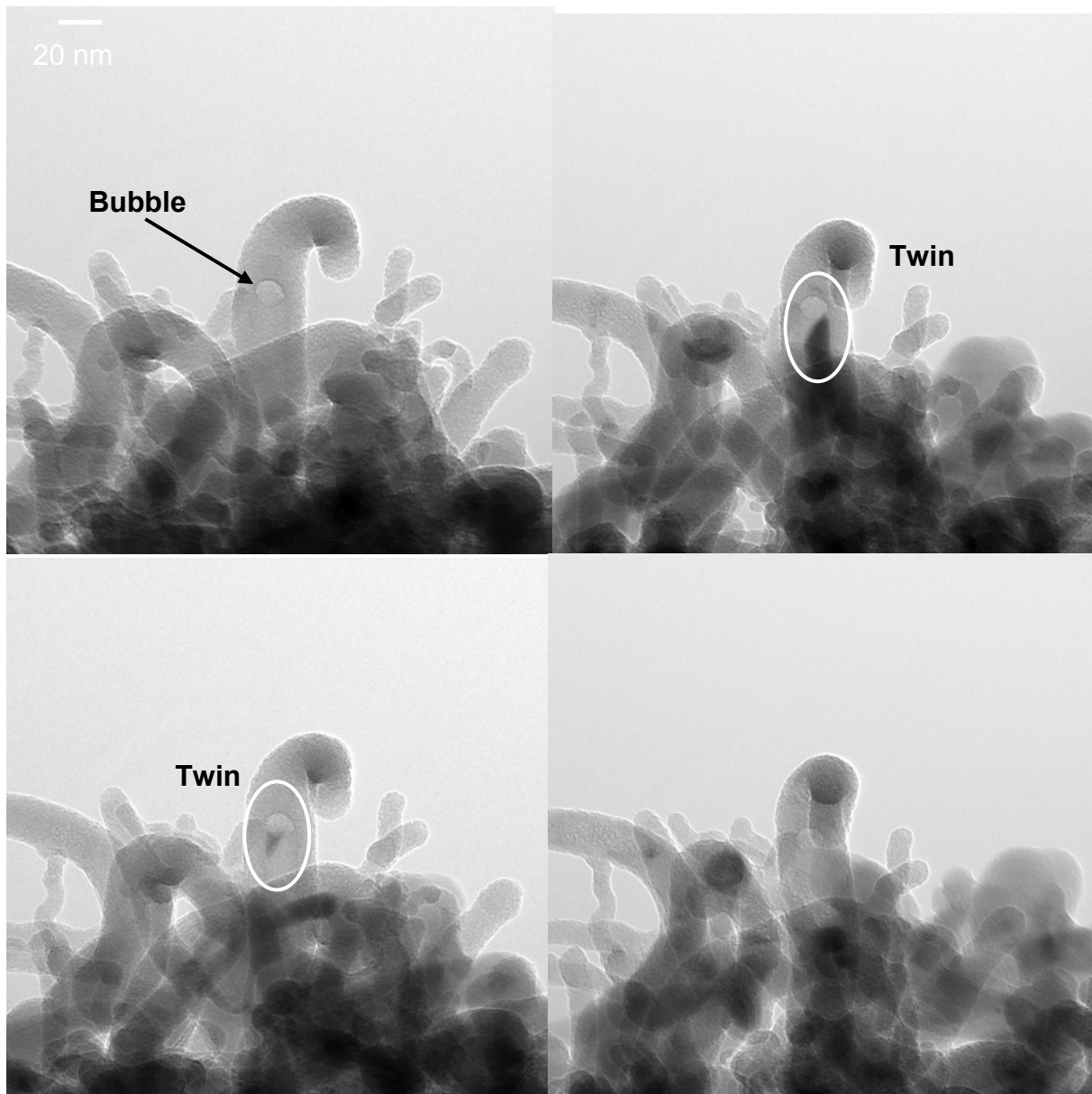
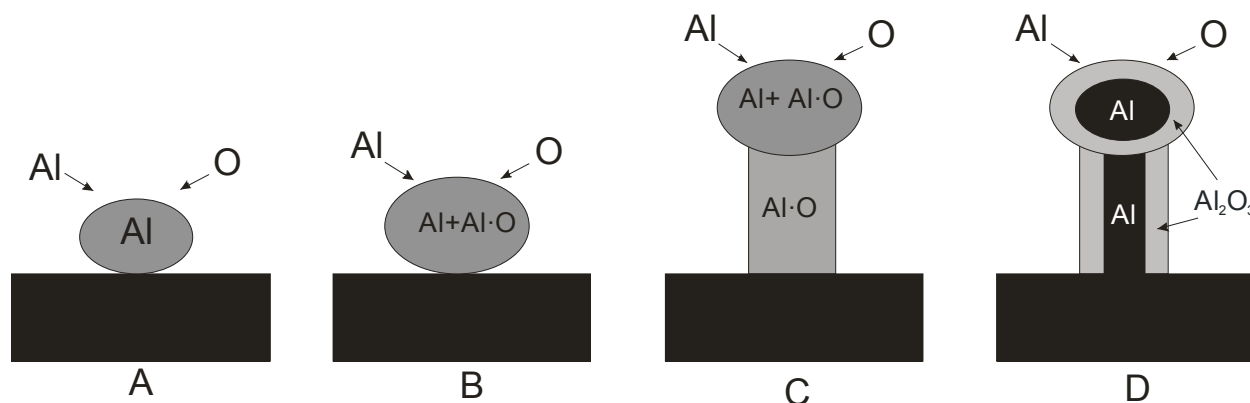


Figure 4-15: Four images of nanowires with different inclination. The big nanowire in the middle displays a bubble and a twin structure in the core.

Two nanowires possess cores where the contrast changes in function of the inclination. The vertical nanowire in the middle ends with a bubble. Moreover, this nanowire's core presents a twin structure. By changing Bragg's angle, the crystalline core can be evidenced in two inclined peaces. To release strengths, such defects can be necessary in a crystallographic arrangement.

For such nanowires a growth model is proposed on scheme 4-1.



Scheme 4-1: Schematic illustration of the self catalytic growth for the synthesis of Al/Al₂O₃ core shell nanowires. (A) Formation of aluminium nanoclusters on the surface. (B) Accumulation of {Al·O} in the Al catalyst and formation of Al-Al-O alloy. (C) Growth of {Al·O} nanowires by precipitation of supersaturated {Al·O} like in VLS process (D) Al segregates to the inside, meanwhile an Al₂O₃ shell is formed.

The most suitable hypothesis is the formation of aluminium nanodroplets on the target surface, {Al·O} vapour from the single source precursor is incorporated and oxygen accumulation in the droplet occurs. It will be evidenced in the following that, in some cases, the creation of aluminium clusters in our system is possible (chapter 4.5). Once the aluminium droplet is saturated with {Al·O}, a growth of a wire with the composition {Al·O} occurs like for a classical VLS process. Due to the high aspect ratio, the {Al·O} NW solidifies with an imperfect diffusion process which leads to segregation i.e. the oxygen atoms migrate to the surface or the aluminium atoms segregate in the core. The segregation process which is already described for example by core-shell Si-Er nanowires⁸⁸ can explain why the centre of the NWs is aluminium rich and why various Al/O phases can be found along the width (Figure 4-38). A sufficient separation of the phases can be noticed in NWs bigger than 25 nm since a core shell structure can be identified.

The morphology of the nanowires can vary in function of preparation. For example, nanowires prepared at higher temperature (615 °C) are shown on the following figure (Figure 4-16).

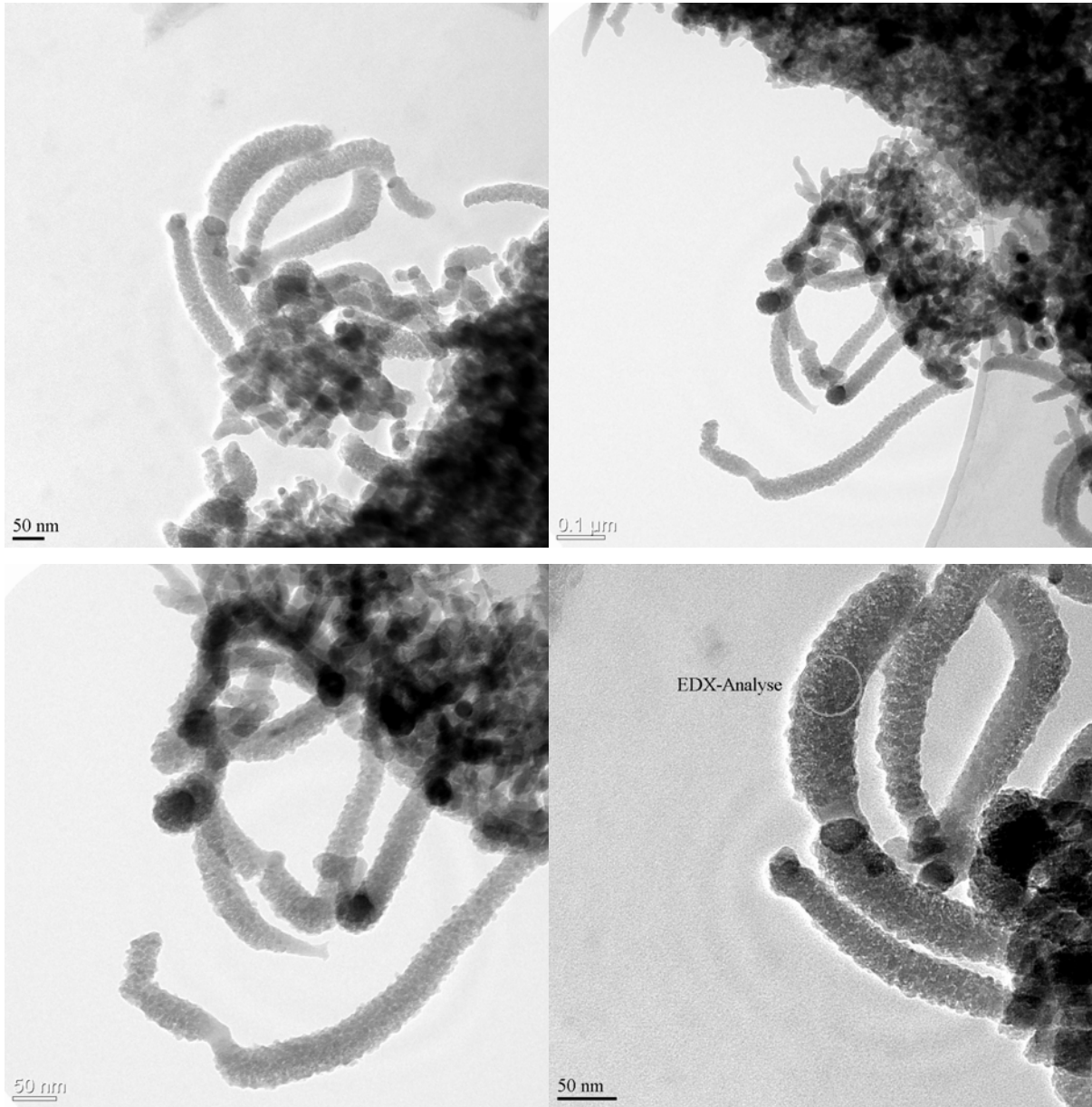


Figure 4-16: SEM images giving an overview on the Al/Al₂O₃ nanowire structure prepared at high temperature (615 °C) displaying nanoparticles at the surface.

This sample differs strongly from the samples analysed before as the nanowires have not constant diameters along their lengths. Moreover the shell is constituted of a compact assembly of small (5 nm till 10 nm) spherical particles. Obviously on figure 4-16 there are two structures on the layer: the nanowires grow from a rather compact layer, which is constituted of objects whose dimensions decrease with layer

thickness. According to EDX analysis, these samples contain more oxygen than in the previous study: 37% aluminium and 63% oxygen are detected (it was app.50%Al / 50%O). Some common points still remain, for example, the heads still appear darker on the bright field image and some single crystalline cores can be found. Contrarily to the recedent study, the heads are smaller than the nanowires themselves and sometimes the tips are not spherical. The nanowires extremities, which are not spherical, seem to be the aluminium core prolongation (same sizes). But it is not clear why the shell did not grow immediately on this prolongation (figure 4-17).

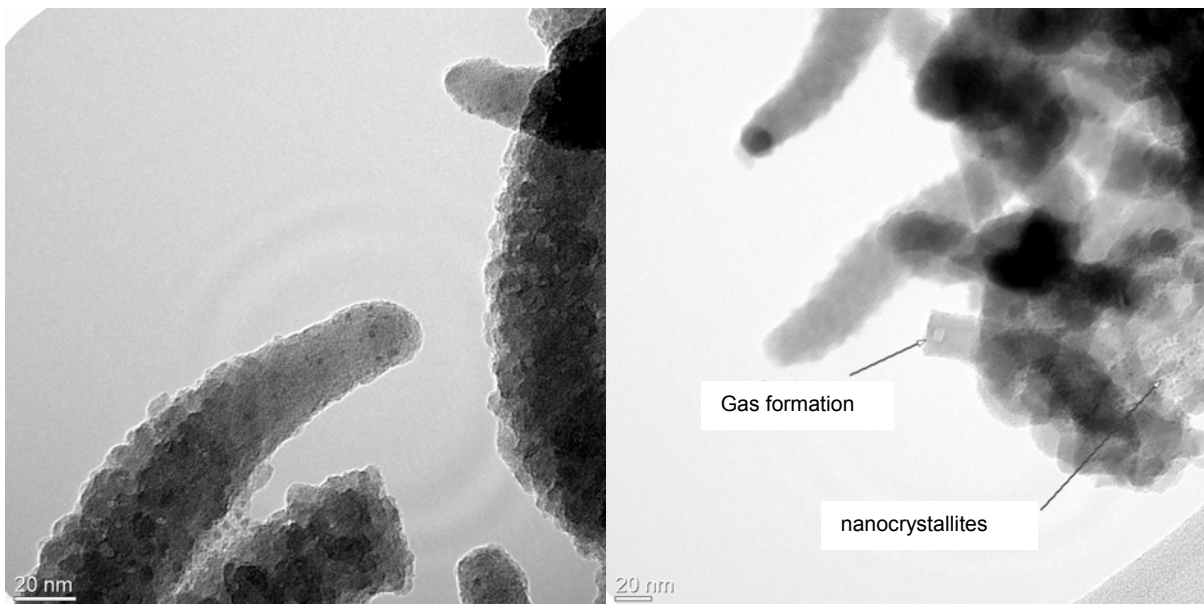


Figure 4-17: TEM images of the tip of the Al/Al₂O₃ nanowires with nano-crystallites at the surface (left). Some nanocrystallites are distributed over the surface and gas formation is detected (right).

Equally to the previous study a blowhole is situated at the tip of a nanowire. The blowhole disappear after a while, it correspond to gas formation, which is probably oxygen. Some very small particles (app. 1 nm) are spread in the layer or on the nanowire tip. The particles are very dark it means that they meet Bragg's law. It is probable that a lot of other particles exist but are invisible as they do not meet Bragg' conditions. Such a structure presents definitely similarity with nanowires after intensive electron irradiation. The effects of irradiation on a nanowire structure and their comparison to present structure will be discussed in chapter 4.4.

To conclude, by varying deposition conditions some nanowires with nanoparticles (app. 1 nm) at the surface are obtained. But generally, the nanowires are several micrometers long with diameters of about 40 nm; they have a head at the tip, which is app. 1.5 times bigger than the nanowire. Sometimes the nanowires's head allows the growth of several (2 or 3) nanowires.

The nanowires display a core shell structure where the core is single crystalline aluminium and the shell is aluminium oxide. Bright field imaging could not detect crystallites in the shell but dark field imaging and HRTEM measurements demonstrated unambiguously that the shell is crystalline. It is nevertheless not possible with HRTEM to determine precisely which Al₂O₃ phase it is; delta, gamma and hexagonal phases have been envisaged. Some crystallites from the shell are oriented with an angle of app. 30° relatively to the aluminium core. A hypothesis has been drawn to explain the growth mechanism in 3 steps: aluminium droplets are suspected to play the role of a catalyst like in the VLS process. Then, {Al·O} nanowires grow and finally a segregation occurs.

4.3 Composition and crystallinity

EDX and electron scattering will now be necessary to measure the composition and the crystalline phases involved in the nanowire structure, in particularly in the shell. An appropriated area to process to EDX measurements is the triple nanowire morphology already studied in precedent chapter (figure 4-18).

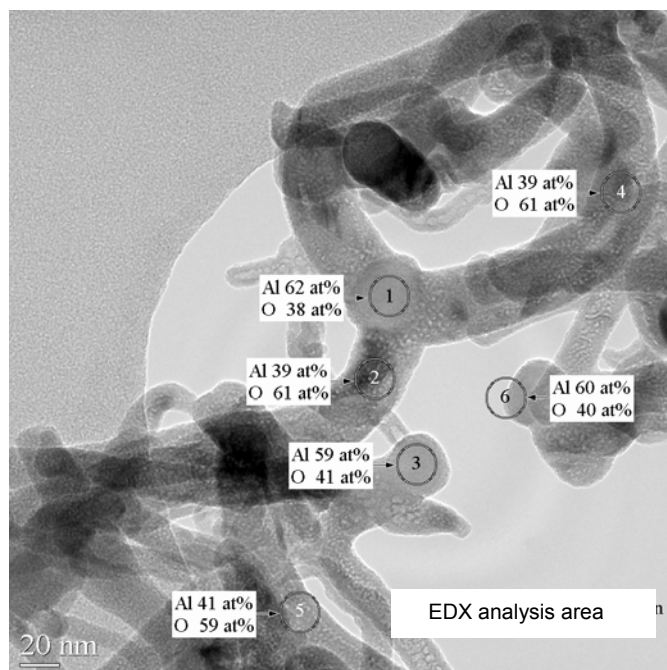


Figure 4-18: EDX analysis of the area where three Al/Al₂O₃ nanowires grow from one head.

The six marked areas represent the areas where EDX measurements have been performed (Figure 4-18 and 4-19). The circles' size represents approximately the lateral propagation of the excitation area for the characteristic X-Ray. The results are semi quantitative as the sample does not meet the requirements for quantitative measurements, which are uniform film with constant thickness. Thus, the electron interaction, the X-Ray absorption and the secondary fluorescence are neglected. Three measuring points have been chosen on the heads (1, 3, 6) and three others on the nanowire itself (2, 4, 5). Despite of the approximation in the sample geometry the differences between the three points are very small, that's why the results are considered as reliable. In the head app. 60% aluminium is measured and 40 % in the nanowire. EDX on the points indicated in figure 4-18 has a lateral resolution on the order of 10 nm due to the interaction volume of electrons and matter in TEM. In our system aluminium oxide and pure aluminium are superposed (scheme 4-1) hence both are measured in the EDX experiment. It means that the 60% aluminium detected in the head can be attributed to the simultaneous measurement of pure aluminium (100% of Al) from the core and Al₂O₃ (40% of Al) around the core. The measurements of the nanowires present 40% aluminium, which corresponds perfectly to Al₂O₃, it means that the core is not simultaneously measured, because the shell is thicker around the nanowire than around the head. The differences from

the ideal value are due to the core-shell geometry; indeed the electron beam will meet both shell and core.

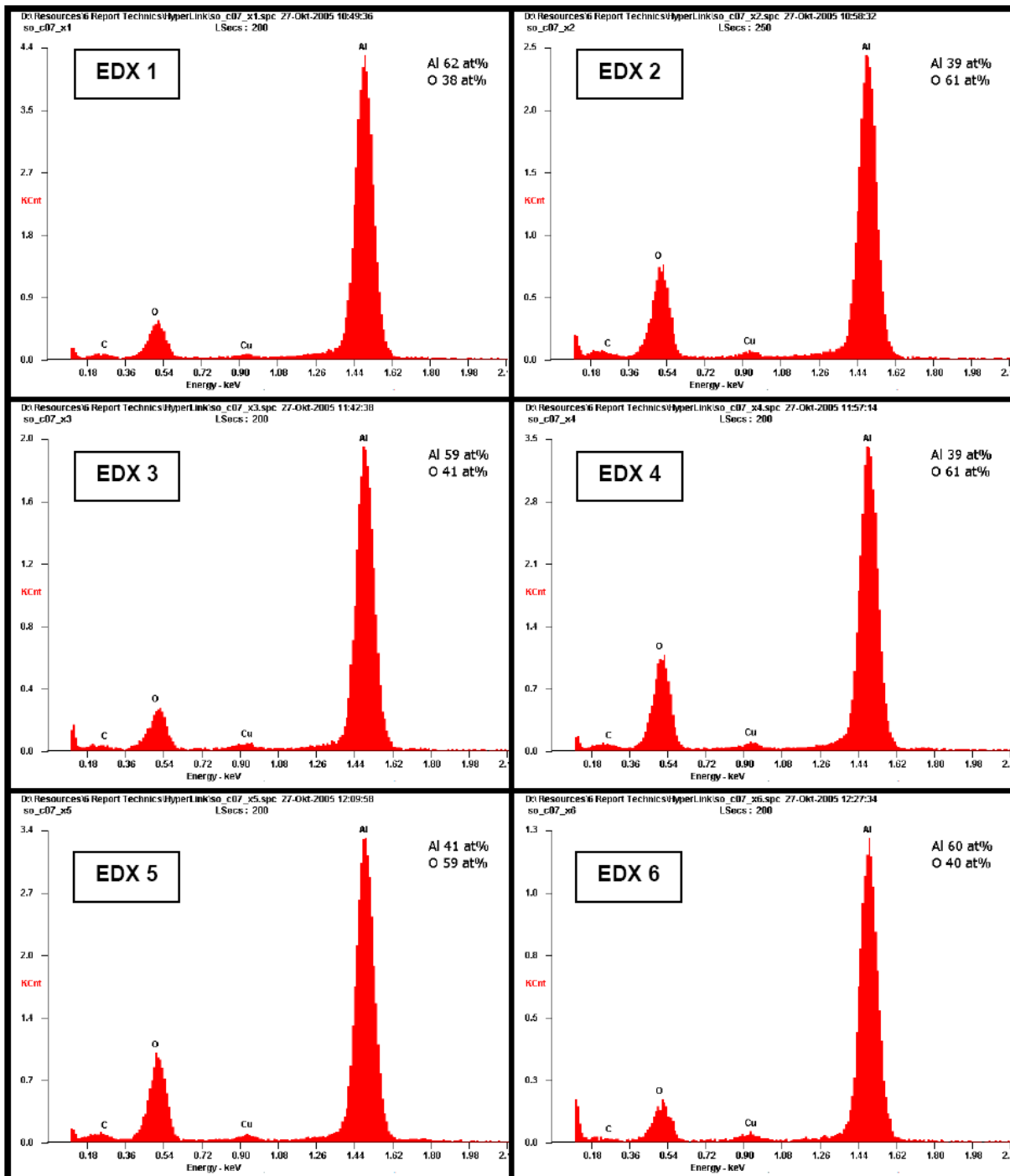


Figure 4-19: EDX spectra of the area where three Al/Al₂O₃ nanowires grow from one head. The analysis areas are shown on Figure 4-18.

Figure 4-20 shows EDX analysis of the same area after intensive electron irradiation, which has altered the nanowires structure. The size of the head's core has increased and the core is liberated from the shell. Thus direct analysis of the core is possible.

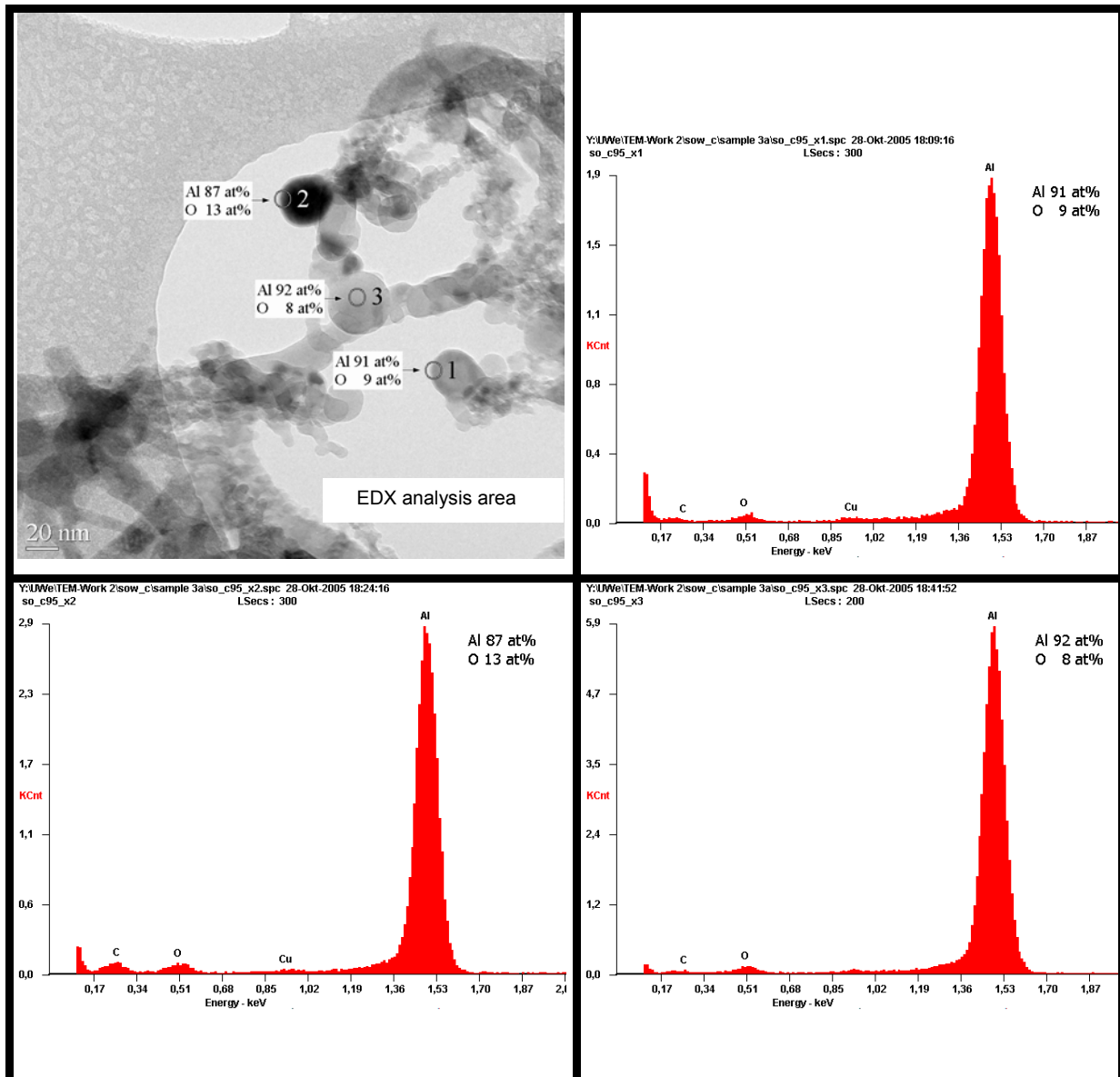


Figure 4-20: EDX analysis of the area where three Al/Al₂O₃ nanowires grow from one head after intense irradiation.

The modification of the nanowires structure like for example, the growth of the head's core after irradiation will be investigated in the following chapter. EDX measurements show that the Al amount has increased a lot after elimination of the shell around the head's core. The small quantity of oxygen detected can be attributed to electron radiation or X-Rays from outside of the analysed area (marked with circles). These results confirm that the core is almost exclusively composed of aluminium.

Figure 4-21 shows a modified selected area electron diffractogram (SAED) of the nanowires structure. A set of sharp diffraction spots and several discrete diffraction

arcs that can be ascribed to aluminium oxide nanocrystals from the shell and aluminium, respectively, can be seen.

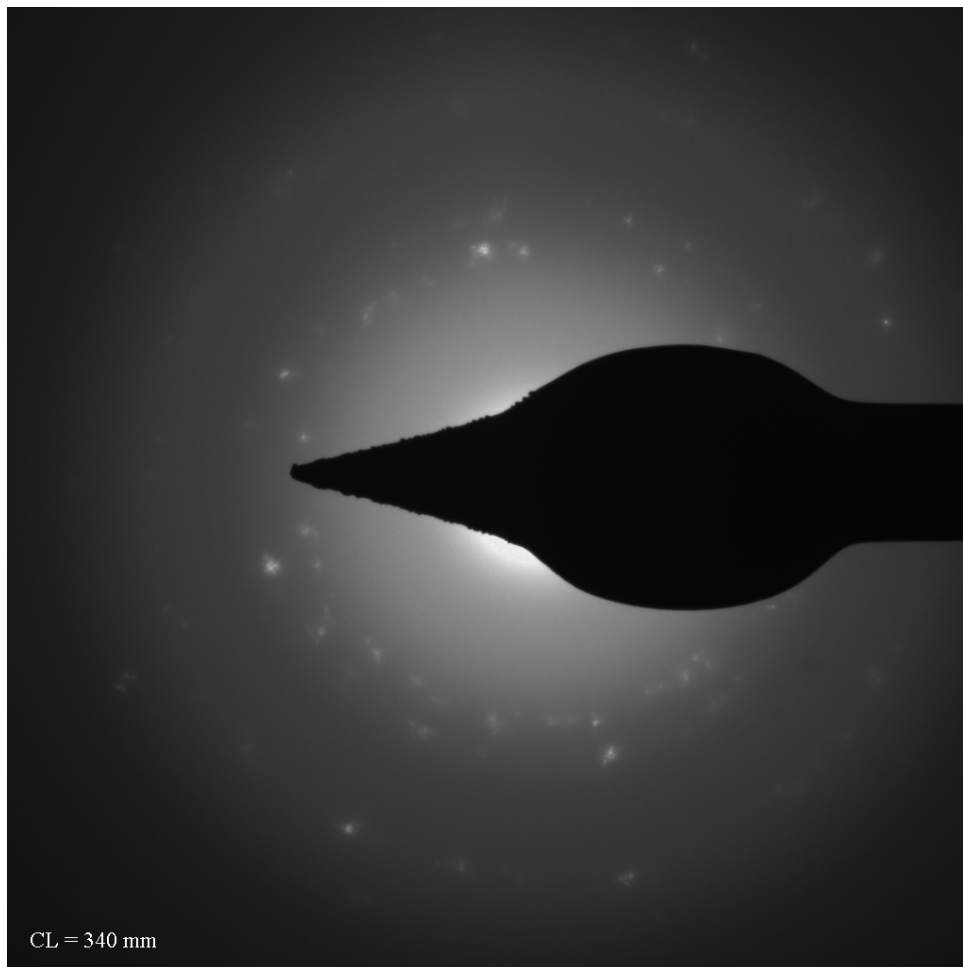


Figure 4-21: SAED on an area where Al/Al₂O₃ nanowires are dense.

Few spots are detected because of a too large magnification. Relatively pronounced diffusion is detected, suggesting that the amorphous fraction is very big, or that the sample is too thick. SAED detection can be optimised to obtain sharper spots and to collect more crystallites. Figure 4-22 shows a SAED where the aperture, the magnification (as small as possible) and the focus have been optimised.

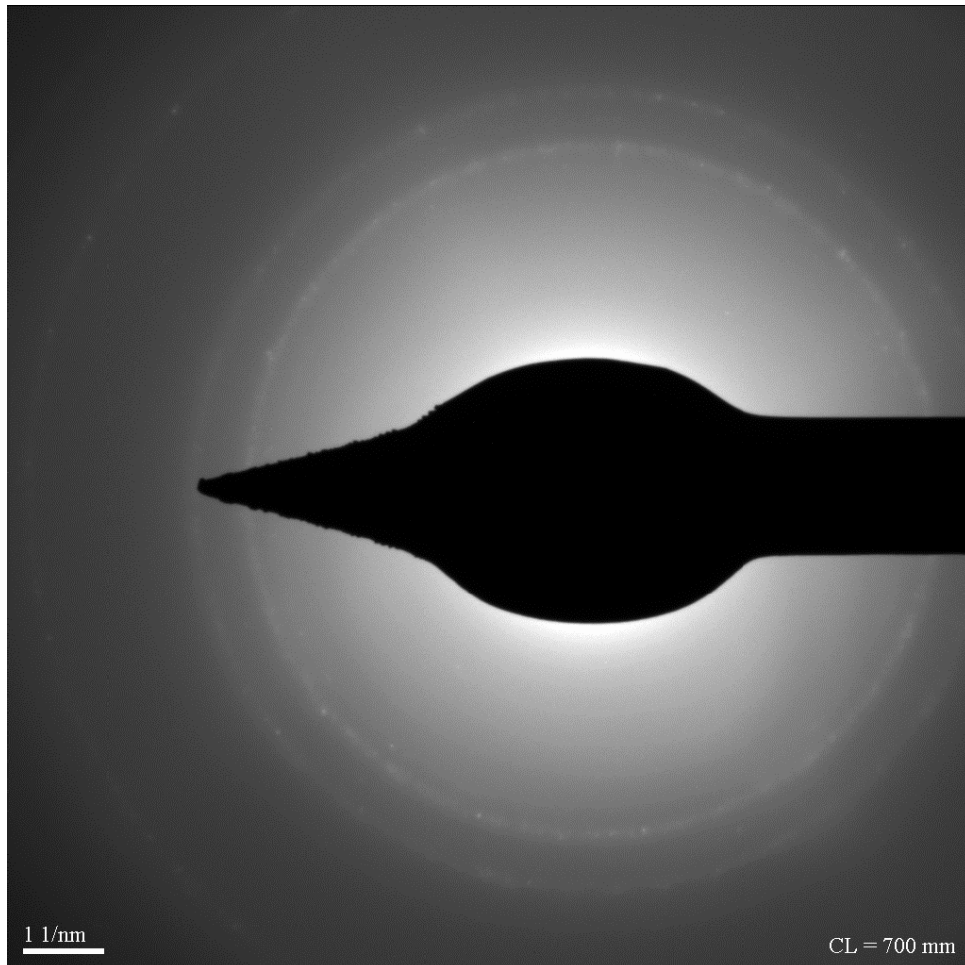


Figure 4-22: optimised SAED of an area where Al/Al₂O₃ nanowires are dense.

The diffusion (the thickness of the arcs) has been reduced but the diffusion background, which is due to inelastic scattering in the layer, could not have been electron-optically removed.

Figure 4-23 shows a SAED with aluminium diffraction arcs from JCPDS. A discrepancy is observed between the literature and the measured diffraction spots. On the SAED, the plane spacing is bigger than expected from the literature. This difference is probably due to the nanowires' network, which is too thick; thus does not represent a perfect diffraction object. As bigger lattice spacings have systematically been recorded on a series of experiments, it is also probable that it illustrate a real characteristic of the sample. Oxygen inclusions in the aluminium could lead to enlarged interplanar spacing. Despite of this difference, aluminium will be used in the following as inner standard for correction; a correction factor of 0.9894 is used. Due to spherical aberration, the correction factor should vary in function of the interplanar spacing, but in our case it will stay constant. This approximation can lead to some

small errors but in our case aluminium does not show sufficient arcs for the calculation of a varying correction factor.

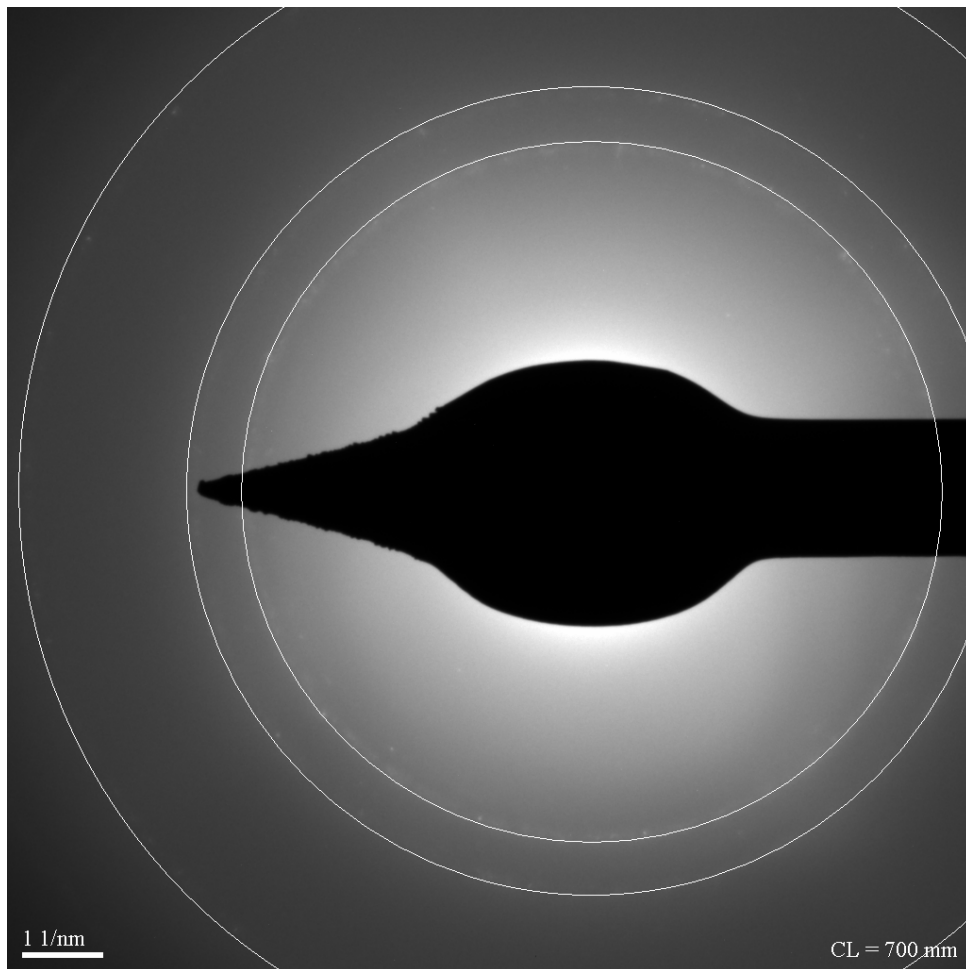


Figure 4-23: optimised SAED of an area where Al/Al₂O₃ nanowires are dense with aluminium diffraction arcs marked

To facilitate the analysis, the diffusion background will be removed and the contrast of the remaining spots will be accentuated. Figure 4-24 is obtained.

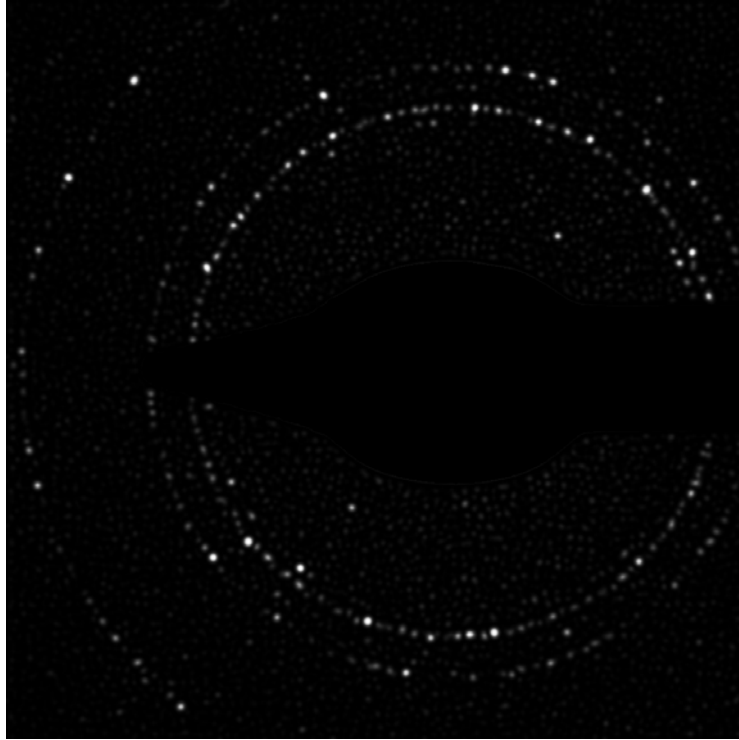


Figure 4-24: modified SAED of an area where Al/Al₂O₃ nanowires are dense with removed background and accentuated spots.

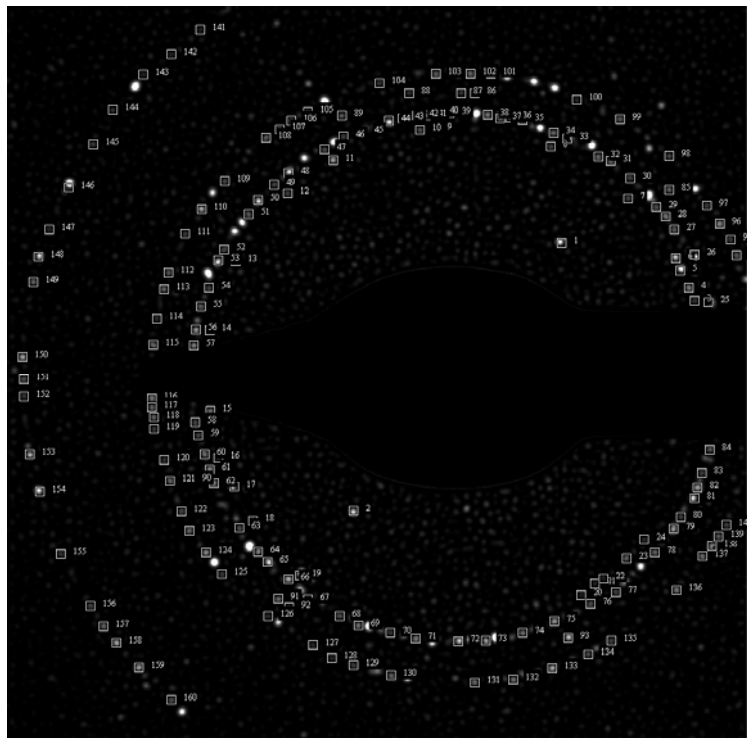


Figure 4-25: Evaluation of diffraction arcs from figure 4-24 with the software *digital micrograph*.

With the software *digital micrograph* it is then possible to calculate averages for each diffraction spots. The following table shows the calculation of average d-spacing for diffraction spots plotted on figure 4-25.

Spot	d-spacing (nm)	d-spacing (nm)	d-spacing (nm)	d-spacing (nm)	d-spacing (nm)	d-spacing (nm)
1	0.3647	0.2504	0.2382	0.2206	0.205	0.1446
2	0.3686	0.2515	0.233	0.2192	0.2042	0.145
3		0.2518	0.2378	0.2193	0.2055	0.1436
4		0.2508	0.237	0.2165	0.2062	0.1436
5		0.252	0.2383	0.2185	0.2038	0.1449
6		0.2505	0.2364	0.2195	0.2044	0.1448
7		0.2502	0.2353	0.2201	0.2067	0.1445
8		0.2496	0.2383	0.2196	0.2043	0.1441
9		0.2497	0.2371	0.221	0.2053	0.1443
10		0.2504	0.2374		0.2053	0.1442
11		0.2504	0.2346		0.2051	0.1448
12		0.2487	0.2354		0.2053	0.1447
13		0.2519	0.2371		0.2047	0.1445
14		0.249	0.2359		0.2049	0.1449
15		0.2518	0.2365		0.204	0.1444
16		0.2513	0.2353		0.2059	0.1451
17		0.2418	0.2368		0.2046	0.145
18		0.2494	0.236		0.2038	0.1451
19		0.252	0.2359		0.2043	0.1455
20		0.2513	0.2358		0.2048	0.1453
21		0.2522	0.2371		0.2048	
22		0.2524	0.2347		0.2053	
23			0.2372		0.2051	
24			0.2365		0.2046	
25			0.2355		0.205	
26			0.2357		0.2041	
27			0.2364		0.2062	
28			0.236		0.2055	
29			0.236		0.2045	

30			0.2378		0.2031	
31			0.2358		0.2048	
32			0.2364		0.2044	
33			0.2366		0.2054	
34			0.2361		0.2059	
35			0.2365		0.2036	
36			0.2376		0.2047	
37			0.2377		0.2047	
38			0.2364		0.2047	
39			0.2366		0.2035	
40			0.2369		0.2044	
41			0.2372		0.2041	
42			0.2381		0.2049	
43			0.2341		0.2046	
44			0.2353		0.2059	
45			0.2344		0.2045	
46			0.2373		0.2045	
47			0.2365		0.2037	
48			0.2371			
49			0.2361			
50			0.2368			
51			0.238			
52			0.2376			
53			0.2341			
54			0.2368			
55			0.2367			
56			0.2371			
57			0.2354			
58			0.2362			
59			0.238			
60			0.2379			
Average	0.3667	0.2504	0.2365	0.2194	0.2048	0.1446

Table 4-1: Evaluation of the d-spacing of the diffraction arcs from figure 4-25

Following interplanar distances are measured:

0.3667 nm,

0.2504 nm,

0.2365 nm corresponding to Al (111), 0.2364 nm,

0.2194 nm,

0.2048 nm corresponding to Al (200), 0.2041 nm,

0.1446 nm corresponding to Al (220), 0.14310 nm

The three non attributed d-spacings must correspond to aluminium oxide. For a complete analysis of the aluminium oxide more spots are needed. Further modifications of the SAED are possible: for example, by binarisation, the spots will appear clearer. Figure 4-26 shows a modified SAED, a binarisation and adjustment of arcs have been performed. This manipulation can lead to the detection of interfering signals, like noise or X-ray quanta and to their confusion with diffraction. To minimize these errors, the binarisation limit is minimal and the spots with a diameter < 2 nm are eliminated by an opening-procedure. The so modified SAED with drawn diffraction arcs, which do not correspond to literature but to the experimental data, are shown in the following figure 4-26.

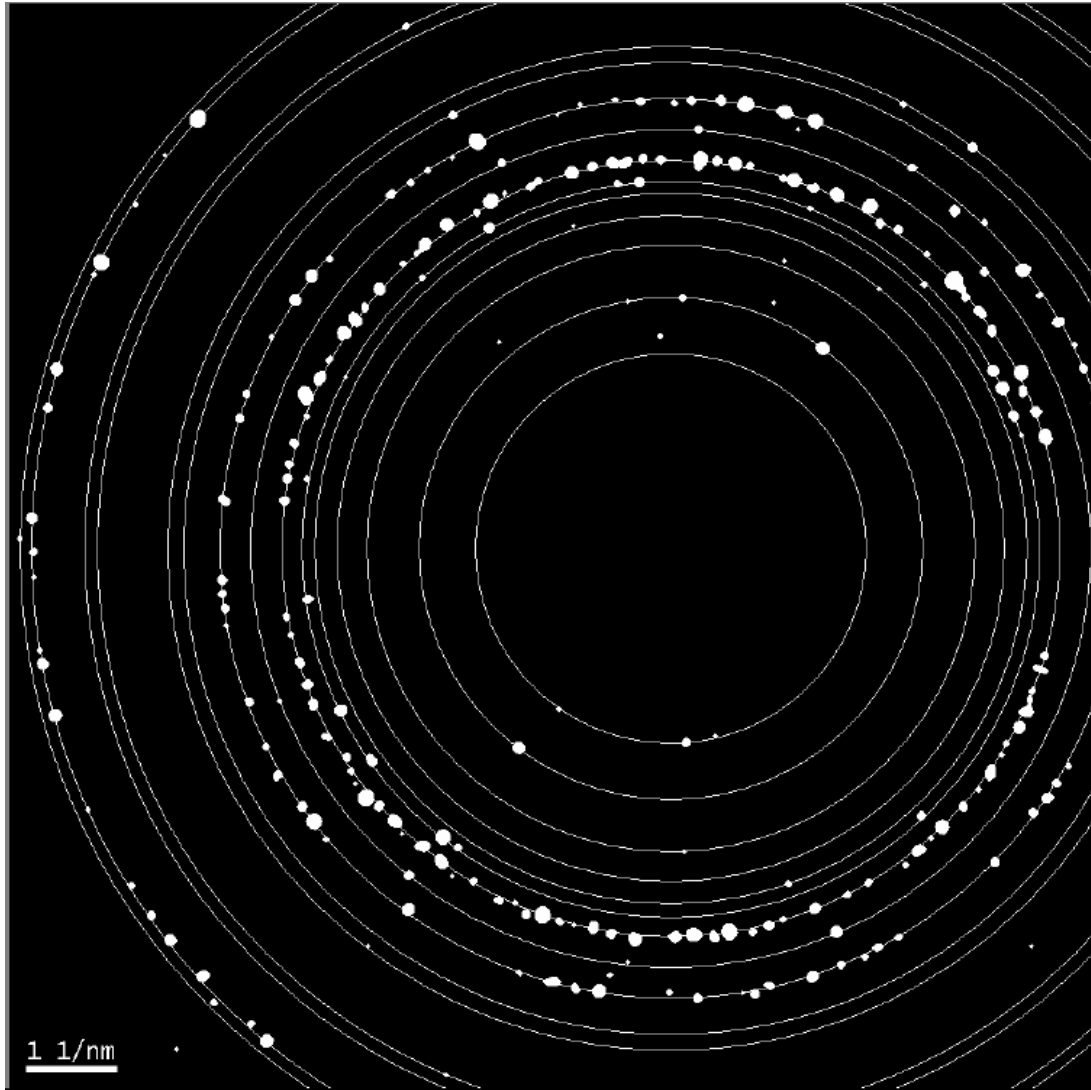


Figure 4-26: Binarised SAED of an area where Al/Al₂O₃ nanowires are dense with experimental diffraction arcs.

15 diffraction arcs are detected. Among them, arc 7, 9 and 14 correspond to aluminium diffraction planes, which have already been detected on Fig 4-21 without binarisation. In comparison with Figure 4-21 more diffraction spots, which meet aluminium diffraction arcs are detected. To investigate the remaining phase, diffraction spots of aluminium are eliminated (Figure 4-27). A lot of diffraction spots (51) are obtained but only one diffraction arc is clearly recognised. Figure 4-28 shows a superposition of the obtained diffraction pattern to the diffraction arcs of δ -Al₂O₃. The diffraction pattern of δ -Al₂O₃ matches very well to the SAED pattern, indeed the herein reported diffraction arcs (from JCPDS 46-1215) are chosen in such a way, that the difference with the experimental spots do not exceed 2%.



Figure 4-27: Binarised SAED of an area where Al/Al₂O₃ nanowires are dense and elimination of spots which are attributed to aluminium.

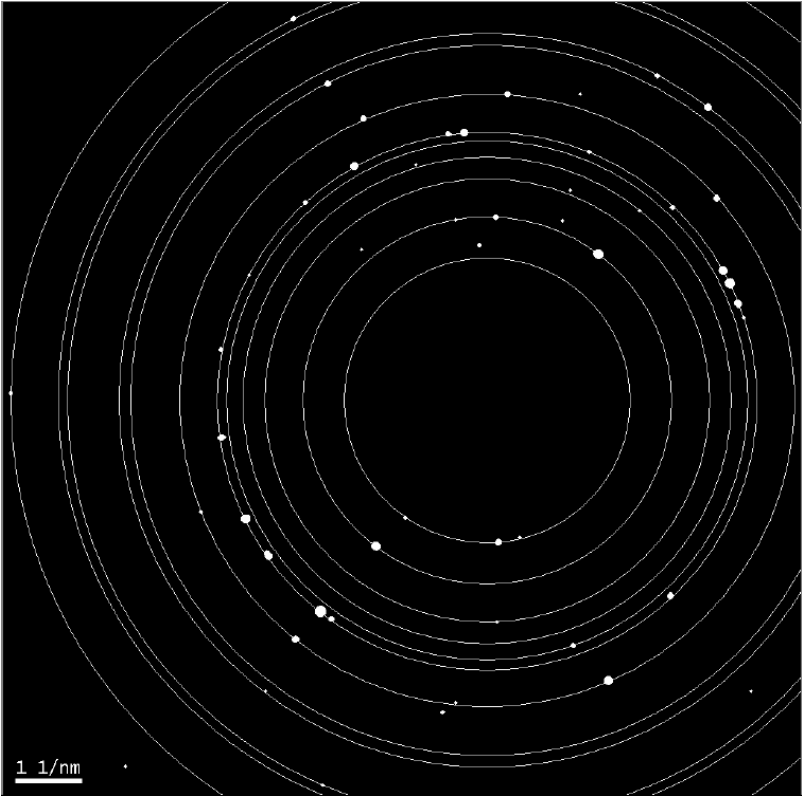


Figure 4-28: Figure 4-27 where diffraction arcs from δ-Al₂O₃ (JCPDS 46 1215) are superposed.

It is now possible to assign twelve diffraction arcs to δ -Al₂O₃, although it must be taken into account that some arcs are just represented by a single diffraction spot. Among the 51 diffraction spots, only eight are still unassigned. It is not easy to determine if either the eight remaining spots are artefacts or real diffraction spots. A test will be performed to detect possible artefacts. For that, the original image (Fig 4-18) will be masked with the binary image (Figure 4-27), after having eliminated the beam aperture and the background. The spots, which are only composed of one or two pixels are suspected to be artefacts on the resulting image shown in figure 4-29., while the real diffraction spots are not sharp.

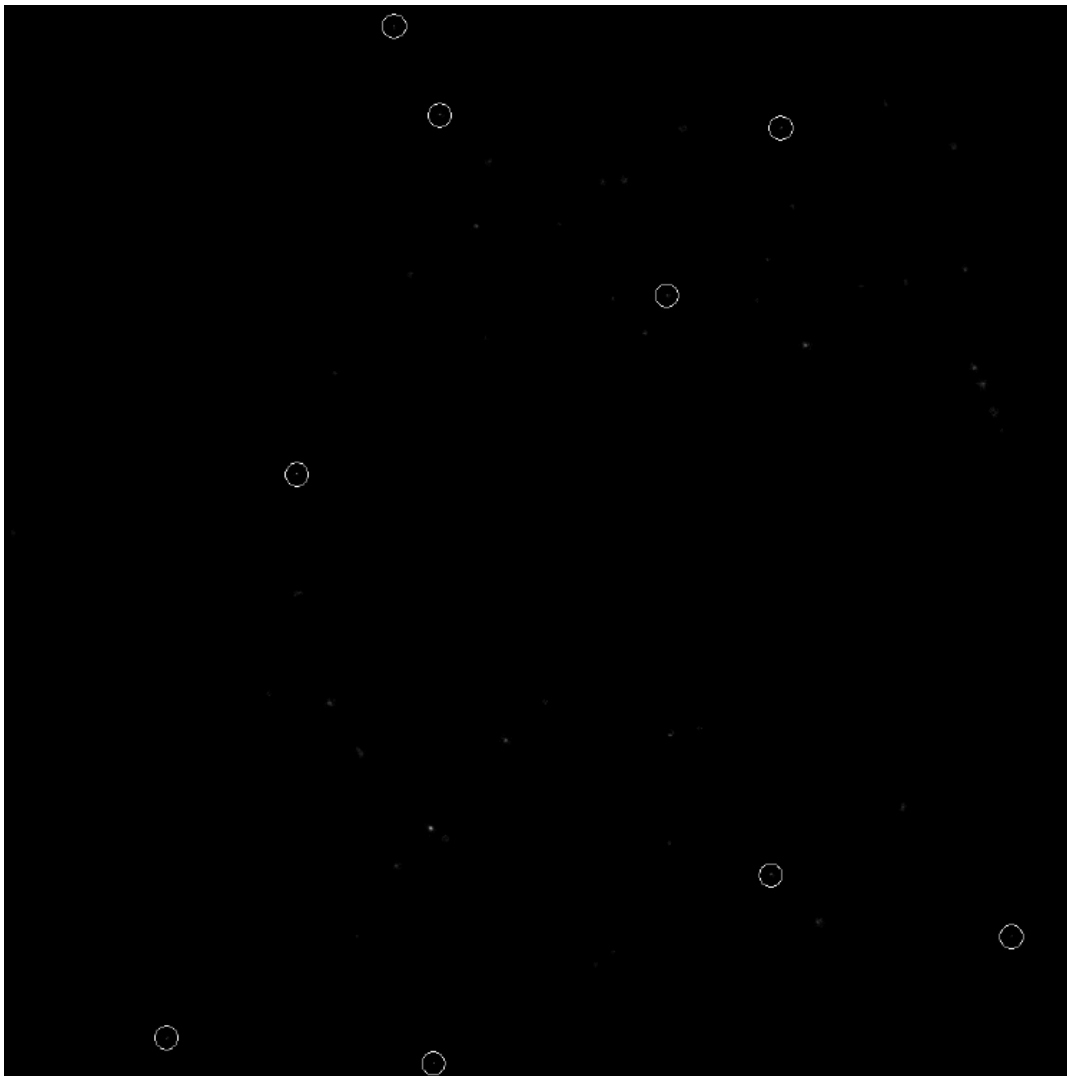


Figure 4-29: Original SAED of an area where Al/Al₂O₃ nanowires are dense (Fig. 4-21) masked with a binary image (Fig. 4-26). Spots suspected as artefacts are circled.

According to this image, 9 spots are suspected to be artefacts. By plotting these 9 spots on figure 4-30, it is then clear that some of the suspected spots match perfectly

with the diffraction arcs previously found. It means that among the suspected spots some are definitely real diffraction spots.

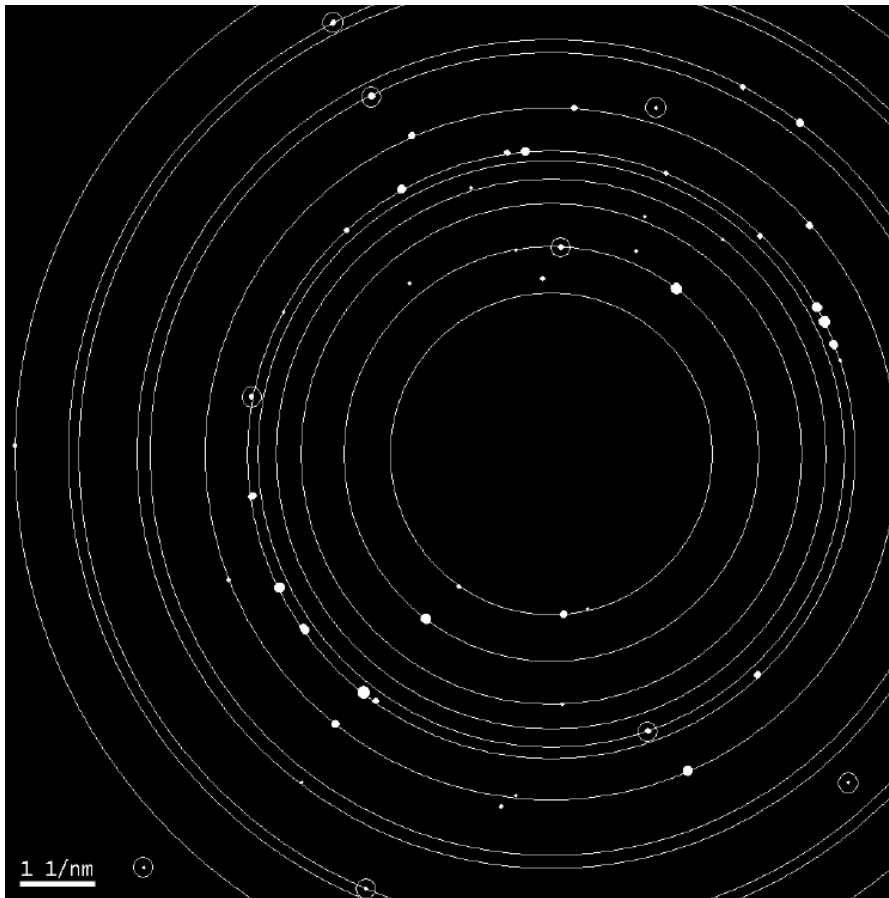


Figure 4-30: Binarised SAED of an area where Al/Al₂O₃ nanowires are dense with experimental diffraction arcs (fig. 4-26) with suspected spots circled.

Another statement, which can be drawn according to Figure 4-28, is that among the eight spots which could not have been assigned some are not suspected; therefore they could be real diffraction spots from another phase. We probably have to deal with a mix of phases.

The results of the complete electron diffraction analysis and a comparison with the diffraction values for δ -Al₂O₃ are presented in the following table (Table 4-2). The values in parenthesis correspond to the spots, which have been defined as “suspected artefacts” during the study. It must be taken into account that the relative X-Ray intensities reported only provide an informative basis, as the scattering mechanism in the case of electron diffraction is different.

Arc N° (begins inside)	N° of spots	Interplanar spacing [Å] from δ -Al ₂ O ₃ JCPDS 46-1215	Corrected measured values [Å]	Difference between arcs and JCPDS 46-1215	Relative X-ray intensities
1	3	4.716	4.663	1.1%	5
2	3 + (1)	3.550	3.620	1.97%	5
3	1	3.006	3.000	0.2%	10
4	2	2.731	2.733	0.07%	50
5	(1)	2.596	2.562	1.3%	80
6	17 + (1)	2.457	2.472	0.6%	80
7	7	2.162	2.172	0.5%	10
8	(1)	1.907	1.873	1.8%	5
9	3	1.799	1.814	0.8%	10
10	(1)	1.602	1.592	0.6%	10
11	(1)	1.542	1.557	1.0%	10
12	1	1.405	1.402	0.2%	80

Table 4-2: Results of SAED analysis and comparison with δ -Al₂O₃

The HRTEM study has shown that the Al₂O₃ exists in the form of very fine crystals, which cause weak signals. Bigger crystals have just been detected in few areas. Therefore the SAED image expected should present isolated weak spots of Al₂O₃ and that is exactly the case. Few diffraction spots are detected for Al₂O₃ and the tabular values for δ -Al₂O₃ are rather close to one another (in particularly below 2 Å), it means that the correspondence could turn to be a coincidence. By considering only the 4 strongest diffraction arcs, the other Al₂O₃ correspond to the diffraction image. The following table shows the Al₂O₃ presenting less than 2% difference with the measured values.

JCPDS N°	Formula	Phase	d [Å] (difference with measured values)			
79-1559	Al _{2.427} O _{3.64}		3.5586 (1,7%)	2.4449 (1.1%)	---	1.8173 (0.18%)
75-0277	Al ₂ O	---	---	2.49 (0.73%)	---	---
46-1215	Al ₂ O ₃	δ- Al ₂ O ₃	3.550 (1.9%)	2.457 (0.61%)	2.162 (0.46%)	1.799 (0.83%)
21-0010	Al ₂ O ₃	ε- Al ₂ O ₃	---	2.451 (0.85%)	2.185 (0.60%)	---
16-0394	Al ₂ O ₃	δ- Al ₂ O ₃ , deleted	3.61 (0.28%)	2.460 (0.49%)	2.160 (0.55%)	1.810 (0.22%)
01-1307	Al ₂ O ₃	γ- Al ₂ O ₃	---	2.45 (0.89%)	2.16 (0.55%)	1.79 (1.3%)
01-1304	Al ₂ O ₃	θ- Al ₂ O ₃ , deleted	---	2.45 (0.89%)	---	1.79 (1.3%)

Table 4-3: Possible aluminium oxides

The fact that many aluminium oxides show similar interplanar spacing, in particularly for the strongest diffraction arcs, hinders a clear determination of a unique phase. The following table suggests for example, that θ-Al₂O₃, a monoclinic phase, is also probable.

However it has been shown in the preceding chapter that the shell can contain rather big aluminium oxide crystals (app. 20 nm), therefore a study of such an area should permit to become shaper diffraction rings. We did not succeed yet to measure diffraction on such an area.

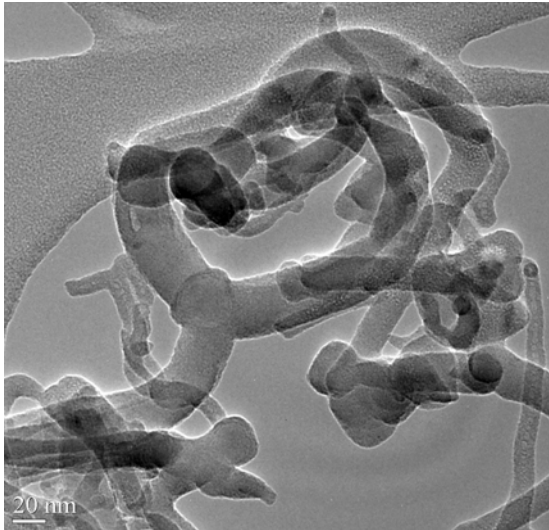
Arc N° (begins inside)	N° of spots	Interplanar spacing [Å] from θ -Al ₂ O ₃ JCPDS 46 1215	Corrected measured values [Å]	Difference between arcs and JCPDS
1	3	---	4.663	---
2	3 + (1)	3.5513	3.620	1.9%
3	1	---	3.000	---
4	2	2.7294	2.733	0.1%
5	(1)	2.5679	2.562	0.2%
6	17 + (1)	2.4478	2.472	1.0%
7	7	---	2.172	---
8	(1)	1.8674	1.873	0.3%
9	3	1.8135	1.814	0.03%
10	(1)	---	1.592	---
11	(1)	1.5429	1.557	0.9%
12	1	1.4052	1.402	0.2%

Table 4-4: Results of SAED analysis and comparison with θ -Al₂O₃

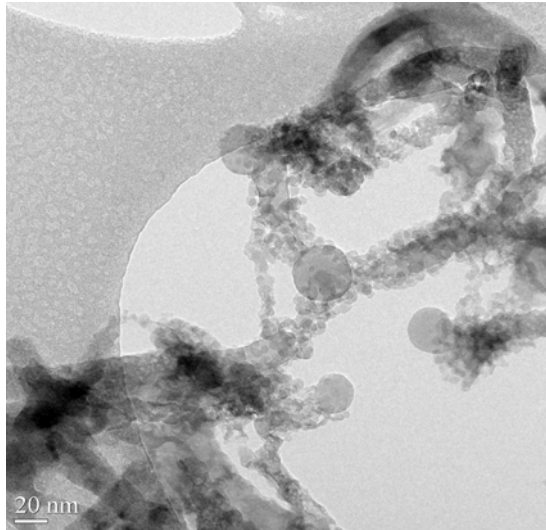
4.4 Effects of intensive electron irradiation

During TEM imaging, the sample must withstand the high vacuum present in the instrument and irradiation in the order of 200 keV. Therefore the main drawback of the TEM technique is that the structure of the sample may be changed or damaged by the electron beam. The nanowires structure was subjected to some important modifications during irradiation. These modifications are not only barriers to the analysis, but also a way to gather information about the behaviour of the nanowires structure. Figure 4-31 shows six bright field images of the area with triple nanowires growth analysed in the previous chapter. Figure A shows the area at the beginning of the analysis, Figure B after app. 3 hours analysis in phase and diffraction contrast, Figure C after EDX analysis and in the following after every 15 minutes intensive electron irradiation.

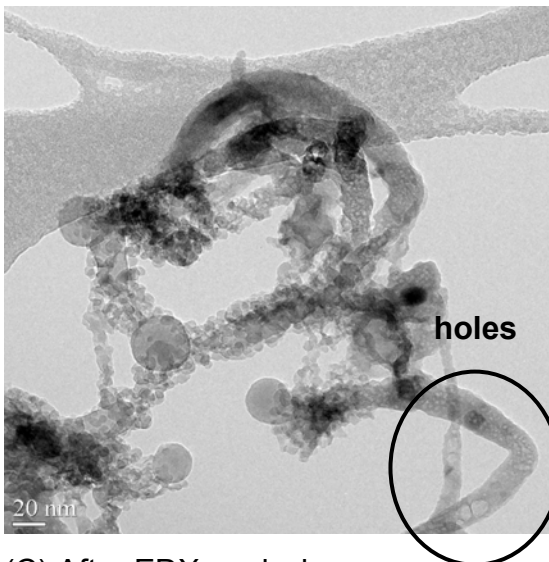
The single crystalline cores in the heads and in the nanowires, grow up, while the shells disaggregate by forming particles. Minuscule variations in the position permit to get different diffraction contrast. The heads and the core are single crystalline as they are black on many images. As the cores appear naked, EDX measurements have been performed to measure the composition with more accuracy as with the shell around (Figure 4-32). It appears that the aluminium amount in the cores has grown while the oxygen amount decreased a lot. The cores are therefore pure aluminium; the small amount of oxygen detected is due to X-Ray irradiations out of the analysed area. Therefore the modifications are probably due to O₂ formation. The bubbles observed on Figure C right below in the nanowire confirm the possibility of a gas emission.



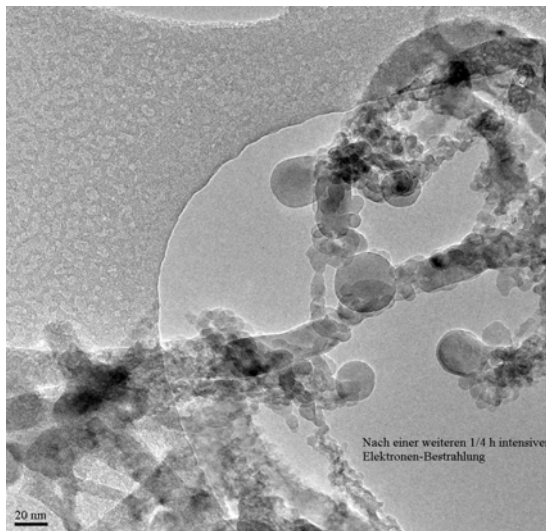
(A) Before intensive irradiation



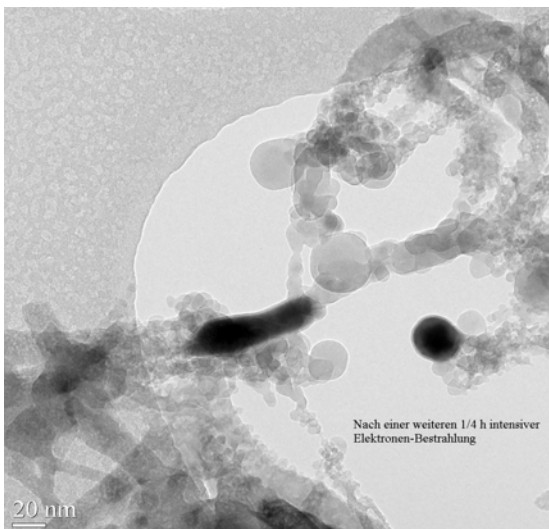
(B) After 3h irradiation



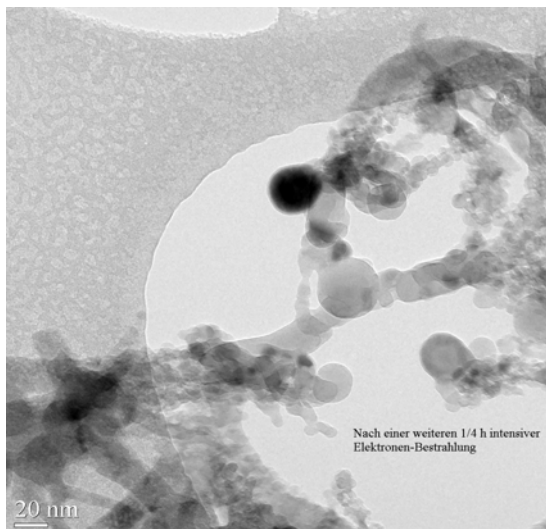
(C) After EDX analysis



(D) After 15 minutes more



(E) After 15 minutes more



(F) After 15 minutes more

Figure 4-31: TEM images of the sample after intensive electron irradiation with TEM.

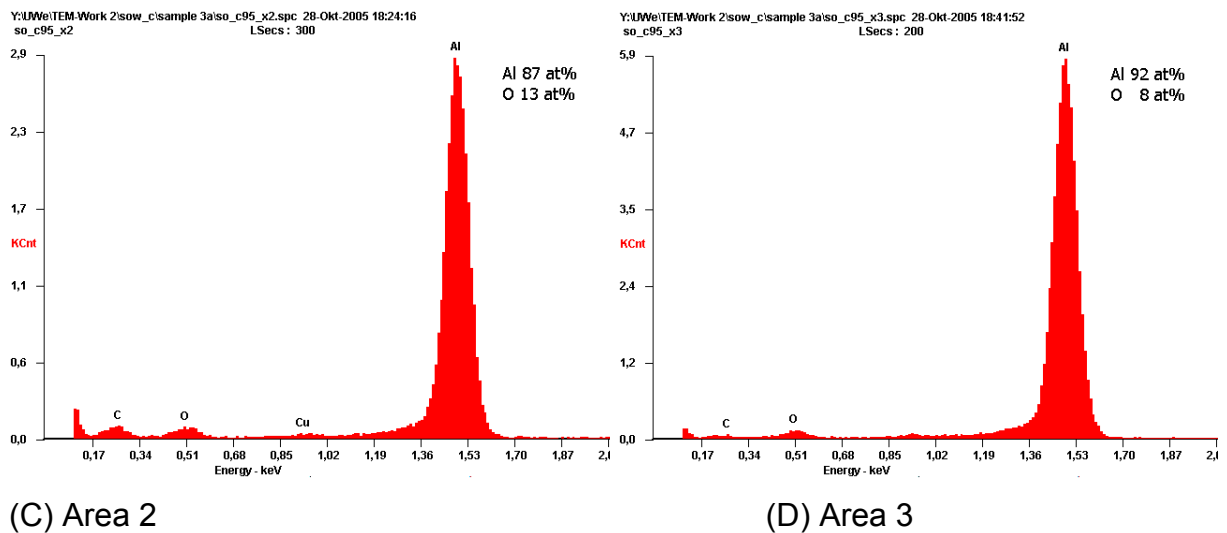
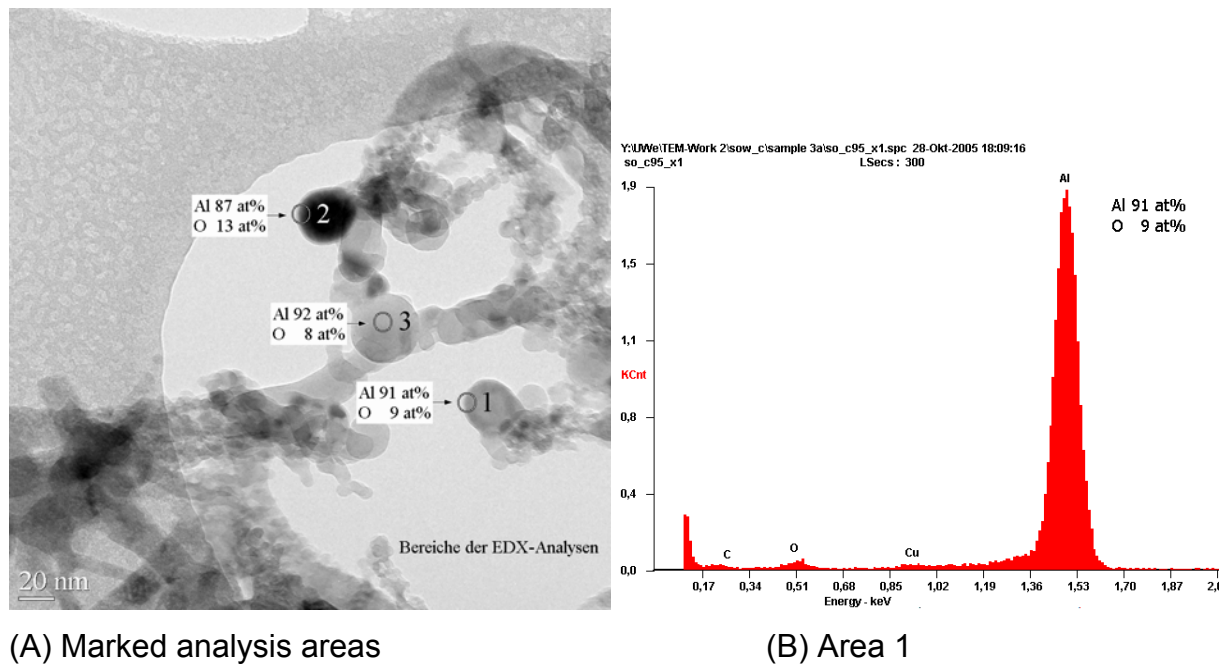
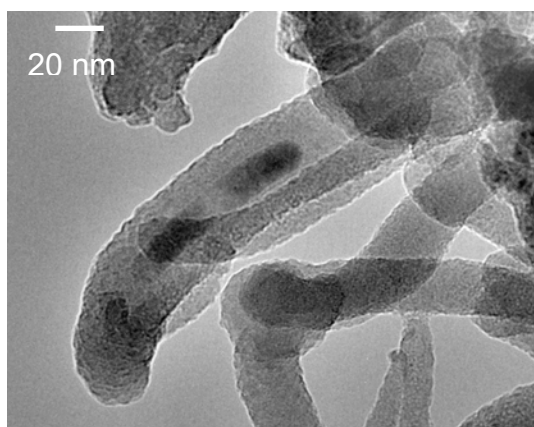
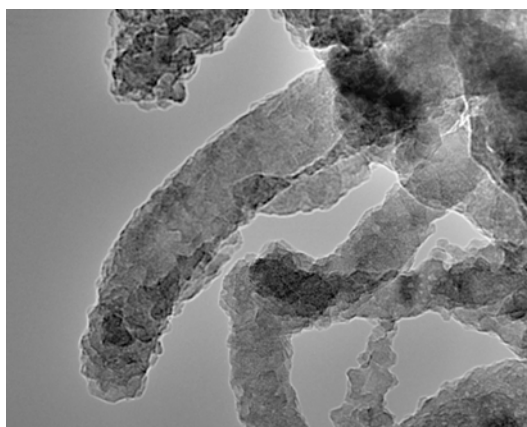


Figure 4-32: EDX analysis of three Al/Al₂O₃ nanowires' heads after irradiation.

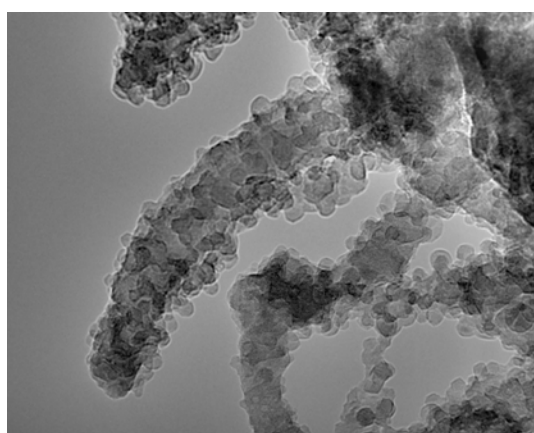
The chronological progression of the modifications has been analysed by making a film made of 81 images taken every 2 minutes during intensive irradiation (200 keV). Some images have been selected from the film to illustrate the evolution of the structure with time (Figure 4-33). The structures observed presented a single crystal core and an amorphous or fine crystalline shell around at the beginning of the analysis.



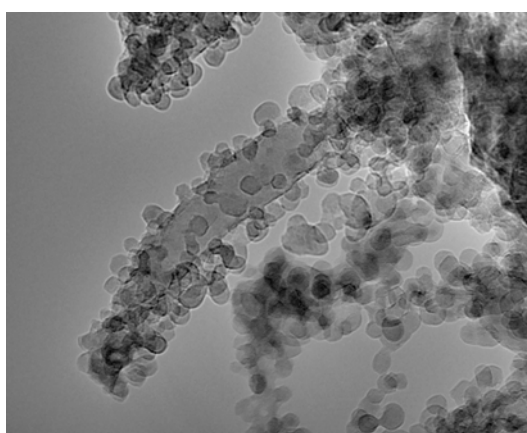
(A) Before irradiation



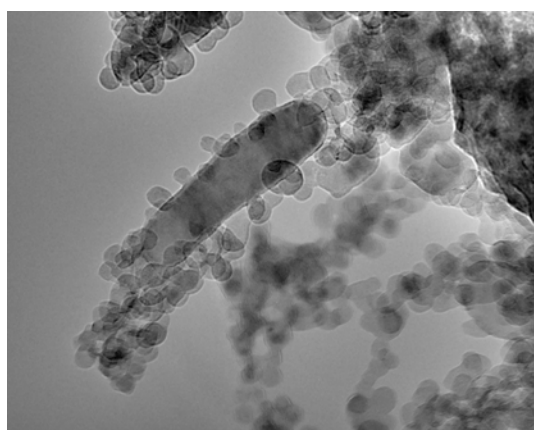
(B) 12 minutes irradiation



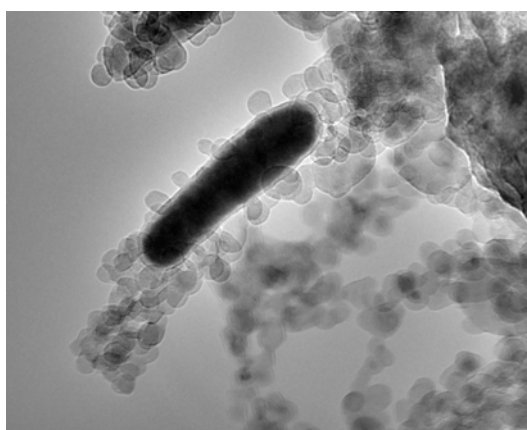
(C) 90 minutes irradiation



(D) 116 minutes irradiation



(E) 120 minutes irradiation

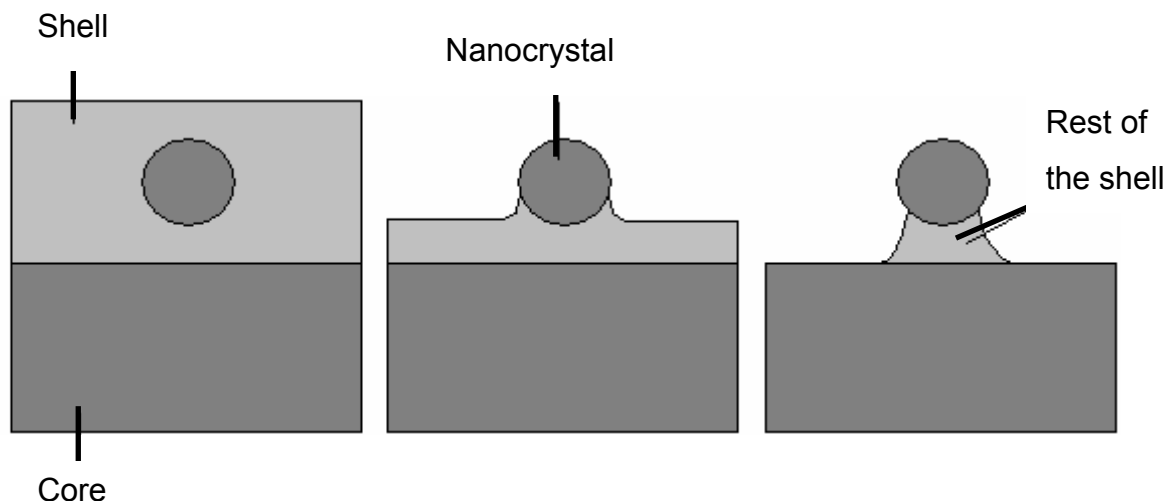


(F) 156 minutes irradiation

Figure 4-33: TEM images showing the chronological progression of the modifications due to irradiation of the Al/Al₂O₃ nanowires.

Due to heating of the sample caused by the electron beam, the orientation of the observed nanowire in the middle of figure B changed. A polycrystalline structure forms slowly in the shell, it is first observed after 12 minutes. It seems to grow from the core and takes a spherical form. The nanowires diameter is about 30 nm at the beginning and only 28 nm after 56 minutes irradiations, while the core grows from 10 nm till 12.5 nm. The diameter decreases until 80 minutes, where the shell begins to decompose into spherical particles.

The shell shrinks and loses oxygen due to intensive irradiation, thus the resulting free aluminium migrates in the core and causes the core growth. Figure 4-33 (D, E, F) shows that some nanocrystals from the shell seem to be attached to the core by a neck. A possible explanation is that the particles created in the shell are still attached to the rest of the shell although the shell has diminished; the neck is constituted of the rest of the shell where the oxygen lost is avoided by the particle. A schematic representation of the neck formation is illustrated on scheme 4-2.



Scheme 4 2: Scheme of the neck formation between the Al/Al₂O₃ nanowires and the nanocrystals grown during irradiation.

At the end of the film, the core is oriented in such a way, that the single crystal structure is visible. It is not clear if the nanocrystals in the shell are aluminium oxide or if they display another Al/O proportion. For that another analysis will be performed with HRTEM, where lattice fringes of the crystallite will be compared with the aluminium single crystal. Figure 4-34 shows a HRTEM image of an aluminium head, where several crystallites with diameters between 2 and 5 nm have grown.

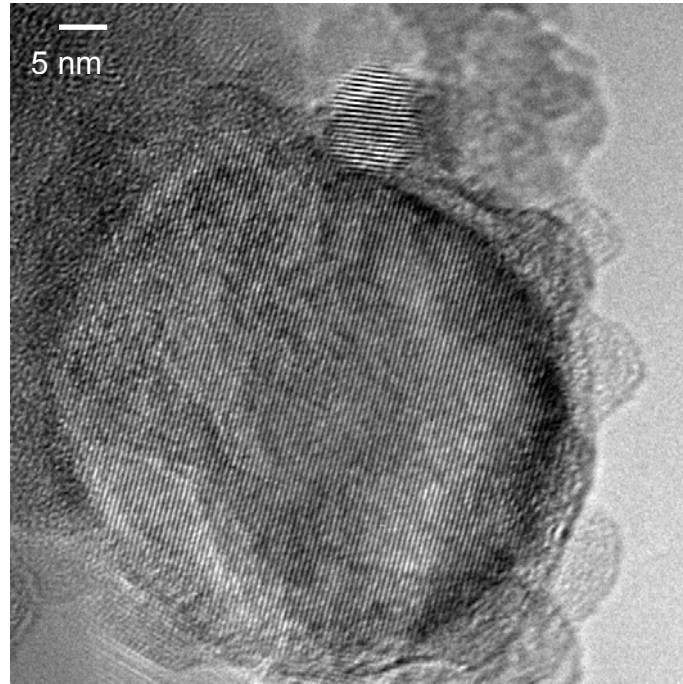


Figure 4-34: HRTEM image of an Al/Al₂O₃ nanowire's head, where some particles have grown.

The head is quasi exclusively constituted of the crystalline core. The interplanar distance measured in the crystallite above in the middle is quasi the same as in the head. Assuming that the head shows Al(111) with interplanar distance of 0.2338 nm, then it results that the lattice fringes observed in the particles show $d = 0.2406$ nm. The lattice plane distances in the particle are 1.029 time bigger than the one from the core. The distance corresponds to the (311) plane of γ -Al₂O₃ (JCPDS 10-425) or to (111) plane of aluminium, which has slightly been inflated by oxygen inclusions. Figure 4-35 shows a HRTEM image of the head with some particles at the surface, superposed with 5 structure images. A comparison with the original image shows that this manipulation permits to accentuate existing lattice planes.

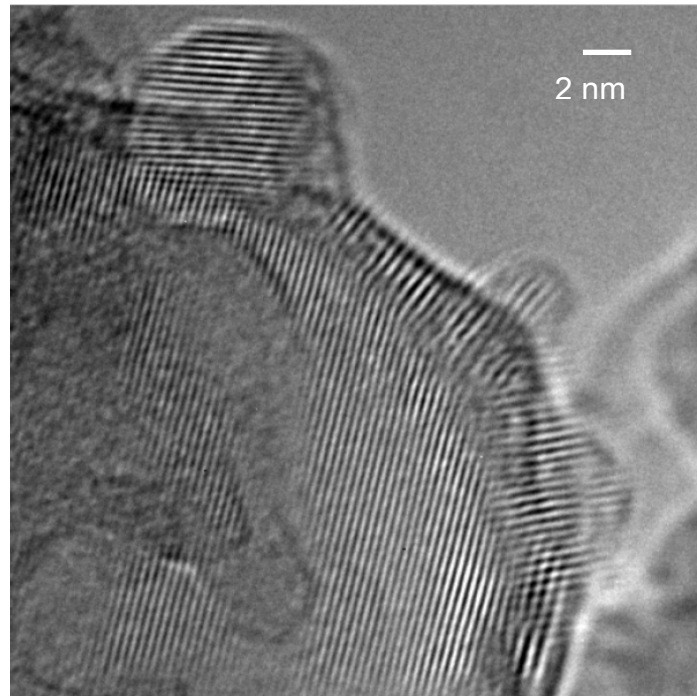


Figure 4-35: TEM image superposed with 5 HRTEM-images of an Al/Al₂O₃ nanowire's head, where some particles have grown.

The particles grow by formation of a coincidence grain boundary with the aluminium core. The lattice planes of the residual shell are quasi perpendicular to the lattice planes in the core, they show interplanar distances of 0.275 nm, which may correspond to (220) of γ -Al₂O₃ (JCPDS 10-425). In the particles the lattice planes measured are still 0.240 nm. Figure 4-36 shows the region of interest as well as its power spectrum (square of the Fourier transform of the image). Selective discrete Fourier filter of the power spectrum permit to separate the lattice planes, which have generated the power spectrum, in the real space.

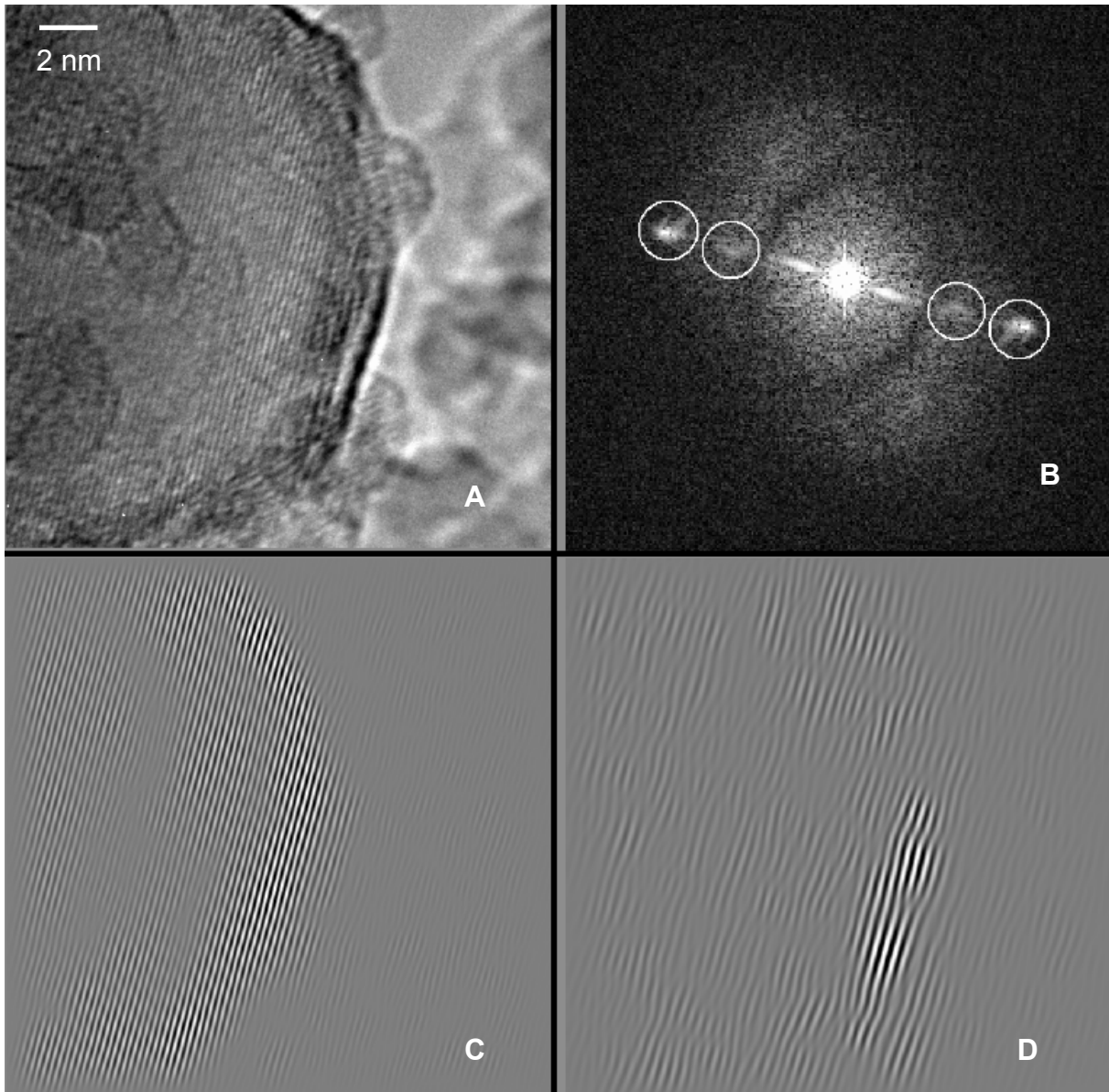


Figure 4-36: HRTEM structure image (A) of an Al/Al₂O₃ nanowire's head with growing particles and the power spectrum (B). Below, the Fourier filter of the regions marked on the power spectrum (C and D)

The power spectrum of the head shows two distinct spots; the outer and the inner spots can be assigned to core and shell respectively by comparing with the reconstituted images below. In the images obtained below, the strong lattice planes are real while the weak ones correspond to artefacts.

A better observation of the spots in the power spectrum shows that the spot corresponding to the core is constituted of a strong aluminium spot and some weaker spots. With a binarisation of the power spectrum, this effect appears clearer (Figure 4-37).

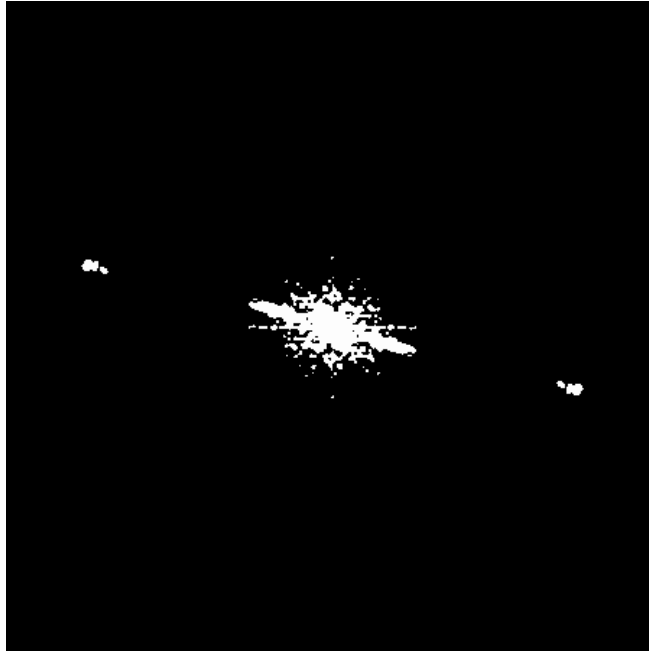
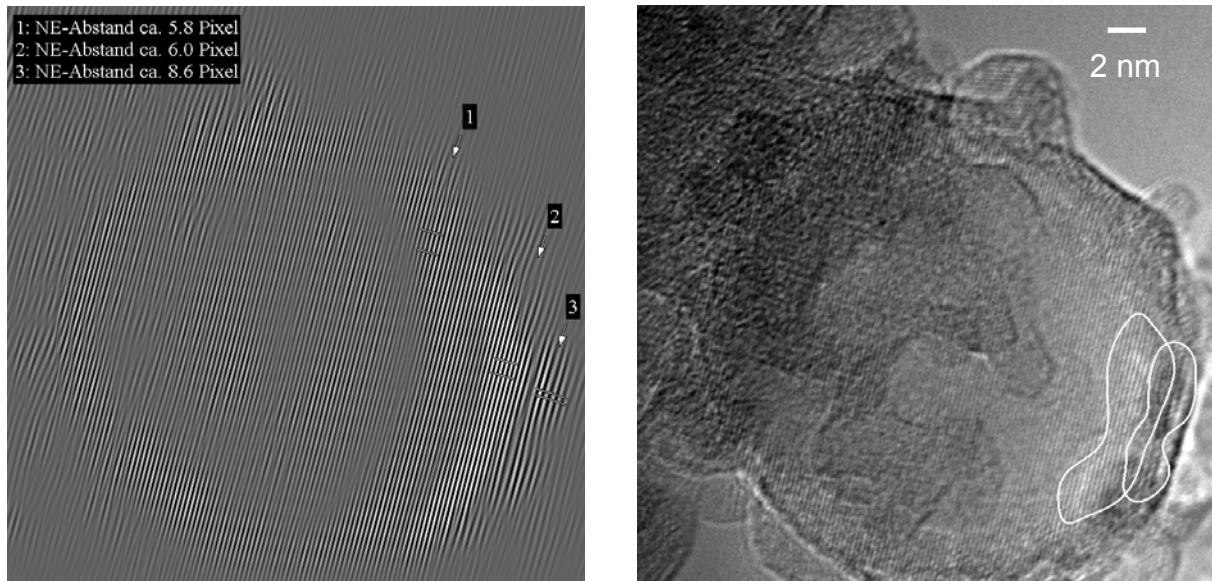


Figure 4-37: Binarisation of the power spectrum from the Al/Al₂O₃ nanowire's head.

On Figure 4-38 it is evidenced that the aluminium spot is at least constituted of three spots. After correction, it is calculated that the core possess an interplanar distance of 0.234 nm (Al (111)) and the extremity of the core region 0.246 nm. This means that oxygen could also be inserted in the core region to produce broad lattice spacing. As the spots of the Al₂O₃ shell is elongated, the values measured are not precise; the interplanar distances in the shell vary from 0.33 nm till 0.39 nm.

The outer spot, the spot in the middle and the spot from the shell (Figure 4-38) are used to create some selective discrete Fourier filter images. By assembling these Fourier filter images the head can be reconstituted with high contrast. By binarisation of the same Fourier filter, regions could have been limited in the real space.



(A) Structure in real space

(B) Regions with different interplanar distances

Figure 4-38: Localisation of three regions with different phases on the Al/Al₂O₃ nanowire's head.

The structures in real space are not very sharp because the masks had a small diameter due to the fact that the spots are too close from one another in the power spectrum. Nevertheless three distinct areas are isolated. In the core interplanar distances of 0.232 nm are measured, in the intermediate region 0.240 nm and in the shell 0.344 nm. It has not been possible to identify precisely the intermediate phase but it is probable that oxygen is migrating and that it results in the formation of different phases around the core with different amount of oxygen. After this analysis the sample was exposed to air and analysed again with a weak electron beam. Figure 4-39 is a HRTEM image of the same head after contact with air.

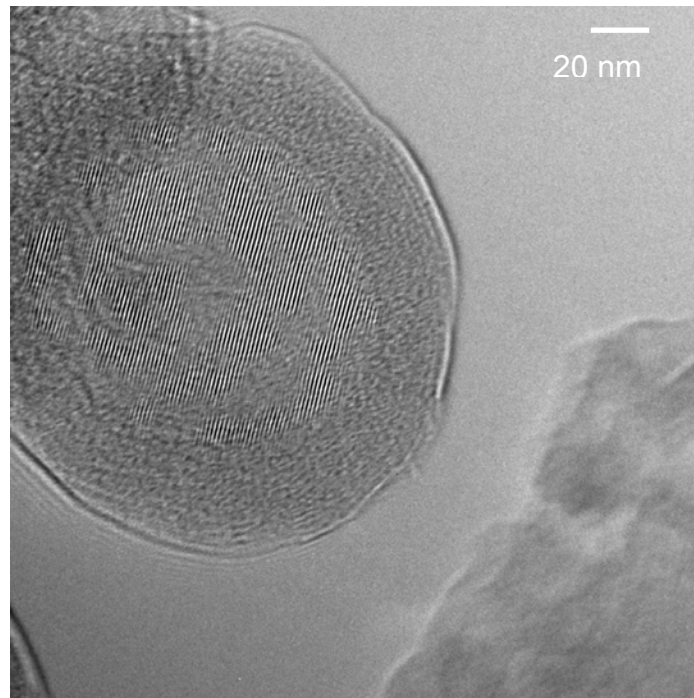


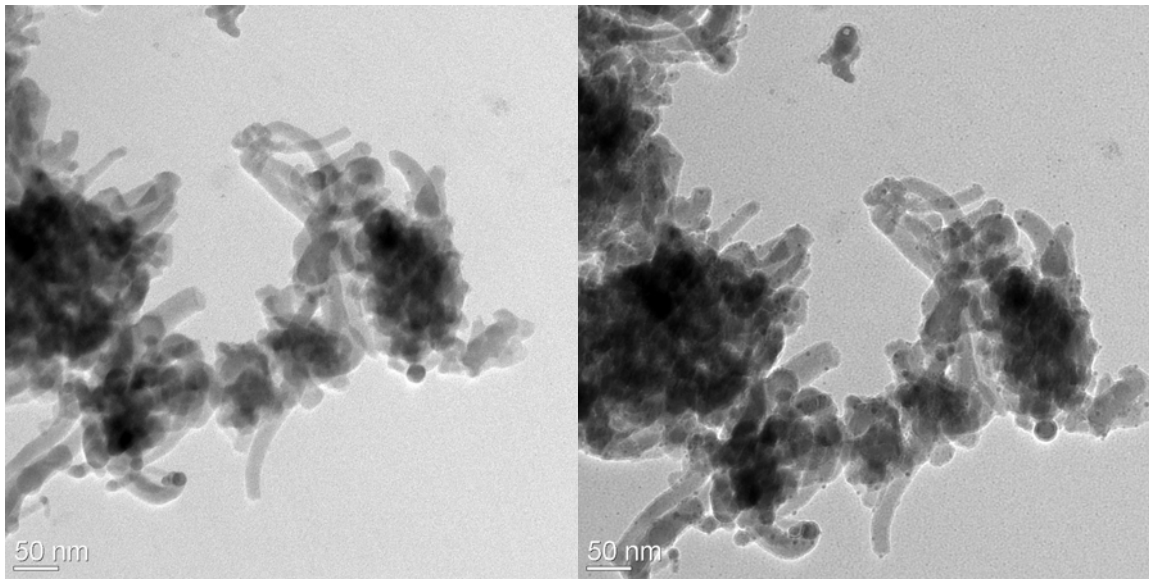
Figure 4-39: HRTEM image of the Al/Al₂O₃ nanowire's head after exposure to air and weak electron irradiation. Effects of irradiation are reversible.

A surprising result is the reversibility of the degradation process. After exposure to air, the head appear like it was before intensive irradiation. This is a supplementary evidence to prove the role of oxygen transport in this phenomenon.

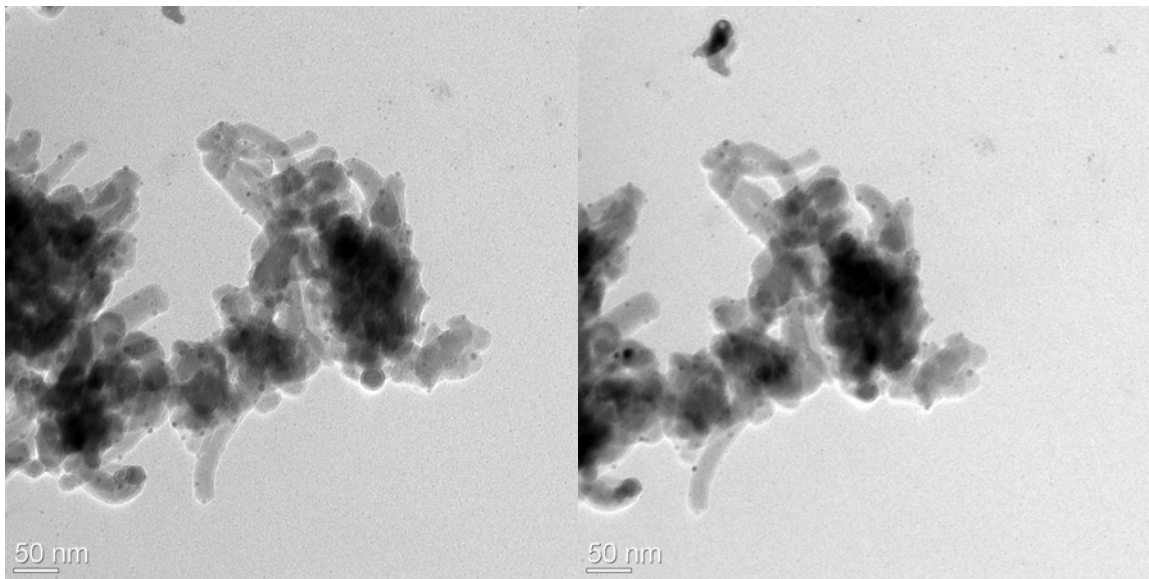
4.5 Effect of temperature on the sample

The intensity of the irradiation described above cannot be governed, therefore no information is known about the transformation conditions. The installation of a heated sample holder allowed to control the sample temperature, the heating duration and it will also permit to heat the sample to higher temperatures. Figure 4-40 shows the nanowire structure before, during and after heating to 190°C.

After 7.5 minutes heat treatment, nanoparticles with diameters between 2 nm and 5.5 nm deposit on the nanowires. On the nanowires' surface, a shell with app. 3 nm thickness, which shows less contrast than the wire itself, is constituted. Maintaining high temperature during 30 minutes allow the growth of the nanoparticles, which reach diameters of 9 nm. After 30 minutes nanoparticles can also be distinguished on the carbon film. After cooling to room temperature, the particles and the shells are still present.



(A) Nanowires before heating (24 °C) (B) After 7.5 minutes at 190 °C

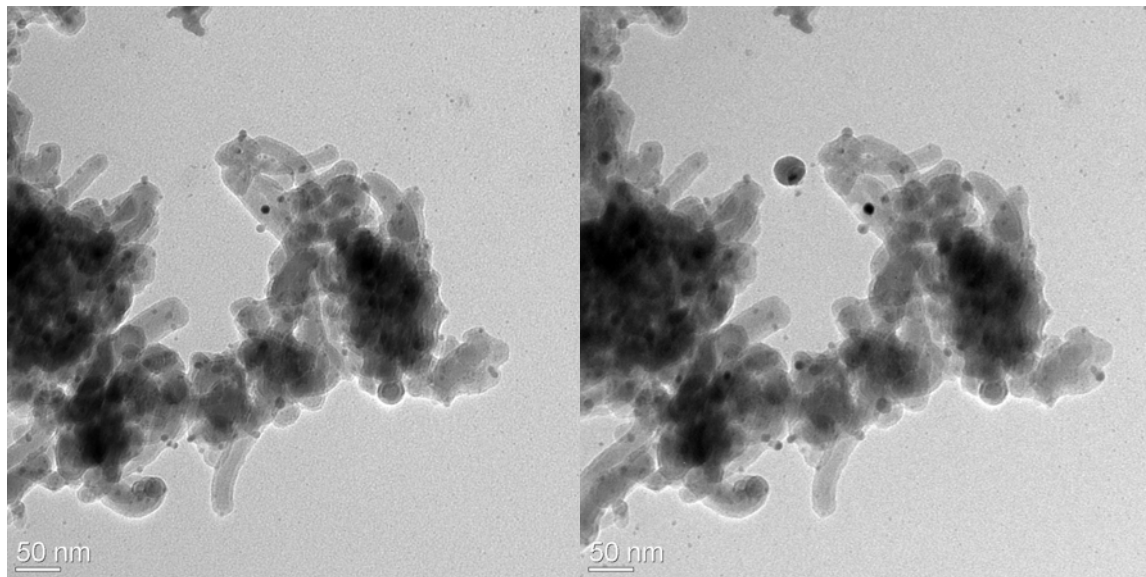


(C) After 30 minutes at 190 °C (D) After cooling to 25 °C

Figure 4-40: TEM image of Al/Al₂O₃ nanowires during heating process.

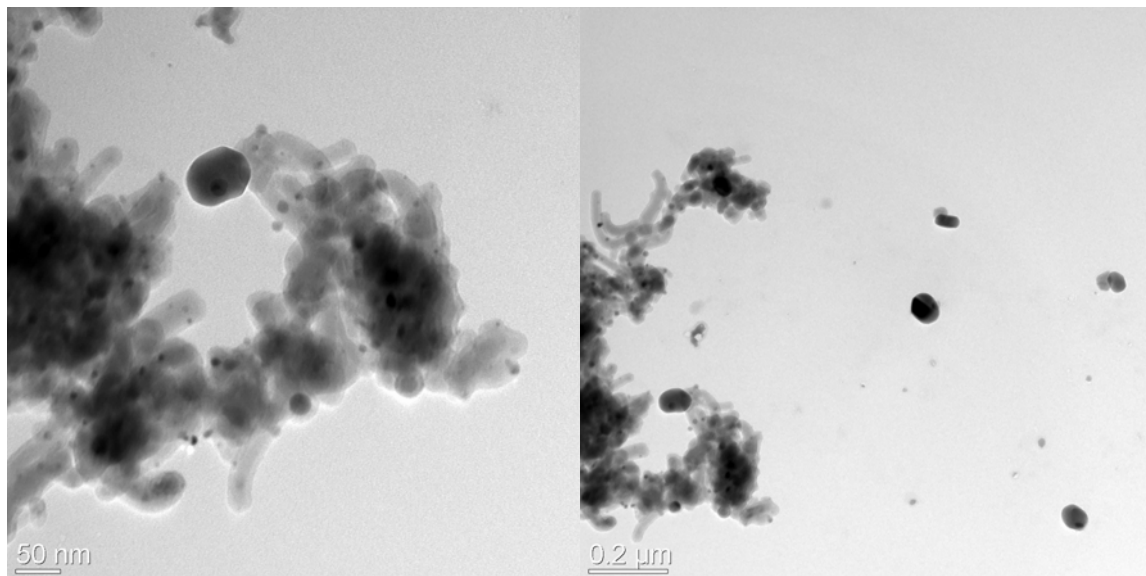
Figure 4-41 shows further transformations of the nanowires structure by heating at 300 °C, 400 °C and 500 °C.

At 300 °C, the shell structure is better visible than at 190 °C. The shell is uniformly formed around the nanowire; hence diffusion, due to temperature, of some elements of the nanowire is probable.



(A) After 30 minutes at 300 °C

(B) After 20 minutes at 400 °C



(C) After 90 minutes at 500 °C

(D) Other area of C-film at 500 °C

Figure 4-41: Evolution of the Al/Al₂O₃ nanowires and the aluminium particles with varying temperature from 300 ° to 500 °C.

Some nanoparticles show a crystalline structure as they appear black in the bright field image. At 400 °C a big crystal (app. 50 nm) appears on the carbon film while the other crystals on the carbon film are not growing. At 500 °C, the small crystals from the carbon film totally disappeared while further growth of the big crystal is observed. A sort of Oswald ripening may occur, where diffusion from smaller crystals to bigger ones permit to reduce the energy of the entire system by reducing the surface-to-

volume ratio. Between each heating steps, the sample is cooled to room temperature but no change is observed during the cooling, although the sample is maintain 17 h at room temperature. Observation of an area near the region observed until now (Figure 4-42 A), permit to testify that other big particles have grown on the C-Film. The particles formed on the C film at 500° C are not only big particles (>20 nm) but there are also smaller particles (<5 nm), which disappear due to the electron beam. Figure 4-42 B shows a SAED of an area on the C film where small and big particles are detected.

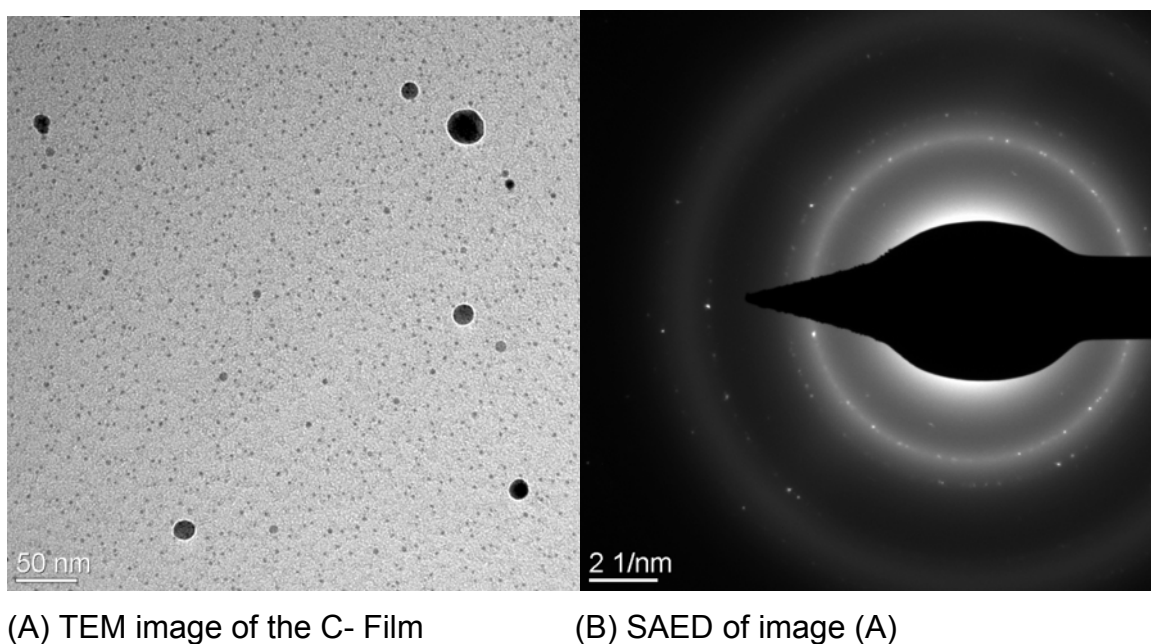


Figure 4-42: Electron diffraction analysis of aluminium particles grown on the C- film.

Particles with varying diameters have been deposited on the C-film in a wide range. Hence it is not clear if the deposition occur through the gas phase or with surface diffusion process. The hypothesis of surface diffusion is nevertheless less probable, otherwise there would be more particles in the range of original nanowires and less particles away.

The sample is deposited on a copper net, which is submitted to deformation due to the temperature variations. Therefore the sample's height has varied and the calibration becomes incorrect. As a result, the identification of the diffraction arcs cannot be achieved with absolute values, thus a strategy will be developed to overcome this problem. Instead of using absolute values, relations between the

diffraction arcs will be determined and compared with calculated relations from databases.

The following interplanar distances are measured 2.616 Å, 2.122 Å, 1.845 Å, 1.299 Å and 1.106 Å; the resulting relations are summed up in table 4-5 and compared with calculated relations for aluminium (JCPDS 04-0787).

Relations measured	Result	Relation from JCPDS 04-0787	Result	Corresponding planes
2.616 / 2.122	1.233	---	---	---
2.122 / 1.845	1.150	2.338 / 2.024	1.155	(111) / (200)
1.845 / 1.299	1.420	2.024 / 1.431	1.414	(200) / (220)
1.299 / 1.106	1.175	1.431 / 1.221	1.172	(220) / (311)

Table 4-5: Results of electron diffraction measurements of the particles on carbon film.

According to the relationship between the arcs, all arcs, except the inner one, have been assigned to aluminium (JCPDS 04-0787). It means that the nanoparticles formed on the C film are aluminium clusters (Figure 4-43).

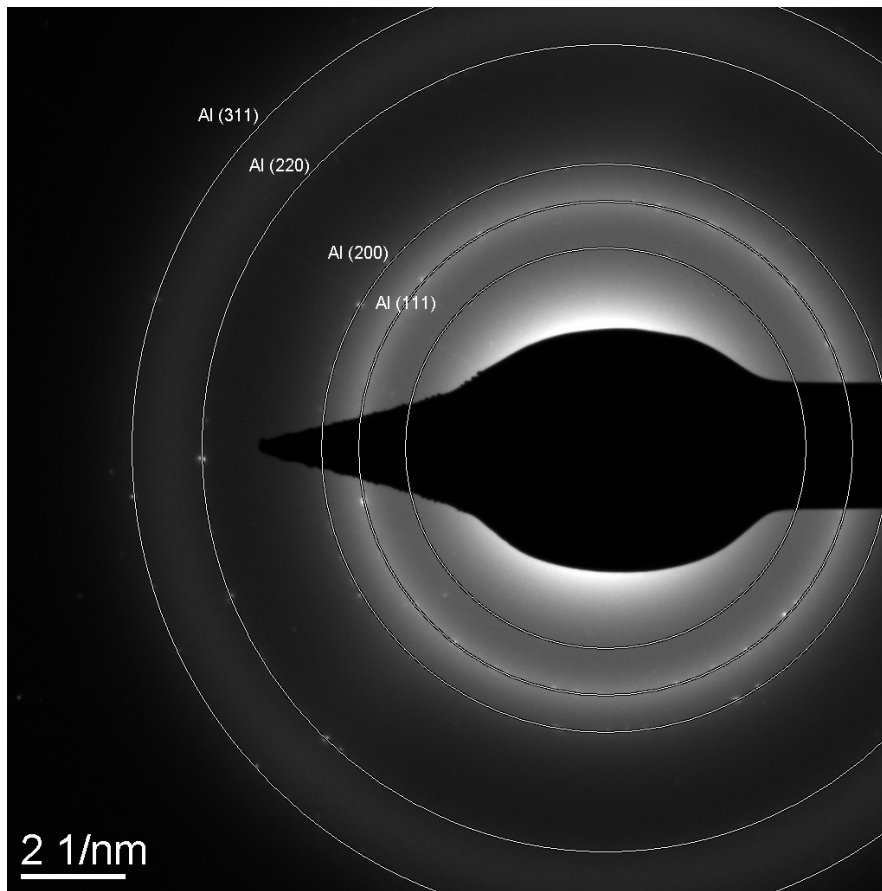
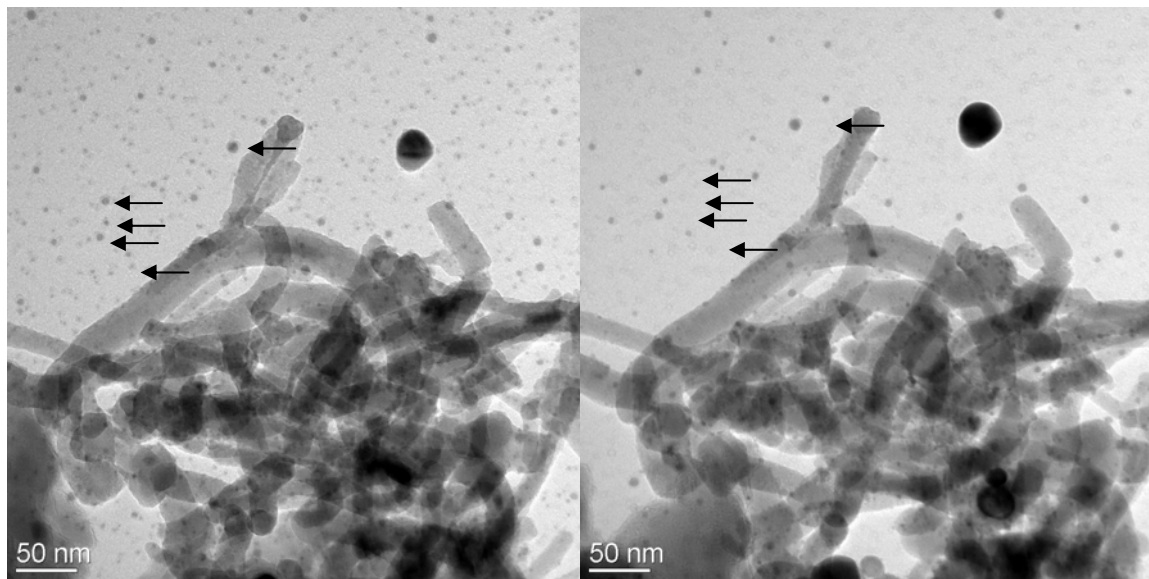


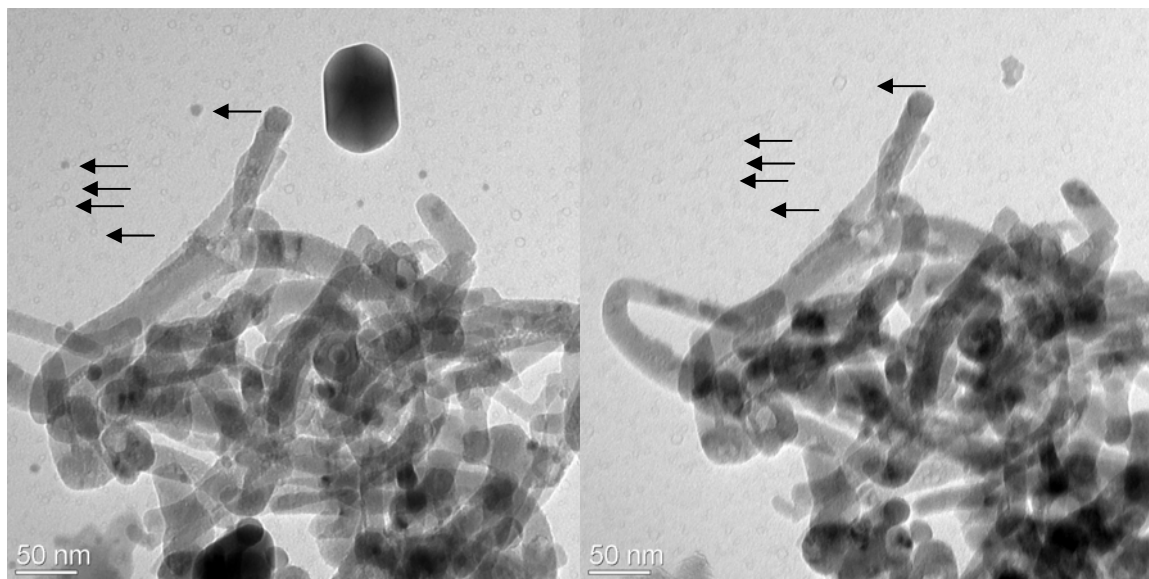
Figure 4-43: SAED of the particles grown on C-film superposed with diffraction arcs of aluminium.

The following figure shows the effect of high temperature (>500 °C) on the nanoparticles (Figure 4-44).



(A) 25 °C

(B) 500 °C



(C) 750 °C

(D) 800 °C

Figure 4-44: Bright field images of the Al/Al₂O₃ nanowires' structure at different temperatures from 25 °C to 800 °C.

The four precedent images permit to follow the evolution of the particles at high temperature. The nanoparticles evaporate at different melting points according to their diameters (smaller particles evaporate easier) and they leave a residual circular shell. The biggest particle grows till 750 °C and displays the morphology of a single

crystal; nevertheless, it reaches its melting point at 800°C and evaporates. The residual shell collapses, hence it is not circular like for smaller particles.

The residual shell is also observed on nanowires like on figure 4-45.

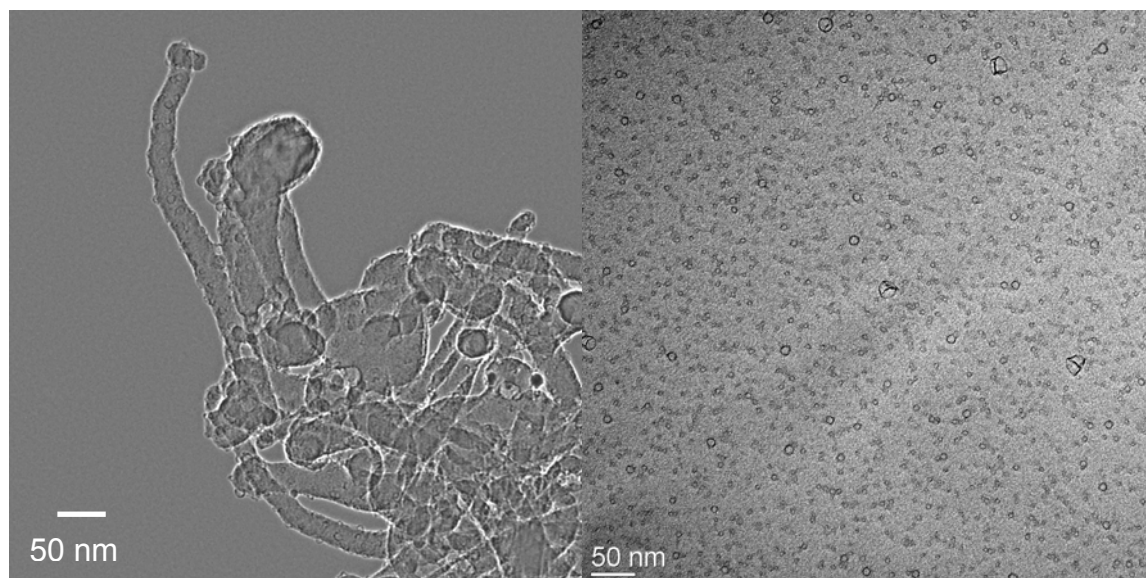


Figure 4-45: Contrast enhanced images of Al/Al₂O₃ nanowires and C-film with residual shells.

The particles grown directly on the nanowires also evaporate and leave residual shells on the nanowires. Some of the shell maintains the crystalline form of the evaporated nanoparticles.

4.6 Conclusion

The nanowires grown above 530 °C by CVD of [H₂Al(O^tBu)]₂ present a core shell structure, where single crystalline aluminium is inside the nanowire's body and head, and the shell is constituted of small aluminium oxide crystals. According to HRTEM and SAED, the most probable crystalline phases are γ -Al₂O₃ and δ -Al₂O₃ but other Al₂O₃ (θ , hexagonal, ϵ) are also discussed in chapter 4.3.

Generally a catalyst or a template is necessary to obtain one dimensional growth but in our case aluminium particles probably play the role of the catalyst (self catalyst growth). Various nanowire types are observed, for example sometime 2 or 3 nanowires are attached to one head. It is also possible to create nanowires covered by nanoparticles (1 nm).

Transmission electron microscopy turned out to be the appropriate tool to analyse the inner structure of such a small structure, although some transformations can occur on the nanowires during analysis due to intensive irradiation and/or heating.

Submitted to intensive irradiation, the shell shrinks, nanoparticles (5 nm) are formed at the surface (probably γ -Al₂O₃) and the aluminium core grows: oxygen probably escapes from the shell and the residual aluminium migrates to the core. This phenomenon is reversible.

When the temperature increases, aluminium particles are formed, at first on the nanowires surface but then on the sample holder. The diameter increases with increasing temperature till 500°C, where the aluminium particles begin to evaporate and leave a residual Al₂O₃ shell.

5 CVD with $[\text{H}_2\text{Ga}(\text{O}^t\text{Bu})]_2$ as precursor

5.1 Gallium oxide layers

Gallium oxide (Ga_2O_3) has attracted interest as a promising material for applications in gas sensing^{89, 90}, for its electrical⁹¹, electroluminescence⁹², as well as optical properties⁹³. The Ga_2O_3 thin films have been produced by various synthetic methods such as evaporation⁹⁴, sol–gel process⁹⁵, sputtering^{96, 88}, plasma enhanced atomic layer epitaxy, and metal organic chemical vapor deposition (MOCVD)^{97, 98}. The MOCVD method has the advantage of producing uniform, pure, reproducible, adherent films with good step coverage. Various precursors like trimethyl-gallium (GaCH_3)⁹⁹, gallium tris-hexafluoroacetylacetonate ($\text{Ga}(\text{hfac})_3$)¹⁰⁰, fluoroalkoxide complexe $\text{Ga}[\text{OCH}(\text{CF}_3)_2]_3$ ¹⁰¹, and $[\text{Ga}(\mu\text{-O-t-Bu})(\text{O-t-Bu})_2]_2$ ¹⁰² with an additional gas flow (mostly O_2) have been developed. However, the formation of GaF_3 was observed in the mass spectrum of $[\text{Ga}(\text{hfac})_3]$ and the presence of fluorine in Ga_2O_3 films could induce problems for gas sensor applications— due to changes in baseline resistance and sensor drift. Thus, there is a real need for new Ga_2O_3 CVD precursors. The use of a single source precursor, like gallium acetylacetonate¹⁰³ or gallium isopropoxide⁹⁶ provides the advantage of controlling the gallium/oxygen ratio and film purity while the synthesis process is simplified due to one step fabrication. Veith et al. developed many molecular single source precursors for MOCVD to fabricate new nanomaterials^{35,36}. Among them, $[\text{H}_2\text{Al}(\text{O}^t\text{Bu})]_2$ turned out to be an efficient precursor, as seen in the preceding chapter, for the creation of thin nanocomposite films with various morphologies^{20, 28}. By analogy, $[\text{H}_2\text{Ga}(\text{O}^t\text{Bu})]_2$ seems a promising precursor to develop divers $\text{Ga}/\text{Ga}_2\text{O}_3$ nanocomposite layers. Amorphous gallium oxide layers are generally obtained by CVD at 470°C till 650°C depending on precursor and pressure¹⁰⁴. Annealing at higher temperature (about

1000°C) is generally necessary to obtain monoclinic β - Ga_2O_3 which is the most current crystalline gallium oxide^{105, 106, 107}. Silicon substrates are generally used to fabricate Ga_2O_3 thin films. 1D nanostructures like nanowires or nanobelts are easily obtained by CVD, even without catalyst^{108, 109}. The use of a catalyst by VLS mechanism is nevertheless preferable when crystalline or well aligned nanowires are desired¹¹⁰. For metallic gallium the most useful morphology are droplets or mongolfieres¹¹¹. Therefore, Ga_2O_3 exists in form of one 2 or 3 dimensional nanostructures. Moreover, unconventional nanostructures of Ga or Ga_2O_3 including zigzag nanowires as well as 3D nanostructures, have been reported^{112, 113, 114}. In this chapter the deposition conditions, like substrate temperature, molecular flow and deposition time will be varied. From the literature it is known that silicon is an appropriated substrate to grow gallium oxide films and that annealing helps getting crystalline films. Therefore we will also investigate the effects of substrate on layer growth and the effect of annealing on the crystallinity. The objective of this chapter is to give an overview about the versatility of the layers which can selectively be grown by choosing appropriate growth conditions. It is nevertheless not possible in the present work to investigate all possibilities: only some representative examples will be shown. The layers will be grown on copper, stainless steel and silicon and some illustrative examples will be shown on annealed layers. We will concentrate on the morphology and crystal structure of the layers, as further investigation methods like TEM or ESCA were not available.

5.2 Morphology and composition of the layers obtained by CVD of $[H_2Ga(O^tBu)]_2$

5.2.1 On stainless steel

First of all the layers grown on stainless steel from 400° C to 630° C were investigated. Figure 5-1 shows the morphology of the layer grown on stainless steel at low temperatures (400° C).

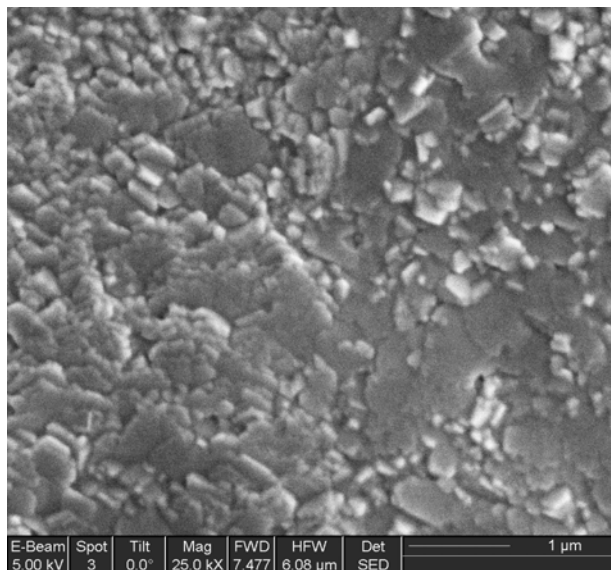


Figure 5-1: SEM image of the Ga/Ga₂O₃ layer grown at 400 °C.

400° C is too low to become a proper layer, no nanostructure is observed. Figure 5-2 shows the layer grown at 500° C.

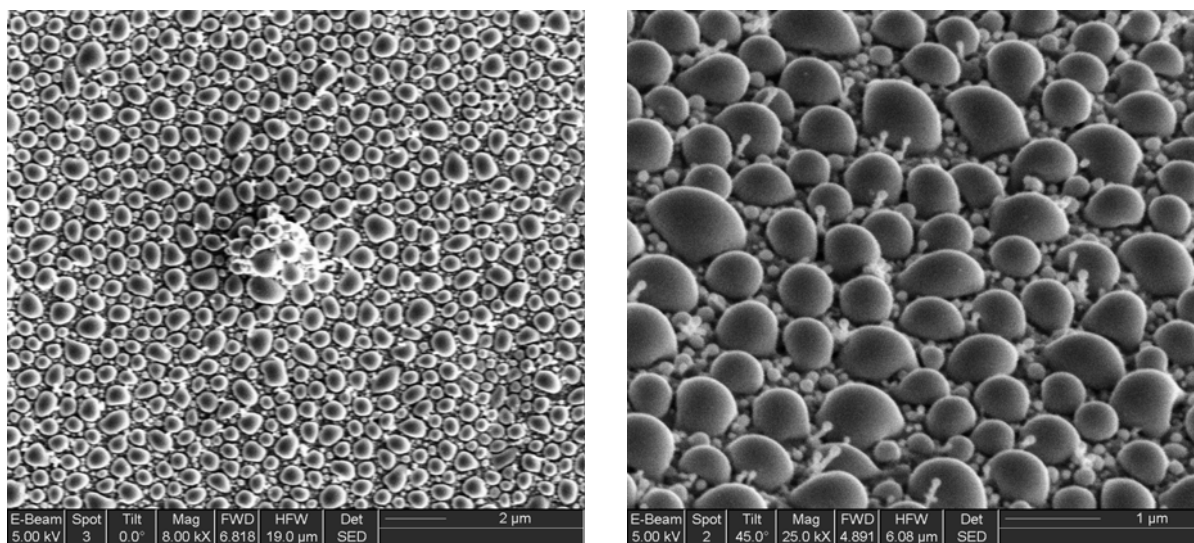


Figure 5-2: SEM images of the gallium droplets grown at 500 °C.

At 500° C gallium droplets are formed on the stainless steel surface. According to EDX, the oxygen content is negligible compared to gallium. Between the droplets, 1D nanostructures can be distinguished, they are constituted of a nanowire with approximately 50 nm diameter and 1 μm length and a head on the top of the nanowire. The head is a spherical particle with nearly 120 nm diameter.

As the gallium droplets do not show any diffraction pattern and as their shape is montgolfier-like, they are high probably liquid. Another indication for the liquid state is that the droplets are able to flow after one month aging (figure 5-3).

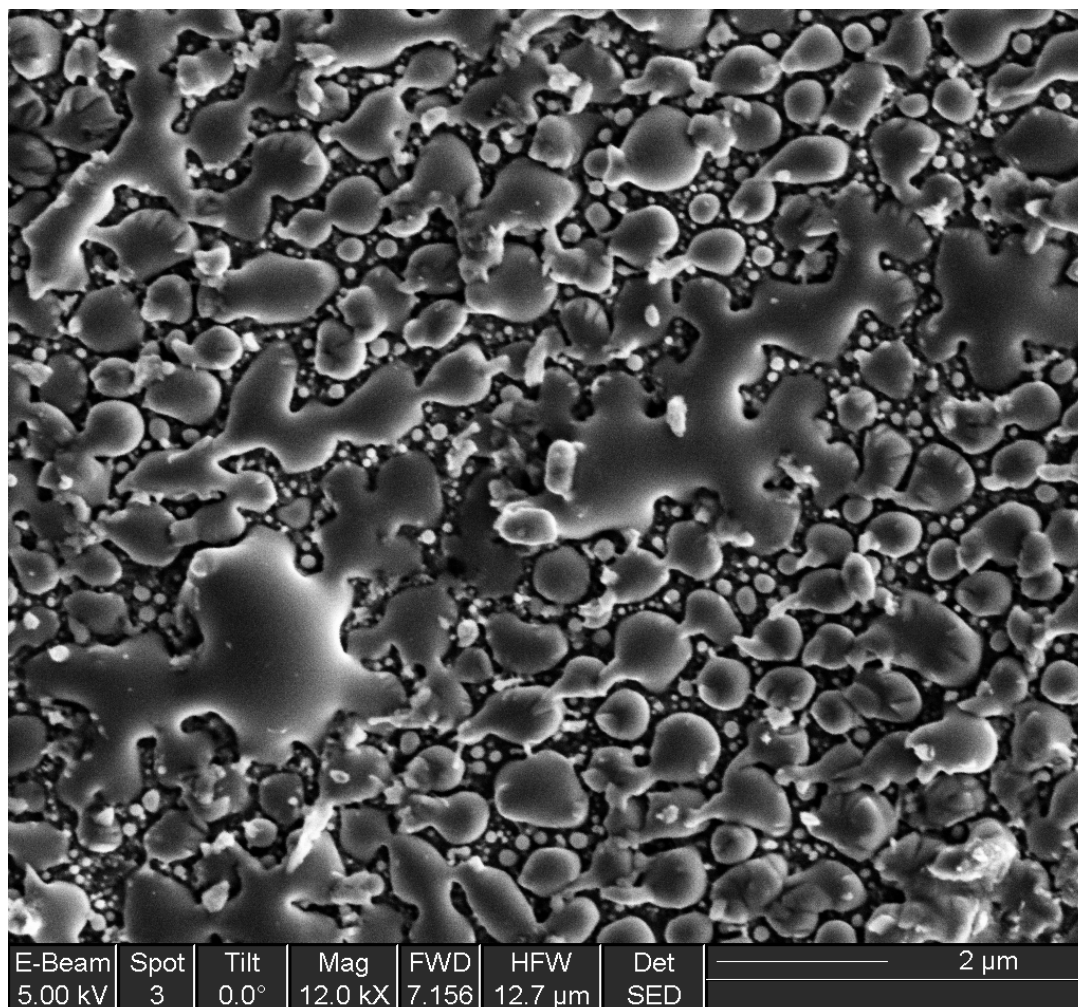


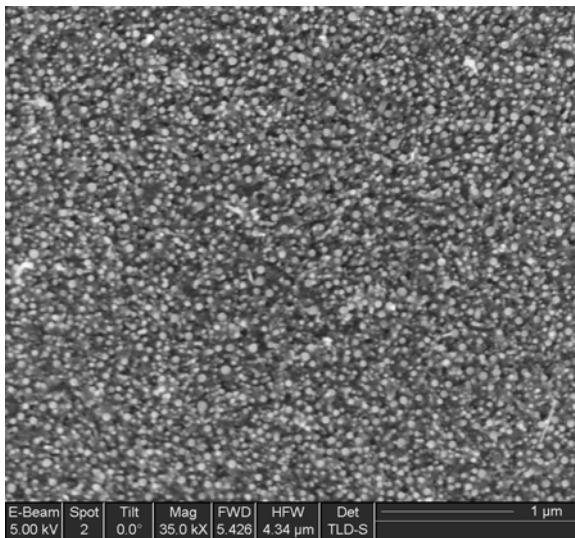
Figure 5-3: SEM image of the gallium droplets grown on stainless steel at 500 °C (shown in Figure 5-2) after 30 days aging. Gallium droplets have flowed.

The behaviour of the gallium droplet (flowing) after aging is typical of liquid phases or phases with low viscosity. The gallium droplets are probably covered by a thin Ga_2O_3 layer; this would explain the solid aspect of the layers after deposition.

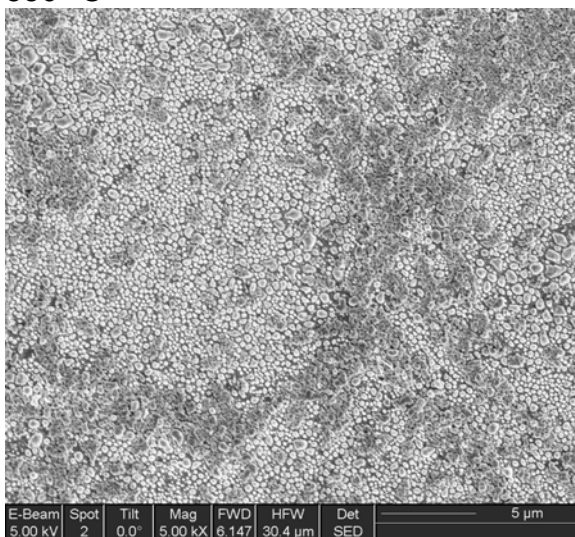
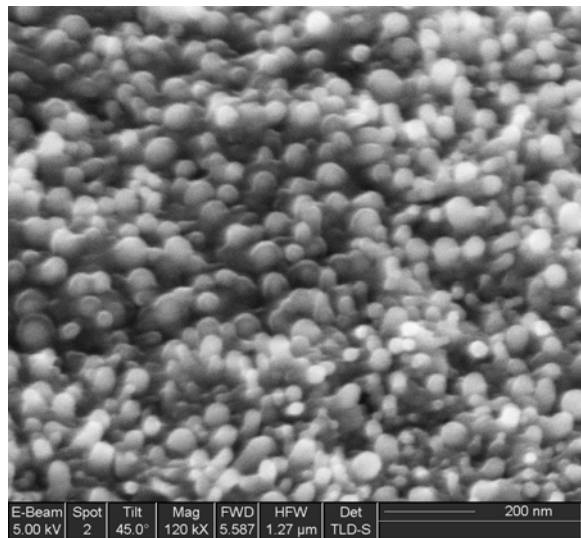
XRD detects wide peaks which correspond to small crystals of iron gallium oxide formed at the interface between the gallium droplets and the target surface.

Gallium droplets have already been fabricated intentionally or accidentally on a surface^{112, 113}. Gallium droplets obtained by MOCVD of $GaCH_3$ by Imhoff presented a montgolfier shape, which is similar to the morphology shown on figure 5-1. In the previous case, the montgolfier base served as nucleation point on the surface,

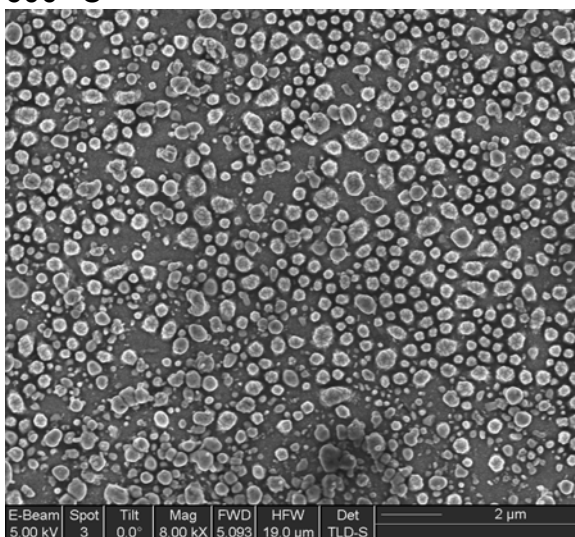
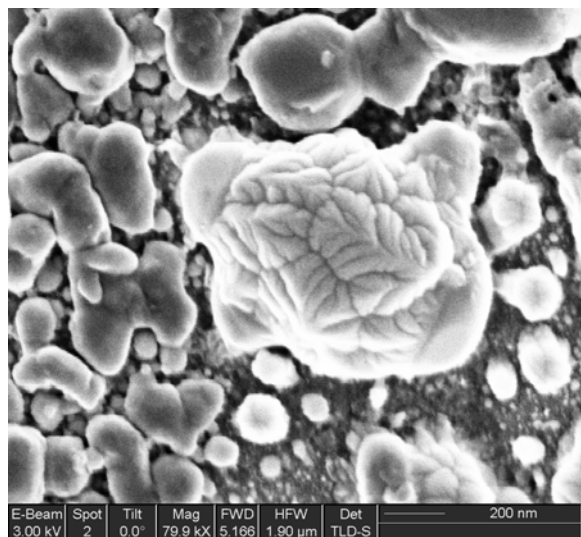
whereas we observe good wettability of our droplets on the substrate surface. Another main difference to the montgolfier shape droplets is the absence of carbon in our case, whereas Imhoff could detect a significant carbon fraction by XPS. Like Imhoff, we have probably to deal with a liquid gallium droplet, whose shape is stabilised by a thin gallium oxide layer. The carbon in their case comes from the GaCH_3 precursor. Increasing the temperature to 550°C and 600°C allows further formation of gallium droplets (Figure 5-4). Some droplets are faceted on their surface when increasing the temperature to 600°C . In general, the droplets size decreases with the target temperature from 500 nm at 500°C to less than 100 nm at 550°C or 600°C .



550 ° C



600 ° C



630 ° C

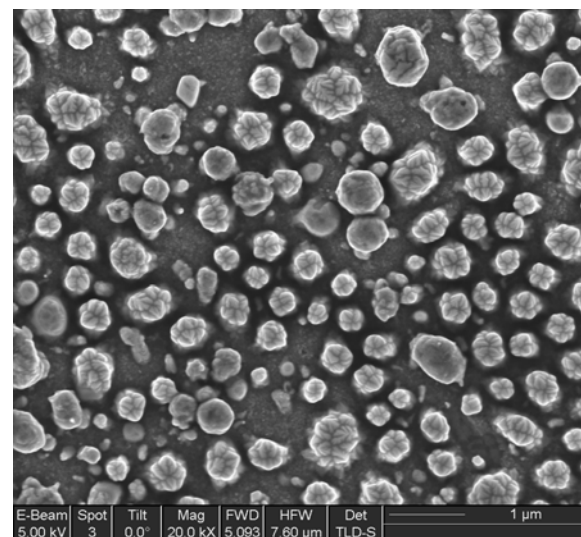


Figure 5-4: SEM images of Ga/Ga₂O₃ layers grown at 550 °C, 600 °C and 630 °C.

By increasing the substrate temperature (630 °C) nanoparticles with faceted surface containing oxygen, gallium and a large amount of carbon are obtained (Figure 5-4), they are in the same size range as the gallium droplets, no 1D nanostructures are present and the films are relatively uniform.

The pattern from the substrate is visible on the XRD of all layers, i.e. iron nickel [PDF 47-1417 or PDF 37-474] and/or iron [PDF 6-696] peaks. Independently from the deposition temperature, nickel iron gallium oxide [PDF 82-465] and gallium nickel [PDF 43-1376] are detected by XRD; therefore the stainless steel substrate has reacted during deposition. Figure 5-5 shows the XRD of a layer grown on stainless steel at 600 °C, where some undesired crystals due to reaction with the substrate are seen [NiFeGaO₄ PDF 82-465] near the gallium oxide peaks [PDF 74-1776]. At 550° C and 600° C, gallium iron carbide is present, but not crystalline. For the aluminium precursor it has already been noticed that by increasing the temperature aluminium carbide pattern could be detected³¹. In the case of gallium, the amount of carbon is much bigger as EDX can detect a large peak due to the presence of carbon in the layer (Figure 5-5). Even by mapping the surface with EDX, it remains impossible to localise the carbide.

By increasing the precursor flow, we hope to change molecule transport phenomenon to the surface and therefore avoid the reactions between substrate and layer and/or carbide formation. The precedent experiment was repeated with the precursor left at room temperature instead of 0° C.

Figure 5-6 shows an overview on the obtained layer as well as some magnifications on interesting areas.

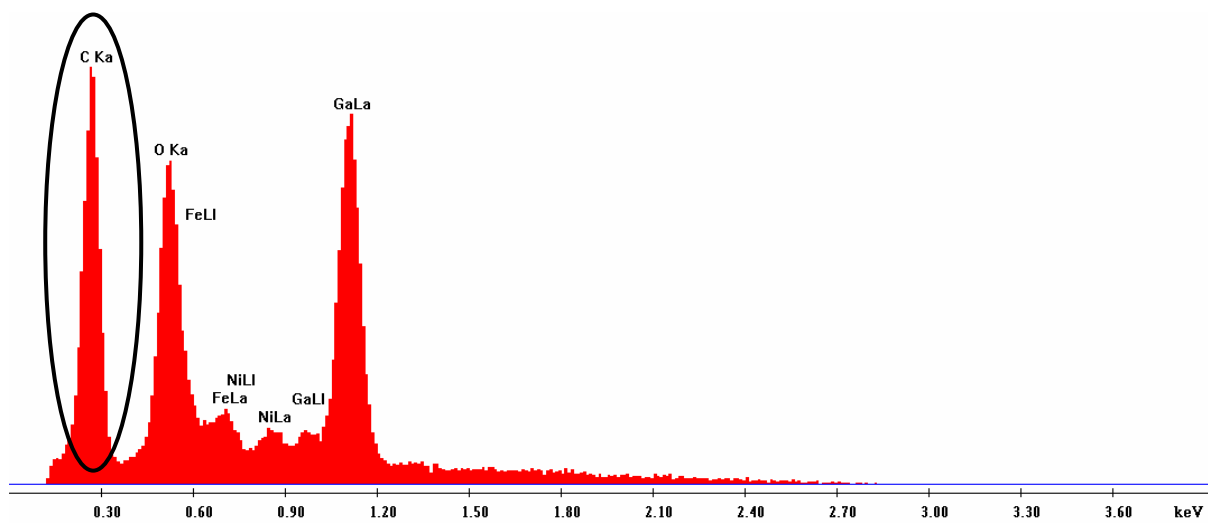
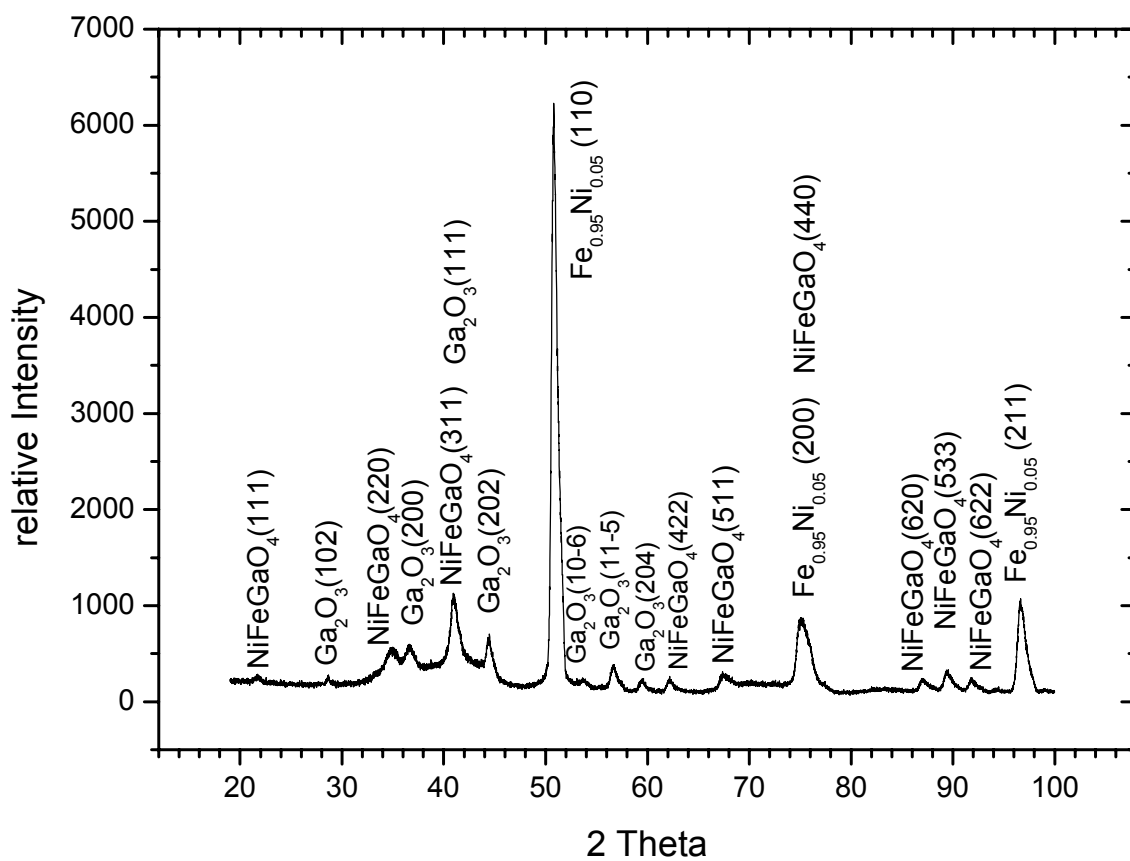


Figure 5-5: XRD and EDX analysis of a Ga/Ga₂O₃ layer grown at 600 °C.

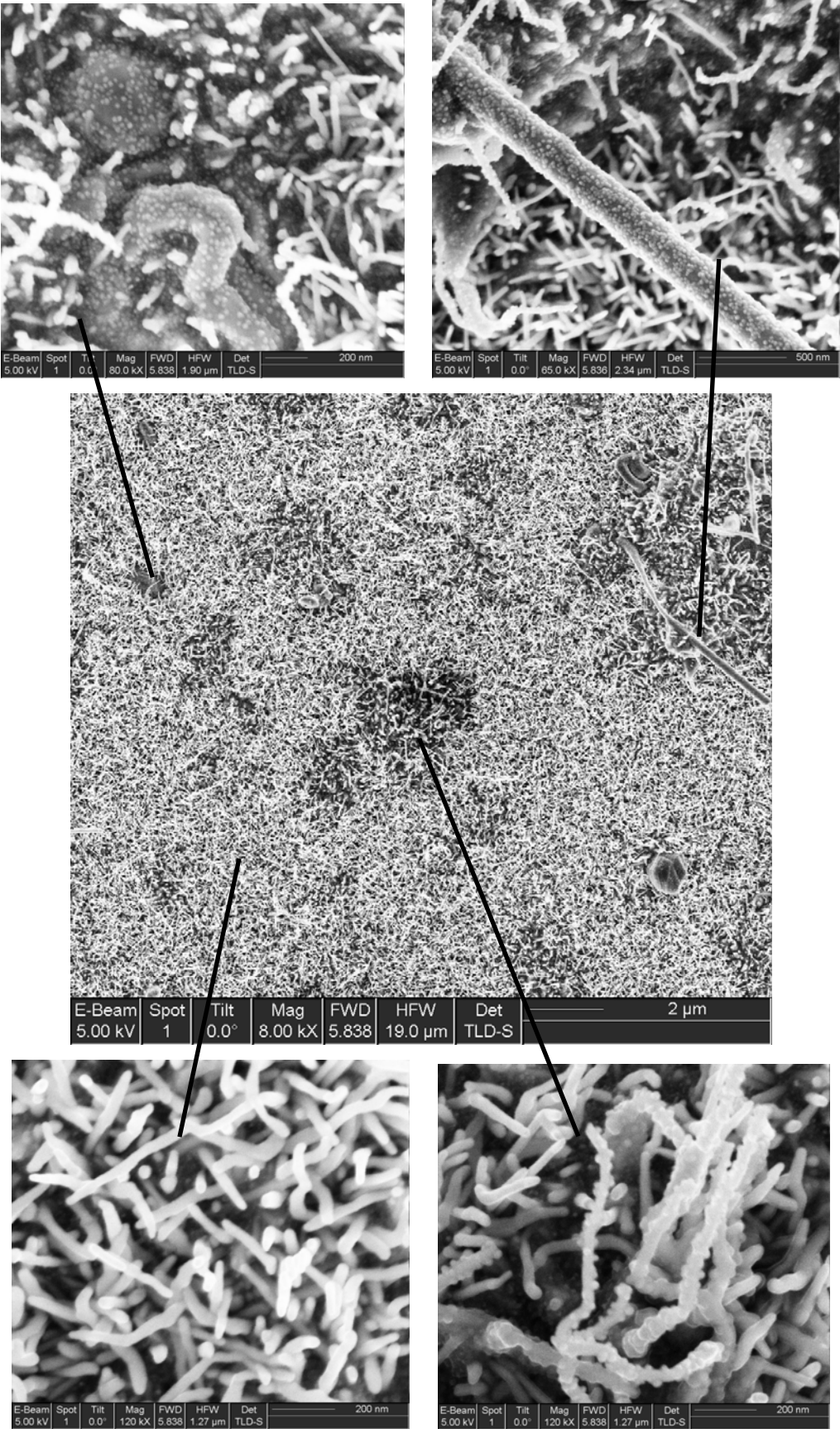


Figure 5-6: SEM images of an inhomogeneous Ga/Ga₂O₃ layer grown on stainless steel at 600 °C at high precursor flow and magnification on different areas.

When the precursor is not cooled, the surface loses its homogeneity and small nanowires, nanoalgae and big nanowires are formed on one layer. The main part of the film is nanowires area; they are 50 nm big and less than one μm long. The darker parts on figure 5-6 are nanoalgae (below right), they have the same shape as the nanowires but they are longer (several microns) and some nanoparticles (app. 15 nm) are growing on their surfaces. Bigger structures are formed like wires with diameters in the range of several hundreds of nanometres (above right); on these structures nanoparticles are also observed. We can conclude that many nanostructures are probable on stainless steel; it remains nevertheless indispensable to control precursor flow for a selective deposition. TEM investigation would be ideal to analyse selectively the composition and inner structure of each nanostructure, the microscope was unfortunately not available for this study.

5.2.2 On copper

Copper was used as substrate while the temperature was varied from 200° C to 630° C.

At very low temperature (200° C) no proper layer was obtained (Figure 5-7).

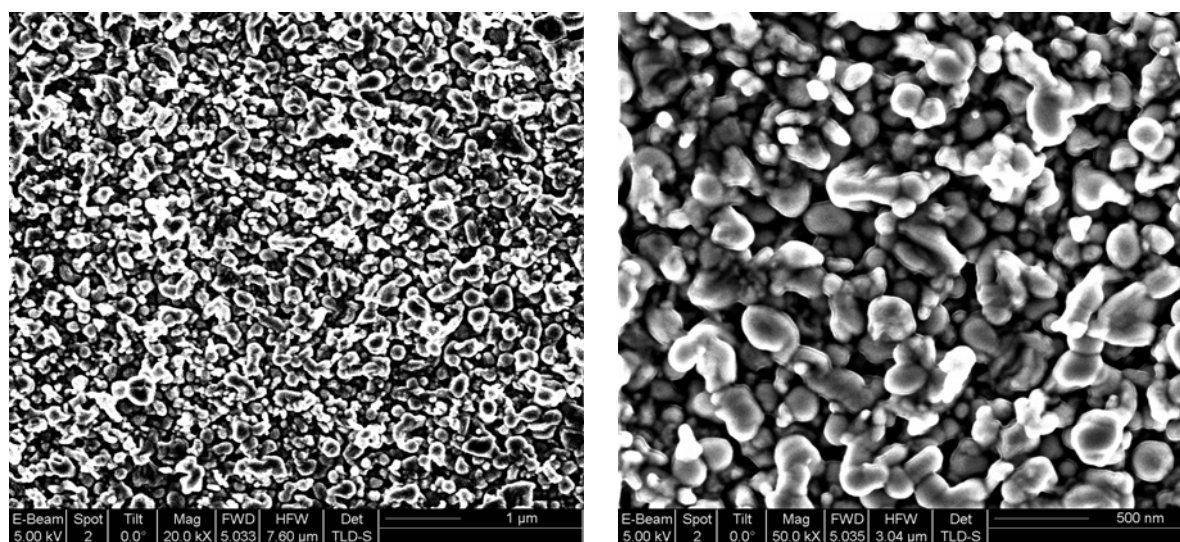


Figure 5-7: SEM images of a layer grown on copper at 200 °C by CVD of $[H_2Ga(O^tBu)]_2$.

An interesting structure begins to form at 300 °C (Figure 5-8).

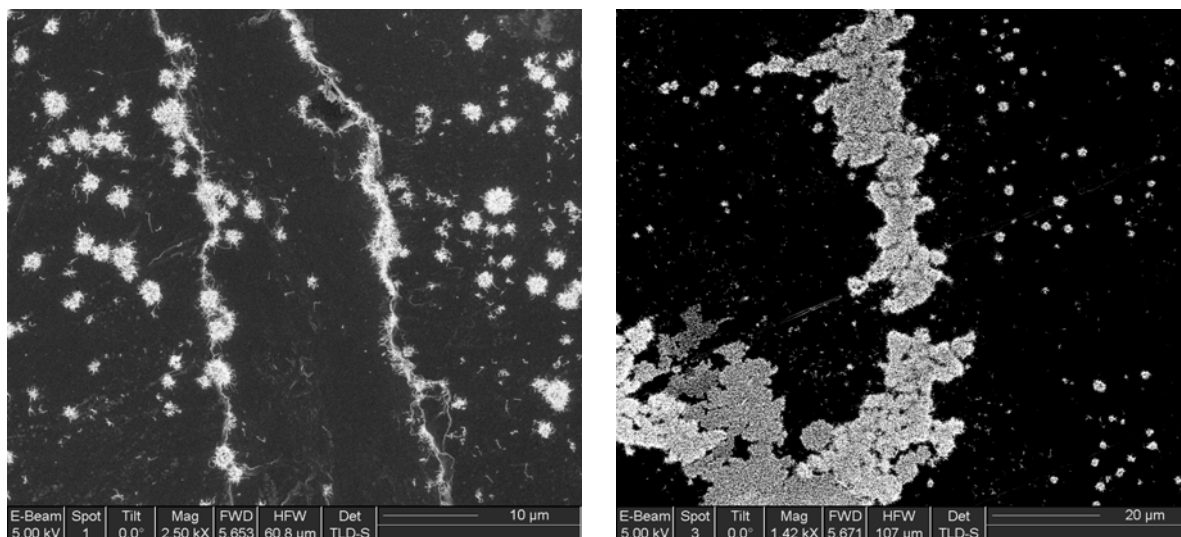


Figure 5-8: SEM images of a Ga/Ga₂O₃ layer grown on copper at 300 °C.

Figure 5-8 left shows that the layer grows on privileged areas on the surface. Two growth lines and several spherical islands can clearly be seen. The privileged areas may be inhomogeneity from the substrate, like segregation for example. Other areas (right) are densely covered; it is an assemblage of many islands near to one another. Figure 5-9 shows enlargements on the densely covered area, on the islands and on single structures.

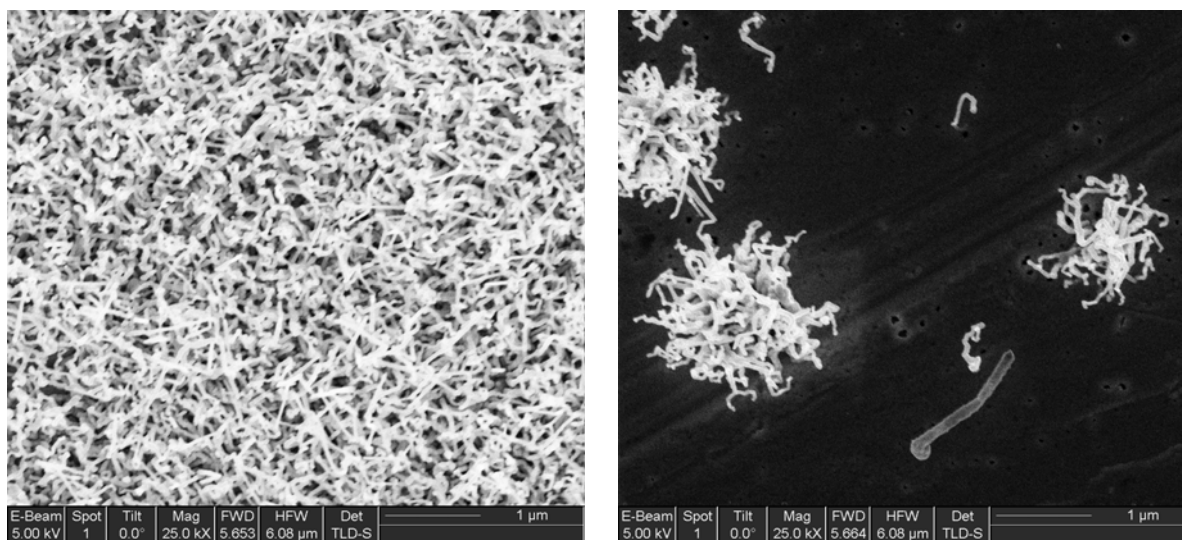


Figure 5-9: Magnification on the layer shown on figure 5-8, shows islands with nanowires.

Nanowires are formed exclusively on the surface, but the surface coverage is inhomogeneous. They grow preferentially on the surface defects and can form islands with about 2 μm diameter. As single nanowires grow as well on the surface, it

is then probable that a single nanowire grows first and that other nanowires use the same defect as seeding point. Therefore a regular flower like structure is obtained. The dense areas are a very regular assembly of nanowires with homogenous diameters and lengths. In comparison to the $\text{Al}/\text{Al}_2\text{O}_3$ nanowires, they are not entangled but straight. Figure 5-10 shows an XRD pattern of the layer.

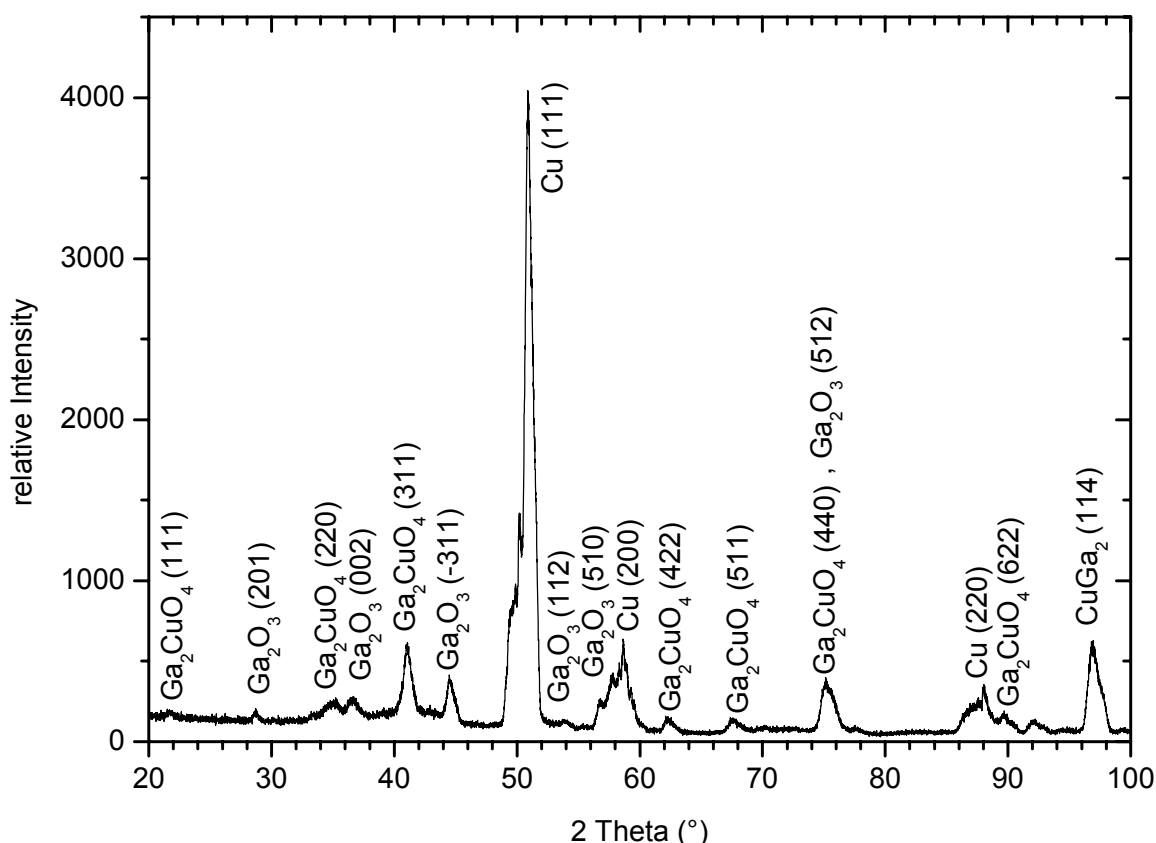
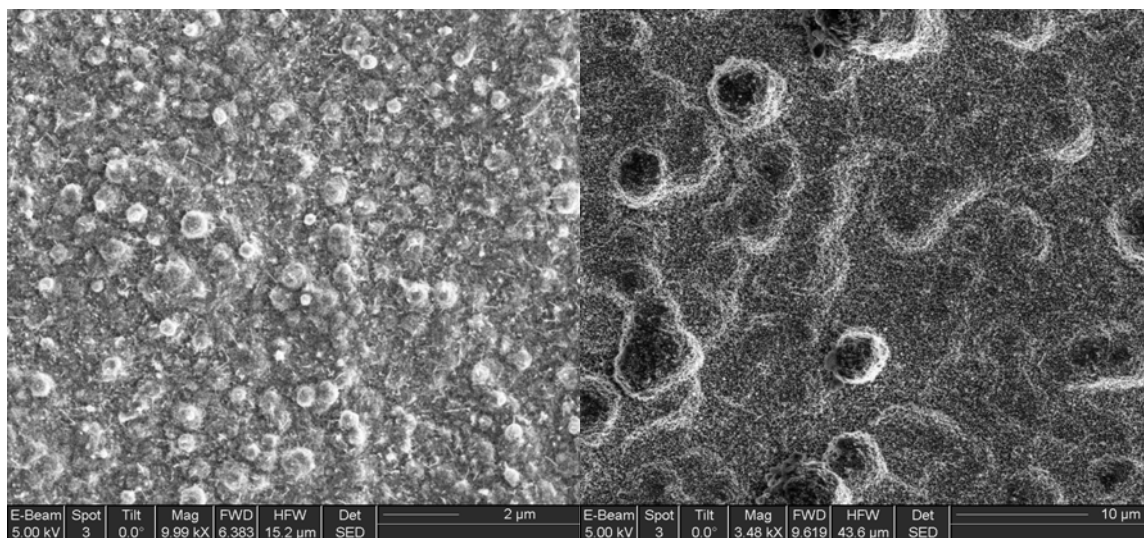


Figure 5-10: XRD pattern of a $\text{Ga}/\text{Ga}_2\text{O}_3$ layer grown on copper at 300 °C

No gallium is detectable by XRD but the substrate has reacted to form several oxides or metallic alloys (Ga_2O_3 PDF 76-573, Ga_2CuO_4 PDF 78-172, and CuGa_2 PDF 25-275) as seen on Figure 5-10. Other oxides can also be considered like Cu_9Ga_4 (PDF 71-458) or Ga_2CuO_4 (PDF 76-2297) and CuGaO_2 (PDF 41-255). The gallium precursor probably facilitates crystallisation of oxides on the surface.

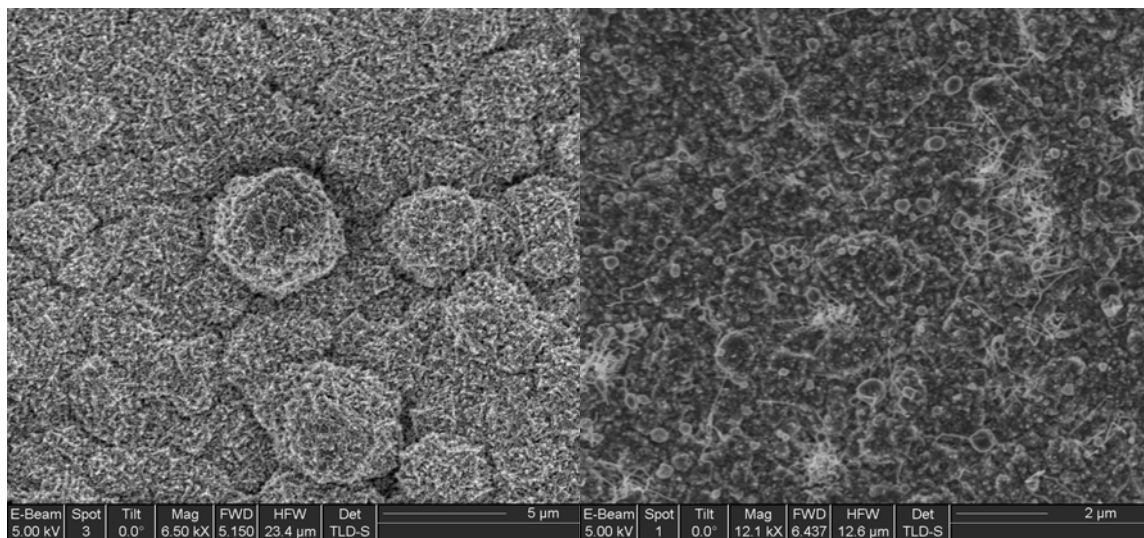
At 500° C, many attempts have been performed to grow homogeneous layers on copper. The deposition time and the precursor flow were changed to investigate the participation of each parameter in the morphological and compositional changes. The only process difference between layer a) and b) is the precursor flow. Layer c) and d) are grown in similar conditions, but the precursor used for layer d) presents less purity (monhydrid has not been totally eliminated). Layer a) and b) are grown during

one hour while c) and d) are deposited during a short time. Figure 5-11 shows an overview on the surfaces.



a-Room temperature, 1h

b-0° C, 1h

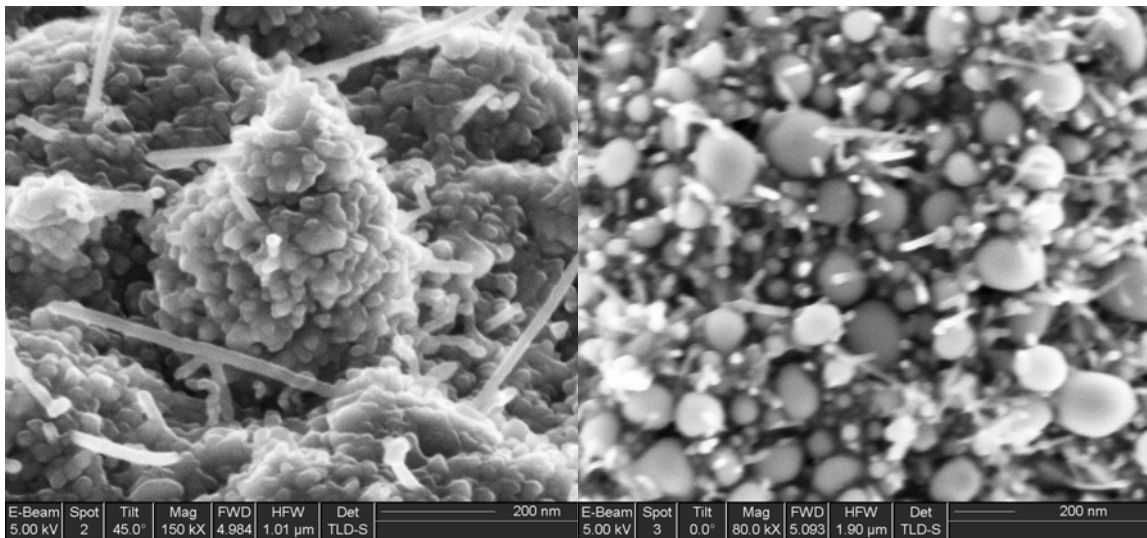


c- Room temperature 5 Min

d- Room temperature 10 min, impure precursor

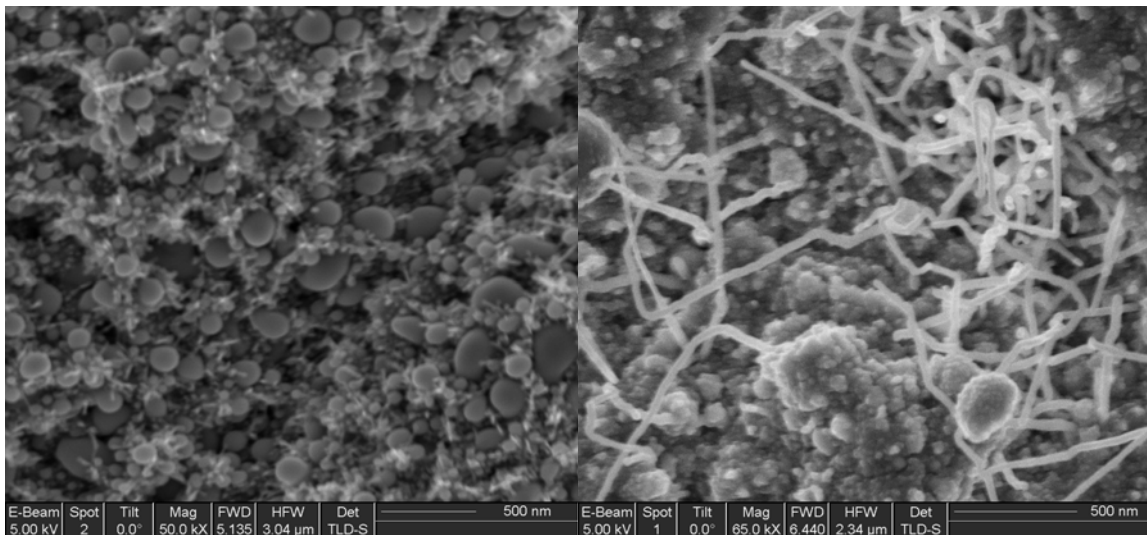
Figure 5-11: SEM images of Ga/Ga₂O₃ layers grown at 500 °C on copper at different conditions. a- Room temperature, 1h; b- 0° C, 1h; c- Room temperature 5 Min; d- Room temperature 10 min, impure precursor.

The overview shows different surface roughness. Microparticles from 1 μm to 5 μm big are seen on the surface. The microparticles seem to be nanostructured and layer d) shows some nanowires. The following images (Figure 5-12) show magnifications on the interesting area to identify the nanostructures.



a-Room temperature, 1h

b-0° C, 1h



c- Room temperature 5 Min

d-Room temperature 10 min, impure precursor

Figure 5-12: Magnification of the Ga/Ga₂O₃ layers shown on Figure 5-11.

At the nanometer scale the layers grown at 500° C on copper display enormous differences. Interestingly the only layers which display similarities are layer b) and c) although the growth conditions are very different. It is possible that the effects of growing precursor flow are compensated by reducing deposition time. These two layers are composed of gallium droplets with short one dimensional nanostructures between the droplets. Layer a) shows a nanoparticle like a blackberry with nearly 400 nm diameter, it is composed of particles with app. 30 nm diameter, some of the particles have grown into nanowires with several micrometers lengths. Layer d) also presents nanowires but the surface does not display any blackberry. Comparing layer

a) and c) permits to observe the effect of duration on the surface morphology. The gallium droplets observed after 5 minutes deposition, disappear after one hour and blackberry nanoparticles are formed. The layer grown with traces of monohydrid displays a surface with nanoparticles nearby some long nanowires.

In summary, maintaining the temperature constant, which is supposed to be the most important parameter, is not sufficient. Deposition has to run during the same time, as the nanostructure changes completely during the deposition. Changing the precursor flow also leads to different nanostructures; this effect can nevertheless be compensated by varying deposition time. The effects of process parameters are known to influence the morphology and composition of layers, but for this system the influence is enormous. Therefore no process inaccuracy is admitted to reproduce selectively the desired layers.

When the precursor is left at room temperature during a long time (3h) many structures are obtained on the surface. The following images (Figure 5-13) show the morphology on different regions of the layer grown 3 hours with a high precursor flow on cooper (chamber pressure is $3 \cdot 10^{-1}$ mbar).

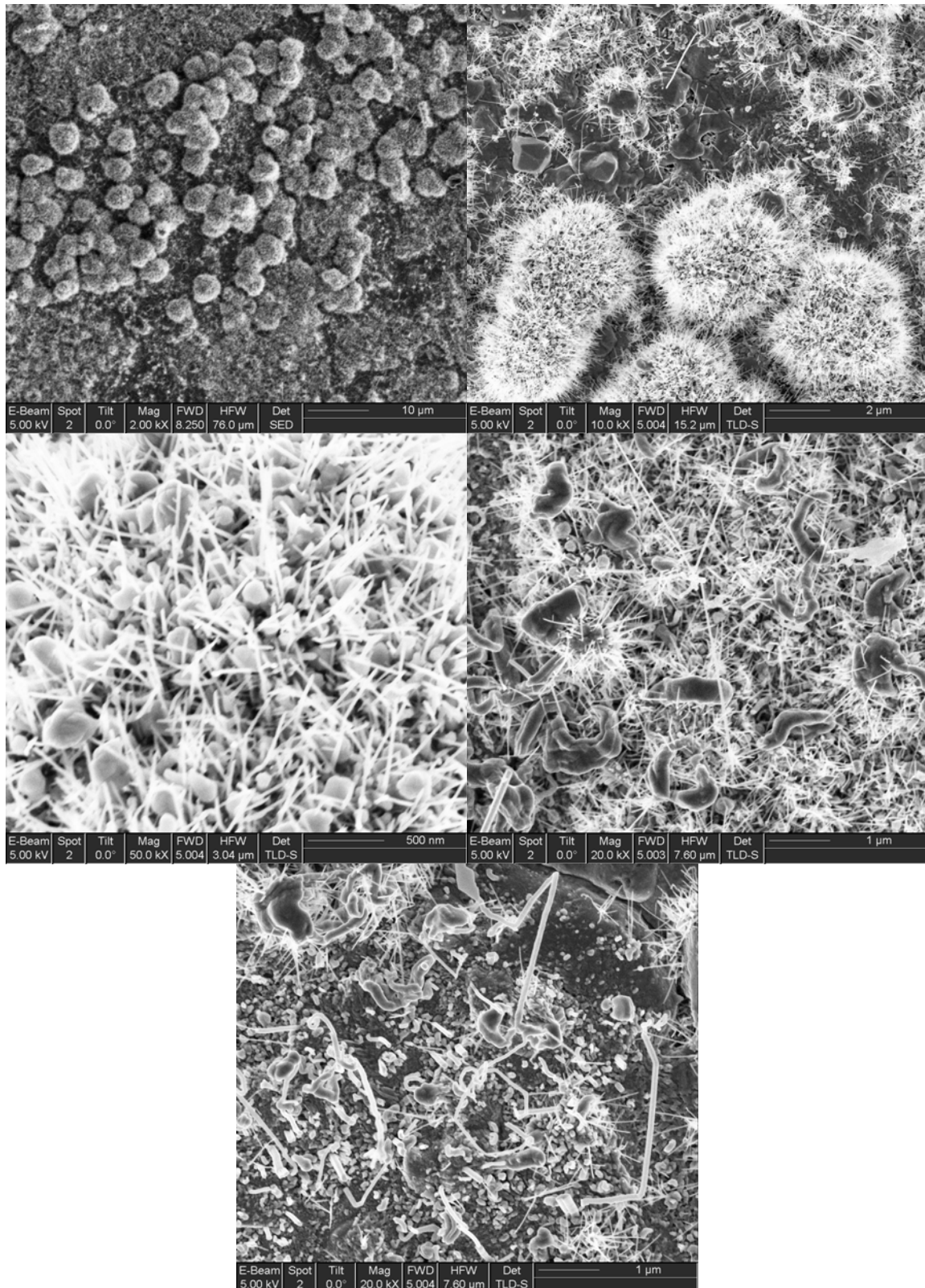


Figure 5-13: SEM images of different areas of an inhomogeneous Ga/Ga₂O₃ layer grown at 500 °C, 3 hours on copper with high precursor flow

The following SEM images (Figure 5-14) show enlargements on some interesting morphologies obtained.

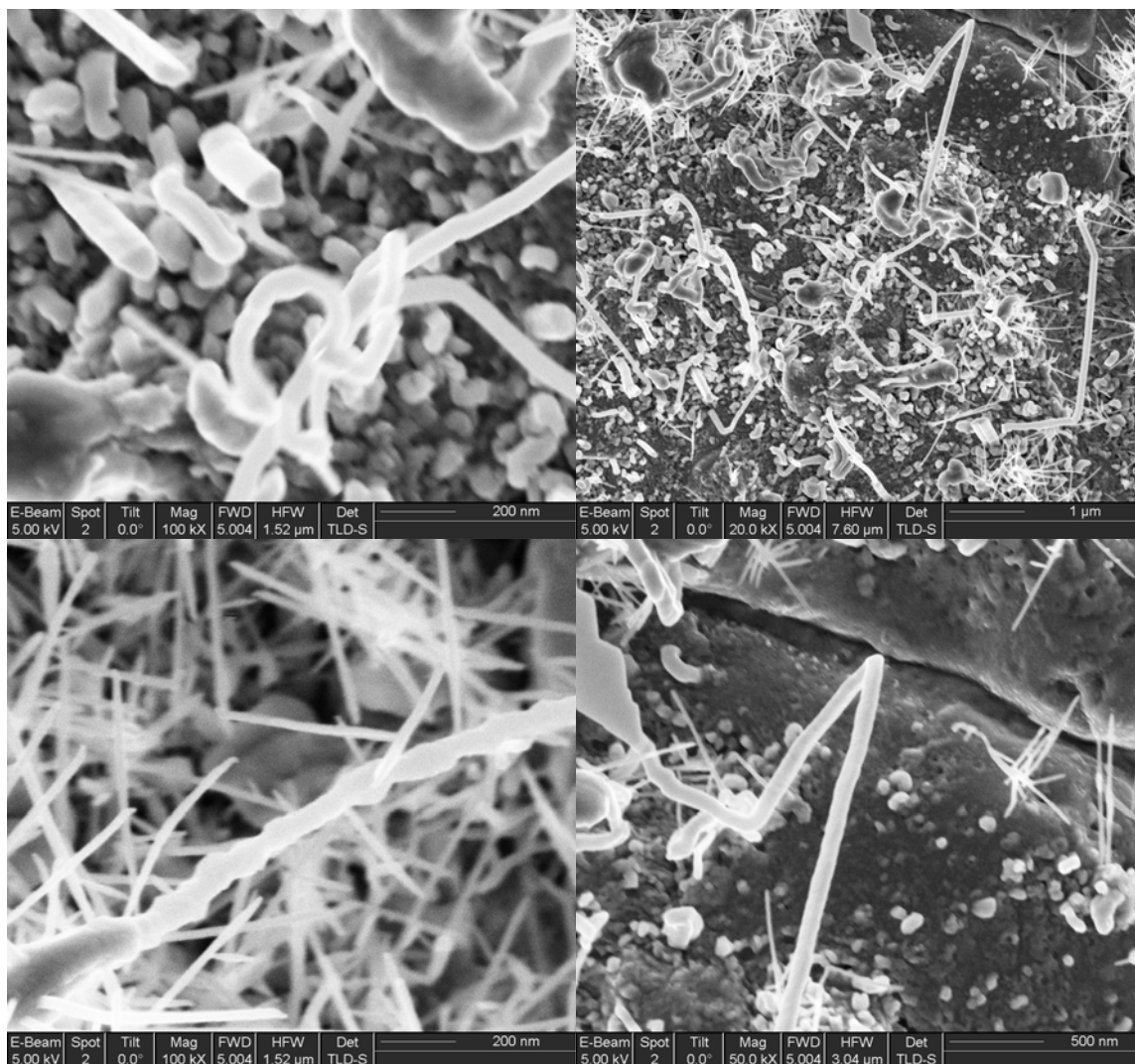


Figure 5-14: SEM images of areas with interesting morphologies from the Ga/Ga₂O₃ layer shown in figure 5-13.

Gallium oxide grows easily in one dimension without using a catalyst. The one dimension growth presents a lot of defects. Figure 5-14 below right shows a zigzag growth; such growth has already been noticed for gallium oxide nanowires¹¹⁴. The nanowires can grow straight away along several microns. Their must be a crystalline plane to direct the wire growth, such growth direction can only be measured with TEM. Another indication to show that some wires must be crystalline is the change in the growth direction (Figure 5-14 below right), which can only be attributed to a crystalline defect.

By changing the substrate from steel to copper, the drawbacks like lack of homogeneity at high precursor flow and contamination due to substrate reaction could not have been avoided. On metals, many different nanostructures have selectively been obtained; the versatility of the grown structures is probably related to the multiple undesired phases obtained on the layer and its interface like for example, iron nickel [PDF 47-1417 and PDF 37-474], iron gallium oxide [PDF 74-2228], nickel iron gallium oxide [PDF 82-465], gallium nickel [43-1376] copper gallium oxide [PDF 44-183 and 77 2495].

5.2.3 On Si (100)

The lack of uniformity in the films grown with high precursor flow (chamber pressure is $3 \cdot 10^{-2}$ mbar) does not permit to get a good reproducibility; therefore further investigations will occur with films grown with cooled precursor. XRD investigations are difficult due to the strong interaction between film and substrate; Si(100) does generally not react with gallium oxide films, that is why Si (100) could be more adequate for further studies.

Figure 5-15 shows SEM images of nanorods grown at 500 °C on Si (100). It is obvious that the nanorods grow perpendicularly to the surface; they self organise along parallel lines, which must be related to the structured Si(100) substrate.

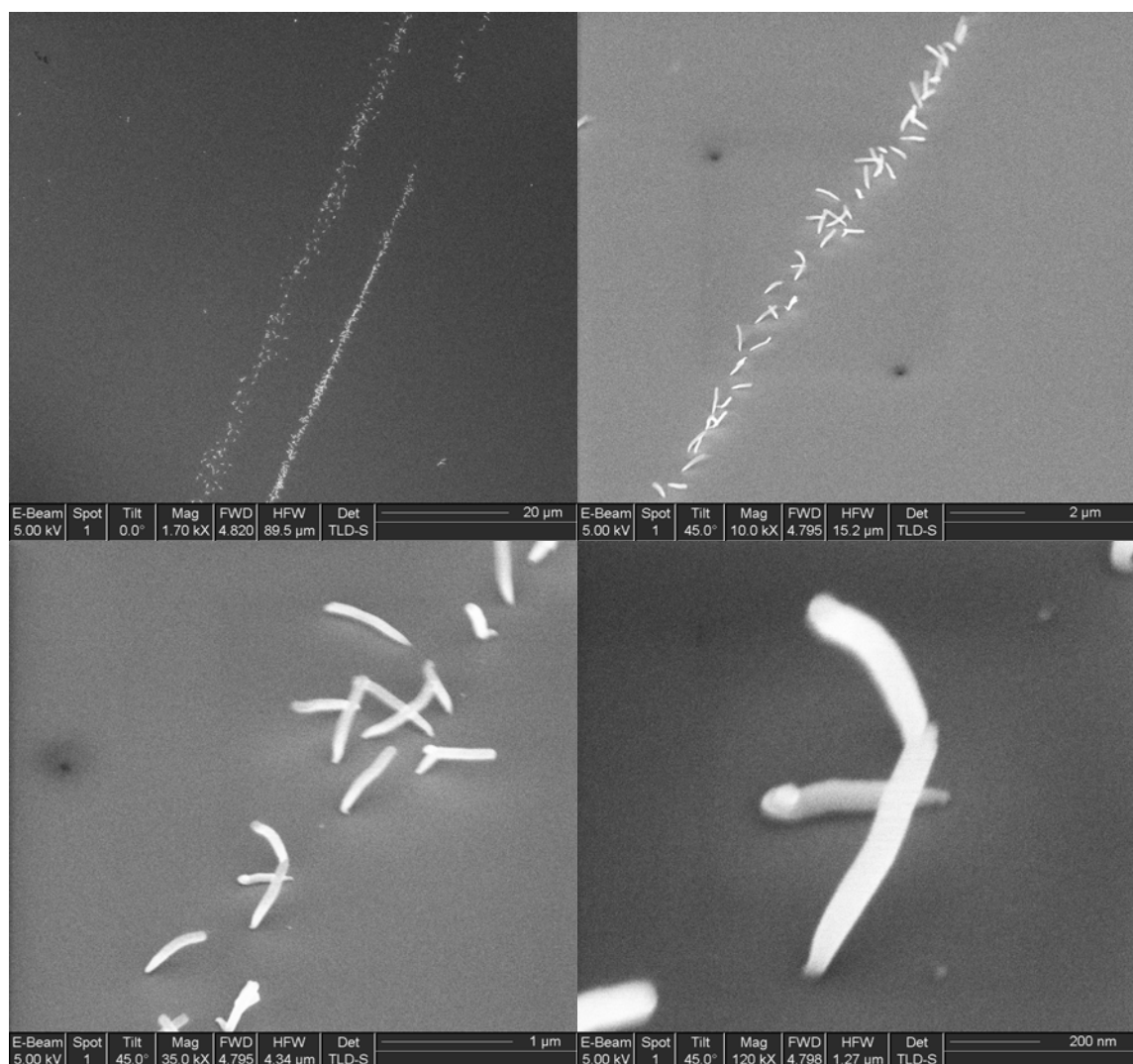


Figure 5-15: SEM images of Ga/Ga₂O₃ nanowires grown on Si (100) at 500 °C.

The nanorods are less than 1 μm long and the diameter is app. 70 nm. They are all in the same size range. Increasing the temperature to 550 °C permits to increase the surface coverage but does not influence the morphology; the same kind of nanorods is obtained (Figure 5-16).

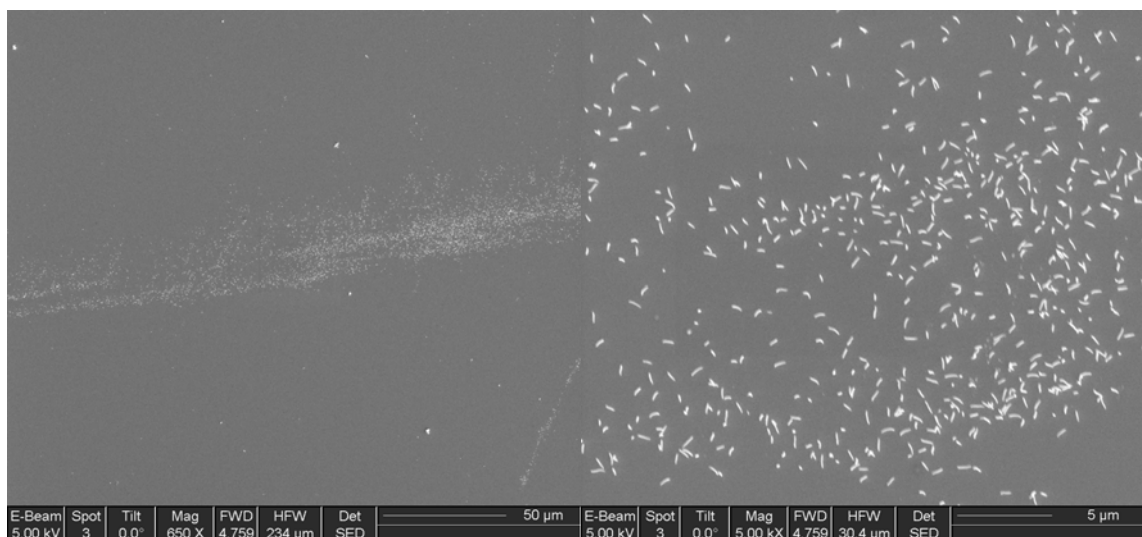


Figure 5-16: SEM images of Ga/Ga₂O₃ nanowires grown on Si (100) at 550 °C.

EDX measurements show gallium and oxygen as main elements as well as carbon traces in the nanorods (Figure 5-17); nevertheless no Ga₂O₃ is detected by XRD. Therefore the nanorods must be amorphous or the material amount on the substrate is too weak to be properly detected. It is not clear either the carbon detected by EDX comes from air contamination or from the precursor.

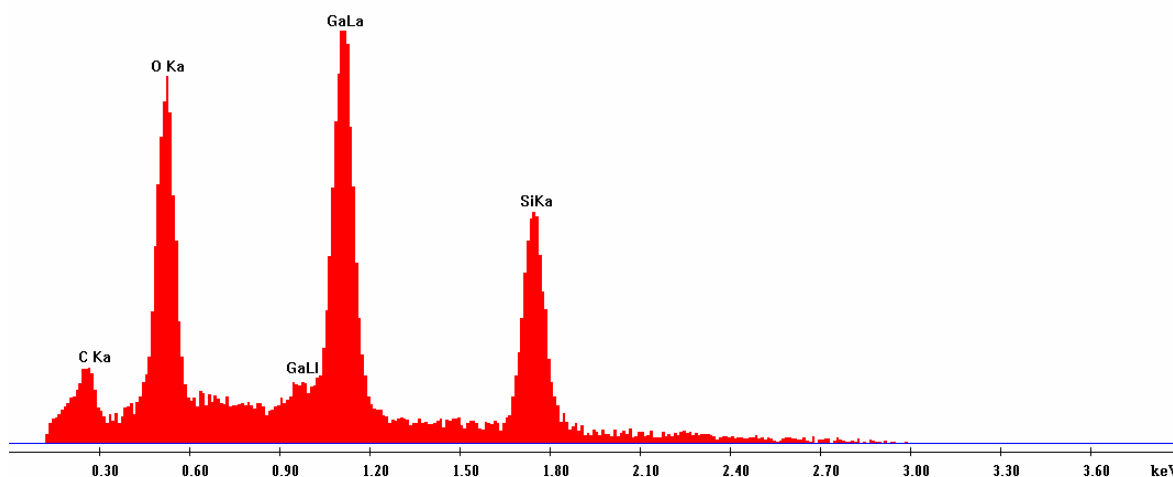


Figure 5-17: EDX analysis of the Ga/Ga₂O₃ nanowires grown on Si (100).

Recently, β -Ga₂O₃ nanowires have been synthesized by an arc-discharge method^{115,116} by physical evaporation via the vapor-solid process^{93,114} or by CVD using VLS growth mechanism¹¹⁰. Catalyst free MOCVD with single or multiple source precursors have already been used to form Ga₂O₃ thin films on Si (100) substrate but

in this case, a smooth film without nanostructure was obtained^{96, 104}. To our knowledge no one dimension growth has been observed by catalyst free single source precursor MOCVD. Moreover, the nanowires obtained by divers methods on Si (100) are usually randomly distributed onto the surface and not self organised.

Figure 5-18 shows SEM images of 3D cauliflower like structure. They are formed on Si (100) by increasing the deposition temperature to 600 °C, deposition time is one hour.

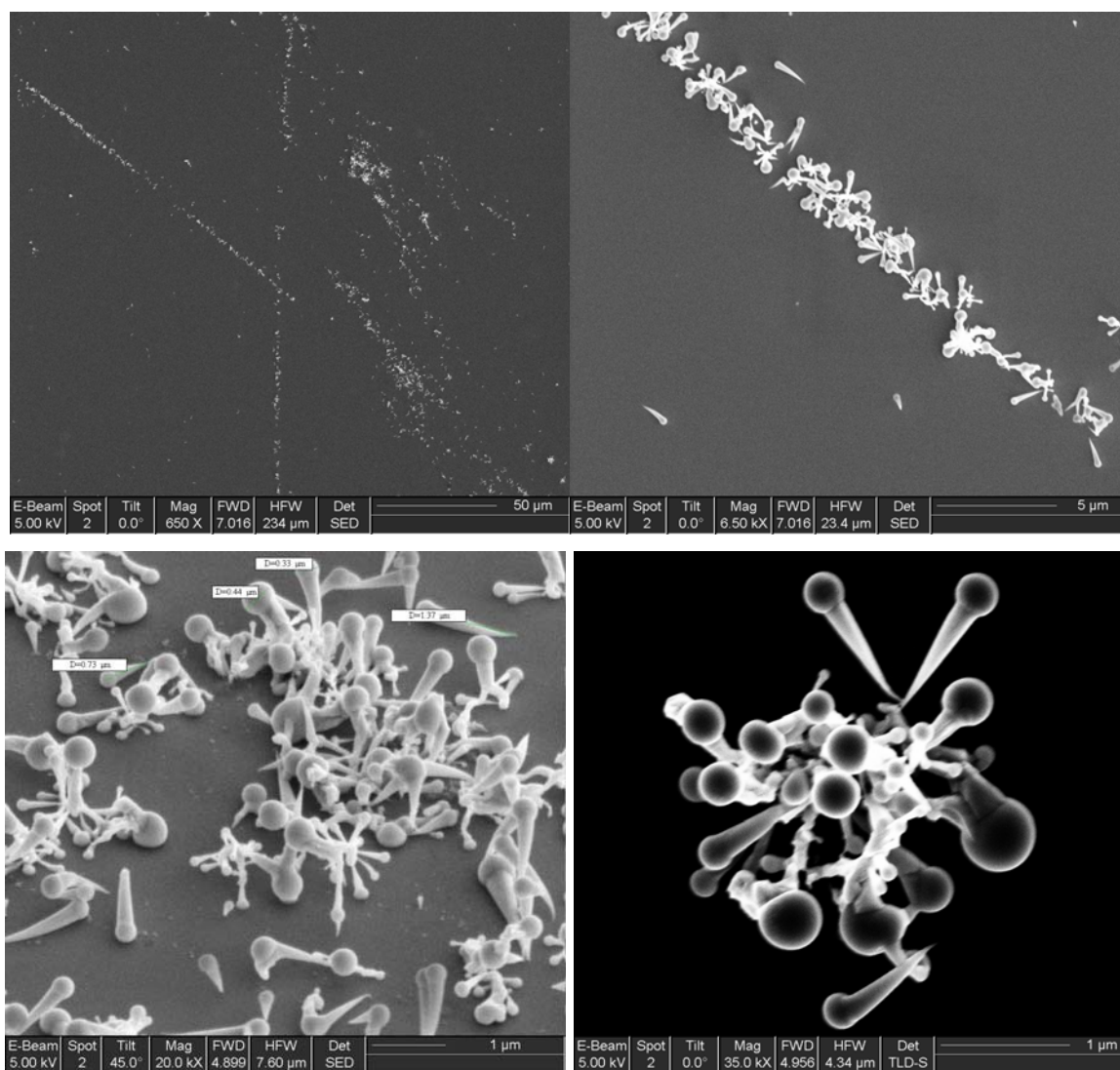


Figure 5-18: SEM images of the Ga/Ga₂O₃ 3D cauliflower like structure grown at 600 °C on Si(100).

Like the nanorods do, the 3D structures grow perpendicularly to the Si surface following privileged direction. The 3D structures are constituted of a cone ca. 1 μm

long and a spherical particle at the tip (the head) with a diameter of nearly 200 nm. They tend to form cauliflower like structures. Figure 5-19 illustrates a layer as well deposited at 600 °C but with a longer deposition time (3 hours).

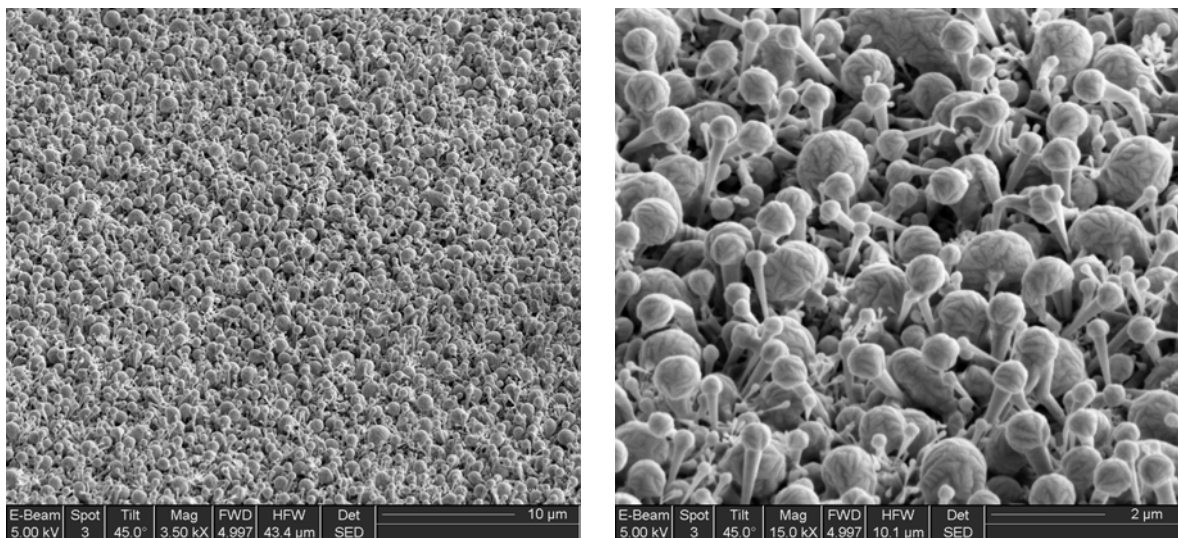


Figure 5-19: cauliflower-like Ga/Ga₂O₃ layer grown after long deposition (3 hours) at 600 °C.

After 3 hours deposition, the layers cover quasi totally the surface hence no growth direction is observed anymore. The same 3D nanostructures as for a shorter deposition time can be observed, but they are much larger (the head can reach 1 µm).

The faceted surface observed in previous chapter (Figure 5-4) can be recognised on the head surface. Differently from all the layers grown, $\beta\text{-Ga}_2\text{O}_3$ and gallium pattern are clearly present in this case (Figure 5-20). EDX mapping (Figure 5-21) shows unambiguously that the head is composed of gallium (green) with a trace of oxygen while the core contains gallium as well as oxygen (red).

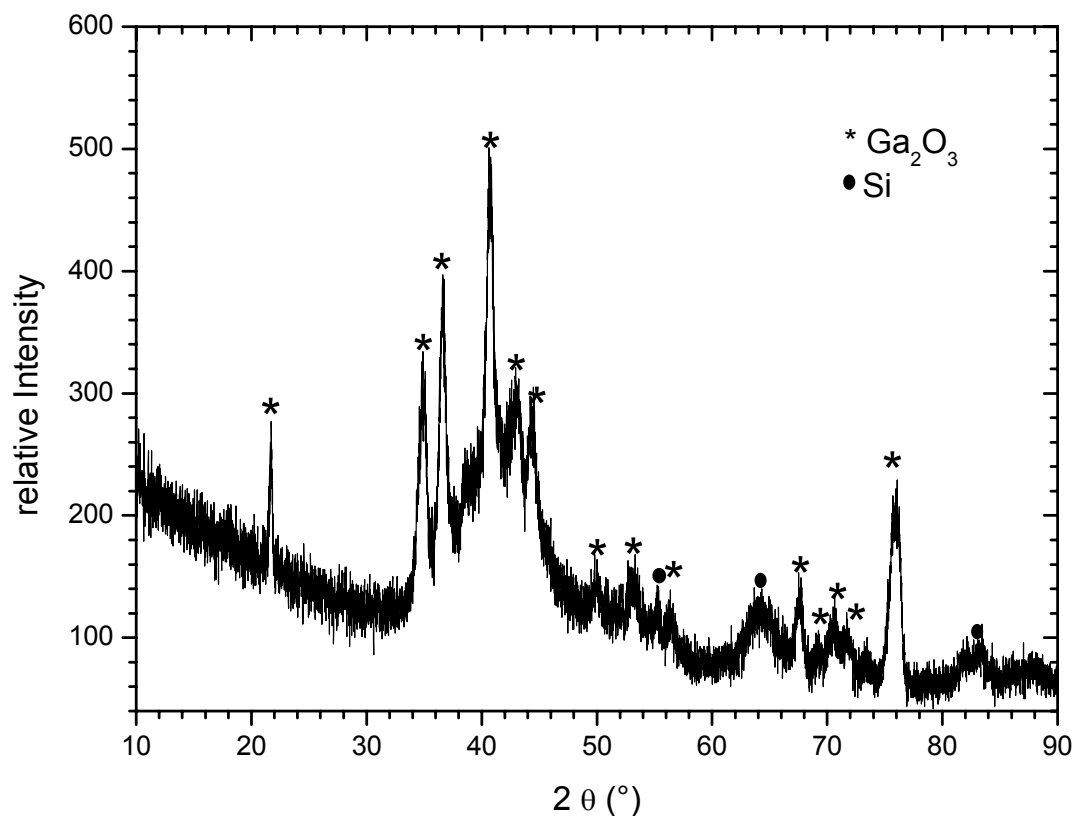


Figure 5-20: XRD of the cauliflower-like Ga/Ga₂O₃ layer grown after long deposition at 600 °C.

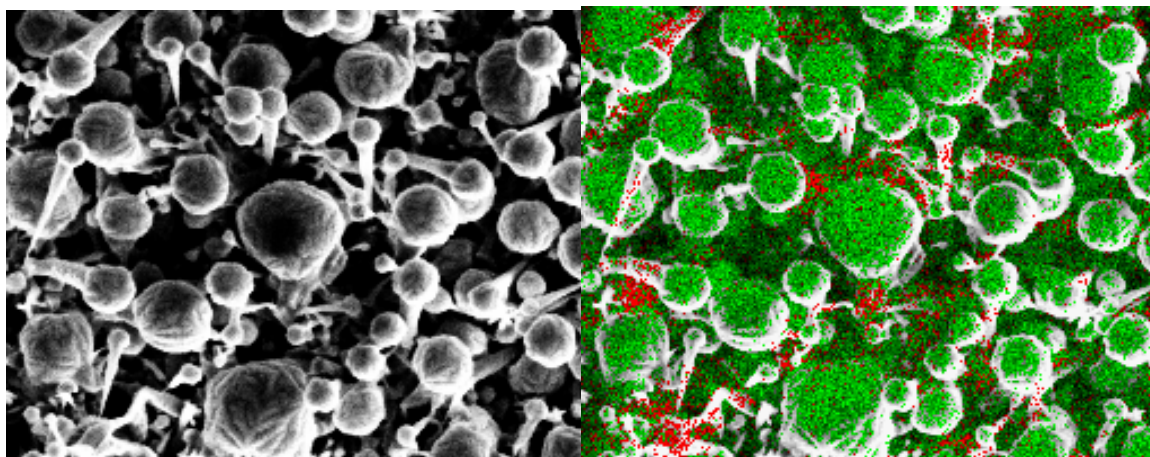
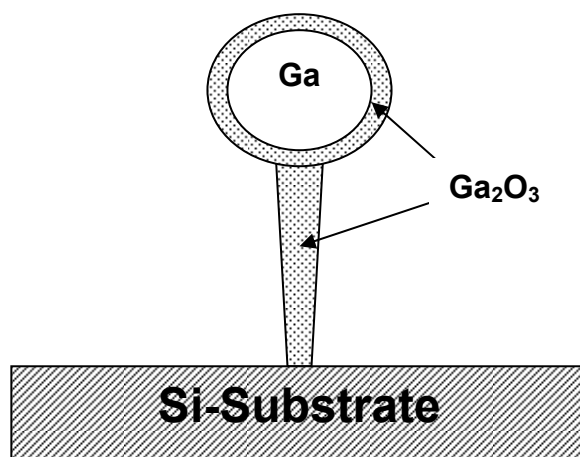


Figure 5-21: EDX mapping of the cauliflower-like Ga/Ga₂O₃ layer grown after long deposition at 600 °C. (Gallium is represented in green, oxygen in red)

Hence, we have to deal with a composite 3D structure of gallium and its oxide like schematised on scheme 5- 1.



Scheme 5-1: Schematisation of the Ga/Ga₂O₃ droplets' composition.

The structure can be schematised as a gallium droplet, which is covered by a thin layer of gallium oxide, supported by a crystalline gallium oxide cone.

By MOCVD of trimethyl gallium on Si (100) Sacioletti et al. succeed to grow similar 3D structures in the same temperature range as we do. Despite of the morphological analogies, the structure evidenced by Sacioletti and al. is amorphous and not faceted at the tip surface. In their case, the cone was principally constituted of carbon from the precursor, whereas we obtain crystalline Ga₂O₃. The choice of a single source precursor with the stoichiometry 1:1 between oxygen and gallium leads to layers which conserve this stoichiometry; therefore in our case a composite with Ga/Ga₂O₃ in which gallium and oxygen are 1:1 is likely to be obtained.

To increase crystallinity, annealing at 600 °C during 16h was efficient, but the 3 D morphology was damaged. Figure 5-22 and 5-23 show XRD as well as SEM images after annealing.

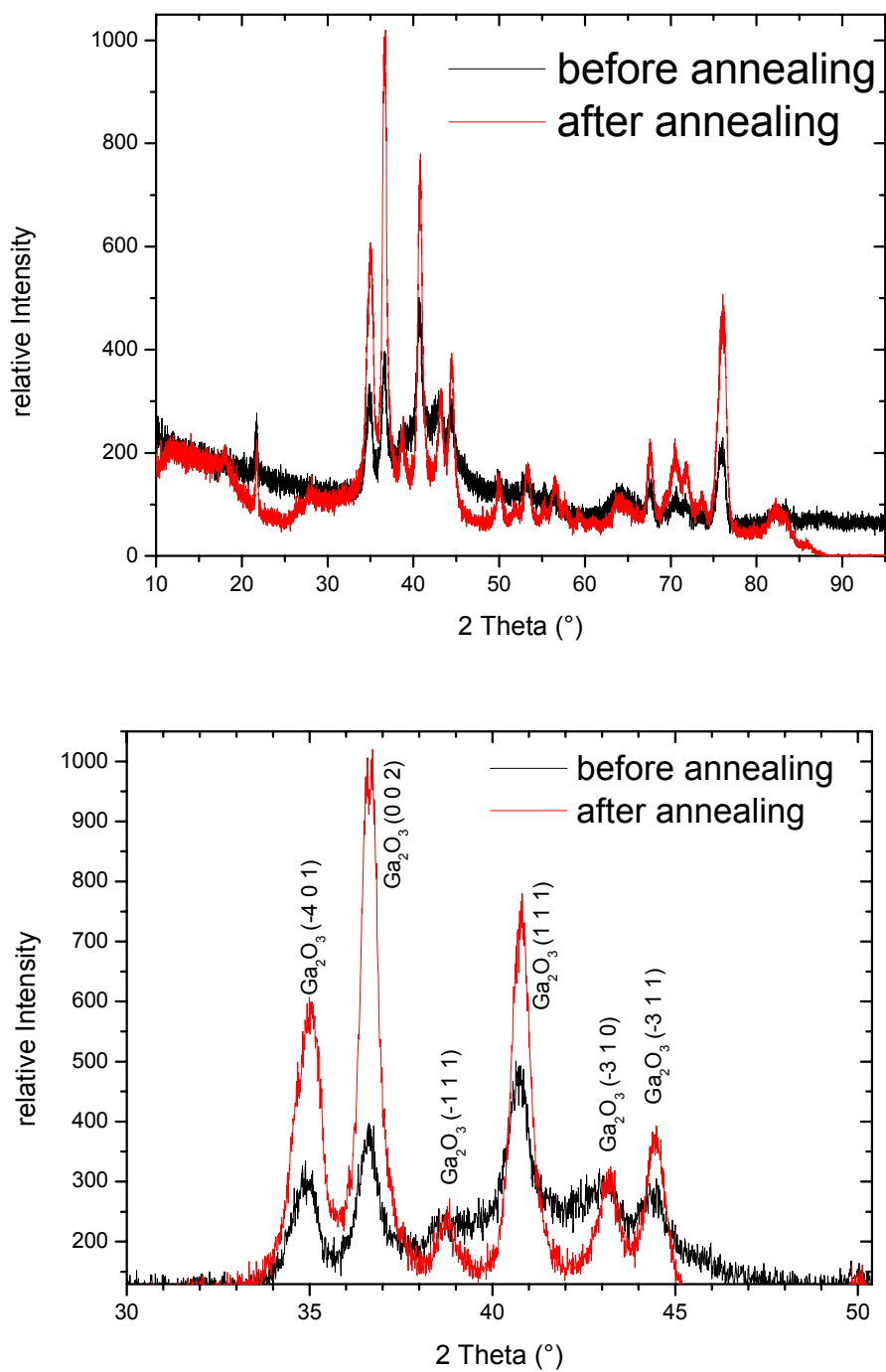


Figure 5-22: Comparison between XRD pattern after and before annealing. Overview on the whole diffractogram and magnification on the area between $2\theta = 30^\circ$ and 50° to show that all the peaks increased after annealing.

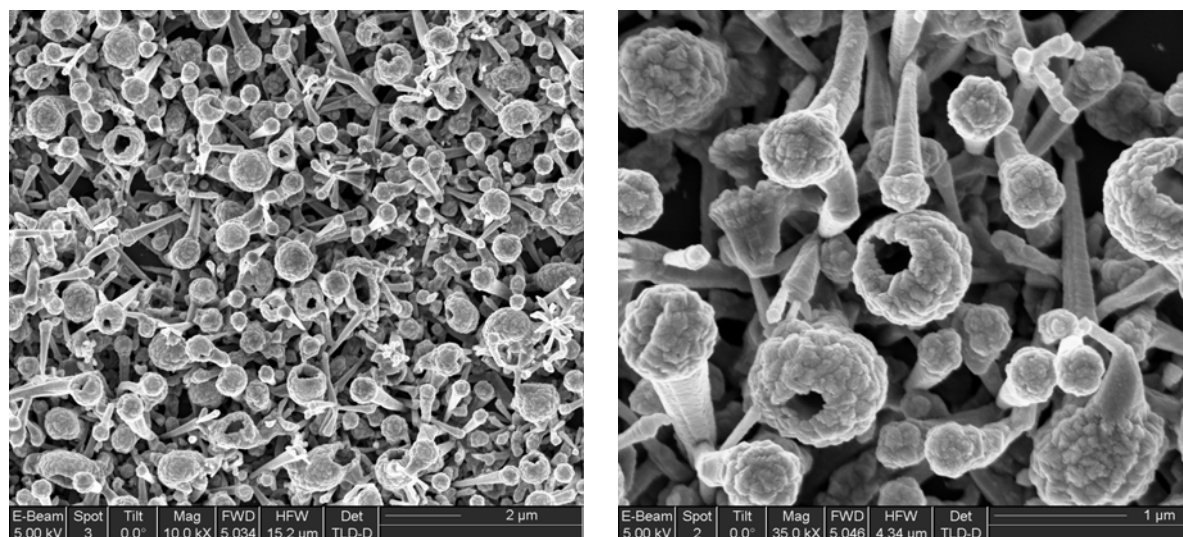


Figure 5-23: SEM image of the cauliflower-like Ga/Ga₂O₃ layer grown during 3 hours at 600 °C after annealing.

After annealing, some of the cones and the heads are separated from another and holes can be distinguished in the head. This thermal modification can be attributed to the escape of liquid gallium from the head, which blows up. In reference 111 it has already been observed that gallium droplets are able to blow up. Despite of this modification, annealing present the advantage of getting a composite with high crystallinity.

Si(100) turns out to be an appropriated substrate for a selective deposition. Contrarily to metallic substrate, Si(100) is not drastically influenced by precursor flow and deposition time. To select between the 2 possible morphologies, the deposition temperature is the most important process parameter. Annealing was efficient to become crystalline Ga₂O₃. Contrarily to previous investigations performed by S. Faber²⁶, where only metallic gallium was obtained, we produce composite layers with $[\text{H}_2\text{Ga}(\text{O}^t\text{Bu})]_2$. We analysed a wider range of temperature and we tested more types of substrates than S. Faber. The resulting nanostructures are therefore more diversified.

5.3 Layers grown with $[\text{H}_2\text{Ga}(\text{O}^t\text{Bu})]_2$ and $[\text{H}_2\text{Al}(\text{O}^t\text{Bu})]_2$.

It was attempted to grow layers with both molecular precursors. $[\text{H}_2\text{Ga}(\text{O}^t\text{Bu})]_2$ has a higher partial pressure than $[\text{H}_2\text{Al}(\text{O}^t\text{Bu})]_2$, that is why $[\text{H}_2\text{Ga}(\text{O}^t\text{Bu})]_2$ will be cooled with ice, whereas $[\text{H}_2\text{Al}(\text{O}^t\text{Bu})]_2$ is used at room temperature. Figure 5-24 shows a typical layer grown at 600 °C with both precursors on steel.

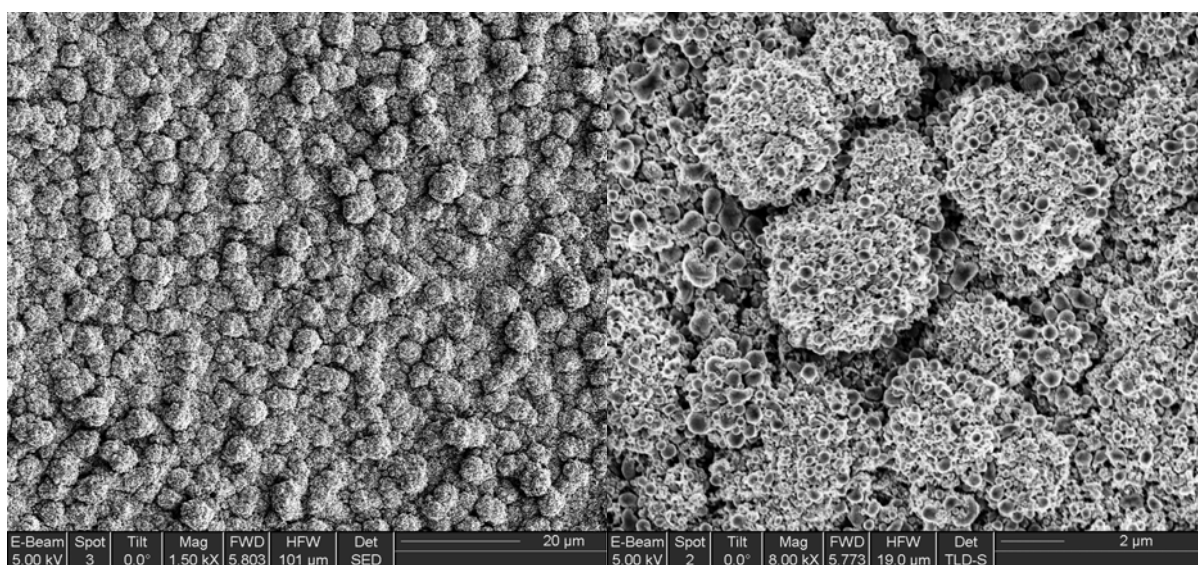


Figure 5-24: SEM images of a layer grown with both precursor ($[\text{H}_2\text{Ga}(\text{O}^t\text{Bu})]_2$ and $[\text{H}_2\text{Al}(\text{O}^t\text{Bu})]_2$) at 600 °C at the same time.

At the microscopic scale, particles with approximately 2 μm diameter cover the surface like the structure obtained by depositing $[\text{H}_2\text{Al}(\text{O}^t\text{Bu})]_2$ at 490 °C (Figure 3-19). These particles are indeed constituted by gallium nanodroplets, which resemble the droplets grown with $[\text{H}_2\text{Ga}(\text{O}^t\text{Bu})]_2$ on stainless steel (Figure 5-2).

The following figure (figure 5-25) shows SEM images of the edges of the target, where the temperature is lower due to inhomogeneous heating.

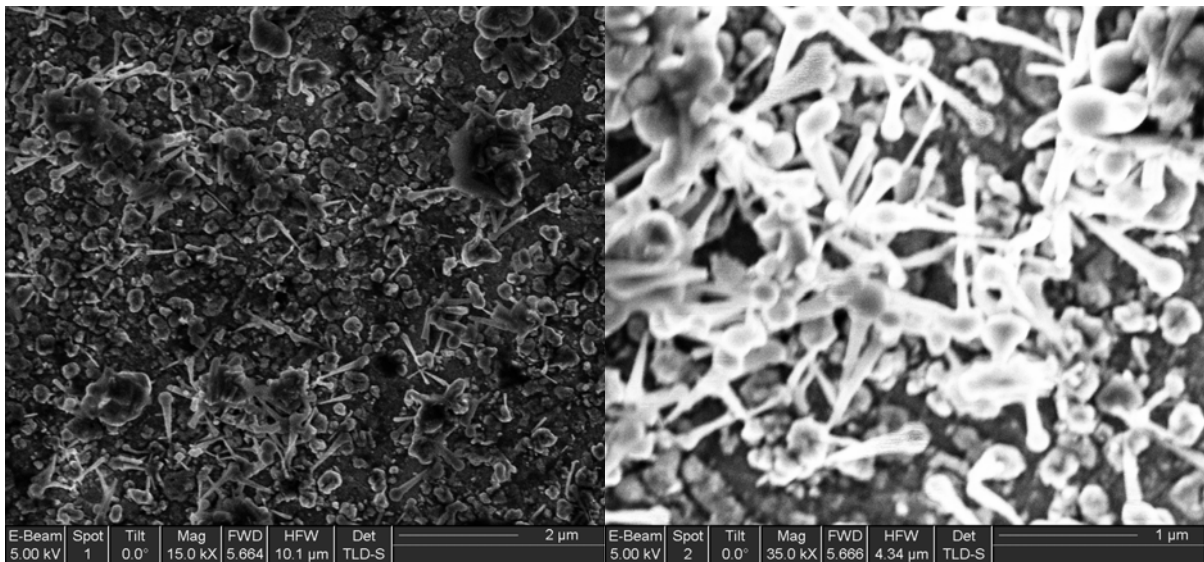


Figure 5-25: SEM image of the edges of a layer grown with $[\text{H}_2\text{Ga}(\text{O}^t\text{Bu})_2]$ and $[\text{H}_2\text{Al}(\text{O}^t\text{Bu})_2]$ at the same time.

The 3 dimensional structure obtained is like the one obtained from $[\text{H}_2\text{Ga}(\text{O}^t\text{Bu})_2]$ deposited at high temperature on Si(100). These results are not completed they just give a hint about the possibility to grow layers having both the properties of aluminium composites and gallium composites.

6 Conclusion and outlook

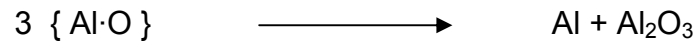
Following the works carried out by AK Veith, the goal of the present study was to produce nanocomposite layers via chemical vapour deposition from the single-source precursors $[\text{H}_2\text{Al}(\text{O}^t\text{Bu})]_2$ and $[\text{H}_2\text{Ga}(\text{O}^t\text{Bu})]_2$ with reproducible compositions and structures.

First, a range of samples are provided starting from $[\text{H}_2\text{Al}(\text{O}^t\text{Bu})]_2$ as precursor by varying the CVD-process parameters deposition duration, precursor flow and substrate temperature, then these samples are analysed with X-Ray diffraction and scanning electron microscopy. The analyses of the obtained layers allow identifying the influence of each deposition parameter on the layer composition, crystallinity and structure: these are the key-steps to reach a reproducible CVD-process.

Firstly, a systematic study focussed on $\text{Al}/\text{Al}_2\text{O}_3$ composite layers grown above $490\text{ }^\circ\text{C}$ has been carried out. XRD investigations confirm the presence of aluminium crystallites and the absence of Al_2O_3 crystal phases. The size of the aluminium crystallites generally increases with deposition temperature and time. According to Scherrer's equation, aluminium crystallites reach a maximum of app. 160 nm after 2 hours of deposition at $600\text{ }^\circ\text{C}$ with a chamber pressure of $3 \cdot 10^{-2}$ mbar. However, Scherrer's equation is not the best method as long as the crystallite shape remains unknown. Aluminium carbide is detected as crystalline by-product in layers grown in long-time deposition (more than 1h 30 at $490\text{ }^\circ\text{C}$ or at $600\text{ }^\circ\text{C}$ after one hour). Cooling the precursor and reducing chamber pressure to $3 \cdot 10^{-2}$ mbar can postpone the by-product formation.

In some cases XRD shows a cubic phase ($\{\text{Al}\cdot\text{O}\}$) containing an unknown relation of oxygen and aluminium. It is assumed to be a distorted $\gamma\text{-Al}_2\text{O}_3$ denoted $\gamma'\text{-Al}_2\text{O}_3$.

As this phase is only detected in freshly prepared samples, it probably reacts to form the composite material according to the following disproportionation equation:



Al/Al₂O₃ layers are easily reproduced and XRD is a versatile tool to control the evolution of the crystallite size and by-product formation.

The morphology of the layers formed at 490 °C is the same as the one reported in previous works from our group (fractal structure)³⁴. A dense assembly of big spheres with some micrometers in diameter is illustrated by SEM (Figure 6-1). The profile of the layer is analysed by EDX by accomplishing a cut with focus ion beam (FIB). It shows that the layer is very dense and homogeneous. It contains an equimolar distribution of aluminium and oxygen, like in the single source precursor.

The layers obtained above 530 °C present an unexpected one-dimensional nanostructure and a cauliflower microstructure (Figure 6-1). Entangled nanowires are homogeneously distributed on the surface. The diameters of the nanowires are between 30 nm and 60 nm and can reach several μm in length. The density and size of the nanowires can be adjusted by controlling the deposition temperature and the precursor flow. To get short nanowires, a low deposition temperature (530 °C) associated with a high precursor flow (chamber pressure 3.10⁻¹ mbar) is necessary. In the contrary, the longer nanowires are deposited with a low precursor flow at 600 °C. Some nanowires can for example assemble into spheres (app. 50 μm) at 560 °C and low precursor flow.

The systematic study allows determining precisely the most important process parameter, i.e. the temperature, at which the structure turns from fractal spherical particles to nanowires (510 °±15 °C). Minimal variations in the composition (by-products) and structure (homogeneity, size, density) can be controlled and reproduced.

Precursor flow is also an important factor as it determines the film quality (size and density of nanowires, homogeneity of the profile) and mechanical resistance (films grown by high precursor flow and relatively low temperature (530 °C) break in contact with air).

Deposition time is the least important factor; it mainly determines the film thickness and the amount of by-product formation.

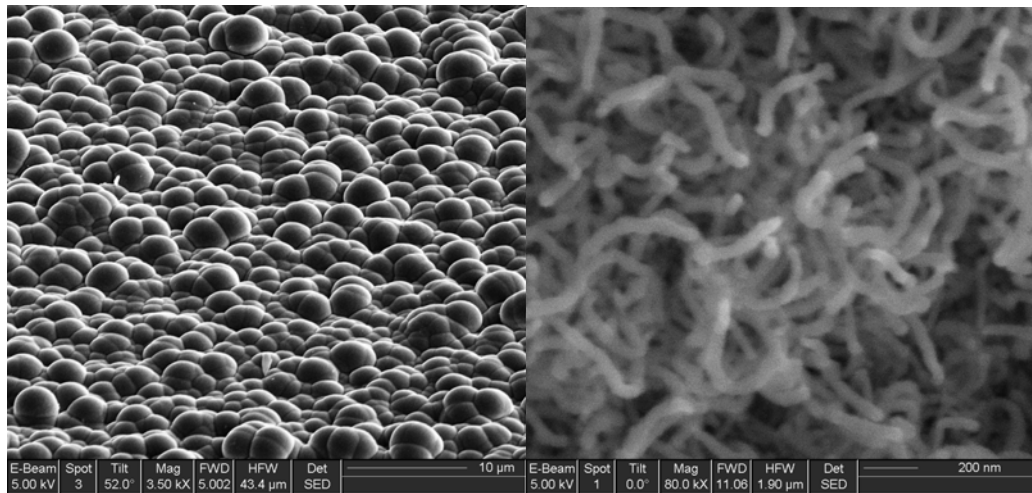


Figure 6-6-1: Two main morphologies for Al/Al₂O₃ layers. At 490 °C: Al₂O₃ spheres with bigger Al crystals fractally distributed in the Al₂O₃ spheres. Above 530 °C: entangled nanowires.

Secondly, the Al/Al₂O₃ nanowires have been investigated with transmission electron microscopy equipped with EDX and SAED. We expected that a detailed investigation of the inner structure of the nanowires would allow understanding the spontaneous one-dimensional growth. Bright and dark field images have revealed the presence of a single crystalline aluminium nanowire embedded in a partially crystalline Al₂O₃ shell. At one extremity of the nanowire, a single crystalline aluminium particle is embedded in an Al₂O₃ shell (Figure 6-2). We have concentrated our efforts in the determination of the crystalline phase in the Al₂O₃ shell.

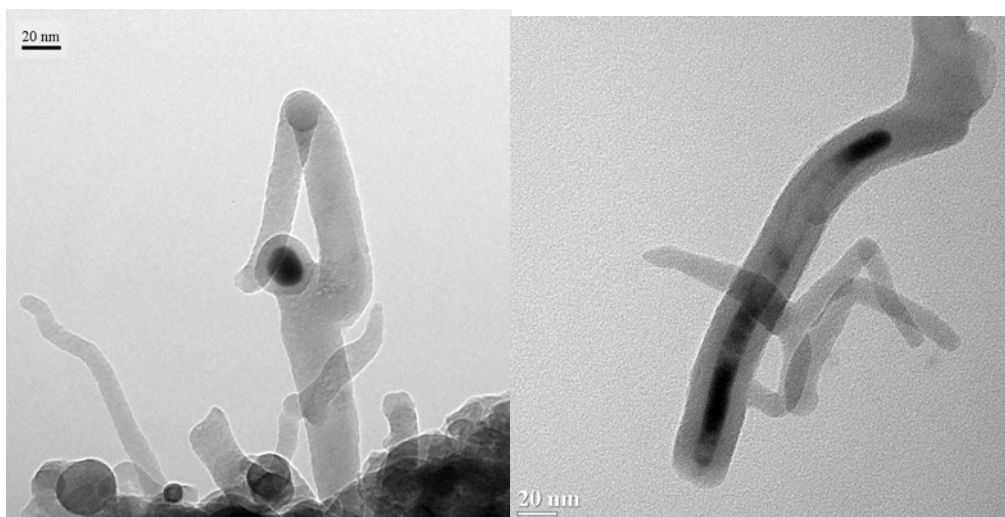


Figure 6-6-2: Single Al/Al₂O₃ nanowires with head (left) and core filled with single crystalline aluminium (right).

The most probable crystalline phase in the shell are γ -Al₂O₃ or δ -Al₂O₃ but other Al₂O₃ (hexagonal, θ , ϵ) are also discussed according to electron scattering analysis.

The lattice planes of the crystallites in the shell often form an angle of app. 30° (Figure 6.3) with the lattice planes of the Al-core; this intentional formation of grain boundaries means that the growth of the nanowire's shell is related to the growth of the core.

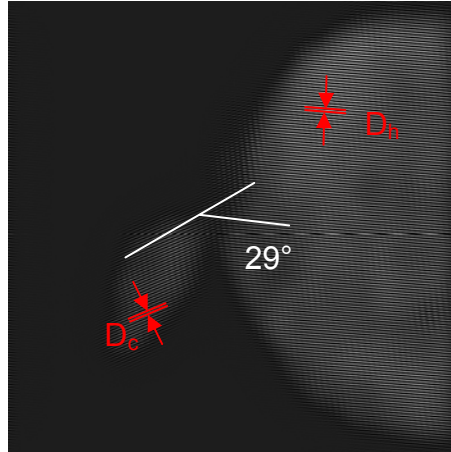


Figure 6-6-3: HRTEM shows that Al core and Al_2O_3 crystallite are oriented with an angle of 28.9° from another.

Anisotropic growth like the growth of nanowires is usually induced by a metal catalyst as exemplified in the well-known VLS growth mechanism. In our case, no catalyst was introduced to the process: obviously, aluminium itself plays the role of the metal catalyst. The morphology of the Al/ Al_2O_3 nanowires presents some similarity to the VLS mechanism, as a single crystal is present at the tip of the nanowires. Nevertheless, the coincident grain boundary between core and shell is not in accord with a VLS mechanism. Thus, an original growth mechanism, which is consistent with the inner structure, is proposed (Figure 6-4).

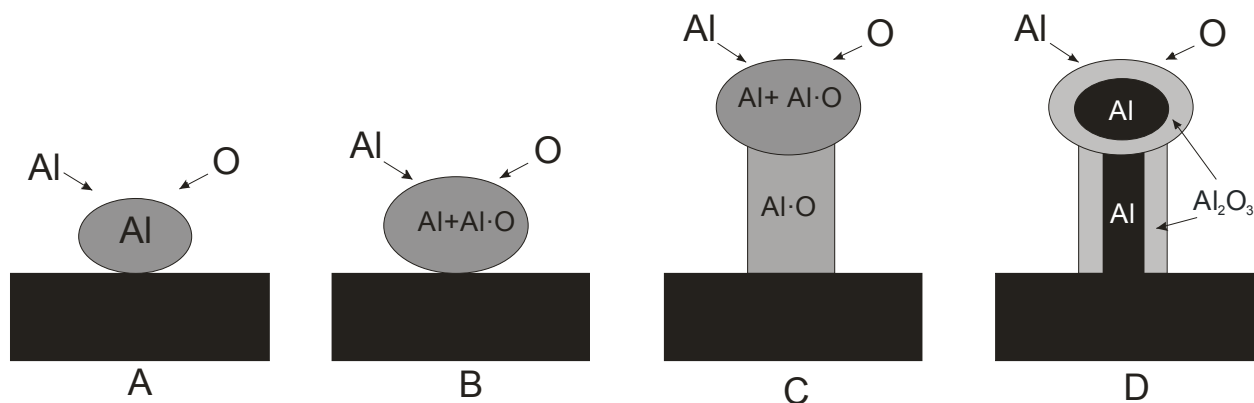


Figure 6-6-4: Schematic illustration of the self-catalytic growth for the synthesis of Al/Al₂O₃ core shell nanowires. (A) Formation of aluminium nanoclusters on the surface. (B) Accumulation of {Al·O} in the Al catalyst and formation of Al-Al-O alloy. (C) Growth of {Al·O} nanowires by precipitation of supersaturated {Al·O} like in VLS process (D) Al segregates to the inside while the Al₂O₃ shell is formed.

TEM also revealed the possibility of growing branched nanowires or nanowires with nanoparticles at the surface. However, TEM investigations are of limited use because of the damages caused to the nanowires due to intensive irradiation (reversible transformations) and heating of the sample (irreversible formation and evaporation of aluminium nanoparticles).

Finally we have tested the homologous precursor [H₂Ga(O^tBu)]₂ in order to grow Ga/Ga₂O₃ layers and to investigate if a spontaneous one-dimensional growth also occurs. Not only nanowires are grown but it seems as if [H₂Ga(O^tBu)]₂ offers a larger structural diversity than its aluminium homologue. Therefore, the systematic study focused on selected layers grown on steel, copper and silicon substrates by different conditions and on the analysis of their structure by SEM (Figure 6-5). XRD evidenced that metals are not the best substrates to grow gallium containing layers because of undesired reactions between metal and layer (for example formation of Ga₂CuO₄ and NiFeGaO₄). Moreover, the layers obtained on metals are often inhomogeneous due to the presence of crystalline phases and nanostructured morphologies such as:

- Gallium droplets covered by a thin Ga₂O₃ film
- Small nanowires (diameter = 50 nm, length = 500 nm)
- Big nanowires (diameter = 300 nm, length = 10 μm)
- Nanoparticles (app. 15 nm) occasionally grown on the surface of nanowires.

The layer diversity is also due to difference in composition, some layers contain carbon, other show amorphous or crystalline Ga_2O_3 . A structure-composition relationship could not be established during these preliminary investigations.

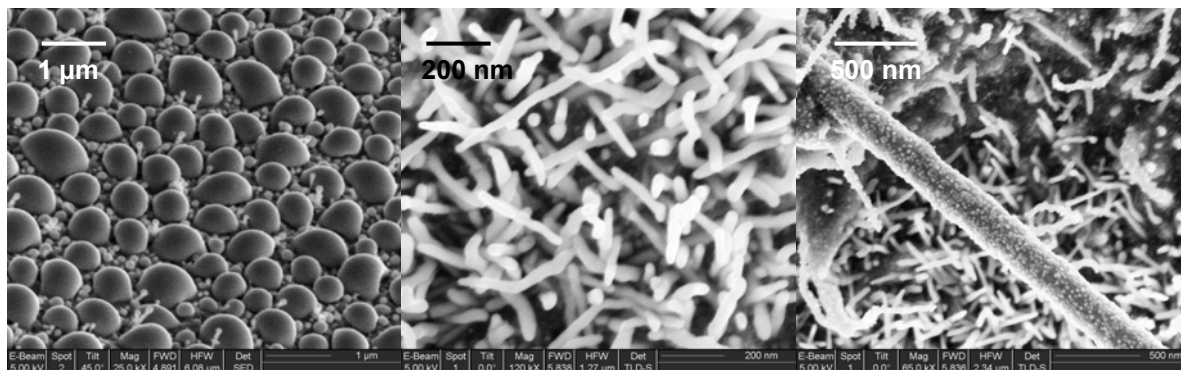


Figure 6-6-5: SEM images showing the different structures obtained by CVD of $[\text{H}_2\text{Ga}(\text{O}^t\text{Bu})_2$ on metal surfaces (gallium droplets, small nanowires, big nanowires with particles at the surface).

Silicon turned out to be the most suitable substrate to grow layers with homogenous structures and compositions (Figure 6-5). Depending on temperature and deposition time characteristic layers are grown including:

- Self-aligned $\text{Ga}/\text{Ga}_2\text{O}_3$ nanorods (diameter=70 nm, length= 1 μm)
- Arrays of $\text{Ga}/\text{Ga}_2\text{O}_3$ nanorods
- Self-aligned 3D structures with a gallium droplet (500 nm) at the tip
- Arrays of 3D structures with a gallium droplet (500 nm) at the tip

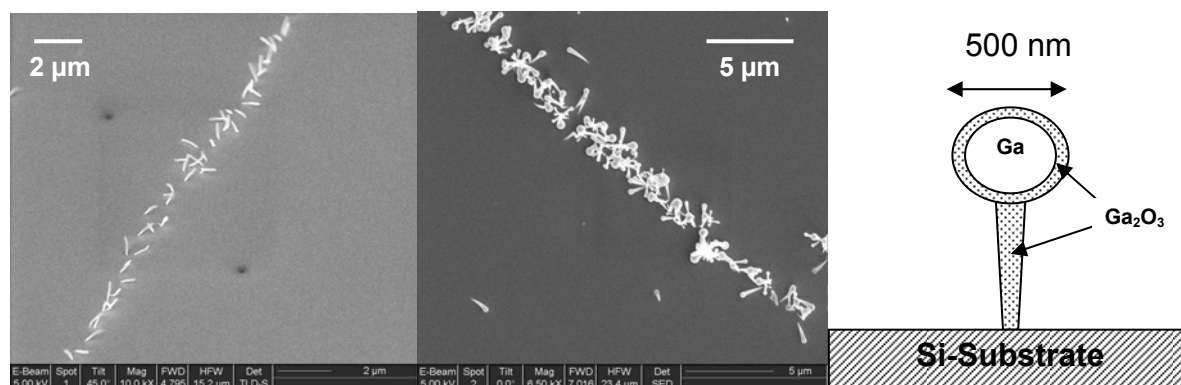


Figure 6-6-6: SEM image of self aligned $\text{Ga}/\text{Ga}_2\text{O}_3$ nanorods and of self aligned 3D structures with gallium droplet at the tip. Schematic representation of a $\text{Ga}/\text{Ga}_2\text{O}_3$ 3D nanostructure.

Increasing deposition temperature (600 °C) and time (3 hours) simultaneously leads to homogeneous $\text{Ga}/\text{Ga}_2\text{O}_3$ composite layers with high crystalline $\beta\text{-Ga}_2\text{O}_3$.

Annealing during 3 hours improves the crystallinity but the liquid gallium inside the droplet evaporates and the residual nanostructure presents a hole (Figure 6-7).

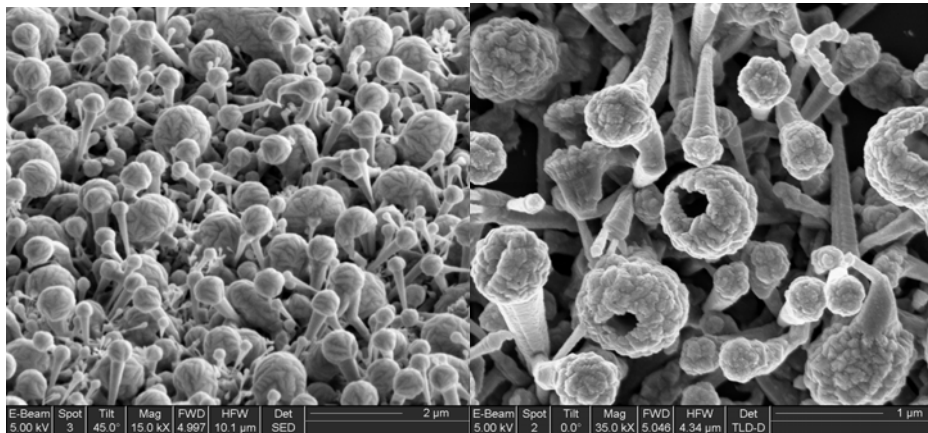


Figure 6-6-7: SEM images of 3D Ga/Ga₂O₃ structures before and after annealing.

The systematic study of the Al/Al₂O₃ layers grown by CVD from [H₂Al(O^tBu)]₂ evidenced a correlation between the properties of the layer to the process parameters. Moreover, a new nanostructure (Al/Al₂O₃ nanowires) was characterised and its formation is reproducible under defined conditions. The detailed investigation of the Al/Al₂O₃ nanowires leads to the proposal of an original self-catalytic growth process, which can be extended to other nanostructures like Ga/Ga₂O₃ nanowires. The understanding of the growth process, as presented in this work, is the key step from basic research to industrial applications. After elucidation of the growth conditions of Al/Al₂O₃ and Ga/Ga₂O₃ nanowires, the method has been applied for a patent¹¹⁸. Thus, industrialisation of the process is highly accomplishable in the near future.

7 Experimental part

Due to the product sensitivity to oxidation and hydrolysis, the synthesis and manipulations have been performed under nitrogen (or argon) gas using Schlenk techniques. The solvents used have been dried by distillation with sodium then have been stored with sodium under nitrogen.

The starting materials AlCl_3 , LiAlH_4 , GaCl_3 and $\text{C}_4\text{H}_9\text{OH}$ have been purchased. LiGaH_4 has been synthesised following established route¹¹⁷.

7.1 Methodology

7.1.1 NMR Spectroscopy in solution

NMR- Spectra have been measured on a Bruker 200 NMR ACF and ACP, in D_6 -Benzene at 295 K as lock solvent. Following intern standards have been used:

^1H (200.13 MHz): D_6H_6 (intern with 7.15 ppm)

^{13}C (50.3 MHz): D_6H_6 (intern with 128.0 ppm)

7.1.2 IR-Spectroscopy

IR Spectra have been measured with a FTIR spectrometer FTS 165 from Bio-Rad. The layers fabricated by CVD are measured by reflection with a Bio Rad variable angle specular reflection accessory with incident angle variable from 30 ° to 85 °.

7.1.3 Powder X-ray Diffraction

For the crystalline phase determination a STOE diffractometer with monochromated $\text{Co-K}\alpha$ radiation ($\lambda=1.78896$) was used. The XRD patterns of layer material were

indexed by comparing with values from Power Diffraction Files ICDD database (Release 2001). The analysis and peak assignment have been accomplished by comparison with literature through the software WinXPow and STOE.

XRD Patterns have been fitted and the size of Aluminium particles has been evaluated using the STOE WinXPow software.

7.1.4 ESCA

The ESCA spectra were recorded on a VG ESCA MKII spectrometer with a Mg-K α source ($E_{kin}= 1253.6$ eV, $E_{pass}=10$ eV, $\Delta E=0.8$ eV) by Frank Müller.

7.1.5 Digital camera

The digital pictures were made with a HP Photosmart M407 (4.1 MP).

7.1.6 Scanning electron microscopy (SEM), focused ion beam (FIB), energy dispersive spectroscopy (EDX),

SEM, EDX and FIB analysis are executed in a Dual Beam Workstation Strata DB 235, FEI with a Schottky field emission source (institute of functional materials, F. Mücklich, Universität des Saarlandes). This instrument combines a SEM with an ion beam system for nanoscale erosion of the sample. The SEM is a high-performance field-emission microscope. In our case, the E- beam tension is generally 5 kV, the spot size 3, the free working distance is 5 mm. These parameters are varied depending on sample requirements. There are two types of detectors, a secondary electron detector and a Through Lens Detector System (TLD). The resolution given by the producer is 2 nm. The machine owns an energy dispersive X-Rays (EDX) system for elemental analysis from the company EDAX (Type Pegasus). To analyse insulator materials, an amorphous conductive carbon film (thickness app. 10 nm) will be deposited at the sample surface by physical vapour deposition in a vacuum evaporator from the company Emitech, Typ K950X.

The ion-beam system has a gallium metal ion source giving a high-brightness ion beam. This beam can cut structures on the scale of nanometers. The minimal beam diameter with a beam intensity of 1 pA is 6 nm. The beam intensity is variable from

1 pA to 20 nA, the acceleration voltage from 5 kV to 30 kV. To protect the surface a platinum layer is deposited in situ with the CVD process.

7.1.7 Transmission electron microscopy (TEM), SAED and EDX

U. Werner preceded to the TEM investigations. The nanowires were mechanically scrapped and sonicated in ethanol and deposited on copper grids covered by a thin amorphous carbon film for TEM (CM 200 FEG) measurements performed on a microscope equipped with a field emission gun. In addition to the investigation by means of conventional scattering and diffraction contrast, the field emission gun (FEG) of this microscope allows a high-contrast observation of the crystalline structure of individual nanowires on the atomic scale by the imaging of their lattice fringes and atom columns (structure contrast). Furthermore, analysing the characteristic X-rays emitted from TEM specimens by using an energy dispersive X-ray spectrometer (EDXS) reveals the elementary composition of the investigated samples. All TEM and EDXS measurements were performed using an electron beam energy of 200 keV. Electron scattering was performed in the TEM to determine the crystalline phases. The TEM is equipped with a “Double Tilt Heating Holder”, Model 652 from the company Gatan Inc with a temperature range from room temperature till 1000 °C (± 30 °C).

7.2 Synthesis of the precursor molecules

7.2.1 Synthesis of $[\text{H}_2\text{Al}(\text{O}^t\text{Bu})]_2$.

Following established routes²⁷ 4.554 g (120 mmol) LiAlH_4 are dissolved in 80 ml diethyl ether in a flask with a reflux cooler. Under cooling 5.334 g (40 mmol) of aluminium trichloride are dissolved in 80 ml diethyl ether and added to the lithium aluminium hydride in a steady flow at room temperature. Lithium chloride precipitates from the mixture. To this suspension 11.859 g (160 mmol) tert-butanole is added dropwise and formation of hydrogen is observed. The procedure is finished by a 4-5 h stirring at ambient temperature. After separation of the lithium chloride by filtration the solvent is evaporated in vacuum. The remaining solid is sublimated at ambient temperature and 100 Pa pressure thus obtaining 15.2 g bis(tert-butoxy aluminium dihydride) (93% yield)

NMR Analysis has been performed for the synthesised product, other information about the product properties stem from the dissertation of S. Faber²⁶.

Calculated molecular mass 204.22 g/mol⁻¹,

Determined by cryoscopy in benzene: 185 g/mol⁻¹,

¹HNMR (5, i-TMS): 1.22 p.p.m. (s, 18H, -C(CH₃)₃), 4.43 p.p.m. (s, -AlH₂);

¹³CNMR (5, i-TMS); 30.36 p.p.m. (-CH₃), 76.43 p.p.m. (-C(CH₃)₃),

IR (hexane solution): 1846 cm⁻¹ (νAlH₂);

Analytical data: 47.02 wt % C (calc. 47.00%), 10.65% H (calc. 10.86%).

Melting point: 71°C

Sublimation point: 20°C / 1 mbar

7.2.2 Synthesis of [H₂Ga (O^tBu)]₂.

The synthesis is carried out in three steps:

- Synthesis of LiGaH₄ in solution
- Synthesis of GaH₃·O(^tBu)₂ in solution
- Reaction of GaH₃·O(^tBu)₂ with tert-butanol

Step 1 and 2 are carried out following established route¹¹⁷.

10 mmol tert-butanol are dropwise added to a recently synthesised solution of 10 mmol GaH₃·O(^tBu)₂ at 0 °C. A weak hydrogen formation is observed. The reaction is finished after 3 hours stirring at room temperature. Ether will be removed by a slow evaporation in a light vacuum. It remains an oily white solid. To purify the solid it will be drawn at 0°C under a vacuum of about 1 mbar in a sublimation tube cooled with acetone and dry ice. Colorless crystals are obtained with a yield of 87%.

NMR Analysis has been performed for the synthesised product, other information about the product properties stem from the dissertation of S. Faber²⁷.

Calculated molecular mass 289.7 g/mol⁻¹,

Determined by cryoscopy in benzene: 273 g/mol⁻¹

¹HNMR (5, i-TMS): 1.15 p.p.m. (s, 18H, -C(CH₃)₃), 5.69 p.p.m. (wide, -GaH₂);

¹³CNMR (5, i-TMS); 30.50 p.p.m. (-CH₃), 74.74 p.p.m. (-C(CH₃)₃),

IR (hexane solution): 1906 cm⁻¹ (νGaH₂);

Analytical data: 31.54 wt % C (calc. 33.16%), 7.59% H (calc. 7.65%).

Melting point: 47°C

Sublimation point: 20°C/ 15 mbar

7.3 MOCVD Technique

The CVD experiments were performed in a horizontal tubular borosilicate reactor operating in a cold-wall configuration. An inductive coupling of radio frequency was used to heat the substrates directly (conductors) or by placing on a graphite sample holder (insulators).

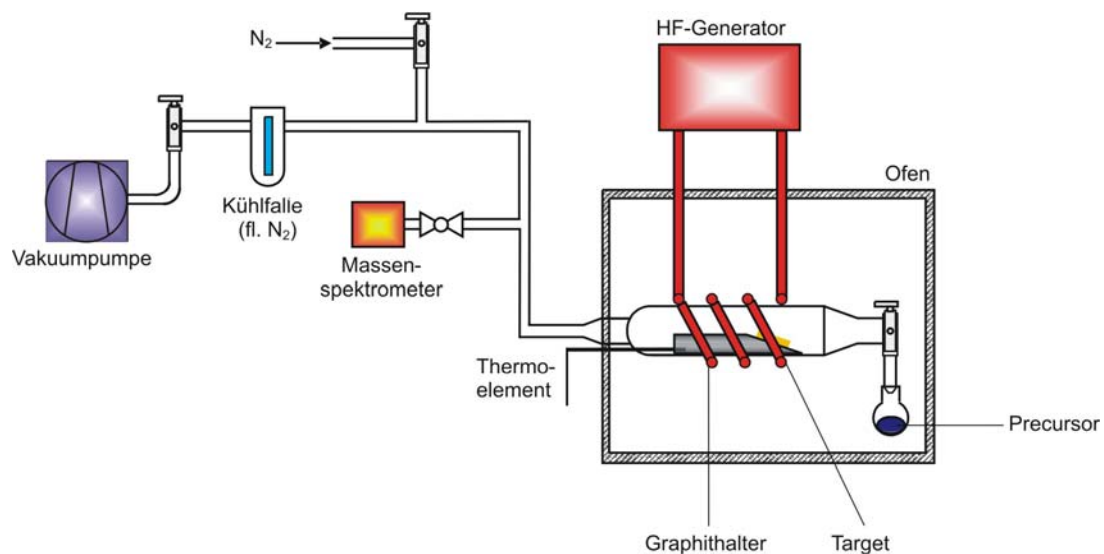


Figure 7-1: Schematic representation of the CVD apparatus

The appropriated precursor was introduced into the reactor through a glass flange by applying dynamic vacuum and cooling the precursor reservoir to the desired temperature. The precursor flux was regulated following the feedback of the pressure measurement in the reactor during the CVD process. The substrate temperature was controlled using a thermocouple, which has been calibrated by an optical pyrometer. The gaseous products of the thermolysis reactions and any unreacted precursor were removed through the pumping end of the reactor connected to rotary vane and turbo molecular vacuum pumps. A quadrupole mass spectrometer was connected to the reaction chamber through a metal flange to provide an on-line analysis of the gaseous products or fragments coming out of the reaction zone.

7.3.1 Substrate preparation

In this work the substrates used are stainless steel, copper and silicon, although the deposition is also possible on many other materials like metals, glass or quartz. The metal substrates are cut from a metal sheet to form metal disks ($\varnothing = 22$ mm) with appropriated dimension for the CVD apparatus. The substrate surfaces have been cleaned by 4 step polishing with a machine Rotopol 11 from the company Struers. First grinding with a plan grinding surface MD–Piano 120, then fine grinding with a MD-Largo accompanied to a diamond suspension (Grain size= 9 μm), finally polishing with DAC and NAP polishing cloths using diamond suspension with 3 and 1 μm grain size, respectively. In order to remove metal dust, the substrates have been sonicated during 5 Minutes with isopropanol after polishing.

7.3.2 High frequency generator

To heat the substrate a high frequency generator from the company Linn High Term, type HGT 750, with an Output power of 750 Watt has been used. The optimal operating frequency is between 350 and 480 kHz. Water cooled induction coils are in copper. Temperature measurement and control have been effected through a Ni-Cr-Ni thermocouple or an IR pyrolyser attached to a PID temperature regulator 847 from Eurotherm.

If the substrate is insulator (silicon), a graphite substrate holder is used to heat the sample. The thermocouple is introduced in a hole at the backside of the metallic substrate or the graphite sample holder.

7.3.3 Vacuum system

To create sufficient vacuum in the reaction chamber of the CVD unit a two stage slide vane rotary vacuum pump type RD4 from Vacuubrand has been used. Purified argon has been utilised as flushing and carrier gas.

7.3.4 CVD process

For each deposition the CVD apparatus is prepared as described in the following: The CVD apparatus has been evacuated during more than one hour until the vacuum reaches $1 \cdot 10^{-2}$ mbar. The substrate has been heated at 700 °C (incandescence temperature) during 15 Minutes. After substrate cooling, the apparatus has been

flushed with argon and the flask with the precursor has been attached to the reaction chamber. Afterwards, the reaction chamber has been once again evacuated during one hour. Then, the substrate has been heated to the required temperature. The precursor could be brought into the reaction chamber not until the substrate temperature has been kept constant. To manage the precursor flow, the precursor vapour pressure and consequently the precursor temperature had to be controlled.

To finish the deposition, the precursor supply has been first stopped, and then the substrate has cooled down slowly to room temperature. Finally, the reaction chamber has been flushed with argon, the precursor flask has been removed from the reaction chamber and the deposited substrate has been retrieved. Some layers are annealed in the reaction chamber by maintaining the desired substrate temperature and closing the flask where the precursor is.

For a given precursor, the three important deposition parameters that can be managed are deposition time, precursor flow (i.e. temperature) and substrate temperature.

7.3.5 CVD with $[H_2Al(O^tBu)]_2$.

Several layers have been deposited on copper and steel by varying the substrate temperature from 450 °C to 600°C.

With $[H_2Al(O^tBu)]_2$ precursor two precursor flows have been tested. Some deposition occurred with $[H_2Al(O^tBu)]_2$ cooled at 0 °C, thus the pressure in the chamber was $3 \cdot 10^{-2}$ mbar, other layers have been deposited with $[H_2Al(O^tBu)]_2$ at room temperature, and thus the pressure in the chamber reached $3 \cdot 10^{-1}$. The layers have been grown during 5 different deposition times: 1 Minutes, 30 Minutes, 1 hour, 1h30 and 2 hours.

Table1 summarised the deposition conditions and shows the three principal layer types obtained.

Substrate Temperatur	490 °C		530 °C		560 °C		600 °C	
	0°C	RT	0°C	RT	0°C	RT	0°C	RT
1 Min	A	A*	B	B	C	C	C	C

30 Min	A	A*	B	B	C	C	C	C
1h	A	A*	B	B	C	C	C	C
1h30	A	A*	B	B	C	C	C	C
2h	A	A*	B	B	C	C	C	C

Table 7-1: Summary of the layers grown by MOCVD of $[\text{H}_2\text{Al}(\text{O}^t\text{Bu})_2]$.

For the layers type A, the colour of the substrate is changing alternatively from gold-yellow or violet to green-blue at the beginning of the deposition. After about 2 Minutes the colour stops changing and the layer becomes light grey. If the layer A* is deposited less than five minutes as well as more than one hour, it breaks off when submitted to the air. The microstructural investigation of layer A (chapter 3.4.1) shows spherical particles. Layer type B are black like velvet, they are obtained at low pressure otherwise the layer breaks off, the microstructural investigation has shown short nanowires. From 560 °C the layers C obtained are black velvet with a discreet bluish colouring, the morphology of the thin film is entangled naowires. The substrate has deposited on the wall of the reaction chamber; a metallic mirror is formed on the surface of the reaction chamber.

For each deposition conditions, the experiment has been reproduced at least 2 times.

7.3.6 CVD with $[\text{H}_2\text{Ga}(\text{O}^t\text{Bu})_2]$.

Layers were grown with $[\text{H}_2\text{Ga}(\text{O}^t\text{Bu})_2]$ following the equivalent procedure as with $[\text{H}_2\text{Al}(\text{O}^t\text{Bu})_2]$. The differences between the two types of precursors are summarised in the following.

The $[\text{H}_2\text{Ga}(\text{O}^t\text{Bu})_2]$ precursor has a higher vapour pressure than $[\text{H}_2\text{Al}(\text{O}^t\text{Bu})_2]$; it was cooled at -80°C with dry ice ($1.0 \cdot 10^{-2}$) or at 0°C with ice ($\approx 3.0 \cdot 10^{-2}$) to get equivalent pressure in the reaction chamber. Layers have been fabricated from 400°C to 600°C with deposition times ranging from 1 minute to 2 hours. A big decrease in the temperature (ca. 80°C) is observed during the 10 first minutes of deposition, then the temperature stabilises.

Most of the layers are red brown at the end of the deposition and they turn grey in contact with the air. Some substrates are only covered in the centre by the layer, they

show a light grey colour: Some substrates are homogeneously covered, they can also be light grey or dark grey. The wall of the reaction chamber is also red brown and turns grey by contact with the air.

7.3.7 CVD with $[\text{H}_2\text{Al}(\text{O}^t\text{Bu})_2]$ and $[\text{H}_2\text{Ga}(\text{O}^t\text{Bu})_2]$.

An attempt has been made to grow mixed-layers of gallium and aluminium. A reaction chamber with two entries has been used. Both precursors have been simultaneously opened. The layers have been grown by cooling gallium precursor at 0°C whereas the aluminium precursor was at room temperature. The layers obtained are dark grey.

References

1. K.L. Choy. Chemical vapour deposition of coatings. *Prog. Mat. Sci.*, 48(2):57–170, **2003**.
2. B.D. Fahlman. Recent advances in chemical vapor deposition. *Curr. Org. Chem.*, 10(9):1021–1033, **2006**.
3. N. Lecerf, S. Mathur, H. Shen, M. Veith, and S. Hüfner. Chemical vapour and sol-gel syntheses of nano-composites and -ceramics using metal-organic precursors. *Scripta Mater*, 44(8-9):2157–2160, **2001**.
4. C. H. Peng and S. B. Desu. Metalorganic chemical vapor deposition of ferroelectric Pb(Zr,Ti)O₃ thin films. *J. Am. Ceram. Soc.*, 77(7):1799–1812, **1994**.
5. R.W. Weber, K.P. Möller, and C.T. O'Connor. The chemical vapour and liquid deposition of tetraethoxysilane on ZSM-5, mordenite and beta. *Microporous and Mesoporous Mat.*, 35-36:533–543, **2000**.
6. M.G. Gladfelter, W.L. *The Chemistry of Metal CVD*. Chapter Chemical Vapor Deposition of Aluminium. In: Simmonds, Wiley VCH, 45–103, **1994**.
7. T.R. Gow, R. Lin, L.A. Cadwell, F. Lee, A.L. Backman, R.I. Masel, Decomposition of Trimethylaluminium on Si (100). *Chem. Mater.* 4, 406-411, **1989**.
8. T. Suzuki and H. Umehara. Formation of aluminium films on pitch-based carbon fibres from triisobutylaluminium by reduced-pressure CVD (chemical vapour deposition), **1987**.
9. A. Hausmann, G. Weidner, M. Weidner, and G. Ritter. Investigation of thin Al layer growth with in situ infrared spectroscopic ellipsometry. *Thin Solid Films*, 318(1-2):124–127, **1998**.
10. J.A. Jegier, W.L. Gladfelter, The use of aluminum and gallium hydrides in materials science. *Coord. Chem. Rev.* 206-207, 631–650, **2000**.
11. J. Han, K. F. Jensen, Y. Senzaki, and W. L. Gladfelter. Pyrolytic laser assisted chemical vapor deposition of Al from dimethylethylamine-alane: characterization and a new two-step writing process. *Appl. Phys. Lett.s*, 64(4):425–427, **1994**.
12. D.-H. Kim and B.-Y. Kim. Characteristics of aluminum films prepared by metalorganic chemical vapor deposition using dimethylethylamine alane on the plasma-pretreated tin surfaces. *Korean J. Chem. Eng.*, 17(4):449–454, **2000**.
13. P. Tan, J. Müller, and D. Neuschütz. Gas-phase kinetic modeling of the AlCl₃ decomposition in the AlCl₃-CO₂-H₂-HCl system for a hot-wall CVD reactor. *J. Electrochem. Soc.*, 152(5), **2005**.
14. D. Samelior, M.M. Sovar, A. Stefanescu, A.N. Gleizes, P. Alphonse, and C. Vahlas. Low temperature CVD route for the preparation of alumina coatings with a high specific surface area. *In Proceedings - Electrochemical Society*, 2005-09, 1051–1058, **2005**.
15. J.A. Aboaf, Decomposition and Properties of Aluminum Oxide Obtained by Pyrolytic Decomposition of Aluminum Alkoxide. *J. Electrochem. Soc.* 114, 948–952, **1967**.

16. V.A.C Haanappel, J.B. Rem, H.D. van Corbach, T. Fransen, P.J. Gellings, Properties of alumina films prepared by metal-organic chemical vapour deposition at atmospheric pressure in the presence of small amounts of water. *Surf. Coat. Technol.* 72, 1-12, **1995**.
17. C. Pflitsch, D. Viefhaus, U. Bergmann, and B. Atakan. Organometallic vapour deposition of crystalline aluminium oxide films on stainless steel substrates. *Thin Solid Films*, 515(7-8):3653–3660, **2007**.
18. M.P. Singh and S.A. Shivashankar. Low-pressure MOCVD of Al₂O₃ films using aluminium acetylacetonate as precursor: Nucleation and growth. *Surf. Coat. Technol.*, 161(2-3):135–143, **2002**.
19. D. Temple and A. Reisman. Formation of aluminum oxide films from aluminum hexafluoroacetylacetonate at 350-450 °C. *J. Electron. Mater.*, 19(9):995–1002, **1990**.
20. M. Veith and K. Andres. Preparation of a thin film of Al/Al₂O₃ using a single source precursor. *J. Metastab. Nanocryst. Mater.*, 15-16:279–282, **2003**.
21. M. Veith, J. Frères, V. Huch, and M. Zimmer. Synthesis and characterization of novel siloxalanes. *Organometallics*, 25(8):1875–1880, **2006**.
22. J Frères. Synthese und Charakterisierung neuer Siloxialane und deren Anwendung in der Metal Organic Chemical Vapour Deposition (MOCVD). PhD thesis, Universität des Saarlandes, **2004**.
23. J.P.Campbell, W.L. Gladfelter, Synthesis and Structure of Alkoxy and (Aryloxy)alanes. Observation of a Ring-Opening Reaction Involving Tetrahydrofuran. *Inorg. Chem.* 36 (18), 4094–4098, **1997**.
24. H. Nöth, A. Schlegel, J. Knizek, H. Schwenk, Di-, Tri-, and Tetranuclear Alkoxyaluminum Hydrides. *Angew. Chemie, Intl. Ed.* 36 (23), 2640–2643, **1997**.
25. H. Nöth; H. Suchy, Über Alkoxyalane und Alkoxyaluminium-boranate. *Z. Anorg. Allg. Chem.* 358, 44–66, **1968**.
26. S Faber. Herstellung von Metall-Metalloxid-Kompositen über "Metal Organic Chemical Vapour Deposition" unter Verwendung neuartiger Precursoren. PhD thesis, Universität des Saarlandes, **1996**.
27. M. Veith, S. Faber, H. Wolfanger, and V. Huch. (tert-butoxy) aluminium and -gallium hydrides. *Chem. Ber.*, 129(4):381–384, **1996**.
28. O. Seeger, S. Faber, M. Veith, E. Fritacher, W. M. Dausch, and R. Schmid. Use of hydride-containing aluminium oxide for producing optically detectable markings and inscriptions, **1998**.
29. E. W. Fritscher. Chemical vapour deposition mit Silanen, Heterometallalkoxiden und Hydridoalkoxiden sowie Anwendungen. PhD thesis, Universität des Saarlandes, **1997**.
30. J Blin. Herstellung und Reaktivität von Hydridoaluminiumalkoxi- und -siloxiverbindungen und Herstellung von Eisen-Zinn heterobimetallischen Komplexen. PhD thesis, Universität des Saarlandes, **1999**.
31. K Andres. Umfassende Untersuchungen zur Oxoaluminiumhydridschicht "HAIO" und zu Al/Al₂O₃ Kompositschichten. PhD thesis, Universität des Saarlandes, **2002**.

32. Y Wolf. Neue Festkörper-Phasengemische im ternären System Wasserstoff-Aluminium-Sauerstoff. PhD thesis, Universität des Saarlandes, **2005**.
33. Christian Petersen. Mikro- und nanostrukturierte Schichten mittels Gasphasenabscheidung von $[H_2Al(O^tBu)]_2$ für den Einsatz in der Nano-biotechnologie. PhD thesis, Universität des Saarlandes, **2007**.
34. M. Veith, S. Faber, R. Hempelmann, S. Janssen, J. Prewo, and H. Eckerlebe. Synthesis and microstructure of nanostructured Al/Al₂O₃ (H)-composite. *J Mater Sci*, 31(8):2009–2017, **1996**.
35. M. Veith. Molecular precursors for (nano) materials - a one step strategy. *J. Chem. Soc. Dalton Trans.*, (12):2405–2412, **2002**.
36. M. Veith. Single-Source-Precursor CVD: Alkoxy and Siloxy Aluminum Hydrides, volume 9, chapter *Precursor chemistry of advanced materials*, pages 81–100. Springer Berlin / Heidelberg, **2005**.
37. M. Veith, K. Andres, S. Faber, J. Blin, M. Zimmer, Y. Wolf, H. Schnöckel, R. Köppe, R. De Masi, and S. Hüfner. The metastable, glasslike solid-state phase of HAIO and its transformation to Al/Al₂O₃ using a CO₂ laser. *Eur. J. Inorg. Chem.*, (24):4387–4393, **2003**.
38. M Burkhart. Experimentelle und theoretische Untersuchungen zu Hydriden des Aluminiums und Galliums. PhD thesis, Universität des Saarlandes, **2006**.
39. M. Veith, K. Andres, C. Petersen, C. Daniel, C. Holzapfel, and F. Mücklich. Periodical microstructuring of hydride containing metastable aluminumoxide using laser interference metallurgy. *Adv. Eng. Mater.*, 7(1-2):27–30, **2005**.
40. R. Pielaszek, W. Lojkowski, S: Gierlotka, S. Doyle. Error estimation in XRD crystallite size measurements, *Diffusion and defect data*, 114, 313-320, **2006**.
41. E.J.W. Verwey. *Z. Kristallogr.*, 91, 317-320, **1935**.
42. R. Klajn, K.J.M. Bishop, M. Fialkowski, M. Paszewski, C.J. Campbell, T.P. Gray, and B.A. Grzybowski. Plastic and moldable metals by self-assembly of sticky nanoparticle aggregates. *Science*, 316(5822):261–264, **2007**.
43. C.J. Kiely, J. Fink, M. Brust, D. Bethell, and D.J. Schiffrin. Spontaneous ordering of bimodal ensembles of nanoscopic gold clusters, *Nature*, 396, 444-446, **1998**.
44. E.V. Shevchenko, D.V. Talapin, N.A. Kotov, S. O'Brien, and C.B. Murray. Structural diversity in binary nanoparticle superlattices, *Nature*, 439, 55-59, **2006**.
45. G.A. Battiston, G. Carta, G. Cavinato, R. Gerbasi, M. Porchia, and G. Rossetto. MOCVD of Al₂O₃ films using new dialkylaluminum acetylacetonate precursors: Growth kinetics and process yields. *Chem Vapor Depos.*, 7(2):69–74, **2001**.
46. N.A. Patankar. Mimicking the lotus effect: Influence of double roughness structures and slender pillars. *Langmuir*, 20(19):8209–8213, **2004**.
47. S. Iijima. Helical microtubules of graphitic carbon. *Nature*, 354(6348):56–58, **1991**.
48. R.H. Baughman, A.A. Zakhidov, and W.A. De Heer. Carbon nanotubes - the route toward applications. *Science*, 297(5582):787–792, **2002**.
49. Y. Xia, P. Yang, Chemistry and physics of nanowires, *Adv. Mater.*, 15, 351-352, **2003**.

50. Y. Xia, P. Yang, Y. Sun, B. Mayers, Y. Yin, F. Kim, H. Yan, One-dimensional nanostructures: synthesis, characterization and applications, *Adv. Mater.*, 15, 353-389, **2003**.
51. Rao and co review , C.N.R. Rao, F.L. Deepak,G. Gundiah, A. Govindaraj, inorganic nanowires, *Prog. Solid State Ch.*, 31 (1-2),5-147, **2003**
52. J.G. Lu, P. Chang, Z. Fan, Quasi-one-dimensional metal oxide materials-Synthesis, properties and applications, *Mater. Sci. Eng. R.* 52 (1-3) 49-91, **2006**.
53. S.V.N.T. Kuchibhatla, A.S. Karakoti, D. Bera, and S. Seal. One dimensional nanostructured materials. *Prog Mater Sci*, 52(5):699–913, **2007**.
54. B. Mayers and Y. Xia. Formation of tellurium nanotubes through concentration depletion at the surfaces of seeds. *Adv. Mater.*, 14(4):279–282, **2002**.
55. B. Gates, Y. Yin, Y. Xia, A solution-phase approach to the synthesis of uniform nanowires of crystalline selenium with lateral dimensions in the range of 10-30 nm *J. Am. Chem. Soc.*, 122, 12582-12583, **2000**.
56. M. Motoyama, Y. Fukunaka, T. Sakka, Y. Ogata, Initial stages of electrodeposition of metal nanowires in nanoporous templates *Electrochim. Acta*, 53, 205-212, **2007**.
57. X.F. Shao, X.L. Wu, G.S. Huang, T. Qiu, M. Jiang, and J.M. Hong. Alumina nanotubes and nanowires from al-based porous alumina membranes. *Appl Phys A*, 81(3):621–625, **2005**.
58. A. Huczko, Template-based synthesis of nanomaterials *Appl Phys A, Springer-Verlag GmbH & Company KG*, 70, 365-376, **2000**.
59. J. A Hulteen, general template-based method for the preparation of nanomaterials *J. Mater. Chem.*,7, 1075-1087, **1997**.
60. J.M. Blakely, K.A. Jackson, Growth of Crystal Whiskers *J. Chem. Phys., AIP*, 37, 428-430, **1962**.
61. R.S. Wagner and W.C. Ellis, Vapor-liquid-solid mechanism of single crystal growth, *Appl. Phys. Lett.*, 4, 89-90, **1964**.
62. Y. Wu and P. Yang. Direct observation of vapor-liquid-solid nanowire growth. *J. Am. Chem. Soc.*, 123(13):3165–3166, **2001**.
63. C. Xu, G. Xu, Y. Liu, and G. Wang. A simple and novel route for the preparation of ZnO nanorods, *Solid State Commun.*, 122, 175-179, **2002**.
64. C. Xu, G. Xu, and G. Wang. Preparation and characterization of NiO nanorods by thermal decomposition of NiC₂O₄ precursor, *J. Mater. Sci.*, 38, 779-782, **2003**.
65. C. Xu, X. Zhao, S. Liu, and G. Wang. Large-scale synthesis of rutile SnO₂ nanorods, *Solid State Commun*, 125, 301-304, **2003**.
66. S. Lin, M. Li, E. Dujardin, C. Girard, and S. Mann. One-dimensional plasmon coupling by facile self-assembly of gold nanoparticles into branched chain networks. *Adv Mater*, 17(21):2553–2559, **2005**.
67. X. Li, X. Wang, Q. Xiong, and P.C. Eklund. Top-down structure and device fabrication using in situ nanomachining. *Appl Phys Lett*, 87(23):1–3, **2005**.

References

68. Y. Sun, D.-Y. Khang, F. Hua, K. Hurley, R.G. Nuzzo, and J.A. Rogers. Photolithographic route to the fabrication of micro/nanowires of iii-v semiconductors. *Adv. Funct. Mater.*, 15(1):30–40, **2005**.
69. Q. Li and C. Wang. One-step fabrication of uniform Si-core/CdSe-sheath nanocables. *J. Am. Chem. Soc.*, 125(33):9892–9893, **2003**.
70. Y.-J. Hsu and S.-Y. Lu. One-step preparation of coaxial CdS-ZnS nanowires. *Chem. Commun.*, 10(18):2102–2103, **2004**.
71. Y.-J. Hsu, S.-Y. , and Y.-F. Lin. One-step preparation of coaxial CdS-ZnS and Cd_{1-x}Zn_xS-ZnS nanowires. *Adv. Funct. Mater.*, 15(8):1350–1357, **2005**.
72. Y. Wang Z. L. Ma, C. Berta. Patterned nanowires produced by electron beam at the surface of AlF₃ single crystals. *Solid State Commun.*, 129 (10):681–685, **2004**.
73. V. Valcarcel, A. Souto, and F. Guitián. Development of single-crystal α -al₂o₃ fibers by vapor-liquid-solid deposition (VLS) from aluminum and powdered silica, **1998**.
74. J. Zhou, S.Z. Deng, J. Chen, J.C. She, and N.S. Xu. Synthesis of cyrstalline alumina nanowires and nanotrees, *Chem. Phys. Lett.*, 365, 505-508, **2002**.
75. X.S. Peng, L.D. Zhang, G.W. Meng, X.F. Wang, Y.W. Wang, C.Z. Wang, and G.S. Wu. Photoluminescence and infrared properties of α -Al₂O₃ nanowires and nanobelts, *J. Phys. Chem. B*, 106, 11163-11167, **2002**.
76. Z. Yuan, H. Huang, and S. Fan. Regular alumina nanopillar arrays. *Adv Mater*, 14(4):303–306, **2002**.
77. Z.L. Xiao, C.Y. Han, U. Welp, H.H. Wang, W.K. Kwok, G.A. Willing, J.M. Hiller, R.E. Cook, D.J. Miller, and G.W. Crabtree. Fabrication of alumina nanotubes and nanowires by etching porous alumina membranes, *Nano. Lett.* 2, 1293-1297, **2002**.
78. X.F. Shao, X.L. Wu, G.S. Huang, T. Qiu, M. Jiang, and J.M. Hong. Alumina nanotubes and nanowires from Al-based porous alumina membranes. *Appl Phys A*, 81(3):621–625, **2005**.
79. J. Kim, Y.C. Choi, K.-S. Chang, and S.D. Bu. Direct observation of alumina nanowire formation from porous anodic alumina membrane via the droplet etching method. *Nanotechnology*, 17(2):355–359, **2006**.
80. H.C. Lee, H.J. Kim, S.H. Chung, K.H. Lee, H.C. Lee, and J.S. Lee. Synthesis of unidirectional alumina nanostructures without added organic solvents, *J. Am. Chem. Soc.*, 125, 2882-2883, **2003**.
81. B. Tang, J. Ge, L. Zhuo, G. Wang, J. Niu, Z. Shi, and Y. Dong. A facile and controllable synthesis of γ -Al₂O₃ nanostructures without a surfactant. *Eur. J. Inorg. Chem.*, (21):4366–4369, **2005**.
82. Q. Zhao, X. Xu, H. Zhang, Y. Chen, J. Xu, and D. Yu. Catalyst-free growth of single-crystalline alumina nanowire arrays. *Appl Phys A*, 79(7):1721–1724, **2004**.
83. Q. Zhao, X.-Y. Xu, H.-Z. Zhang, Y.-F. Chen, J. Xu, and D.-P. Yu. Synthesis and characterization of single-crystalline alumina nanowires. *Trans Nonferrous Met Soc China*, 15(2):306–309, **2005**.

84. C.Y. To, L.Y. Cheung, Y.F. Li, K.C. Chung, D.H.C. Ong, and D.H.L. Ng. Synthesis of ultra thin α -alumina nanobelts from aluminum powder by chemical vapor deposition. *J. Eur. Ceram. Soc.*, 27(7):2629–2634, **2007**.
85. G. Gundiah, F.L. Deepak, A. Govindaraj, and C.N.R. Rao. Carbothermal synthesis of the nanostructures of Al_2O_3 and ZnO, *Top. Catal.*, 24, 137-146, **2003**.
86. G. Gundiah, A. gavindaraj, C.N.R. Rao, Nanowires, nanobelts and related nanostructures of Ga_2O_3 , *Chem. Phys. Lett.*, 351, 189-194, **2002**.
87. D.H.L. Ng, P. Yu, N.G. Ma, C.K. Lo, W.Y. Kwok, M.Y. Yau, C.Y. To, T.K. Li, and C.-J. Deng. Formation of micron-sized and nanometer-sized single crystal alumina whiskers by displacement reactions. *J. Eur. Ceram. Soc.*, 26(9):1561–1565, **2006**.
88. H.-J. Choi, J.H. Shin, K. Suh, H.-K. Seong, H.-C. Han, and J.-C. Lee. Self-organized growth of Si/silica/ $\text{Er}_2\text{Si}_2\text{O}_7$ core-shell nanowire heterostructures and their luminescence. *Nano Lett.*, 5(12):2432–2437, **2005**.
89. C. Baban, Y. Toyoda, and M. Ogita. Oxygen sensing at high temperatures using Ga_2O_3 films. *Thin Solid Films*, 484(1-2):369–373, **2005**.
90. M. Ogita, S. Yuasa, K. Kobayashi, Y. Yamada, Y. Nakanishi, and Y. Hatanaka. Presumption and improvement for gallium oxide thin film of high temperature oxygen sensors. *Appl Surf Sci*, 212-213, 397–401, **2003**.
91. G.X. Liu, F.K. Shan, J.J. Park, W.J. Lee, G.H. Lee, I.S. Kim, B.C. Shin, and S.G. Yoon. Electrical properties of Ga_2O_3 -based dielectric thin films prepared by plasma enhanced atomic layer deposition (PEALD). *J Electroceram*, 17(2-4):145–149, **2006**.
92. J. Hao, Z. Lou, I. Renaud, and M. Cocivera. Electroluminescence of europium-doped gallium oxide thin films. *Thin Solid Films*, 467(1-2):182–185, **2004**.
93. M. Rebien, W. Henrion, M. Hong, J.P. Mannaerts, and M. Fleischer. Optical properties of gallium oxide thin films. *Appl Phys Lett*, 81(2):250, **2002**.
94. M.F. Al-Kuhaili, S.M.A. Durrani, and E.E. Khawaja. Optical properties of gallium oxide films deposited by electron-beam evaporation. *Appl Phys Lett*, 83(22):4533–4535, **2003**.
95. Y. Kokubun, K. Miura, F. Endo, and S. Nakagomi. Sol-gel prepared β - Ga_2O_3 thin films for ultraviolet photodetectors. *Appl Phys Lett*, 90(3), **2007**.
96. M. Ogita, K. Higo, Y. Nakanishi, and Y. Hatanaka. Ga_2O_3 thin film for oxygen sensor at high temperature. *Appl Surf Sci*, 175-176:721–725, **2001**.
97. D.H. Kim, S.H. Yoo, T.-M. Chung, K.-S. An, H.-S. Yoo and Y. Kim. Chemical vapor deposition of Ga_2O_3 thin films on Si. *Bull. Korean Chem. Soc.*, 23, 225–228, **2002**.
98. H.W. Kim and N.H. Kim. Growth and structural properties of gallium oxide nanowires prepared by chemical vapour deposition. *Adv. Appl. Ceram.*, 105(2):84–87, **2006**.
99. P. Viste, I. Colombier, F. Donatini, J.C. Vial, P. Baldeck, R. Herino, A. Duc-Maugé, J. Godfroyd, Y. Lacroute, and M. Sacilotti. Optical and structural studies of GaN 3D structures selectively grown by MOCVD. *J Cryst Growth*, 272(1-4 SPEC. ISS.):466–474, **2004**.

References

100. G.A. Battiston, R. Gerbasi, M. Porchia, R. Bertinello, and F. Caccavale. Chemical vapour deposition and characterization of gallium oxide thin films. *Thin Solid Films*, 279(1-2):115–118, **1996**.
101. L. Mîinea, S. Suh, S.G. Bott, J.-R. Liu, W.-K. Chu, and D.M. Hoffman. Synthesis of aluminium and gallium fluoroalkoxide compounds and the low pressure metal-organic chemical vapor deposition of gallium oxide films. *J. Mater. Chem.*, 9(4):929–935, **1999**.
102. M. Valet and D.M. Hoffman. Synthesis of homoleptic gallium alkoxide complexes and the chemical vapor deposition of gallium oxide films. *Chem. Mater.*, 13(6):2135–2143, **2001**.
103. K.-W. Chang and J.-J. Wu. Low-temperature growth of well-aligned β -Ga₂O₃ nanowires from a single-source organometallic precursor. *Adv Mater*, 16(6):545–549, **2004**.
104. H.W. Kim, N.H. Kim, and C. Lee. Growth of Ga₂O₃ thin films on Si(100) substrates using a trimethylgallium and oxygen mixture. *J Mater Sci*, 39(10):3461–3463, **2004**.
105. S. Fujihara, Y. Shibata, and E. Hosono. Chemical deposition of rodlike GaOOH and β -Ga₂O₃ films using simple aqueous solutions. *J Electrochem Soc*, 152(11), **2005**.
106. F.K. Shan, G.X. Liu, W.J. Lee, G.H. Lee, I.S. Kim, and B.C. Shin. Ga₂O₃ thin film deposited by atomic layer deposition with high plasma power. *Integr Ferroelectr*, 80(1):197–206, **2006**.
107. M. Ogita, N. Saika, Y. Nakanishi, and Y. Hatanaka. Ga₂O₃ thin films for high-temperature gas sensors. *Appl Surf Sci*, 142(1):188–191, **1999**.
108. H.J. Chun, S.Y. Bae, and J. Park. Controlled structure of gallium oxide and indium oxide nanowires. *Quantum Dots, Nanoparticles and Nanowires*, 789, 291–296, Boston, MA, **2003**.
109. F. Zhu, Z. Yang, W. Zhou, and Y. Zhang. Synthesis of β -Ga₂O₃ nanowires through microwave plasma chemical vapor deposition. *Appl Surf Sci*, 252(22):7930–7933, **2006**.
110. K.-W. Chang and J.-J. Wu. Low-temperature growth of well-aligned β -Ga₂O₃ nanowires from a single-source organometallic precursor. *Adv Mater*, 16(6):545–549, **2004**.
111. M. Sacilotti, L. Imhoff, S. Bourgeois, C. Dumas, J. Decobert, P. Baldeck, and I. Colombier. MOCVD growth of Ga 3D structures for fabrication of GaN materials. *J Cryst Growth*, 261(2-3):253–258, **2004**.
112. L. Imhoff, M. Sacilotti, C.J. Courty, M. Mesnier, M.C. Marco De Lucas, and S. Bourgeois. Structural characterization of original 3D gallium structures grown by LP-MOCVD. *Phys. Status Solidi C Conf., Couches Minces et Nanostructures*, 1, 388–391, **2004**.
113. L. Imhoff et al. hemical characterization of gallium droplets grown by LP-MOCVD. *Appl Surf Sci*, 253(5):2820–2824, **2006**.
114. J. Zhan, Y. Bando, J. Hu, F. Xu, and D. Golberg. Unconventional gallium oxide nanowires. *Small*, 1(8-9):883–888, **2005**.
115. W.Q. Han, P. Kohler-Redlich, F. Ernst, and M. Rühle. Growth and microstructure of Ga₂O₃ nanorods, 10, 527-529, **2000**.
116. G.-S. Park, W.-B. Choi, J.-M. Kim, Y.C. Choi, Y.H. Lee and C.-B. Lim. Structural investigation of β -Ga₂O₃ nanowires grown by arc-discharge. *J Cryst Growth*, 220, 494 **2000**.
117. Shriver D. F., S.A.E. Trihydrido(Trimethylamine)Gallium *inorganic syntheses*, 17, 42 , **1977**.
118. M. Veith; C. Petersen, E. A. Sow. Fabrication of metal nanowires with an oxide covering layer. Application: DE 2006-102006013484 20060323. Priority: CAN 147:396800; **2007**.

Figures

Figure 2-1: Schematic representation of the key steps of the CVD process.	8
Figure 2-2: Molecular structure of the precursor $[H_2Al(OtBu)]_2$ as described in reference 27.....	11
Figure 2-3: Reaction of $[H_2Al(O^tBu)]_2$ in the CVD apparatus at low temperature ($< 530\text{ }^\circ\text{C}$).....	13
Figure 2-4: Reaction of $(HAIO)_n$ during annealing.....	14
Figure 2-5: Reaction of $[H_2Al(O^tBu)]_2$ in the CVD apparatus above $450\text{ }^\circ\text{C}$	15
Figure 2-6: Summary about the layers obtained after direct CVD of $[H_2Al(O^tBu)]_2$	16
Figure 2-7: Molecular structures of the precursors $[H_2Ga(O^tBu)]_2$ and $[HGa(OtBu)]_2$ as described in reference 28.....	17
Figure 2-8: Decomposition of $[HGa(O^tBu)]_2$ during CVD process.	18
Figure 2-9: Decomposition of $[H_2Ga(O^tBu)]_2$ during CVD at $250\text{ }^\circ\text{C}$	19
Figure 3-1: Pictures of films from $[H_2Al(O^tBu)]_2$ deposited by MOCVD on steel target at $490\text{ }^\circ\text{C}$, $450\text{ }^\circ\text{C}$ and $600\text{ }^\circ\text{C}$	27
Figure 3-2: Typical representative XRD pattern of a composite layer	28
Figure 3-3: ESCA spectrum of a typical Al/Al_2O_3 layer and enlargement on the aluminium band.....	29
Figure 3-4: XRD of Al/Al_2O_3 layers grown at $600\text{ }^\circ\text{C}$ at low deposition rate overview (above) and magnification (below), where aluminium carbide [PDF 79-1736] crystals are detected.	31
Figure 3-5: Evolution of the aluminium crystallites by increasing deposition time: focus on (111) aluminium peak of XRD pattern of precedent figure (Fig. 3-4).....	32
Figure 3-6: Calculated grain size of aluminium particles for layers grown with $[H_2Al(O^tBu)]_2$ at $600\text{ }^\circ\text{C}$ at low precursor flow (chamber pressure 3.10^{-2} mbar) by different temperatures.	33
Figure 3-7: Focus on (100) iron peak of XRD pattern of layers grown with $[H_2Al(O^tBu)]_2$ at $600\text{ }^\circ\text{C}$ with low precursor flow (chamber pressure 3.10^{-2} mbar).	34
Figure 3-8: XRD patterns of layers grown with $[H_2Al(O^tBu)]_2$ at $600\text{ }^\circ\text{C}$ at high deposition rate(chamber pressure 3.10^{-1} mbar) and XRD of a layer where Al_4C_3 can be detected after 30 minutes deposition.	36
Figure 3-9: XRD of an Al/Al_2O_3 layer grown by $490\text{ }^\circ\text{C}$ at high precursor flow (chamber pressure 3.10^{-1} mbar): only the substrate peaks are detected.	37
Figure 3-10: XRD pattern of layers grown with $[H_2Al(O^tBu)]_2$ at low precursor rate (chamber pressure 3.10^{-2} mbar) during one hour.....	38
Figure 3-11: Evolution of the aluminium crystals by increasing temperature: focus on (111) aluminium peak of XRD pattern of figure 3-10.....	39
Figure 3-12: Calculated grain size of aluminium particles for layers grown with $[H_2Al(O^tBu)]_2$ during one hour at low precursor flow (chamber pressure 3.10^{-2} mbar).....	39
Figure 3-13: XRD pattern of layers grown with $[H_2Al(O^tBu)]_2$ at high precursor rate (chamber pressure 3.10^{-1} mbar) during one hour.	41
Figure 3-14: XRD pattern of a layer grown with $[H_2Al(O^tBu)]_2$ at $530\text{ }^\circ\text{C}$ during 2 hours at low precursor flow. $\{Al\cdot O\}$ crystals are detected and assigned to $\gamma\text{-}Al_2O_3$ on the graph.	42

Figure 3-15: XRD pattern of two layers showing {Al₂O₃} crystals. The layers are grown at 560 °C, 2h, low precursor flow (above) and at 600 °C, 2h, high precursor flow (below)..... 44

Figure 3-16: XRD pattern of layers with {Al₂O₃} peaks assigned to γ'-Al₂O₃ (or γ-Al₂O₃). The layers are grown at 560 °C, 1h30 with low precursor flow (above), 530 °C, 1h30 with low precursor flow (middle) and 560 °C, 1 minute with high precursor flow (below). 46

Figure 3-17: Instant formation of Al and Al₂O₃ from the unknown {Al₂O₃} phase. 47

Figure 3-18: SEM images of an Al/Al₂O₃ layer grown at 490 °C with a low precursor flow during 10 minutes. Particles (app. 70 nm) aggregate to form chains or bigger particles..... 50

Figure 3-19: SEM images of an Al/Al₂O₃ layer grown at 490 °C with a low precursor flow during 1 hour. Big particles (app. 2 μm) grow densely on the surface. 51

Figure 3-20: SEM images of a layer grown at 490 °C with a high precursor flow during one hour. Big particles (app. 2 μm) grow densely on the surface. 52

Figure 3-21: EDX mapping of aluminium (above), oxygen (below left) and carbon (below right) in the layer grown at 490 °C at low precursor flow during one hour. 53

Figure 3-22: Layer profile: SEM images of a cross section performed by FIB on the Al/Al₂O₃ layer grown one hour at 490 °C at low precursor flow. 54

Figure 3-23: Layer profile: SEM images of a cross section performed by FIB on the Al/Al₂O₃ layer grown one hour at 490 °C at high precursor flow..... 54

Figure 3-24: EDX mapping in the cross section of the layer grown at 490 °C, one hour with low precursor flow. Iron from the substrate (pink) and the protective platinum layer (blue) are detected. Aluminium (turquoise) and oxygen (green) are homogeneously distributed.. 55

Figure 3-25: Ion beam images of the cross section of the Al/Al₂O₃ layer grown at 490 °C, one hour with low precursor flow..... 56

Figure 3-26: EDX mapping in the cross section of the layer grown at 490 °C, one hour with high precursor flow. Iron from the substrate (pink), the protective platinum layer (blue), aluminium (turquoise) and oxygen (green) are detected. 57

Figure 3-27: Region of interest and EDX analysis along a line in the cross section of the Al/Al₂O₃ layer grown at 490 °C, one hour with low precursor flow..... 58

Figure 3-28: Region of interest and EDX analysis along a line in the cross section of a Al/Al₂O₃ layer grown at 490 °C, one hour with high precursor flow. 59

Figure 3-29: Pictures of layers grown one hour at 530 °C at low (left) and high precursor flow (right). 61

Figure 3-30: SEM image of a HAIO-like layer grown one hour at 530 °C at high precursor flow. 61

Figure 3-31: FTIR spectra (Al-H band) of a layer grown one hour at 530 °C at high precursor flow compared to a HAIO layer. 62

Figure 3-32: SEM images of the surface of a layer grown at 530 °C during one hour at low precursor flow. Short Al/Al₂O₃ nanowires are seen. 63

Figure 3-33: SEM images of an Al/Al₂O₃ layer with spherical particles grown one hour at low precursor flow at 560 °C. 64

Figure 3-34: SEM pictures of the background and a spherical particle from precedent figure (fig. 3-34) with 80,000 time magnification. Al/Al₂O₃ nanowires are seen in the background as well as in the particle. 65

Figures

Figure 3-35: SEM image of spherical particles formed on an Al/Al ₂ O ₃ layer grown at 560 °C during 1h30 at low precursor flow.....	66
Figure 3-36: SEM images of an Al/Al ₂ O ₃ layer grown at 560 °C with high precursor flow after 1h deposition	67
Figure 3-37: SEM images of a Al/Al ₂ O ₃ layer grown at high temperature (600 °C) during one minute.	68
Figure 3-38: SEM images of an Al/Al ₂ O ₃ layer grown at high temperature (600 °C) during one hour..	68
Figure 3-39: Contrast enhanced HR- SEM image of nanowires.....	69
Figure 3-40: SEM image of an Al/Al ₂ O ₃ layer with nanowires containing Al ₄ C ₃ and its XRD pattern. ...	70
Figure 3-41: Illustration of the different layers grown by varying deposition conditions. SEM images and composition of the HAIO layer grown at 490 °C, the composite layer with ball like structure grown at 490 °C and the Al/Al ₂ O ₃ nanowires grown above 530 °C	72
Figure 4-1: TEM bright field image of an area of entangled Al/Al ₂ O ₃ nanowires (left) and single nanowires (right) at the border of the TEM grid.....	83
Figure 4-2: bright and dark field images of entangled Al/Al ₂ O ₃ nanowires	84
Figure 4-3: Single Al/Al ₂ O ₃ nanowires with head (left) and core filled with single crystalline aluminium (right).	85
Figure 4-4: Entangled Al/Al ₂ O ₃ nanowires with some heads displaying triple (left) and double (right) nanowires growth	86
Figure 4-5: Dark field imaging of the area where three Al/Al ₂ O ₃ nanowires are branched.	87
Figure 4-6: HRTEM images of an Al/Al ₂ O ₃ nanowire's head with Fourier filtration of the core (above) and the shell (below).	88
Figure 4-7: HRTEM image of a Al/Al ₂ O ₃ nanowire's head with its core and shell. The images with Fourier transform (B, C, D) correspond to the real image (A).	90
Figure 4-8: HRTEM image of the area where three Al/Al ₂ O ₃ nanowires grow from a head. lattice fringes are present in the core of the head and in a crystallite from the nanowire's shell	91
Figure 4-9: Inverse Fourier transform of the signals from the head illustrated on figure 4-8. Two signals for (200) lattice planes are intensified to illustrate the [001] orientation of the head.....	92
Figure 4-10: Masked Fourier transform of Al core and Al ₂ O ₃ crystallite (above). SAED of the same area shows similar lattice spacing for Al core and Al ₂ O ₃ crystallite.....	93
Figure 4-11: Magnification of the masked Fourier transform from figure 4-10. Al core and Al ₂ O ₃ crystallite are oriented with an angle of 28.9 from another.	94
Figure 4-12: Al-core in the nanowire's head displaying lattice fringes (D _n) and nanowire's shell with Al-oxide crystallite displaying lattice fringes (D _c). The area with relatively high coincidence is marked by the square and the boundary between head and nanowire is delimited by the line.	95
Figure 4-13: Representation of the coincidence grain boundary between Al and γ-Al ₂ O ₃ . The atoms circled present perfect coincidence between aluminium and aluminium oxide.....	97
Figure 4-14: HRTEM image with Fourier transform of a double Al/Al ₂ O ₃ nanowire with crystallites on the shell.	98

Figure 4-15: Four images of nanowires with different inclination. The big nanowire in the middle displays a bubble and a twin structure in the core.	99
Figure 4-16: SEM images giving an overview on the Al/Al ₂ O ₃ nanowire structure prepared at high temperature (615 °C) displaying nanoparticles at the surface.	101
Figure 4-17: TEM images of the tip of the Al/Al ₂ O ₃ nanowires with nano-crystallites at the surface (left). Some nanocrytallites are distributed over the surface and gas formation is detected (right).	102
Figure 4-18: EDX analysis of the area where three Al/Al ₂ O ₃ nanowires grow from one head.....	104
Figure 4-19: EDX spectra of the area where three Al/Al ₂ O ₃ nanowires grow from one head. The analysis areas are shown on Figure 4-18.	105
Figure 4-20: EDX analysis of the area where three Al/Al ₂ O ₃ nanowires grow from one head after intense irradiation.	106
Figure 4-21: SAED on an area where Al/Al ₂ O ₃ nanowires are dense.....	107
Figure 4-22: optimised SAED of an area where Al/Al ₂ O ₃ nanowires are dense.	108
Figure 4-23: optimised SAED of an area where Al/Al ₂ O ₃ nanowires are dense with aluminium diffraction arcs marked	109
Figure 4-24: modified SAED of an area where Al/Al ₂ O ₃ nanowires are dense with removed background and accentuated spots.	110
Figure 4-25: Evaluation of diffraction arcs from figure 4-24 with the software <i>digital micrograph</i>	110
Figure 4-26: Binarised SAED of an area where Al/Al ₂ O ₃ nanowires are dense with experimental diffraction arcs.	114
Figure 4-27: Binarised SAED of an area where Al/Al ₂ O ₃ nanowires are dense and elimination of spots which are attributed to aluminium.....	115
Figure 4-28: Figure 4-27 where diffraction arcs from δ -Al ₂ O ₃ (JCPDS 46 1215) are superposed.....	115
Figure 4-29: Original SAED of an area where Al/Al ₂ O ₃ nanowires are dense (Fig. 4-21) masked with a binary image (Fig. 4-26). Spots suspected as artefacts are circled.	116
Figure 4-30: Binarised SAED of an area where Al/Al ₂ O ₃ nanowires are dense with experimental diffraction arcs (fig. 4-26) with suspected spots circled.....	117
Figure 4-31: TEM images of the sample after intensive electron irradiation.....	123
Figure 4-32: EDX analysis of three Al/Al ₂ O ₃ nanowires' heads after irradiation.....	123
Figure 4-33: TEM images showing the chronological progression of the modifications due to irradiation of the Al/Al ₂ O ₃ nanowires.	124
Figure 4-34: HRTEM image of an Al/Al ₂ O ₃ nanowire's head, where some particles have grown.	126
Figure 4-35: TEM image superposed with 5 HRTEM-images of an Al/Al ₂ O ₃ nanowire's head, where some particles have grown.....	127
Figure 4-36: HRTEM structure image (A) of an Al/Al ₂ O ₃ nanowire's head with growing particles and the power spectrum (B). Below, the Fourier filter of the regions marked on the power spectrum (C and D)	128
Figure 4-37: Binarisation of the power spectrum from the Al/Al ₂ O ₃ nanaowire's head.....	129
Figure 4-38: Localisation of three regions with different phases on the Al/Al ₂ O ₃ nanaowire's head. .	130

Figures

Figure 4-39: HRTEM image of the Al/Al ₂ O ₃ nanoowire's head after exposure to air and weak electron irradiation. Effects of irradiation are reversible.	131
Figure 4-40: TEM image of Al/Al ₂ O ₃ nanowires during heating process.	132
Figure 4-41: Evolution of the Al/Al ₂ O ₃ nanowires and the aluminium particles with varying temperature from 300 ° to 500 °C.	133
Figure 4-42: Electron diffraction analysis of aluminium particles grown on the C- film.	134
Figure 4-43: SAED of the particles grown on C-film superposed with diffraction arcs of aluminium ..	136
Figure 4-44: Bright field images of the Al/Al ₂ O ₃ nanowires' structure at different temperatures from 25 °C to 800 °C.	137
Figure 4-45: Contrast enhanced images of Al/Al ₂ O ₃ nanowires and C-film with residual shells.	138
Figure 5-1: SEM image of the Ga/Ga ₂ O ₃ layer grown at 400 °C.	143
Figure 5-2: SEM images of the gallium droplets grown at 500 °C.	143
Figure 5-3: SEM image of the gallium droplets grown on stainless steel at 500 °C after 30 days aging. gallium droplets have flowed.	144
Figure 5-4: SEM images of Ga/Ga ₂ O ₃ layers grown at 550 °C, 600 °C and 630 °C.	146
Figure 5-5: XRD and EDX analysis of a Ga/Ga ₂ O ₃ layer grown at 600 °C.	148
Figure 5-6: SEM images of an inhomogeneous Ga/Ga ₂ O ₃ layer grown at 600 °C at high precursor flow and magnification on different areas.	149
Figure 5-7: SEM images of a layer grown on cooper at 200 °C by CVD of [H ₂ Ga(O ^t Bu) ₂] ₂	150
Figure 5-8: SEM images of a Ga/Ga ₂ O ₃ layer grown on cooper at 300 °C.	151
Figure 5-9: Magnification on the layer shown on figure 5-8, shows islands with nanowires.	151
Figure 5-10: XRD pattern of a Ga/Ga ₂ O ₃ layer grown on cooper at 300 °C	152
Figure 5-11: SEM images of Ga/Ga ₂ O ₃ layers grown at 500 °C on cooper with different conditions. a- Room temperature, 1h; b- 0° C, 1h; c- Room temperature 5 Min; d- Room temperature 10 min, impure precursor.	153
Figure 5-12: Magnification of the Ga/Ga ₂ O ₃ layers shown on Figure 5-11.	154
Figure 5-13: SEM images of different areas of an inhomogeneous Ga/Ga ₂ O ₃ layer grown at 500 °C, 3 hours on cooper with high precursor flow.	156
Figure 5-14: SEM images of areas with interesting morphologies from the Ga/Ga ₂ O ₃ layer shown in figure 5-13.	157
Figure 5-15: SEM images of Ga/Ga ₂ O ₃ nanowires grown on Si (100) at 500 °C.	159
Figure 5-16: SEM images of Ga/Ga ₂ O ₃ nanowires grown on Si (100) at 550 °C.	160
Figure 5-17: EDX analysis of the Ga/Ga ₂ O ₃ nanowires grown on Si (100).	160
Figure 5-18: SEM images of the Ga/Ga ₂ O ₃ 3D cauliflower like structure grown at 600 °C on Si(100).	161
Figure 5-19: cauliflower-like Ga/Ga ₂ O ₃ layer grown after long deposition (3 hours) at 600 °C.	162
Figure 5-20: XRD of the cauliflower-like Ga/Ga ₂ O ₃ layer grown after long deposition at 600 °C.	163
Figure 5-21: EDX mapping of the cauliflower-like Ga/Ga ₂ O ₃ layer grown after long deposition at 600 °C.	163

Figure 5-22: Comparison between XRD pattern after and before annealing. Overview on the whole diffractogramm and magnification on the area between $2\theta = 30^\circ$ and 50° to show that all the peaks increased after annealing.	165
Figure 5-23: SEM image of the cauliflower-like Ga/Ga ₂ O ₃ layer grown during 3 hours at 600 °C after annealing.	166
Figure 5-24: SEM images of a layer grown with both precursor ([H ₂ Ga(O ^t Bu)] ₂ and [H ₂ Al (O ^t Bu)] ₂) at 600 °C at the same time.	167
Figure 5-25: SEM image of the edges of a layer grown with [H ₂ Ga(O ^t Bu)] ₂ and [H ₂ Al (O ^t Bu)] ₂ at the same time.	168
Figure 6-1: Two main morphologies for Al/Al ₂ O ₃ layers. At 490 °C: Al ₂ O ₃ spheres with bigger Al crystals fractally distributed in the Al ₂ O ₃ spheres. Above 530 °C: entangled nanowires.	171
Figure 6-2: Single Al/Al ₂ O ₃ nanowires with head (left) and core filled with single crystalline aluminium (right).	171
Figure 6-3: HRTEM shows that Al core and Al ₂ O ₃ crystallite are oriented with an angle of 28.9 from another.	172
Figure 6-4: Schematic illustration of the self-catalytic growth for the synthesis of Al/Al ₂ O ₃ core shell nanowires. (A) Formation of aluminium nanoclusters on the surface. (B) Accumulation of {Al·O} in the Al catalyst and formation of Al-Al-O alloy. (C) Growth of {Al·O} nanowires by precipitation of supersaturated {Al·O} like in VLS process (D) Al segregates to the inside while the Al ₂ O ₃ shell is formed.	173
Figure 6-5: SEM images showing the different structures obtained by CVD of [H ₂ Ga(O ^t Bu)] ₂ on metal surfaces (gallium droplets, small nanowires, big nanowires with particles at the surface).	174
Figure 6-6: SEM image of self aligned Ga/Ga ₂ O ₃ nanorods and of self aligned 3D structures with gallium droplet at the tip. Schematic representation of a Ga/Ga ₂ O ₃ 3D nanostructure.	174
Figure 6-7: SEM images of 3D Ga/Ga ₂ O ₃ structures before and after annealing.	175
Figure 7-1: Schematic representation of a CVD apparatus	176

Tables

Table 3-1: Temperature correspondences	26
Table 3-2: Crystallographic data of γ -Al ₂ O ₃ from PDF 75-921 compared to the measured peaks from figure 3-16.....	43
Table 3-3: Crystallographic data of γ -Al ₂ O ₃ from PDF 10-425. The marked areas correspond to the peaks detected by XRD on figure 3-15.	45
Table 3-4: Overview on the crystallinity of the layers obtained by CVD of [H ₂ Al(O ^t Bu)] ₂	48
Table 4-1: Evaluation of the d-spacing of the diffraction arcs from figure 4-25.....	113
Table 4-2: Results of SAED analysis and comparison with δ -Al ₂ O ₃	118
Table 4-3: Possible aluminium oxides	119
Table 4-4: Results of SAED analysis and comparison with θ -Al ₂ O ₃	120
Table 4-5: Results of electron diffraction measurements of the particles on carbon film	135
Table 7-1: Summary of the layers grown by MOCVD of [H ₂ Al (O ^t Bu)] ₂ . A is light grey, the microstructure shows spheres.....	184

Lebenslauf

Geboren am 28. August 1979

Staatsangehörigkeit: französisch

Familienstand: ledig

Studium

Seit 2004	Promotion unter Leitung von Prof. Dr. Veith „Importance of CVD-process parameters for the synthesis of Al/Al ₂ O ₃ and Ga/Ga ₂ O ₃ composite nanostructures“, Institut für anorganische Chemie, Universität des Saarlandes (UdS), Saarbrücken, angestrebter Abschluss: Mai-Juni 2008
03/2004	Doppeldiplom Werkstofftechnik der Universität des Saarlandes und der Ecole Européenne d'Ingénieurs en Génie des Matériaux, Diplomarbeit zum Thema „Herstellung dünner Polyurethan-Schichten auf Aluminium, Kupfer und Gold“ bei der Arbeitsgruppe Strukturforschung, Polymere und Grenzschichten, Prof. Dr. rer. nat. habil. Wulff Possart
03/2002- 03/2004	Studium der Werkstofftechnik, UdS, Saarbrücken Stipendium der Deutsch-Französische Hochschule
09/2000- 03/2002	Studium der Werkstofftechnik, Ecole Européenne d'Ingénieurs en Génie des Matériaux, Nancy, Frankreich
09/1999- 06/2000	Licence de Chimie, Université Saint Jérôme, Marseille, Frankreich
09/1997-09/1999	DEUG sciences et technologie (Vordiplom), Université Saint Jérôme, Marseille, Frankreich
07/1997	Abitur (Schwerpunkt Naturwissenschaften), Martigues, Frankreich

Berufserfahrung

- Seit 01/2008 Wissenschaftliche Mitarbeiterin an dem Leibniz Institut für neue Materialien, Saarbrücken
- 03/2004- 12/2007 Wissenschaftliche Mitarbeiterin an dem Institut für anorganische Chemie, UdS, Saarbrücken
- Promotion
 - Betreuung von Praktika für Studenten höherer Semester
 - Betreuung von Vertiefungsarbeiten
 - Partnerschaft mit GRK 532: „Physikalische Methoden in der strukturellen Erforschung neuer Materialien“
- 06/2003- 12/2003 Wissenschaftliche Hilfskraft, Arbeitsgruppe Strukturforschung, Polymere und Grenzschichten, UdS, Saarbrücken

Praktika

- 01/2004-02/2004 Decoma GmbH, Sulzbach
Abteilung Quality Management,
Werkstoffprüfung an Kunststoffteilen für Fahrzeugaußenteile und –
komponenten, Prüfung lacktechnologischer Eigenschaften nach
Kundenspezifikationen, Wareneingangsprüfung
- 07/2001- 08/2001 Gebrüder Dorfner GmbH & Co., Hirschau
Quantitative und qualitative Bestimmung der Qualität der Roherde vom
zukünftigen Abbaugelände der Lagerstätte

